Spectroscopic Studies of Hot, Luminous Stars

Kaj Wik Siebert

Thesis submitted for the degree of Doctor of Philosophy
of the University of London.

Department of Physics & Astronomy
University · College · London

January 1999

Til

Tia og David

and

in loving memory of

Grandpa

Abstract

Results of detailed spectroscopic analyses of selected early-type stars are presented. Atmospheric parameters are derived for 23 O-type stars by comparing high-resolution echelle observations with hydrogen/helium non-LTE model spectra. Effective temperatures, surface gravities and helium abundances are derived for each star, and the effects of microturbulence on the adopted parameters are investigated.

The derived helium abundances are considered in an evolutionary context, concentrating on trying to understand the chemically divergent OC/ON stars. A clear relation between carbon/nitrogen abundance anomalies and derived helium number fractions is found. Other possible explanations for the observed abundance anomalies are considered.

There has also been proposed (and appears to be) a relation between the line broadening in early-type stars and their surface chemical composition. Two possible sources for line broadening, stellar rotational and macroturbulence, are considered and the 'best-fit' broadening type is found by careful fitting of stellar absorption lines. Both macroturbulent and rotational velocities are derived for the O-star sample.

A statistical analysis of the line-broadening properties of early-type stars is also undertaken. By cross-correlating *International Ultraviolet Explorer* spectra of B stars against several stellar template spectra, the effects of line-broadening on the cross-correlation functions (CCFs) are investigated, and calibrations between CCF full-width half-maximum and rotational velocity are derived. These calibrations are used to find rotational velocities for over 700 stars.

Contents

List of Figures

List of Tables

Acknowledgements

The work done in this thesis would not have been possible without the help of many people. I'm indebted to my supervisor, Ian Howarth, for his expert guidance and our many discussions about astronomy. I'm especially grateful for his careful reading of this work. His numerous comments and suggestions have been of great help. Secondly, Keith C. Smith has been invaluable throughout this project. The model grids and many of the analysis codes were written by him, and I hope that this thesis shows that I understood at least a few of the things he tried to explain to me. Thanks are also due to my second supervisor, Raman K. Prinja, for his encouraging comments and always cheerful attitude. A special thanks is also due to Tony Lynas-Gray for lending me his lecture notes on stellar astrophysics and for many drinks/dinners etc. (The list is too long to include here, but I'm sure Tony can remember them all.) Thanks also to Serena for being my 'presence' in college ... without you I would never have had any papers, Ian would never have received anything from me, and people would have thought I'd gone missing (hang on — they did think that didn't they?).

This work could also not have been done (or should that be 'would have been done a lot quicker'?) without the A25/Dive Control Centre mob: Andy (for being a very good friend), Chris E. (for asking very simple questions which turn out to be extremely difficult to answer; MAMBO), Matthew (for lying on the floor so I had someone to step on) and Richard (for this LaTeX style file, xpilot and ALSorts-of-stuff).

A very warm thanks to Susan for her artistic influences. I really hope some of her talents have 'leaked' into this work. I also hope that Adrian has taught me to design and build a solid foundation for my work (and I could always ask Andy Richardson for help if the plaster is cracking – or I could copy Chris 'Mental/Palm-master' J. and knock a big hole in the wall instead). Thanks to Orsola and Nic for the use of their kitchen-shower, to the Smog-Dog for *Zzzzz* 'or something', til OK, Monica og Anne for alle de

oppmuntrende e-postene, to Debs and Phil for all the cakes, chocolates and biscuits, to Yiannis for making us wait in Warren Street station for two hours, and to all the 'little ones': Tammay, Richard P., Greg and everyone else I can't list here.

I would also like to thank my family for all their help and support, and especially to Nana, Grandpa, John and Kate both for their financial support and for always being there for me.

Tusen takk til hele min norske familie, særlig Lilla og Anton, fordi dere alltid var entusiastiske og snille, og alltid ga meg støtte hvis jeg trengte det. Og selvfølgelig til Tia og David: Tusen takk for alt. Dere er de beste foreldre i hele verden!

E alla fine, grazie tanto a Serena perché sei la mia 'Bella'.

Chapter 1

Introduction

This thesis discusses the spectroscopic properties of hot, luminous stars. The term 'hot stars' is used to mean all normal stars of spectral types O and B (OB for short); 'luminous' means luminosity classes I–V. The terms 'hot stars', 'early-type stars' and 'OB stars' will be used synonymously in this work. The thesis is roughly divided into two parts; part one (chapters 4 – 6) will deal with analyses of high-resolution, high signal-to-noise optical observations of 23 late-type O stars, and a discussion of the significance of the results. Part two (chapter 7) will investigate the line broadening parameter, $v_e \sin i$, by cross-correlating high-resolution, short-wavelength *IUE* data, and expand the work of Howarth et al. (1997b) to include more stars, especially B-stars.

The properties of early-type stars are of interest for a variety of reasons. These stars live relatively short, but violent, lives. During the main stages of their life cycles, they lose a significant amount of mass through their stellar winds (e.g. Puls et al., 1996) and this mass loss can affect their evolution substantially (Maeder and Meynet, 1987). The stellar winds can also have a great effect on the interstellar medium (ISM) surrounding the star, both kinetically heating it and enriching it with nuclear processed material (e.g. Castor, 1993). At the end of their lives, they may inject vast amounts of enriched material into the ISM as Wolf-Rayet stars and/or supernovae.

Lately, thanks to the new generation of large telescopes and sensitive detectors, observations of single early-type stars in other galaxies have become more and more common. It has been possible to investigate, among other things, metallicity gradients in nearby galaxies (Monteverde et al., 1997; Monteverde and Herrero, 1998). Also, very recently, many high-redshift faint, blue galaxies were discovered in the Hubble Deep Field (Williams

et al., 1996). Although it will, probably, never be possible to observe individual stars in these galaxies, the early-type stars are apparently a major contributor to the galaxies' overall luminosity. If we could learn more about the early-type stars in these galaxies, we should be able to tell a lot about the conditions in the early universe, the early populations of stars, and the star-forming history of the early universe (e.g. Franceschini et al., 1998).

1.1 Spectroscopic properties

The optical spectra of O and B stars are dominated by absorption lines of neutral hydrogen (H I in spectroscopic notation) and neutral helium (He I). For the O stars, singly ionised helium (He II) also becomes increasingly important, increasing in strength towards the earlier (hotter) types; whereas He I (which is at its strongest around B2 – B3) slowly decreases in strength towards hotter types. The He II lines, having only one electron orbiting the nucleus, behave spectroscopically very much like those of neutral hydrogen, and the lines are often grouped into the Pickering series (analogous to the Bracket, $n \rightarrow 3$, series of hydrogen) with lines at $\lambda\lambda$5411, 4860, 4541, 4339, 4200, 4100, 4025 and 3968Å etc., and the Fowler series (analogous to Paschen, $n \rightarrow 4$, series of hydrogen) with lines at $\lambda\lambda$4686, 3204Å etc.

Several other atomic species can also be observed in the optical; in particular, carbon, oxygen, nitrogen and silicon. At later spectral types, especially in the late-B stars, other metals become increasingly more important. For the highest-luminosity stars, several of these lines can sometimes be seen in emission. There are also many 'dynamic' features in the spectra. P Cygni profiles, signatures of mass-loss and stellar winds, are often observed, especially in the Balmer-α (Hα) line. Wind effects are even more obvious in the UV, often seen in the resonance doublets, C IV $\lambda\lambda$1548, 1551Å, Si IV $\lambda\lambda$1394, 1402Å, and Ni V $\lambda\lambda$1249, 1242Å. These lines are extremely sensitive to the effects of stellar wind, and are often used to 'probe' these effects (e.g. Howarth and Prinja, 1989).

1.2 Spectroscopic classifications

With a huge number of observable stars in the Galaxy (a number which is constantly growing thanks to technological advances for both detectors and telescopes), it is clear that the stars somehow need to be grouped together to make a more manageable dataset. As an example of the number of observable stars, the original version of the Henry Draper

(HD; Cannon and Pickering, 1918) catalogue contained 225,300 stars. The Guide Star Catalogue[1], contains the positions of over 1.9×10^7 stars between magnitudes six and fifteen. To make interpretation of this number of stars more manageable, the stars are grouped into spectral types.

1.2.1 Harvard and Yerkes classifications

The basis for most 'modern' spectral types is rooted in the development of the letter based classifications of the Harvard scheme. At first, the stars were divided into spectral classes symbolized by capital letters (introduced by Edward C. Pickering), arranged in alphabetical order, starting with class A, which contained stars with only hydrogen series visible (and interstellar Ca K lines) at the low dispersion used. In class B, the lines in class A were supplemented with He I λ4026Å and λ4471Å. Class C contained stars of spectral types A and B but with Hδ and Hγ observed as double lines. The order of the classifications was later revised, and some types (like class C above) were suppressed. The main groups were later complemented by Annie J. Cannon with subdivisions denoted by numbers from zero to nine, except for the O and M stars. For these groups, lower case letters were used to denote the subtypes. The final order of the classifications is:

O – B – A – F – G – K – M

This order is related to temperature, with O being hottest, and M coldest. Each spectral type was further divided into subtypes as indicated in table 1.1.

The Harvard system was used to classify the stars listed in the HD catalogue mentioned above. Roughly 99% of the stars in the catalogue (about 2.2×10^5) are classified into no more than 30 types.

As early as 1914, Adams and Kohlschütter had shown that certain lines in a stellar spectrum were sensitive to the luminosity of the star. The Yerkes system takes the Harvard classifications and introduces luminosity classes from I–V, where I is the brightest (see table 1.2). The Yerkes system is also often referred to as the MK system, after W. W. Morgan and P. C. Keenan, two of the principal scientists who worked on developing the scheme. In the Yerkes scheme, stars are classified from slit spectrograms at a typical dispersion of 115Å/mm, in contrast to the Harvard scheme which used objective prism plates with many low-dispersion stellar spectra per plate. The Yerkes system also uses subtype numbers for

[1] Lasker et al., 1990; Russell et al., 1990; Jenkner et al., 1990

Table 1.1: Spectral types used in the Harvard system

O	a, b, c, d, e
B	1, 2, 3, 5, 8, 9
A	0, 2, 3, 5
F	0, 2, 5 ,8
G	0, 5
K	0, 2, 5
M	a, b, c, d

REFERENCES: *Adopted from Jaschek and Jaschek (1987)*

Table 1.2: Luminosity classes in the Yerkes system

Symbol	Name	Subdivisions
I	Supergiant (or hypergiant)	I, Ia, Iab, Ib
II	Bright Giant	
III	Giant	II – III, IIIa, IIIab, IIIb, III – IV
IV	Subgiant	
V	Dwarf	

REFERENCES: *Adopted from Jaschek and Jaschek (1987)*

the O stars, from O4 to O9. O3, O9.5, O9.7 are later additions, as are intermediate types for the B stars (like B0.5 and B9.5).

1.2.2 'Modern' classifications

Walborn (1970, 1971b and subsequent papers) re-classified a large number of O and early-B type stars. He used several lines of H I, He I, He II, Si III and Si IV to derive spectral types and luminosity classes simultaneously. Walborn also extended the MK subtypes, and introduced O9.7, B0.2 and B0.7. We have chosen to adopt Walborn's spectral types, where these are available, throughout this thesis. Walborn has also studied the UV spectral

morphology of early-type stars (Walborn and Panek, 1984a; Walborn and Panek, 1984b; Walborn and Panek, 1985; Walborn and Nichols-Bohlin, 1987).

With the development of photoelectric plate-measuring devices and spectral tracers, it became possible to classify stars from actual measurements of lines, as opposed to the by-eye comparisons used in the Harvard and Yerkes/MK schemes. Equivalent width classifications of early-type stars have been performed by, among others, Conti and Alschuler (1971) (also Conti and Leep, 1974 and Conti and Frost, 1977). They chose to base their classifications solely on the equivalent-width ratios of the He I lines λ4471Å to λ4541Å (for spectral type) and Si IV λ4089Å to He I λ4143Å (for luminosity class). Although these classifications are generally of good quality, they do not reflect chemical peculiarities as well as Walborn's classifications.

Bisiacchi et al. (1982) performed an in-depth analysis of equivalent widths of the N III λ4514Å line in a large number of O-type stars. They found a good agreement between the ON phenomenon and the strength of the N III line. They also concluded that there is a continuous distribution of N abundances, and not a marked discontinuity between normal O-type stars and the ON stars (see section 1.2.3 for more about the ON stars). Mathys (1988) and Mathys (1989) used equivalent width measurements to derive spectral types that were consistent with both the results of Conti et al. and of Bisiacchi et al., and therefore also consistently treat the OBN/OBC phenomenon. The spectral type of Mathys was used for the star BD+36 4063 (ON9.7 I) — the only star in the WHT sample not classified by Walborn (see chapter 2).

1.2.3 OBN/OBC stars

Early-type stars with unusually weak nitrogen spectra were first observed by Jaschek and Jaschek (1967), and the opposite phenomenon, stars with unusually strong N spectra, was first reported by Walborn (1970). The classifications OBN/OBC were first suggested by Walborn (1976) to describe stars with strong nitrogen and/or weak carbon and weak nitrogen and/or strong carbon respectively. These stars are also sometimes referred to as CNO stars (e.g. Jaschek and Jaschek, 1974).

Several scenarios have been suggested to explain these anomalies;

1. Walborn (1976) proposed that the spectroscopic sequence OC $\rightarrow$ O $\rightarrow$ ON, corresponding to a gradual increase in nitrogen abundance and a depletion of carbon,

is an evolutionary sequence. Mixing of CNO-cycled material into the photosphere could explain the observed abundances if (i) the OBC supergiants show their 'natal' abundances, (ii) morphologically normal OB supergiants all show some mixing, and (iii) OBN stars are at an advanced state of mixing.

2. Walborn also suggested that the abundance abnormalities could merely reflect the abundances of the material the stars were born from. There is some evidence that this could be the case. The strongest (and possibly only) case is with the Orion Belt stars, which all show a similar degree of nitrogen deficiency.

3. Bolton and Rogers (1978) found that a significant fraction (possibly all) of the OBN stars were in fact binaries, whereas they could find no indication of binarity in any of the OBC stars (this has later been confirmed in a study by Levato et al., 1988). It is possible that at least some of the OBN stars could come from mass-transfer, tidal mixing, or some other effect caused by a binary companion.

Further to scenario 1 above, 'classical' evolutionary models for massive stars (e.g. Schaller et al., 1992) do not predict the exposure of CNO processed material until the stars are at very advanced stages of stellar evolution, and not at the evolutionary stage where the OB stars appear to be. However, recent models taking into account the effects of rotation on the stellar evolution (Maeder, 1998; Meynet, 1998) do predict a possible increase in the surface N/C abundance ratio at an evolutionary stage that is compatible with this scenario, at least for the OBN supergiants.

If the nitrogen and carbon anomalies arise from the exposure of CNO processed material in the stars, then other by-products of the CNO cycle should also be apparent. In chapters 4 – 5 we will derive helium abundances for several normal and ON/OC stars, and if CNO material is exposed we would expect to see increased (above solar) helium abundance for the ON stars, with possibly a helium abundance slightly above solar in the morphologically normal O stars.

1.2.4 Be stars

A different group of 'peculiar' hot stars is the Be stars. These stars are commonly defined as "all non-supergiant B-stars whose spectra have, or have had, one or more Balmer lines in emission" (Slettebak, 1988). There is also a subgroup of the Be stars, called the

shell stars, which show narrow absorption lines of several ionised metals superimposed on the Be star spectrum. Be star spectra often show very broad lines, implying projected equatorial rotational velocities of 200 – 300 km s^{-1} or higher (Slettebak, 1982). The spectral features in Be stars can show sometimes dramatic variability, on periods from tens of years for shell appearance and disappearance, to as little as a matter of days, or even hours for line-profile variations (e.g. Smith et al., 1997). Many Be stars are part of binary pairs; however, it appears that there are not enough eclipsing binary Be stars to attribute the Be phenomenon exclusively to binarity (Plavec, 1976). Recent observations in IR, UV and X-ray have led to the following possible scenarios to explain the observed properties of Be stars (Slettebak, 1988 and references therein):

1. *Rotationally-enhanced stellar-wind model.* Rotation can cause radiation-driven winds to be denser around the equator than at the poles, creating a disk-like structure around the equator (e.g. Bjorkman and Cassinelli, 1993)

2. *Spheroidal/ellipsoidal, variable mass-loss, decelerated Be-star model.* Variable mass outflow, caused by "nonthermal subatmospheric modes" passes through several atmospheric layers surrounding the photosphere. The outflow cools and is deaccelerated through interactions with mass flows of other velocities or the local stellar environment, and form a cool, Hα emitting region surrounding the star. A coupling of the expanding flow with rotation will cause an ellipsoidal shape for the emitting region (Doazan, 1987).

3. *Nonradial pulsation model.* Most of the rapidly rotating Be stars show rapid line profile variations, which could be explained by nonradial pulsations. Occasional mode-switching of the pulsations could provide the energy to drive the mass-loss events (e.g. Baade and Balona, 1994).

4. *Interacting binary model.* The formation of the Be envelope is a result of evolutionary processes and interactions in a binary system (Harmanec, 1987).

5. *Magnetic-loop model.* A low-density wind forms a disk from interactions with magnetically supported plumes around a rapidly rotating star (Underhill, 1987).

There is observational evidence both to support and to refute most of these models. In chapter 7 we will concentrate on the rotational properties of a sample of Be stars.

Table 1.3: Typical parameters for OB stars

	$T_{\rm eff}$ (kK)		$\log(L/L_\odot)$		$R/R_\odot$		$M/M_\odot$
Sp. Type	I	V	I	V	I	V	ZAMS
O3	45.0	48.8	6.21	6.00	21	14	88
O5	41.0	44.0	6.20	5.69	25	12	58
O7	36.0	39.3	5.94	5.33	24	10	36
O9	31.0	34.3	5.57	4.90	21	8	24
B0	25.0	30.1	5.34	4.56	25	7	17
B3	15.0	17.7	4.49	3.35	26	5	9
B5	13.5	15.3	4.27	3.09	25	5	6

NOTES: *The radii for supergiants are representative of luminosity class Ib objects.*
REFERENCES: *Reid (1994) and references therein.*

1.3 Physical properties of hot stars

The point has already been made that OB stars are among the hottest, most luminous and most massive stars known (all these parameters are of course related); however, the O stars sample considered in this thesis is fairly limited in range[2]. The earliest-type star investigated is an O8 supergiant, on the other hand, the latest-type star is the cross-correlation template, α Lyr which is an A0 main-sequence star. Table 1.3 lists some 'typical' parameters for OB stars.

There are several different approaches to measuring (or estimating) the physical properties of these stars. If the stars are part of a binary system, and the orbits of the components can be found, then the masses of the components can be calculated. If the system also happens to be inclined so that eclipses occur, then it is also possible to calculate radii and luminosity ratios of the components. Unfortunately, such systems are rare.

For stars that are hot enough to ionise the ISM surrounding them, forming a compact H II region, one can apply the *Zanstra method*. It is assumed that all the Lyman-continuum photons emitted by the star are converted into Balmer series photons in the H II region. A measurement of the radio continuum or a Balmer line can give an estimate of the Lyman

[2] By choosing stars of a limited range in $T_{\rm eff}$ and $\log_{10} g$ it should be possible to measure differential chemical abundances relatively accurately. This will be discussed further in chapter 2.

flux emitted by the star. Comparison with theoretical stellar models yields the effective temperature, $T_{\rm eff}$ (e.g. Hjellming, 1968 and Morton, 1969). This method is very sensitive to the model predictions of the EUV flux.

A different approach is to integrate the observed flux from all the available wavelength regions. The measured flux has to be corrected for atmospheric and interstellar absorption, and missing wavelength regions have to be 'filled in' by predicted values from stellar models. If the angular diameter of the star is known, say from interferometry, then $T_{\rm eff}$ can be calculated (e.g. Code et al., 1976; Underhill et al., 1979; Underhill, 1982). This technique has been shown to be unreliable by Hummer et al. (1988) for stars earlier than O9.5.

The determination of stellar parameters through comparison of observations to theoretical models is now usually the 'standard approach' for hot stars (see Kudritzki and Hummer, 1990 for several examples). The development of detectors capable of capturing high resolution, high signal-to-noise spectra of even quite faint stars, and steady progress in the field of theoretical modelling (helped by advances in computer technology), have made it possible to get good agreement between models and observations. This is also the method used in this thesis to find effective temperatures and surface gravities of 23 O-type stars.

1.3.1 Line broadening

One of the most notable characteristics of the hot stars, and especially of the O stars, is the absence of stars with narrow absorption lines. Equivalent widths computed by non-LTE models (see chapter 3) compare reasonably well with those measured from observations. However, the model line profiles are consistently too narrow, and have to be convolved with a line-broadening function before they reproduce the observations satisfactorily.

For any large sample of stars, even if they are all rotating, there should at least be some stars that are observed nearly pole-on, and thus have narrow lines. The narrowest-lined O stars observed have a velocity of the order 15 – 30 km s^{-1} (e.g. Conti and Ebbets, 1977; Penny, 1996; Howarth et al., 1997b). For the supergiants the case is even worse; the minimum line broadening appears to be in the order of 50 km s^{-1} for an O9 supergiant (Howarth et al.). Conti and Ebbets and Howarth et al. suggested that, apart from large rotational velocities, there also appears to be another form of line broadening taking place in the O stars, perhaps attributed to some turbulent velocity field in the

stars' atmospheres. This turbulence also appears to be more important in the supergiants than in the main-sequence stars (see also chapter 7).

1.4 Main-sequence evolution

It is difficult to know where to start when discussing massive star evolution. Hanson (1998) defines a ZAMS star as follows: "A zero-age main-sequence (ZAMS) star has its minimum radius, its maximum mass (for single-star evolution), its bluest colour (or hottest effective temperature), and its central core possesses its peak H/He". However, she then points out that Palla and Stahler (1993) have found that as soon as a hydrostatic, mass-accreting protostar has a mass of over $10M_{\odot}$, it will start burning hydrogen, no matter what its final mass will eventually be. Thus, when the term ZAMS is used in this thesis, it will be in the sense of the *theoretical* ZAMS — the starting point for stellar evolutionary models.

Early-type main-sequence stars 'burn' hydrogen to helium through the CNO bi-cycle. Although they have a large quantity of hydrogen in their cores, the high energy-production rate quickly converts hydrogen into helium, and the stars have a relatively short lifetime compared to low mass stars. The evolutionary models published by Schaller et al. (1992) predict a core H-burning (i.e. main-sequence) lifetime of about 10^8 years for a $5M_{\odot}$ star, 8×10^6 for $20M_{\odot}$ and only 3×10^6 for a $60M_{\odot}$ star.

While burning hydrogen, the massive stars evolve slowly towards colder temperatures in the H–R diagram, and their luminosity also increases slightly. This means that, unlike for colder stars, even giant and supergiant O stars are core H-burning. These stars also lose an appreciable amount of mass during their main-sequence lifetimes. A $40M_{\odot}$ star, is only predicted to contain $36M_{\odot}$ of material by the time it has exhausted the hydrogen in the core, and a $60M_{\odot}$ star will have lost over $12M_{\odot}$ through its stellar wind. It is also possible, as mentioned earlier, that effects caused by stellar rotation can mix the atmosphere sufficiently to bring CNO processed material up to the surface of massive stars while they are still on the main-sequence. In chapter 6 we will try to place the O stars in the sample on the H-R diagram, and determine their evolutionary status.

Chapter 2

Observations and data reduction

2.1 WHT observations of late O-type stars

The high-resolution, high signal-to-noise data needed for the line analysis were acquired using the Utrecht Echelle Spectrograph (UES) during four nights in August 1995. The UES is permanently mounted on one of the nasmyth platforms at the f/11 focus of the 4.2 metre William Herschel Telescope (WHT), which is part of the Isaac Newton Group (ING) of telescopes at La Palma.

One of the main criteria for selecting target stars was brightness. In order to get high-quality spectra of as many stars as possible, it was important to keep exposure times to a minimum. After the second night of observing, it was decided to remove the image de-rotator from the instrument. This disabled the WHT's auto-guider, forcing us to guide the telescope manually, but it also increased the throughput (i.e. reduced the exposure times) by about 30 per cent.

Most of the four nights were spent observing with the UES, however several lower resolution spectra were acquired with both the red and blue arms of the ISIS double beam spectrograph. These spectra were not used for the analysis discussed in this thesis, but they were obtained to help define the wings of the broad hydrogen lines. They have also sometimes been used as a comparison to check for faults in the reduction of the high-resolution data, and to help correct for the echelle blaze in the data. A special routine was later developed to automatically de-blaze the spectra (see section 2.1.5).

2.1.1 The sample

One of the main aims of this thesis is to look for object-to-object variations in the helium abundance of O stars. To look for evolutionary tracers, we wanted a large sample of stars that populate a small part of the HR diagram, and with a bias towards stars that have been proposed to show abnormal surface abundances. By choosing stars with similar effective temperatures and surface gravities, we hope that reliable *differential* parameters for the stars can be derived. To test the hypothesis that OC – O – ON is an evolutionary sequence, and that the nitrogen enhancements should be reflected in the helium abundance, several stars that were classified as OC and ON by Walborn (1976) were chosen. The "new" ON star identified in Mathys (1989), BD+36 4063, was also observed, and recent observations show that this star is a single-lined spectroscopic binary (Howarth, private communication). See table 2.1 for a complete list of the UES target stars.

These stars are probably not a representative sample of the O stars. There are only 4 stars (roughly 17 % of the sample) classified as belonging to luminosity class V, corresponding to a main sequence star. It is difficult to say what the "true" distribution of luminosity classes are, but as a quick estimate we can check with Garmany's unpublished catalogue of O stars. This catalogue contains a more or less complete sample out to approximately 2 kpc (Garmany et al., 1982) and although the spectral types are not always consistent with those we have adopted (see table 2.1) there are probably no important differences. For the list containing about 1000 stars (some without luminosity classifications), there are 375 stars classified as either If, I, II or III and 394 as IV or V.

The sample does, however, contain a mix of morphologically normal stars, and stars which have been at one point or another been classified as chemically peculiar. These stars include the ON and OC stars, the Orion belt stars, δ Ori and ζ Ori, and several other stars which have been noted to have moderate chemical anomalies. In particular, the Orion belt stars are interesting because, although not classified as OCs, they both have been noted by Walborn (1976) to be slightly N deficient.

2.1.2 The Utrecht Echelle Spectrograph

The UES is a cross-dispersed echelle, used in our observations with the 31.6 grooves/mm echelle grating. The slit was opened to $1.5''$, which gave a resolution element of about 65 microns at the detector (approximately 3 pixels). This corresponds to a resolving power

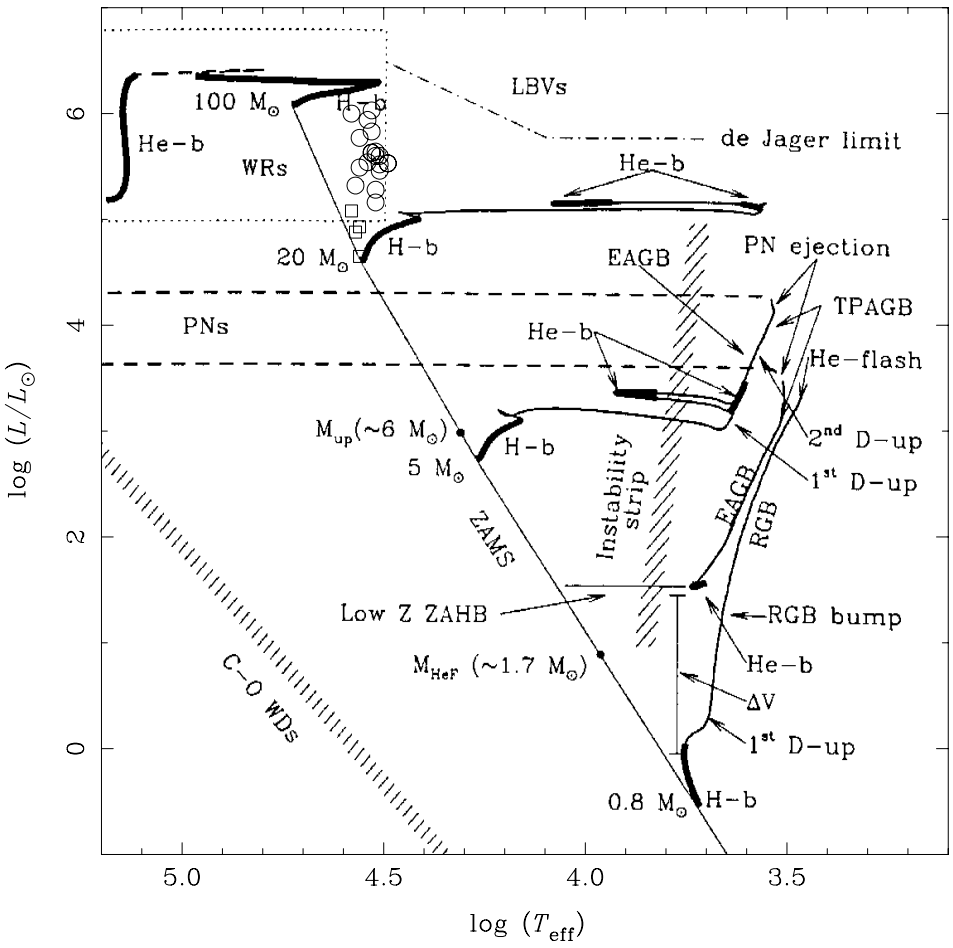

Figure 2.1: *HR Diagram showing the positions of the sample stars as open symbols (the symbols are explained in chapter 6). The physical parameters for the stars are calculated in this thesis. Also indicated are the core hydrogen (H-b) and helium burning (He-b) phases of the evolutionary tracks, and predicted positions of the zero-age main-sequence (ZAMS), dredge-ups (D-up), extended part of asymptotic giant branch (EAGB), thermal pulsing part of the AGB (TPAGB), and the positions of planetary nebulae (PNs), Wolf-Rayet stars (WRs), luminous blue variables (LBVs) and the white dwarf (WD) cooling track. The thick black lines denote 'slow' parts of the evolutionary tracks, i.e. where the stars are most likely to be observed. Diagram adapted from Chiosi (1998).*

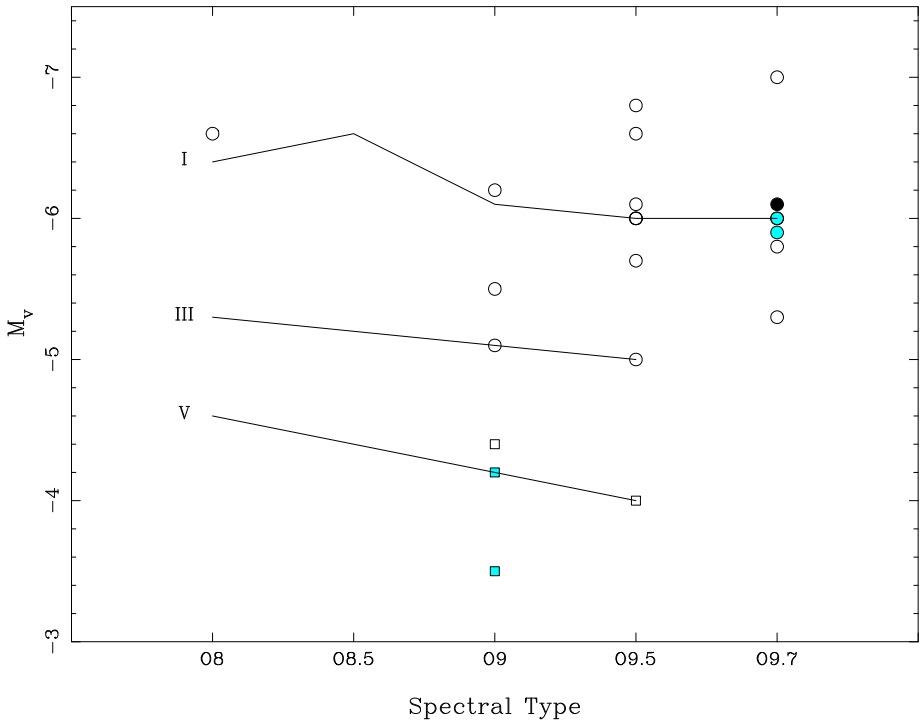

Figure 2.2: *Absolute magnitudes and spectral types for the sample stars. The magnitudes are from Garmany's unpublished catalogue, and the spectral types are taken from the various references discussed in the text. The lines show the loci of absolute magnitudes adopted by Howarth and Prinja (1989). The symbols are explained in chapter 6.*

Table 2.1: UES target stars

HD/BD	Name	Spectral Type		V	No. exposures		Tot. time		S/N
					4190Å	5426Å	4190Å	5426Å	
10125		O9.7 II	W76	8.22	2	2	3000	2700	300
12323		ON9 V	W76	8.90	2	2	2700	2400	300
13745		O9.7 II((n))	W76	7.88	2	2	1600	1500	450
16429		O9.5 II((n))	W76	7.67	2	2	2700	1500	300
30614	α Cam	O9.5 Ia	W76	4.26	2	2	160	100	400
34078	AE Aur	O9.5 V	W73	5.81	2	2	420	350	300
36486	δ Ori	O9.5 II	W76	2.20	3	2	30	10	350
37742	ζ Ori	O9.7 Ib	W76	1.75	2	3	24	19	300
188209		O9.5 Iab	W76	5.64	3	3	550	400	350
189957		O9.5 III	W73	7.22	3	2	1200	1000	300
191781		ON9.7 Iab	W76	9.54	3	2	4500	2500	300
194280		OC9.7 Iab	W76	8.39	3	2	4500	3000	200
195592		O9.7 Ia	W76	7.08	2	2	2000	500	300
201345		ON9 V	W76	7.66	2	3	2000	3000	250
202124		O9.5 Iab	W76	7.80	2	2	1600	1000	400
207198		O9 Ib-II	W76	5.96	3	3	1300	600	350
209975	19 Cep	O9.5 Ib	W76	5.11	2	3	300	300	350
210809		O9 Iab	W76	7.55	3	2	2400	1000	400
214680	10 Lac	O9 V	W73	4.87	3	3	150	150	350
218195		O9 III	W76	8.34	2	2	1600	1400	300
218915		O9.5 Iab	W76	7.18	3	3	2600	3000	400
225160		O8 Ib(f)	W71	8.19	2	2	2400	2000	300
+36 4063		ON9.7 I	M89	9.71	5	2	6900	3000	150

NOTES: *Columns three and four list classifications and published reference. Column 5 gives the V magnitude listed in Garmany's catalogue (see text). The wavelengths for columns 6 to 9 represent the central wavelength setting of the spectrograph (see text). Signal-to-noise (column 10) is calculated for a small spectral region between 4200Å and 4300Å and is not necessarily representative for the entire wavelength range.*

REFERENCES: *W71, W73, W76 – Walborn 1971b; 1973; 1976 respectively, M89 – Mathys, 1989.*

$R = \lambda/\Delta\lambda = 40000$ (about 8 km s^{-1}). The detector was the Tektronix 5 (TEK5) with 1124×1124 pixels (1024×1024 usable imaging size).

Several exposures with two spectrograph settings were obtained for all the target stars. Centering the grating at $\lambda_{\rm cen} = 4190$Å in order 136 and $\lambda_{\rm cen} = 5426$Å in order 105 gave complete spectral coverage from roughly λ3780Å to λ5670Å, and further coverage with inter-order gaps up to λ6980Å. These wavelengths are in the rest-frame of the observer, and so the actually stellar wavelengths depend slightly on the radial velocity of the stars observed and on heliocentric corrections.

2.1.3 Data reduction

The echelle data reduction was performed using the Starlink packages ECHOMOP (Mills et al., 1997), FIGARO (Shortridge et al., 1997), and DIPSO (Howarth et al., 1997a). ECHOMOP was originally developed to extract data from the UES' "twin" instrument, the UCL Echelle Spectrograph (UCLES) at the Anglo Australian Telescope (AAT). The 2-D images were first bias subtracted and cleaned of cosmic rays using the Starlink software BCLEAN. The data were then transfered to the ECHOMOP environment. ECHOMOP is a multi-step reduction package that can either be run interactively or automated through shell scripts. For this project, ECHOMOP was used interactively on the first exposure of each spectrograph setting of each star; the resulting 'reduction data structure' was then used to automatically reduce the remaining spectra at the same settings. The data structure contains information about the extracted spectra, such as the order positions and shapes, the cross-dispersion profile and so on. It did, however, sometimes turn out to be necessary to reduce each exposure manually, usually because of slight changes to telescope positioning, or instrument setup.

There is a good summary of the general properties of echelle spectra in *Starlink Guide 9* (Clayton, 1996). Below is a brief description of the steps involved in the reduction and extraction of these data.

Order identification and tracing

Before the stellar spectra can be extracted, the orders have to be identified. ECHOMOP proved very good at locating the orders in the stellar frames, and no manual intervention was necessary. The orders were then traced using a centroid tracing routine, and polynomials of the 5th degree were fitted to the orders. For each order, the differences between

the centroid trace and the fitted polynomial were plotted, and points that fell more than 0.3 pixels away from the polynomial were then removed and the order re-fitted. This was iterated until no points fell outside the 0.3 pixel limit.

Sky & background fitting

An averaged flat-field frame was then used to determine the dekker limits, which mark the extent of each order in the spatial (cross-dispersed) direction. When the dekker limits had been determined, the orders were examined manually and each pixel along the slit was marked as either belonging to the star or sky. The mean (in the spatial direction) of the "sky" pixels was used to correct for sky emission/scattered light. From measuring the FWHM of the arc lines we can estimate the spectrograph resolution, $R = \lambda/\Delta\lambda$ which we find to be about 40000 – 50000 dependent on the wavelength.

Spectrum extraction

Finally, the object profile was calculated using the star mask created above, and the stellar and arc spectra were extracted using an optimal extraction routine. This routine weights each pixel by the product of the calculated profile, $P(i, j)$, and an estimate of the uncertainty of the pixel intensity (see next section). The star and arc spectra were extracted simultaneously to ensure that the same weights were used in both cases. Arc lines were identified using ECHARC and the wavelength information mapped on to the extracted spectra.

2.1.4 Flat-fielding

Flat-fielding of echelle spectra is far more complicated than for normal grating spectra. Although the flat-field frames should be quite sensitive to pixel-to-pixel variations in the detector, it is far more difficult to model the variations caused by the instrumental profile (see section 2.1.5). Since both of these are present in the flat-field frames, it is difficult to extract any useful information from them.

Several tests were performed using flat-field frames obtained in the afternoon before each night's observing. Cross-dispersion 'drift' in the spectrograph (perhaps due to temperature changes in the spectrograph[1]) meant that a straight division of the flat-field

[1]The refractive index of the cross-dispersion prism is temperature sensitive, and although the UES is in a temperature controlled area, there does appear to be a drift in the cross-dispersion direction throughout

frames into the data frames degraded rather than improved the quality of the extracted spectra. We also tried to extract the flat-field frames using the same object profile obtained during the spectrum extraction and several different *weighting schemes*: simple, profile and optimal.

- **Simple:** all object pixels are assigned equal weights.
- **Profile:** Weights each pixel by $P(i,j)^2$ where $P(i,j)$ is the calculated normalisation profile at spatial offset j from the trace centre, and i is the column number.
- **Optimal:** Each pixel is weighted by the product of $P(i,j)$ and an estimate of the uncertainty of the pixel intensity.

However, none of these methods seemed to be able to correct satisfactorily for pixel defects in the detector or the echelle blaze. No flat-fielding was carried out, therefore. This was acceptable from the point of view of pixel-to-pixel sensitivity differences, which were small, but left the problem of correcting the echelle blaze.

2.1.5 Echelle blaze correction

The shape of the extracted spectra is dominated by the so-called echelle blaze function. This is just the angle (i.e. wavelength) dependence of the light reflected by the grating. There are several ways of correcting for the blaze, but none of them are straight-forward. One of the most common ways is to divide through by the normalised flat-field, but, as noted above, this method did not work well for these data – possibly due to difference in the optical paths in the spectrograph between the flat-fields and the actual observations (see also section 2.1.4). However, several other methods of correcting for the echelle blaze were tried. In particular, two different routines were written in FORTRAN 77 and incorporated into the DIPSO environment.

Barker method

The method of Barker (1984) involves dividing the spectral orders by a theoretical ripple function, $R(\lambda)$. For a plane grating used in near-Littrow mode (basically when the angle of incidence is not very different from the facet normal; see Gray, 1992), the blaze function

the nights of observing.

is given by

$$R(\lambda) = \frac{\sin^2 \pi\alpha X}{(\pi\alpha X)^2} \tag{2.1}$$

where $X = m[1-\lambda_c(m)/\lambda]$. The order number, m, and the central wavelength of order m, $\lambda_c(m)$, are related through the grating constant, $k = m\lambda_c(m)$, and α is another grating constant which depends on the facet width, the spatial frequency of facets, and the blaze angle (Barker, 1984).

The above equation for the blaze function fits well, but not well enough to remove all the ripple. The Barker routine finds a correction to the grating constant, k, for each order – allowing k to vary as a function of the order, m. The correction is found by examining the overlap region between two orders after they have been de-blazed with an initial estimate of the value of k (usually $m\lambda_c(m)$). For each overlap region, the orders should match up. The fluxes, F_+ and F_-, of the de-blazed orders, are then measured in the overlap region. F_+ and F_- just denotes the flux of the order with the higher flux and lower flux respectively (see fig 2.3).

A differential correction, Δk, to the grating constant is then calculated for each order from

$$\Delta k_m = \frac{\frac{F_+}{F_-} - 1}{\frac{1}{R_m}\frac{\partial R_m}{\partial k} - \frac{F_+}{F_-}\frac{1}{R_{m+1}}\frac{\partial R_{m+1}}{\partial k}} \tag{2.2}$$

The process is then repeated until Δk is sufficiently small.

The Barker routine works well when the correct value for α has been found, but the major problem is the need for order overlap. As mentioned in section 2.1.2, redwards of λ5670Å there is only partial coverage of the full spectral range. It is possible that a function could be fitted to the corrected values of k and extrapolated into the region without overlap. This has not been tried for this project, but Howarth and Prinja (1989) smoothed the k values and introduced a 2σ rejection. They found that this greatly reduced the chance of erroneous values of k caused by cosmic-rays and phosphor decay spikes.

Splif

A very different approach was taken in a previously empirical method by Howarth (private communication), called SPLIF. The extracted echelle orders are treated as a surface in the spectral vs. spatial (order number) plane. This surface is then fitted using a very simple approach. Briefly, this involves:

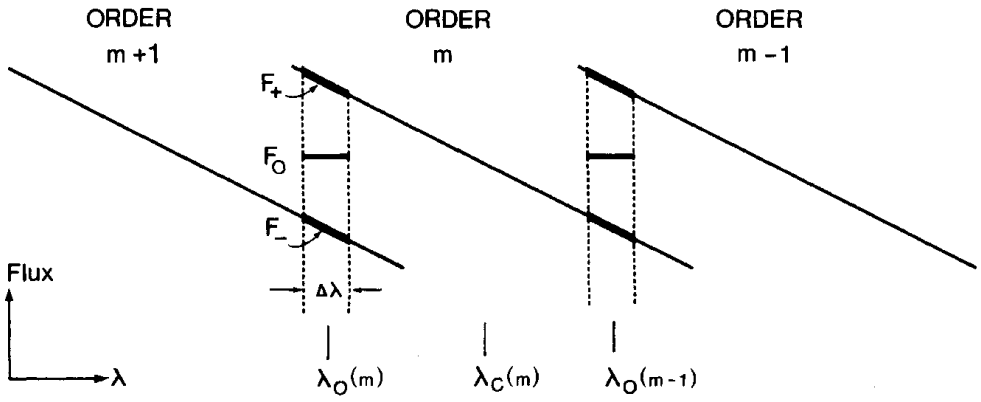

Figure 2.3: *Schematic of three adjacent orders in an echelle spectrum with incorrect blaze removal. From Barker, 1984.*

1. Each order is "normalised" by dividing by the mean intensity of that order. This step removes the large order to order variations in intensity and allows the use of a simple fit surface. This step can also be slightly improved by fitting a polynomial to a plot of mean intensity against order and dividing through by the fitted values, since orders with strong lines, or many weak lines, will lower the mean intensity of that order.

2. For each pixel in the dispersed direction, a straight line is fitted to a plot of intensity as a function of order number. This returns (for the TEK5) two arrays of 1024 elements, one holding the gradients of each fitted line, and the other the intercepts.

3. The two arrays are then optionally fitted with polynomials to create a smoothed surface.

4. The spectral data from step (1) are divided by this surface.

5. A linear 'ramp' is applied to each order to ensure agreement in regions of order overlap.

6. Orders are merged with a ramped weighting function.

Because of the several layers of smoothing, the method is fairly robust against spectral features, and does not require order overlap. As shown in figure 2.5, even wide spectral features which span several orders are preserved in the fitting process.

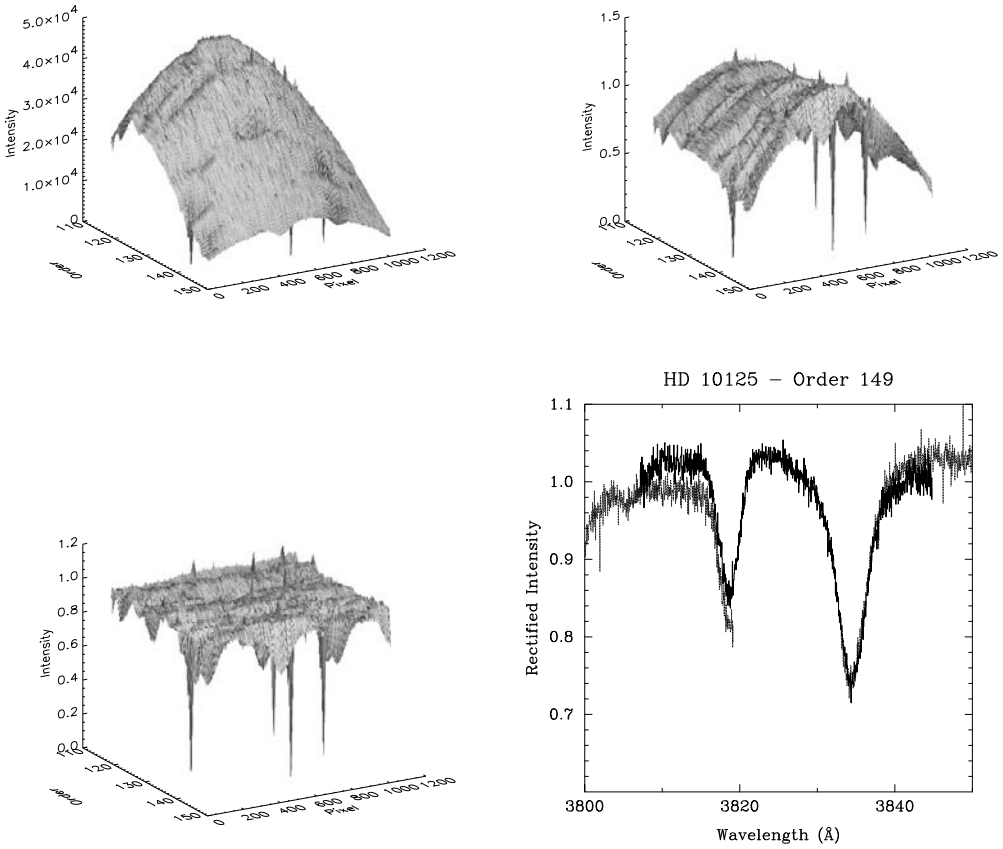

Figure 2.4: *The four steps of* SPLIF*ing:* ***top left*** *— raw extracted orders;* ***top right*** *— 'normalised' orders;* ***bottom left*** *—* SPLIF*ed orders;* ***bottom right*** *— almost done, spectral orders just need to be normalised before merging.*

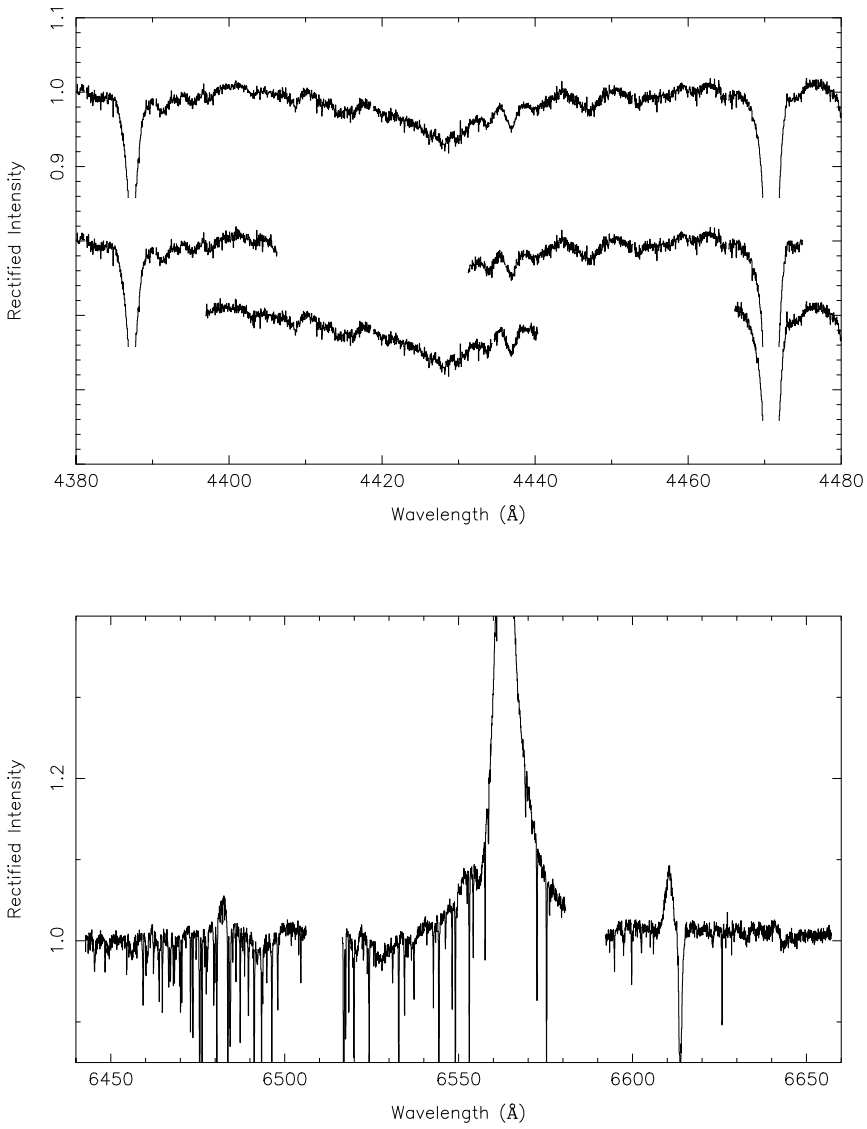

Figure 2.5: *The SPLIF method preserves wide spectral features that span several echelle orders. The* ***top panel*** *shows the strong diffuse interstellar band at λ4430Å in HD 218195. The merged spectrum is shown with the individual orders offset underneath. The spectra have been clipped at a rectified intensity of 0.85 for clarity. The* ***bottom panel*** *shows Hα emission in HD 195592. In this wavelength region there is a large inter order gap. The strong emission meant that we had to saturate Hα to get decent S/N for the rest of the spectrum. Scattered light from this strong emission might have caused the small features seen at approximately λλ6480 and 6640Å in the adjacent orders.*

All the UES data were de-blazed using SPLIF and all the orders containing lines used in the analysis were carefully inspected before they were merged to form a single, continuous spectrum. Neighbouring orders were usually in good agreement in the overlap region, but in a few cases there were differences of the order of a few per cent of the continuum intensity. The orders were merged using a gradient function in the overlap region. This would slope linearly from 1 to 0 and give less weight to the end points in each order.

The SPLIFed, merged and normalised WHT spectra are included on the attached CD-ROM. See appendix E for details.

2.2 *IUE* data

The second part of this thesis (chapter 7) investigates photospheric line broadening in UV spectra of O and B stars. The O (and some B) stars were initially analysed as part of an undergraduate project undertaken before starting this Ph.D. research, and subsequently published in Howarth et al. (1997b). We have subsequently automated the analysis procedures and have expanded the sample to include later-type B supergiants than those investigated in Howarth et al., and also B main-sequence stars.

As before, UV spectra taken with the *International Ultraviolet Explorer* (*IUE*) satellite's Short Wavelength Prime (SWP) camera were used for the analysis. *IUE*, launched in January 1978 by a collaboration of SERC, ESA and NASA, had four UV sensitive cameras. The Long Wavelength Prime and Redundant (LWP and LWR) cameras observed in the range 1900-3200Å, and the Short Wavelength Prime camera in the range 1150-2000Å (the Short Wavelength Redundant camera had a faulty readout section and was not used).

Each of the two spectrographs on board (LW & SW) could operate in high or low-resolution mode. The low-resolution spherical gratings produced spectra with a resolution of about 6Å, and the high-resolution echelle spectrographs produced spectra with a resolution of approximately 0.1Å. Only high-resolution spectra have been used in this study.

2.2.1 The *IUE* sample

Using the electronic version of the Bright Star Catalogue (Hoffleit and Warren Jr., 1991), all stars classified as type B were extracted and cross-checked with the IUE catalogue. Where appropriate observations existed, these were downloaded from the IUE archives available at `http://ast.star.rl.ac.uk/iues/iues.html`. Some additional stars from

Howarth et al. (1997b) were included to test the automatic analysis routines. The sample of stars is discussed in more detail in chapter 7.

2.2.2 Data extraction

The *IUE* data were extracted in a very similar manner to that described in Howarth and Prinja (1989) using the Starlink *IUE* data reduction package IUEDR (Giddings et al., 1996). A good review of *IUE* data reduction and analysis can be found in *IUE Analysis — A tutorial* (Tweedy and Clayton, 1996). Briefly, the steps involved include:

- Using the commands SCAN and AGSHIFT successively to find the geometric shift used to trace the orders.
- Performing centroid tracing and order extraction using TRAK.
- Applying a wavelength correction of the form $m\Delta\lambda = \text{constant}$ to bring interstellar lines in the spectrum to their laboratory wavelengths.
- Correcting for Echelle ripple using the method of Barker (see section 2.1.5).
- Subtracting inter-order background (approximately 12% at Lyα for the B stars and 15% for the O stars).
- Merging and mapping the orders onto a uniform wavelength grid.

The reduction process was greatly simplified by using modified procedures created by I. D. Howarth and M. Clayton (private communications) with some new additions, mainly to try to automatically detect if the archive images are both geometrically and photometrically corrected (GPHOT) or just photometrically[2] corrected (PHOT/PI). These corrections were necessary to transform the faceplate charge of the detectors to linear intensity units. Around the end of 1980, the correction type changed from GPHOT to the superior PI. Unfortunately the exact date of change depends on which ground station processed the images. Thus, for stars where there is doubt about the correction type, the spectra were extracted twice, trying both corrections (IUEDR needs to know the correction type to set default extraction parameters). In most cases it is very obvious when the wrong type has been used, as seen in figure 2.6. The spectra are tested by calculating the pixel intensity

[2] For the PI images, the photometric calibration frames were corrected to match the image geometry, not the other way around as for the GPHOTs

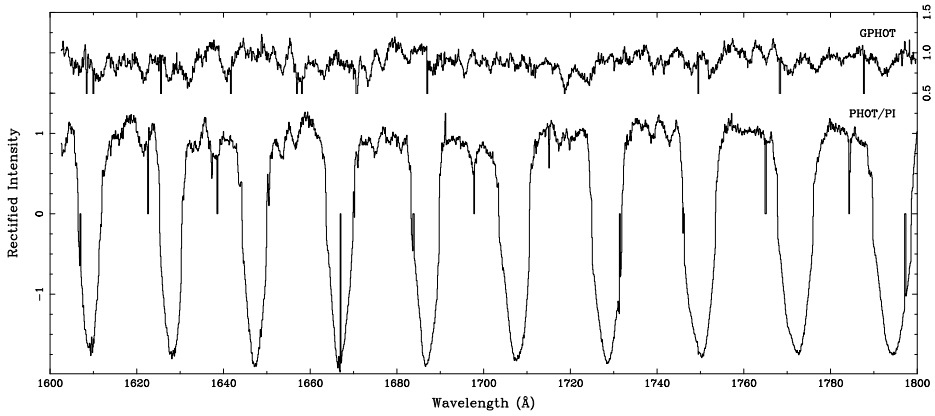

Figure 2.6: *Example of IUE spectrum extracted assuming the wrong correction type. This spectrum is clearly of the older GPHOT type.*

range over small areas of the spectrum around order overlap regions. The correction type that gives the smallest spread of intensities (i.e. less noisy) is assumed to be the correct one. This seemed to work well and only failed where there were problems with the data reduction (in some cases the wrong aperture was listed in the logs). Finally, all the spectra were visually examined to check for flaws.

Chapter 3

Models

Having obtained spectroscopic observations of the sample stars, we now would like to extract information from those observations about the physical properties of these stars. We do this by comparing the observations with published theoretical models. The complete theory of stellar atmospheres is far beyond the scope of this work, but some of the more important aspects of the models are presented below.

3.1 Modelling stellar atmospheres

There is today a vast variety of different computer codes available for the modelling of stellar atmospheres (for a good, but now slightly outdated, summary see Hummer and Hubeny, 1991). Although these codes sometimes vary substantially in their approach and/or emphasis they all more or less trace their ancestry to the work of Unsöld in the 1930s.

3.1.1 Basic assumptions

The 'classical stellar atmosphere theory' is based on several assumptions, which are still commonly made in modern atmospheric models:

- **Plane-parallel geometry** assumes that the stellar atmosphere can be divided into plane-parallel layers (see figure 3.1). This reduces the geometrical dimensions from 3 to 1 and simplifies numerical calculations. Such an assumption is only valid if the thickness of photosphere constitutes a small fraction of the stellar radius. For stars

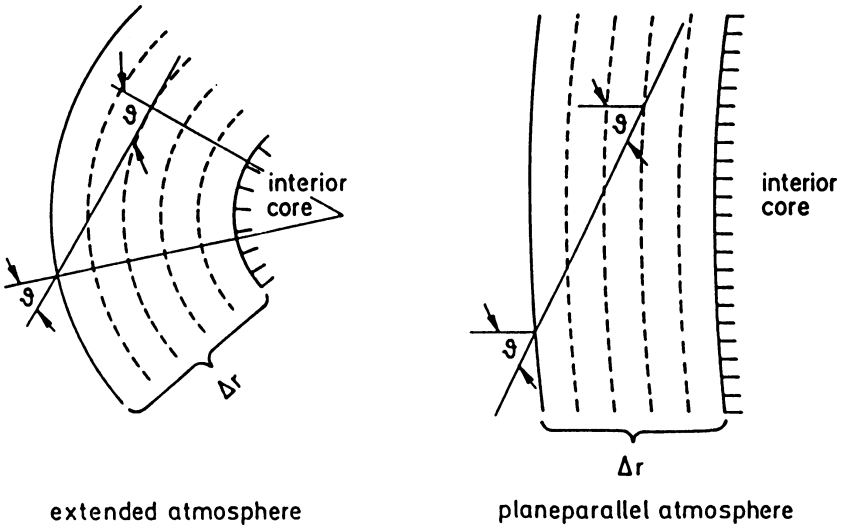

Figure 3.1: *The geometry of plane-parallel and extended atmospheres. From Kudritzki, 1988.*

with extended atmospheres, the geometry is likely to play an important role, and more rigorous spherical models are preferable.

- **Steady State**, i.e. no time-dependent phenomena (like shocks or pulsations).
- **Hydrostatic equilibrium** implies that gravitational forces are exactly balanced by gas pressure. There is no net flow of mass.
- **Radiative equilibrium** assumes that radiation is the only (or at least the dominant) carrier of energy through the atmosphere. Other processes which transport energy, in particular convection, are neglected.
- **Chemical homogeneity**. It is generally assumed that the chemical composition is constant throughout the stellar atmosphere.

3.1.2 Radiative transfer

The general aim of a model atmosphere is to calculate the emergent flux at the surface of a star. The interaction of radiation with the stellar material can simply be considered as the sum of the losses and gains in intensity when the radiation has travelled a length ds

$$\mathrm{d}I_\nu = -\kappa_\nu \rho I_\nu \mathrm{d}s + j_\nu \rho \mathrm{d}s \tag{3.1}$$

where j_ν and k_ν are the mass coefficients for emissivity and absorption respectively. We now define the *optical depth* which is simply the amount of absorbing matter the radiation

encounters over a length L

$$\tau_\nu = \int_0^L \kappa_\nu \rho \mathrm{d}s \tag{3.2}$$

and the *source function* which describes the ratio of the emissivity and absorption coefficients

$$S_\nu(\tau_\nu) = \frac{j_\nu}{k_\nu}. \tag{3.3}$$

By combining these three equations we get

$$\mathrm{d}I_\nu \mathrm{d}\tau_\nu = -I_\nu + S_\nu \tag{3.4}$$

which is called the *equation of radiative transfer* and describes the change in intensity when radiation travels along an infinitesimal length $\mathrm{d}\tau_\nu$. The formal solution of this equation can be written as

$$F_\nu = 2\pi \int_0^\infty S_\nu(\tau_\nu) E_2(\tau_\nu) d\tau_\nu \tag{3.5}$$

where F_ν is the total emergent flux at frequency ν and $E_2(x)$ is the second exponential integral given by

$$E_2(x) = \int_1^\infty \frac{e^{-xt}}{t^2} dt. \tag{3.6}$$

The mass emissivity and absorption coefficients depend on details of the interactions of photons with the stellar material, and can only be found if we know the physical properties of this material. This is the main difficulty in modelling a stellar photosphere: the radiation field depends on the properties of the matter, but the state of the material itself depends on the radiation field which, through interaction with photons, heats it and determines its excitation and ionisation characteristics.

3.1.3 Local Thermodynamic Equilibrium

The properties of a gas are most easily found if the gas is in *thermodynamic equilibrium* (TE). In TE, the state of the gas (the distribution of atoms over bound and free states) is described by the equations of statistical mechanics, and can be uniquely defined by two thermodynamic variables. In the physics of stellar atmospheres it is customary to use the temperature, T, and the particle number density, n.

However, it is clear that a stellar atmosphere is far from Thermodynamic Equilibrium. New energy is constantly being created in the core and 'pumped' into the atmosphere, and at the same time photons are escaping from the surface (otherwise we would not be able to observe the star at all). Instead, since TE does not hold, we make the assumption of *Local Thermodynamic Equilibrium*, or LTE, which means that state of the gas is at its equilibrium value as determined by the *local* values of $T(r)$ and $n(r)$.

More specifically, this means that for the local values of T and n,

(i) the particle velocity distributions are Maxwellian

$$f(v)\mathrm{d}v = \left(\frac{m}{2\pi kT}\right)^{3/2} \exp\left(\frac{-mv^2}{2kT}\right)\mathrm{d}v \tag{3.7}$$

where m and v are the particle mass and velocity and k is the Boltzmann constant.

(ii) the excitation equilibrium is given by the Boltzmann distribution

$$\frac{n_j}{n_i} = \frac{g_j}{g_i} \exp\left[\frac{-(E_j - E_i)}{kT}\right] \tag{3.8}$$

where g_i is the statistical weight assigned to level i to account for degenerate sub-levels, and E_i is the level energy (measured from the ground state).

(iii) the ionisation equilibrium is given by Saha's equation

$$\frac{N_j}{N_{j+1}} = n_e \frac{U_j}{U_{j+1}} \left(\frac{h^2}{2\pi mkT}\right)^{3/2} \exp\left(\frac{\chi_{Ij}}{kT}\right) \tag{3.9}$$

where N_j is the total number density, and χ_{Ij} is the ionisation potential, of ionisation stage j. U is the partition function, given by $U_j = \sum_1^\infty g_j \exp(-\chi_j/kT)$.

(iv) the source function, S_ν, is given by the Planck function, B_ν.

3.1.4 Departures from simple model

With all the assumptions discussed in the previous sections is relatively easy to compute the properties of a 'simple' stellar atmosphere, which in many cases will be fairly successful in describing the gross properties of the observed stellar spectrum, like the visual continuum. However, there are also many cases where these assumptions fail completely.

In the late 1960s and early 1970s, important work was done on developing computational procedures that relieved the need for LTE. In this approach, usually referred to as non-LTE or nLTE, the populations of atomic and ionic states are allowed to deviate

from their LTE values, yielding (one hopes) a more realistic description of the atmosphere. However, non-LTE routines are both relatively complex and computationally expensive, and often only a few selected ionic levels are allowed to depart from LTE.

A lot of work in the 1990s has been on the creation of 'unified' model atmospheres which simultaneously and consistently treat the photosphere and the stellar wind. Classically, the outer boundary of the photosphere was considered to be in hydrostatic equilibrium (something that clearly is not the case, especially if the stars are experiencing mass loss). The emergent flux from the static-atmosphere model was then imposed as the lower boundary of the expanding envelope — a "core–halo" model. In unified atmospheres this artificial segregation is removed and the photosphere and expanding envelope are treated self-consistently, taking into account opacity effects in the envelope.

Also several of the 'new-generation' models remove the assumption of plane-parallel atmospheres, and include the 3-dimensional angle dependence in the radiation-transfer equations.

However, perhaps the most important of all has been the increased quality (and quantity) of atomic and molecular data. Although it might appear from the visible spectrum (see appendix A) that hydrogen and helium are the dominant sources of opacity in early-type stars, UV spectra of these same stars show a wealth of lines of heavier atomic species. The combined opacity from these sources can significantly alter the temperature structure in the upper layers of the stellar photosphere (e.g. Hubeny, 1998).

A graphical summary of the physics of O-star atmospheres is shown in figure 3.2.

3.2 Model grid

The grid of model spectra used in this work for the analyses of O stars was primarily calculated by K. C. Smith (unpublished) at UCL. Details of this grid can be found in Smith and Howarth (1994), and will only be summarised here. The grid consists of over 2200 individual model spectra calculated for several different values of four independent variables, namely effective temperature, surface gravity, helium number fraction and microturbulence. It spans a range in effective temperatures, $T_{\rm eff}$, from 27 kK to 3.5 kK in steps of 1 kK, and in surface gravity, $\log_{10} g$, from close to the effective Eddington limit[1]

[1]The lowest gravity models are 2.7 dex and 3.3 dex for effective temperatures of 27 kK and 40 kK respectively.

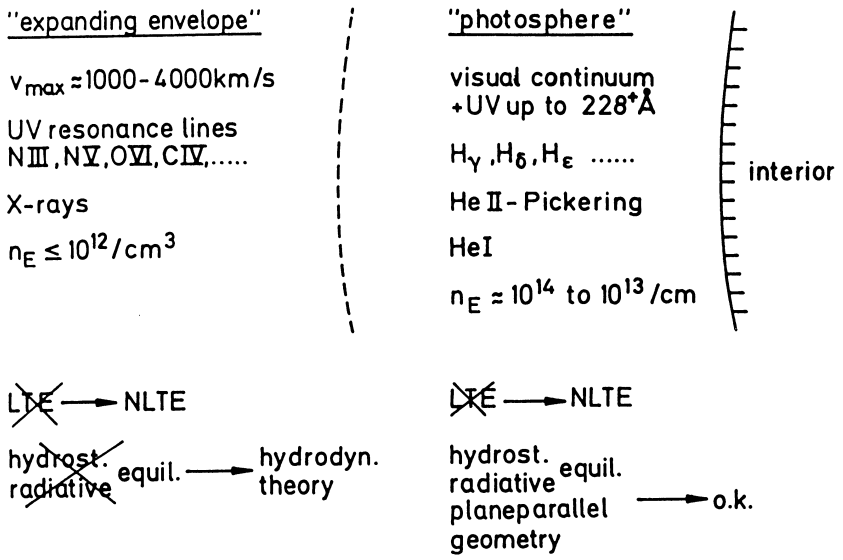

Figure 3.2: *The physics of hot star atmospheres. From Kudritzki, 1988.*

to 3.7 dex (c.g.s.) at intervals of 0.1 dex, with additional 'main-sequence' models calculated for 4.0 and 4.5 dex at each temperature. Each of these $T_{\rm eff}$–$\log_{10} g$ grids is repeated for helium number fractions of 0.05, 0.09 (solar), 0.20 and 0.30, and for microturbulent velocities of 0, 5, 10 and 15 km s^{-1}.

3.2.1 Atmospheric structure calculations

The model atmospheres were calculated using TLUSTY version 160 (Hubeny, 1988; Hubeny and Lanz, 1995), assuming plane-parallel geometry and hydrostatic and radiative equilibria. Only hydrogen and helium were considered explicitly in the structure calculations, with 8 non-LTE levels each of H I and He II and 14 non-LTE levels of He I. In addition to these, series of LTE hydrogenic levels were considered, extending to principal quantum numbers, $n = 16$, 16, and 32 for H I, He I, and He II respectively.

3.2.2 Synthetic spectra

Using the atmospheric structures discussed above, line-formation calculations were carried out using the codes DETAIL and SURFACE (Giddings, 1981; Butler, 1984; Butler and Giddings, 1985).

DETAIL solves the coupled equations of statistical equilibrium and radiative transfer, using the fixed atmospheric structure calculated above. It uses the method of complete linearization as formulated by Auer and Heasley (1974). The advantage with this formula-

tion is that the computational timing is linearly proportional to the number of frequency points. This, coupled with the fact that good agreement between model and observed line profiles is very dependent on the complexity of the model atoms used in this step (e.g. Herrero 1987a and 1987b), meant that line-formation calculations were carried out using an increased number of non-LTE levels for all ions (see Smith and Howarth, 1994, for specific details about the model atoms used).

Finally, synthetic H/He spectra were computed using SURFACE for each of the values of $T_{\rm eff}$, $\log_{10} g$, y and microturbulence discussed above. These grids of spectra were then loaded into an analysis package, TGKIEL, written by K. C. Smith, that for a given value of microturbulence will interpolate the grid of model spectra in all 3 dimensions (i.e. $T_{\rm eff}$, $\log_{10} g$ and y). These interpolated models were then used for the analyses.

3.2.3 Model predictions

In subsequent chapters we compare these models to observed spectra; in particular, we will concentrate on the equivalent widths of certain He I and He II lines, and the profiles of H I lines. Before attempting such analyses, it is useful to investigate the theoretical behaviours of the lines in question. Figures 3.3 and 3.4 show the equivalent width behaviour predicted by the models for the helium lines considered in the analyses. It is worth keeping in mind when selecting lines for $T_{\rm eff}$–$\log_{10} g$ fit-diagram techniques (as explained in chapter 4), lines which show a low equivalent width sensitivity to the model input parameters (i.e., $T_{\rm eff}$ and $\log_{10} g$) might 'amplify' uncertainties in measured equivalent widths when used in the analyses. This is discussed further in chapter 4. Similarly, lines which have a high sensitivity might emphasise missing physics or assumptions made in the models. This is clearly seen for the He I triplet lines, in particular for He I λ4471Å, where the models consistently fail to reproduce observed equivalent widths (see also chapter 5).

Although it has previously been demonstrated (e.g. Smith and Howarth, 1994) that these models are successful in reproducing, at least to an acceptable level, certain H and He lines in spectra of hot stars, they still do fail, sometimes catastrophically, in modelling others. In particular, these hydrostatic models neglect the effects of the stellar wind envelope surrounding the stars, and are unable to reproduce the wind-induced emission features or distortions often observed in lines such as the lower members of the hydrogen Balmer series (for example Hα and Hβ) and He II λ4686Å.

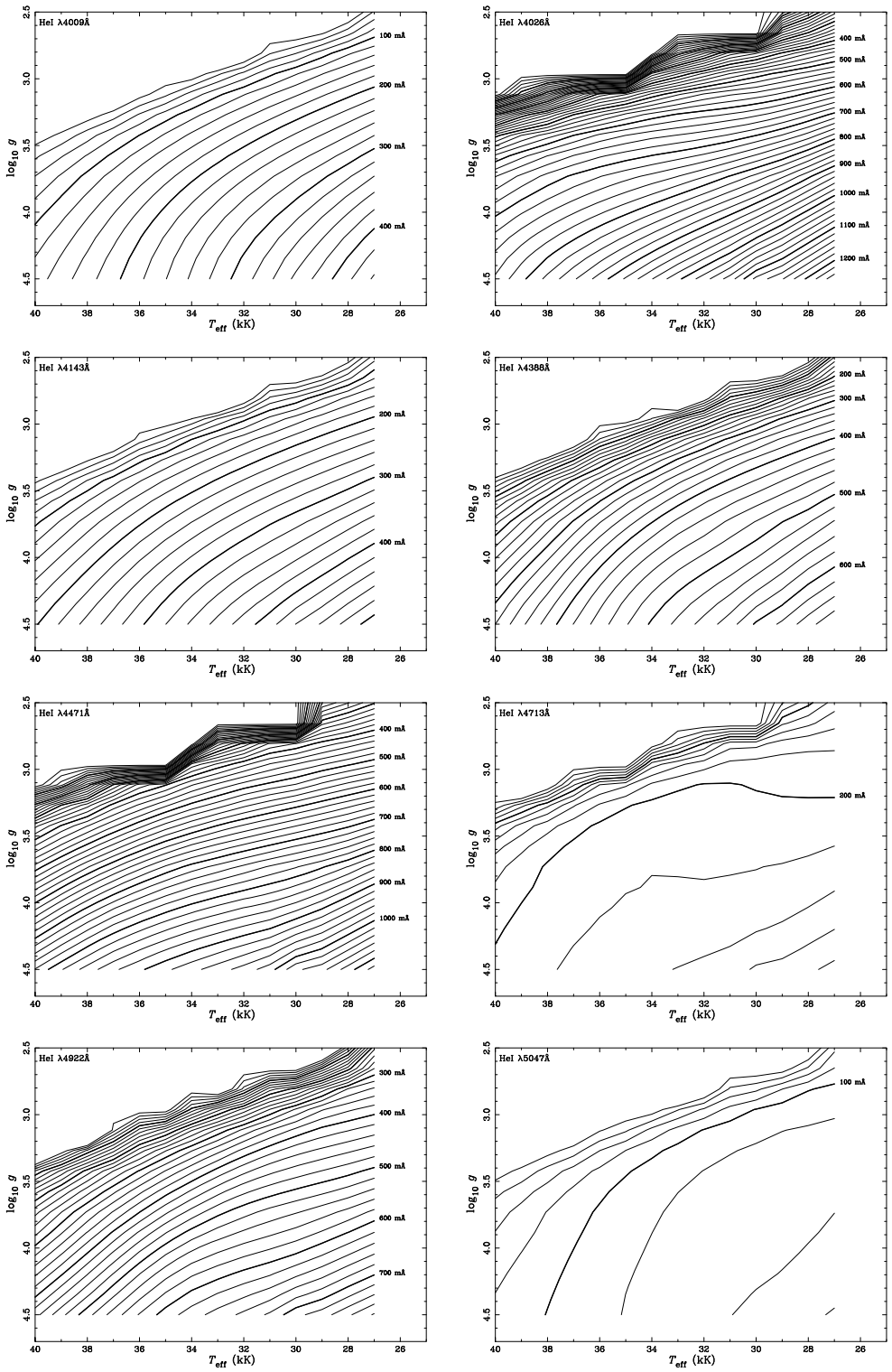

Figure 3.3: *Equivalent-width contours for* He I *lines for models with solar helium abundance ($y = 0.09$). Contours are drawn every 20mÅ, with thick lines every 100mÅ.*

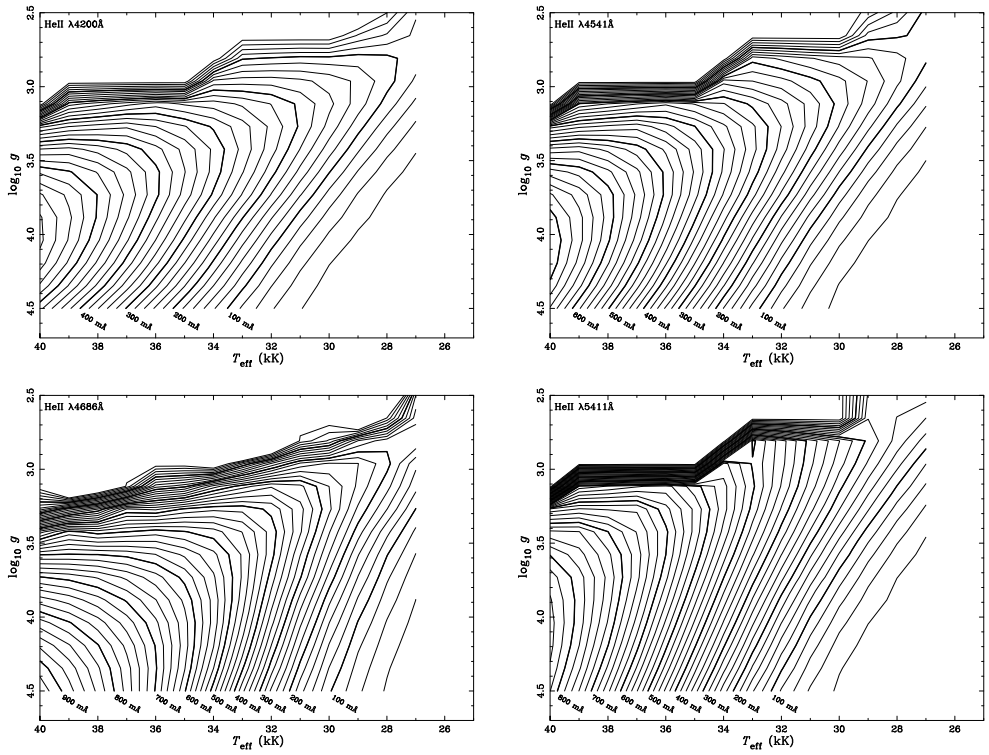

Figure 3.4: *Equivalent-width contours for* He II *lines. Contours as in previous figure. Note 'edge effects' caused by interpolation defects close to edge of the grid (determined by the Eddington Limit).*

3.2.4 Effects of microturbulence

Microturbulence was originally incorporated into curve-of-growth analyses to explain the observed fact that equivalent widths of certain lines are larger than those predicted by models[2] not taking this parameter into account.

Lately there has been a lot of interest in microturbulence in O and B-type stars. McErlean et al. (1998) and Smith and Howarth (1998) have both performed in-depth analyses of the effects of microturbulence when comparing models to observations. Both groups have found that including microturbulence in the line formation calculations results in an increase in the model He I-line equivalent widths. This is an unavoidable consequence of desaturation if only line formation is considered, but Smith and Howarth also showed that this is not true for all lines if microturbulence is treated in both line formation *and* statistical equilibrium calculations. However, it still holds for some important lines (e.g. He I λ4921Å and λ4471Å) commonly used in the analysis of O stars. This increase in equivalent width can lead to a lower adopted helium abundance than if microturbulence is neglected, something that could, at least partly, help resolve the so-called 'helium discrepancy' identified in OB-type stars by Herrero et al. (1992). It also appears that the inclusion of microturbulence has a greater effect on the He I triplet lines than on the singlet lines. This could help explain the 'generalized dilution effect' described by Voels et al. (1989). There is a more detailed discussion of this in chapters 4 and 5.

In the model grid used in this thesis[3], microturbulence was only included in the line-formation step of the modelling, and its effect on the statistical-equilibrium was neglected. Microturbulence was incorporated into the Voigt functions by including a non-thermal term thus:

$$\Delta\lambda_{\rm D} = (\lambda/c)\sqrt{(2kT/Am_{\rm H}) + v_{\rm turb}^2} \tag{3.10}$$

where c is the speed of light, k is the Boltzmann constant, T is the gas temperature, A is the atomic mass (of He in this case), $m_{\rm H}$ is the mass of an H atom, and $v_{\rm turb}$ is the microturbulent velocity.

The effects of microturbulence for He I lines can be seen in figure 3.5. Including 15 km s^{-1} microturbulence can add almost a third to the equivalent width of certain

[2] Models here does not necessarily refer to computer models, but to any predicted behaviour of the curve-of-growth

[3] Work is underway to construct a grid which treats microturbulence in both line-formation and statistical-equilibrium calculations.

He I lines. It is also appears that microturbulence is slightly more important in supergiants, with a low surface gravity, than it is for main-sequence stars, with $\log_{10} g \sim 4.5$. The He II lines are relatively unaffected by the inclusion of microturbulence in the line formation calculations only (maximum changes are only of the order of a few per cent).

3.2.5 Rotational or macroturbulent broadening

A subject which we will repeatedly come back to throughout this work is the question of whether the dominant 'macroscopic' broadening process in O-type stars is rotational Doppler broadening, or some other 'macroturbulent' velocity field. We distinguish between 'microscopic' processes which act on, essentially, atomic scales (Stark broadening, thermal broadening, etc.) or which otherwise affect the intrinsic line profile (like microturbulence), and 'macroscopic' processes which do not affect the line strength, but only the observed line profile (like rotation and macroturbulence).

To try to resolve this problem, we will in chapters 4 and 5 compare observations to model spectra convolved with either a rotational Doppler function (Gray, 1992 p. 374):

$$\mathrm{f}(\Delta x, \Delta\lambda, \epsilon) = \frac{2(1-\epsilon)\sqrt{1-\Delta x^2} + \frac{1}{2}\pi\epsilon(1-\Delta x^2)}{\pi\Delta\lambda(1-\epsilon/3)} \tag{3.11}$$

or a Gaussian function which simulates a macroturbulent velocity field in the stellar atmosphere:

$$\mathrm{f}(\Delta x, \Delta\lambda) = \frac{\sqrt{\pi}}{\Delta\lambda \times \exp(-\Delta x^2)} \tag{3.12}$$

where ϵ is the limb-darkening coefficient, $\Delta\lambda$ is the apparent velocity shift. The value x is the x-coordinate of an imaginary strip (see figure 3.6) of the stellar disk, and, for rotation, is related to $\Delta\lambda$ through:

$$\Delta\lambda = v = x\Omega \sin i \tag{3.13}$$

where Ω is the angular velocity and i is the angle of inclination as illustrated in figure 3.6.

Figure 3.7 shows the model He I λ4143Å line convolved with the rotational function (solid line) and the macroturbulent function (dashed line). The rotational convolution gives the line a much deeper rounder shape, whereas the macroturbulent convolution gives a sharper and broader profile, almost a 'v'-shape.

In an attempt at determing which of these line broadening functions best reproduce the observed line profiles, model spectra convolved with the above functions are compared to observations using a χ^2 fitting procedure. This analysis is described in section 4.4.

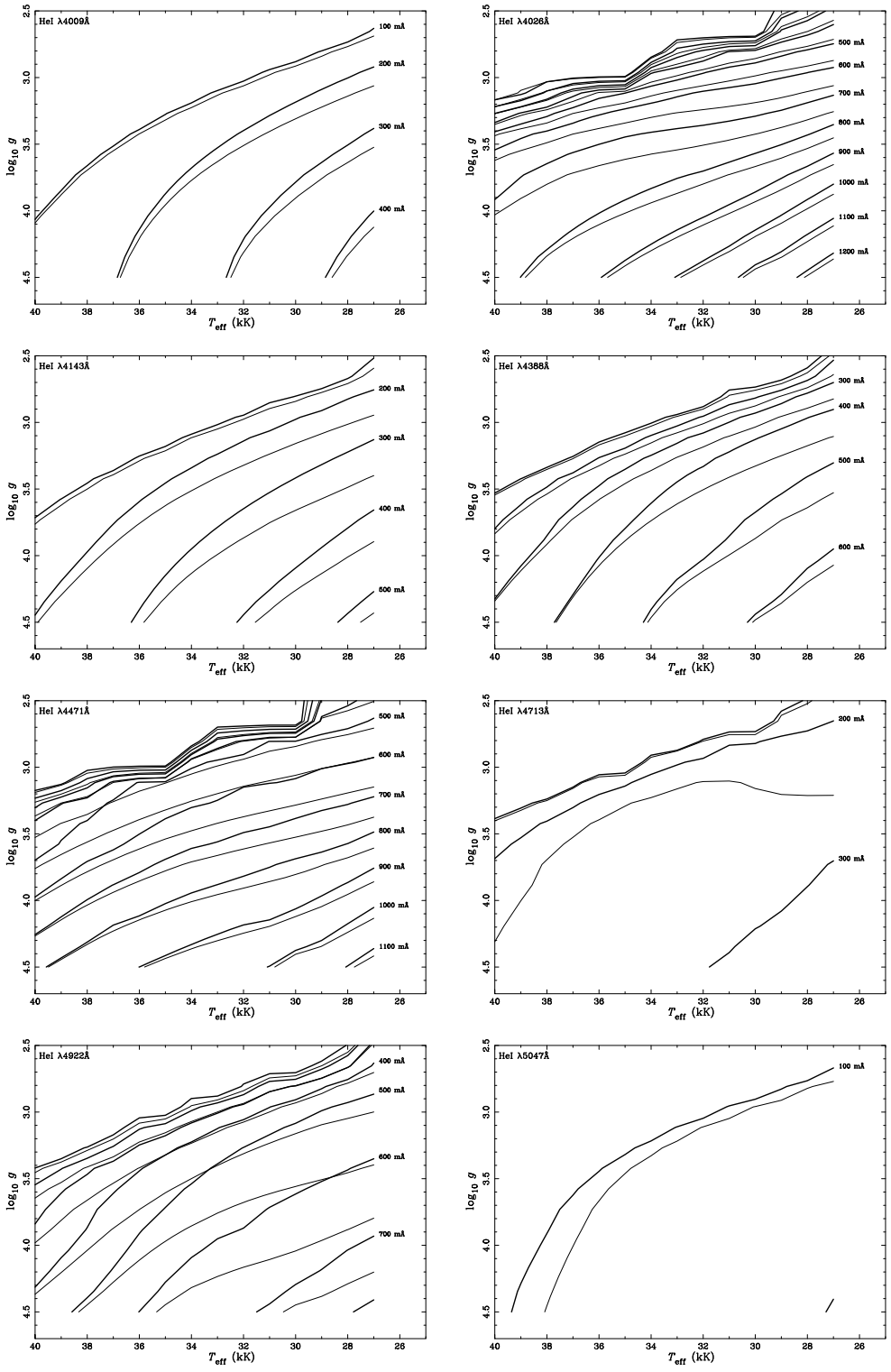

Figure 3.5: *Equivalent-width contours for* He I *lines highlighting the effects of the microturbulence parameter. Contours are drawn every 100mÅ. Thick lines are for a microturbulent velocity of 15 km* s^{-1}*, and thin lines for zero microturbulence.*

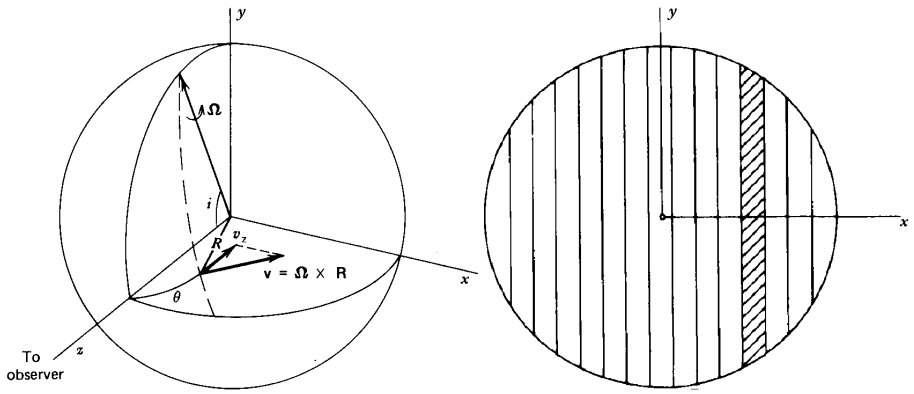

Figure 3.6: *Schematic of a rotating star.* ***Left diagram*** *illustrates symbols discussed in text. The y axis is chosen to make Ω lie in the y – z plane.* ***Right diagram*** *shows how the apparent disk of a star can be thought of as a series of strips, each with a Doppler shift according to equation 3.13. From Gray (1992).*

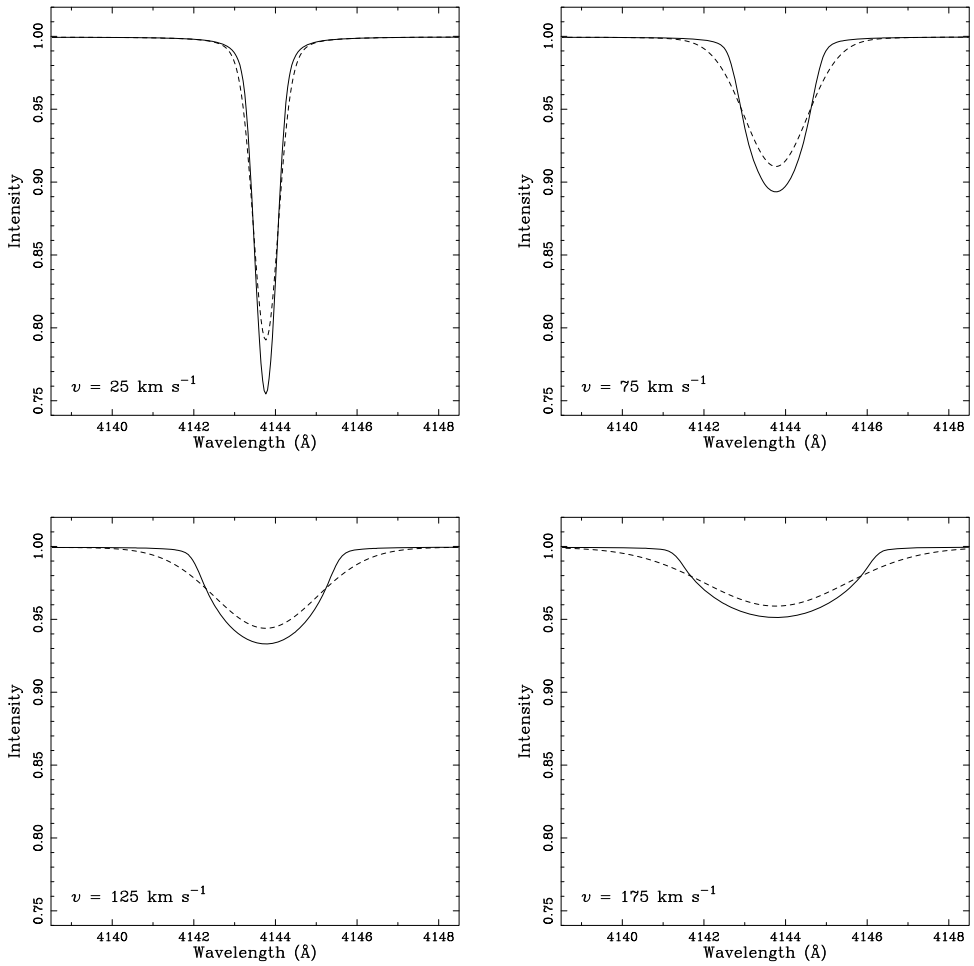

Figure 3.7: *Comparison of rotational Doppler and macroturbulent broadening profiles for* He I *λ4144Å. Solid lines show the rotationally broadened line profiles, and the dashed lines are the line profile broadened by macroturbulence.*

Chapter 4

10 Lac — a case study

10 Lacertae (HD 214680) is one of a very few narrow-lined O-stars. Its projected equatorial rotation velocity is only of the order 25–35 km s^{-1} (35 km s^{-1} in Howarth et al., 1997b; 31 km s^{-1} in Penny, 1996; see also table 4.6). This makes 10 Lac a good star to use as a case study. The narrow lines make line identification relatively easy, and many lines that are either badly blended or too broadened to be reliably measured for most of the other O stars in the sample are easily measured. This chapter will primarily look at the method used to find the stellar parameters for the O stars in this thesis, and demonstrate its use by applying it to 10 Lac. It is important that, although the strength of this analysis is in its consistency, the method should yield good results for individual stars. However, the results of a single star should always be considered in the context of the complete sample.

4.1 Spectral features

The 10 Lac spectrum is a good example of a typical late O-type main-sequence spectrum[1]. Figure 4.1 shows some of the spectral features considered in this thesis. The optical spectrum is dominated by strong, broad hydrogen lines of the Balmer series and by the relatively strong He I triplet lines (e.g. $\lambda\lambda$4026 and 4471Å). The He II lines are relatively weak compared to the H and He I triplet lines, although these lines are considerably stronger in stars with higher effective temperatures, $T_{\rm eff}$ (i.e. earlier spectral types).

Also visible are many weaker lines, in particular lines from several ions of C, N, O

[1] We are here only considering the optical spectrum, but UV spectra of 10 Lac has also been studied in detail by several authors (e.g., Walborn and Bohlin, 1996).

and Si. Only some of these are shown in the figure. See appendix A for more complete diagrams.

The 4630–4640–4650Å region contains a wealth of C, N and O lines, and the strong lines here are often used to check for carbon and nitrogen abundance anomalies in these stars (see also appendix B).

4.2 Determining stellar parameters

As a general aim we want to find the effective temperature, $T_{\rm eff}$, the surface gravity, $\log_{10} g$, and the helium number fraction, y. These parameters define the most important properties of the star, and are intimately connected to other stellar parameters like the stellar mass and age. (There is also a fourth parameter which turns out to have an important effect on the final results: the microturbulence.) Using the grid of pre-calculated models discussed in chapter 3 we want to find a method to estimate these parameters by comparing the models to the observations.

In practice, we need to optimize pairs of parameters in tandem, since rigorous multi-dimensional optimisation is impractical (the models do not perfectly match the observations). After some initial testing, the method that was found to yield the most consistent results for the lines available was the construction of temperature – gravity diagrams; 2-D slices through the 3-D parameter space (4-D with microturbulence) being explored. The measured equivalent widths of the helium lines are traced in the diagrams as the locii of temperatures and gravities of the models that reproduce the measured values. The He II lines are, in the parameter space explored, mostly sensitive to the effective temperature, whereas the He I lines are sensitive to both $T_{\rm eff}$ and $\log_{10} g$.

The plots give an intersection zone where most of the lines cross, and the best-fit model is likely to fall somewhere inside this intersection zone. Due to observational errors and noise, as well as inadequacies in the models, there will always be a certain scatter of the lines. The wrong choice of the microturbulence parameter or of the helium abundance will also affect the plotted lines, and the aim of the analysis is to find the values of the free parameters that minimise the size of the intersection zone.

To constrain the solution further, a χ^2 fitting technique is applied to the wings of H10 λ3797Å, H9 λ3835Å, H8 λ3889Å and Hϵ λ3970Å. Unfortunately, the strong, wide hydrogen lines are often contaminated by blends with other lines and by wind emission;

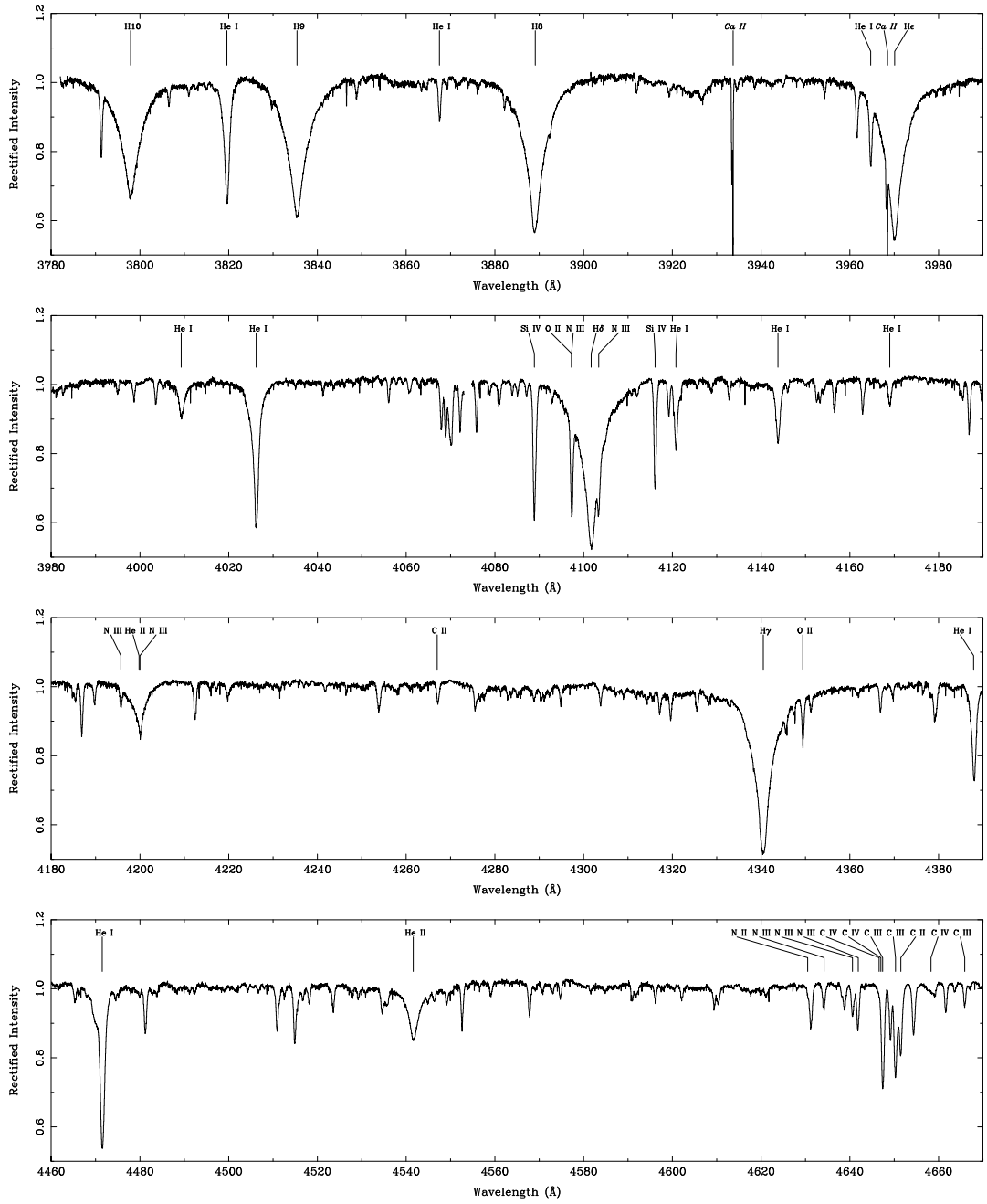

Figure 4.1: *Selected wavelength regions from the spectrum of 10 Lac with some important lines labelled. Several of the lines used in the analyses are shown, as well as the 4630 – 4640 – 4650Å CNO region (only C and N lines are identified here). Interstellar lines are labelled in italics. The spectrum of 10 Lac is shown in its entirety in appendix A.*

however, the pressure broadened wings are very sensitive to the surface gravity. By fitting the wings (and removing blends where they occured) consistent results could be obtained, even for the stars that show strong wind contamination.

The steps above are then repeated for a range of values of y (usually between 0.09 and 0.18 in steps of 0.01) and microturbulence (for 0, 5, 10 and 15 km s^{-1}). The 'best' solution is determined by using an impact-parameter analysis to find the point on each diagram that minimises the sum of the distances to individual lines. The best-fit diagram in all 4 dimensions is the one with the overall smallest value of the summed impact parameter. Figure 4.2 demonstrates the method, and each step is described in more detail in the following sections.

4.3 Equivalent widths of helium lines

There are a large number of helium lines in the observed spectrum. However, a number of these are either too badly blended or too weak to be measured reliably for all the stars in this dataset. The possible lines available for analysis are shown and commented on in tables 4.1 and 4.2. Some of the possible He I lines are very insensitive to changes in the effective temperature and/or the surface gravity. Including these lines in the analysis can degrade the quality of the results rather than improve them, since even a small error in measuring the equivalent width can give rise to large errors in both $T_{\rm eff}$ and $\log_{10} g$. The line that showed the least sensitivity to these parameters, He I λ5016Å, has been left out of the analysis. However, He I λ4713Å, which is also fairly insensitive (see figure 3.3) has been included to see what effects this line might have on the analysis (see also fig 4.7). In cases where this line gives discrepant results it has been left out of the impact-parameter calculations.

The lines originating in the $2\ ^3S$, $2\ ^1S$, $2p\ ^3P^\circ$ and $2p\ ^1P^\circ$ levels (in order of decreasing sensitivity), are very sensitive to the so-called *generalized dilution effect* discussed in detail by Voels et al. (1989). For stars where the plane-parallel assumption is no longer accurate (most likely all stars not belonging to luminosity class V), the models fail to reproduce the strengths of these lines. The strongest lines of each series are the most sensitive to this effect, and Voels et al. found that the weaker lines (like $\lambda\lambda$4713 and 4388Å) reproduced observations well. Smith and Howarth (1998) showed that including microturbulence in both statistical equilibrium and line formation calculations increased the strength of the

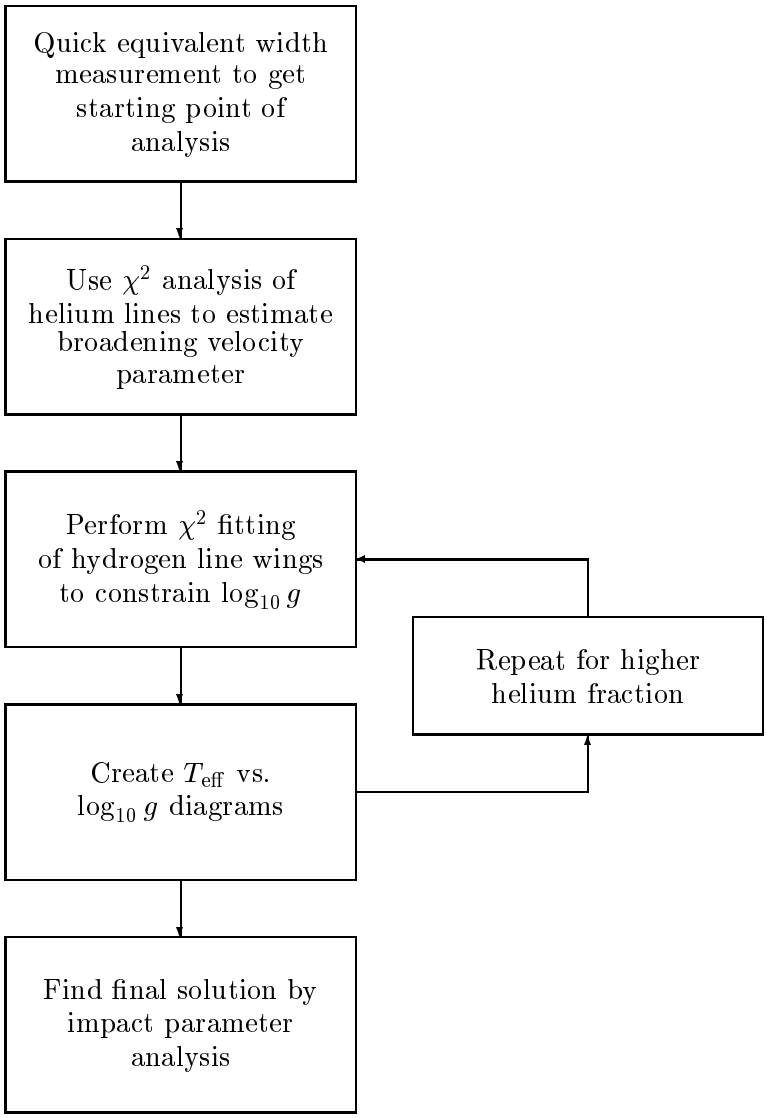

Figure 4.2: *Summary of method used to determine stellar parameters*

Table 4.1: Observed He I lines

λ (Å)	Transition	Comment
3819.6	$2p\ ^3P^\circ - 6d\ ^3D$	
3867.5	$2p\ ^3P^\circ - 6s\ ^3S$	Blended with several weak lines
3964.7	$2s\ ^1S - 4p\ ^1P^\circ$	Blended with H I
4009.3	$2p\ ^1P^\circ - 7d\ ^1D$	
4026.2	$2p\ ^3P^\circ - 5d\ ^3D$	
4120.8	$2p\ ^3P^\circ - 5s\ ^3S$	Blended with several strong lines
4143.8	$2p\ ^1P^\circ - 6d\ ^1D$	
4169.0	$2p\ ^1P^\circ - 6s\ ^1S$	Very weak and possibly blended
4387.9	$2p\ ^1P^\circ - 5d\ ^1D$	
4437.5	$2p\ ^1P^\circ - 5s\ ^1S$	Very weak and in the middle of diffuse interstellar band.
4471.5	$2p\ ^3P^\circ - 4d\ ^3D$	
4713.1	$2p\ ^3P^\circ - 4s\ ^3S$	Model predictions insensitive to $T_{\rm eff}$ and $\log_{10} g$
4921.9	$2p\ ^1P^\circ - 4d\ ^1D$	
5015.7	$2s\ ^1S - 3p\ ^1P^\circ$	Model predictions insensitive to $T_{\rm eff}$ and $\log_{10} g$. Excluded since it might introduce large errors into analysis.
5047.7	$2p\ ^1P^\circ - 4s\ ^1S$	
5875.6	$2p\ ^3P^\circ - 3d\ ^3D$	Very strong line expected to be extremely sensitive to the dilution effect (discussed in text).
6678.1	$2p\ ^1P^\circ - 3d\ ^1D$	Sometimes lost in interorder gap

NOTES: *The lines used in this analysis are shown in* ***bold*** *type.*

REFERENCES: *Line identifications and wavelengths from Scholtz (1972); Transitions from Striganov and Sventitskii (1968).*

Table 4.2: Observed He II lines

λ (Å)	Transition	Comment
3968.4	$4f\ ^2F^\circ - 14g\ ^2G$	Very weak. Blended with H I
4025.6	$4f\ ^2F^\circ - 13g\ ^2G$	Very weak. Blended with He I λ4026Å
4100.0	$4f\ ^2F^\circ - 12g\ ^2G$	Blended with H I
4199.8	$4f\ ^2F^\circ - 11g\ ^2G$	
4338.7	$4f\ ^2F^\circ - 10g\ ^2G$	Blended with H I
4541.6	$4f\ ^2F^\circ - 9g\ ^2G$	
4685.7	$3d\ ^2D - 4f\ ^2F^\circ$	Sometimes contaminated by wind emission
4859.3	$4f\ ^2F^\circ - 8g\ ^2G$	Blended with H I
5411.5	$4f\ ^2F^\circ - 7g\ ^2G$	
6683.2	$5g\ ^2G - 13h\ ^2H^\circ$	Very weak

NOTES: *The lines used in this analysis are shown in* ***bold*** *type.*

REFERENCES: *Line identifications and wavelengths from Scholtz (1972); Transitions from Striganov and Sventitskii (1968).*

lines assumed to be affected by the dilution effect more than some of the weaker lines. They suggested that microturbulence could possibly explain the dilution effect. We have only included microturbulence in the line formation calculations and, according to Smith and Howarth, this might not be enough to bring He I λ4471Å into agreement with the observations. However, we have chosen to include this line to evaluate the effects of microturbulence.

The spectra were measured using the Starlink data analysis program DIPSO (Howarth et al., 1997a). In DIPSO there are two basic ways of measuring the equivalent width of an absorption (or emission line). One is using the command EW. Using a user defined continuum the program calculates the equivalent width between two interactively defined points by simple trapezoidal integration. This method is quick and works very well for strong, unblended lines with a well defined continuum. However, where the lines are blended or the signal-to-noise is low, fitting a gaussian (using the DIPSO subroutine ELF) and using the equivalent width of the fit seems to give better and more consistent results. This works well for stars where the rotational broadening is large enough to give the lines a broad profile that can be approximated well by a gaussian. However, for the stars with narrow profiles the gaussians are poor approximations of the line profiles (figure 4.3).

Table 4.3 shows a comparison of equivalent widths measured using ELF and EW for 10 Lac and for HD 195592. HD 195592 is the third slowest rotator in the dataset, with a $v_e \sin i$ of approximately 50 – 60 km s^{-1} (Slettebak, 1956; Conti and Ebbets, 1977; this thesis). In the case of the slower rotators it appears that there there is a clear tendency for the equivalent widths measured using ELF to be smaller than those measured using EW. However, this trend disappears for HD 195592 where already the gaussians are a fairly good approximation of the line shape. It also appears that the typical differences in equivalent widths are of the order 5 to 10 per cent. By comparing this to figures 4.7 and 4.8 it appears that this corresponds to a difference of less than 1000K in temperature and 0.1 dex in $\log_{10} g$ for most lines. In the interest of maintaining consistency, the ELF equivalent widths are used for the analysis, but the uncertainty on the final results for 10 Lac (and the slow rotators in general) is likely to be slightly larger than for the fast rotators.

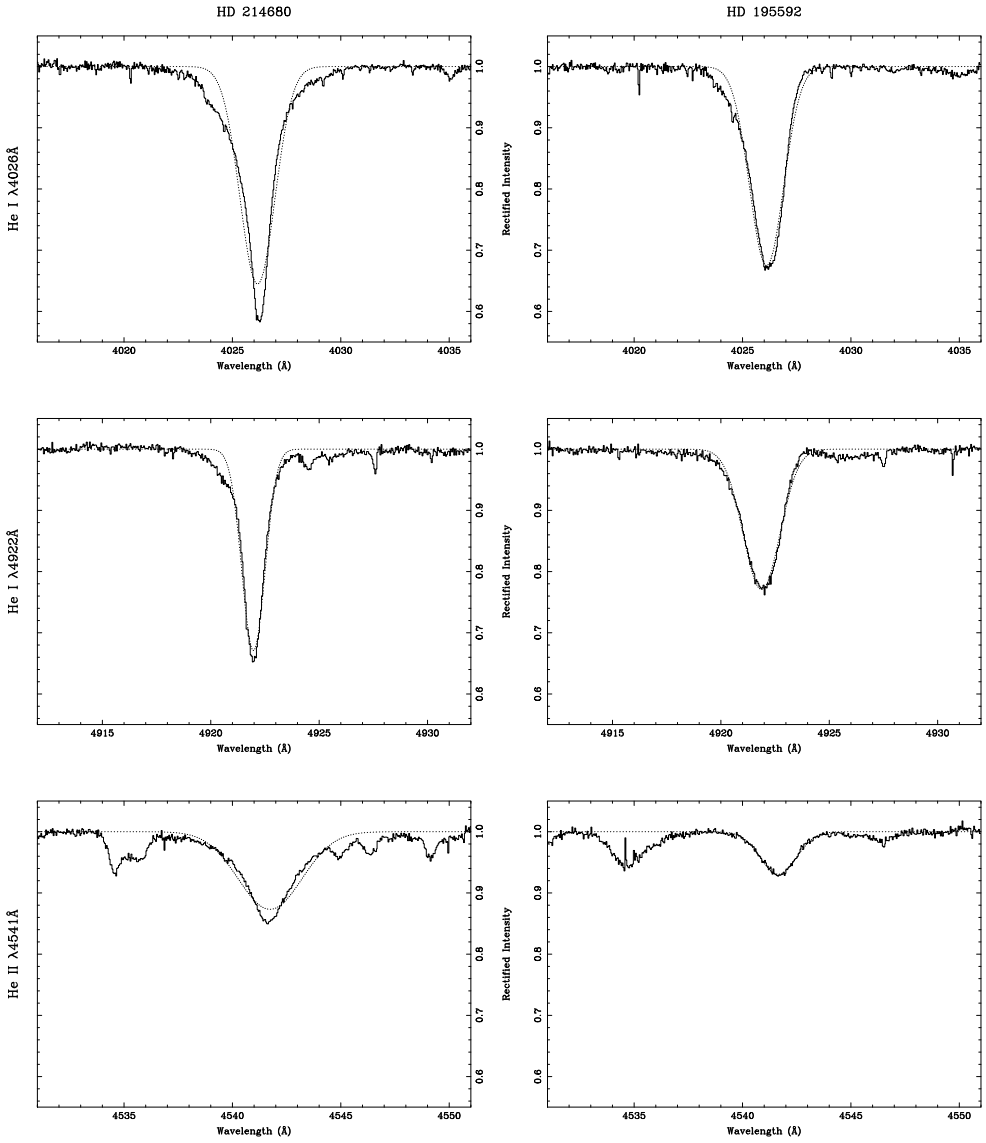

Figure 4.3: ELF *fits to selected lines in HD 214680 and HD 195592. The gaussians do not fit the narrow line profiles of the slow rotator (HD 214680) very well, but reasonable fits are obtained for the slightly broader lines in HD 195592.*

Table 4.3: Comparison of the DIPSO commands ELF and EW

HD 214680

Line	ELF (mÅ)	EW (mÅ)	$\frac{\text{EW}-\text{ELF}}{\text{ELF}} \times 100$
He I λ4009Å	224	200	−10.7
He I λ4026Å	791	851	7.5
He I λ4143Å	247	290	17.4
He I λ4388Å	399	421	5.5
He I λ4471Å	646	715	10.6
He I λ4713Å	265	266	0.3
He I λ4922Å	466	510	9.4
He I λ5047Å	117	121	3.4
He II λ4200Å	632	650	2.8
He II λ4541Å	562	680	20.9
He II λ4686Å	797	850	6.6
He II λ5411Å	764	780	2.0
Mean			6.3 ± 7.8

HD 195592

Line	ELF (mÅ)	EW (mÅ)	$\frac{\text{EW}-\text{ELF}}{\text{ELF}} \times 100$
He I λ4009Å	215	196	−8.8
He I λ4026Å	641	650	1.4
He I λ4143Å	207	210	1.4
He I λ4388Å	386	378	−2.0
He I λ4471Å	811	828	2.0
He I λ4713Å	309	319	3.2
He I λ4922Å	500	504	0.8
He I λ5047Å	145	135	−6.8
He II λ4200Å	202	193	−4.4
He II λ4541Å	264	249	−5.6
He II λ4686Å	*contaminated by emission*		
He II λ5411Å	364	362	−0.5
Mean			−1.8 ± 3.9

NOTES: *Comparison of equivalent widths for 10 Lac and HD 195592. HD 195592 is the third slowest rotator in the sample, and with a relatively slow* $v_e \sin i$ *of approximately 50 km* s^{-1}*. It is clear that the agreement between* ELF *and* EW *is better for the faster rotator.*

4.4 Rotational velocity and macroturbulence

The χ^2 fitting of the hydrogen line wings requires an estimate of the 'macroscopic' and 'instrumental' broadening of the lines (at least if either of the two are significantly large; see figure 4.4) As it turns out, in the case of the broad hydrogen wings, the contribution due to the instrumental broadening is negligible, and rotation/macroturbulence only have to be considered if the velocity is sufficiently high (negligible for velocities less than 100 – 120 km s^{-1}, so only important for the fastest rotators). Rotation is unimportant for the He I and He II line statistics, since we use measured equivalent widths for these.

One way of determining the projected rotational velocity, $v_e \sin i$, in the stars in this sample, would be to measure the FWHM of the absorption lines of metallic species like C, N, Si and O. These lines are relatively unaffected by atmospheric broadening mechanisms compared to the hydrogen and helium lines. These metallic lines are, however, usually weak compared to H and He. Although they are easy to measure in the slow rotators like 10 Lac, in the faster rotators the lines are broadened too much to be accurately measured with our signal-to-noise.

Since consistency is paramount in this part of the analysis, a different approach to finding the $v_e \sin i$ is needed that will work for stars with broad lines and for stars with narrow lines. A method that seems to work well is to perform a quick equivalent width analysis similar to that described in section 4.6 but without the hydrogen line analysis. The results of this quick analysis are used to fix a starting point for the effective temperature and surface gravity. A χ^2 fitting method is then use to find the values of $v_e \sin i$ and y in the models that will best fit the observed line profiles of the helium lines. Since the χ^2 value is dependent on the number of 'spectral bins', it will vary depending on how much of the spectrum is examined. To make comparisons between individual lines possible, we usually use the normalised-χ^2, $\chi^2_\nu = \chi^2/\nu$, where ν is the *number of degrees of freedom*, which is usually the number of bins minus two.

The effective temperature, $T_{\rm eff}$, and surface gravity, $\log_{10} g$, both affect the widths of the lines. Varying y only changes the strengths of the lines and does not directly affect any of the broadening functions. Thus it is possible to get a good fit for the line broadening in a consistent way for all the He I lines, even when the initial estimates of the stellar parameters could be slightly wrong.

Two different line broadening functions are compared to the observations, as described

Table 4.4: Fitted values for $v_e \sin i$ and macroturbulence for 10 Lac

He I λ	$v_e \sin i$			m.turb.		
(Å)	v (km s^{-1})	y	χ^2_ν	v (km s^{-1})	y	χ^2_ν
4009	61	0.07	1.548	50	0.07	1.515
4026	21	0.09	2.122	14	0.10	2.148
4143	44	0.07	0.412	33	0.08	0.382
4388	23	0.08	0.718	16	0.08	0.732
4922	31	0.12	2.717	22	0.13	2.727
5047	29	0.10	0.222	22	0.10	0.212
Median:	30			22		

NOTES: *Values are fitted for initial 'guesstimate' of stellar parameters ($T_{\rm eff}$ = 37 kK; $\log_{10} g$ = 4.3). Note that in this case, y is not an accurate representation of the actual helium number fraction of the star, but indicates whether the model line for the given parameters is too strong ($y < 0.09$) or too weak ($y > 0.09$). However, if all the lines are too weak it could indicate that the star does have a helium abundance higher than the solar value (but could also indicate the wrong choice of $T_{\rm eff}$ and/or $\log_{10} g$).*

in chapter 3. From table 4.4 it appears that there is no statistically significant difference between the goodness of fit (given by the χ^2_ν value) for the rotational and the macroturbulent broadening functions for 10 Lac and we adopt the rotational function. The reasons for this choice will be further discussed in chapter 5; however as noted above, the line broadening is unimportant for the final results when the line broadening velocity is low.

Howarth et al. (1997b) found the $v_e \sin i$ of 10 Lac to be 35 $\pm$ 14 km s^{-1}, and other analyses of this star (see table 4.6) adopted values between 25 and 30 km s^{-1}. These values compare well with the 30 km s^{-1} adopted here (typical uncertainties on velocity measurements are of the order 10–15 km s^{-1}; see chapter 5).

4.5 χ^2 maps of hydrogen line wings

The pressure-broadened wings of the hydrogen lines are used to fix the surface gravity. They are relatively insensitive to changes in $T_{\rm eff}$ and show almost no dependence on the helium abundance (see fig 4.4).

The equivalent width, W, is not a useful parameter for the hydrogen lines since their cores are very sensitive to stellar wind contamination and also because their broad wings make the measured W very sensitive to continuum placement. Because of their broad profiles, they are also often blended with other lines. However, it is possible to extract useful information from these lines by concentrating on the wings. The method developed for this thesis involves extracting just the wings from the spectra by removing the cores of the lines and any blends that might occur. Then the wings are compared to the synthetic model spectra. For each grid-point (i.e. value of $T_{\rm eff}$ and $\log_{10} g$) a χ^2_ν fit value is calculated as in the previous section. These χ^2_ν values are tabulated in a two-dimensional 'map' in the $T_{\rm eff}$- $\log_{10} g$ plane and an automatic routine traces the χ^2_ν minima. The resulting locus of points describes a line of best-fit values of $T_{\rm eff}$ and $\log_{10} g$.

This is a very time consuming (both human and cpu) and due to the H I lines' insensitivity to the helium abundance, y, it usually only calculated for $y = 0.09$. However, if the star has a high helium abundance (say $y \geq 0.14$) then the χ^2_ν map is re-calculated.

4.6 Fit diagrams

The measurements discussed in sections 4.3 and 4.5 are used to construct fit diagrams similar to those used by, among others, Herrero et al. (1992) and Smith and Howarth

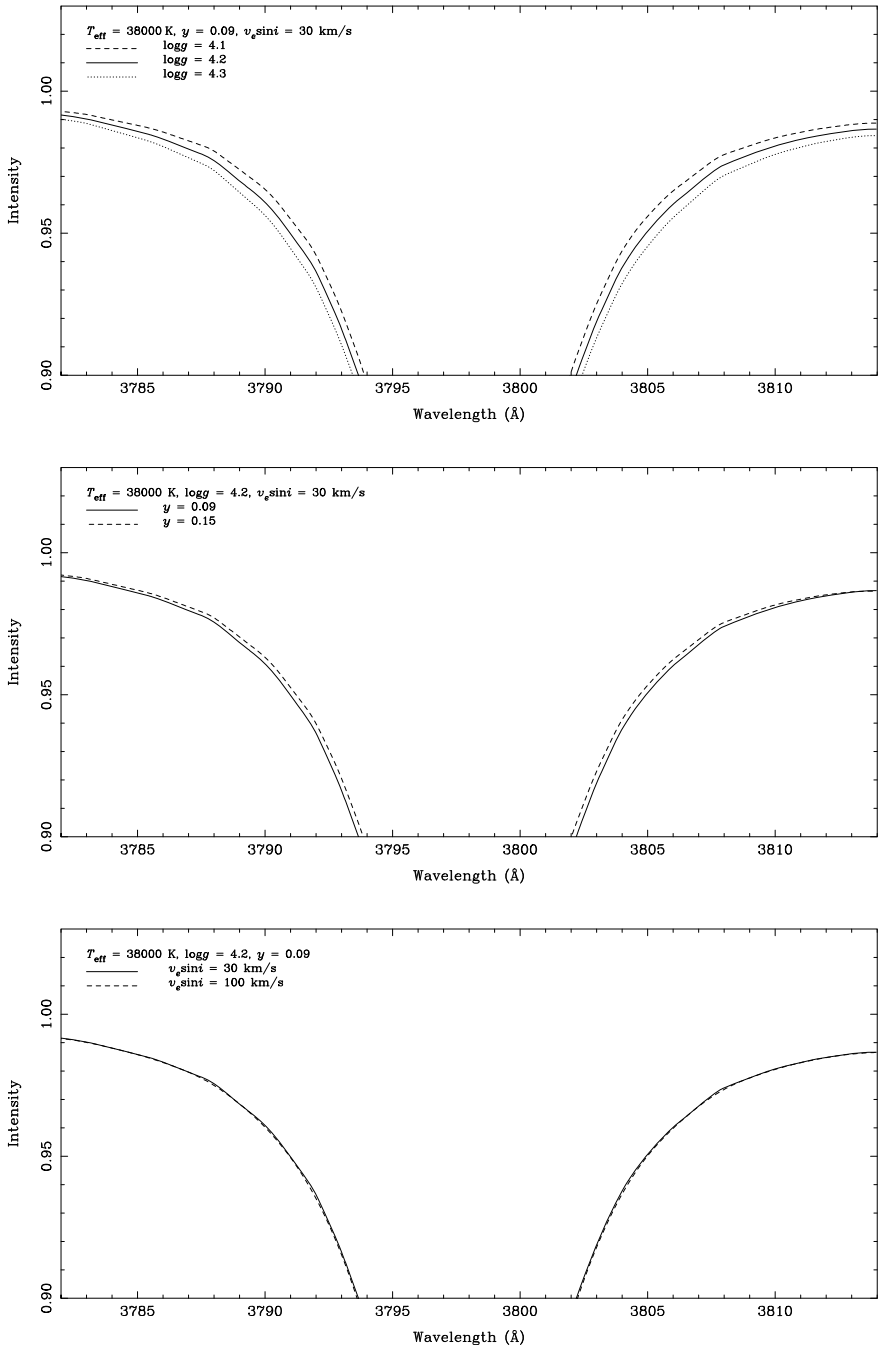

Figure 4.4: *Model predictions of the sensitivity of H10 λ3797Å to physical parameters. Diagrams illustrate, from top to bottom, sensitivity to changes in gravity, in helium number fraction (y), and in rotational broadening parameter ($v_e \sin i$). It is clear that of these, gravity is the most important parameter. Only a small part of the wings is shown to emphasize differences between models.*

(1994). The loci of closest equivalent widths for helium lines, and best-fit wings for hydrogen lines, are plotted in the $T_{\rm eff}$ – $\log_{10} g$ plane for a given value of y and microturbulence. The best-fit parameters are found by calculating the point of closest approach to all the fitted lines. The goodness-of-fit is estimated from the root-mean-square distance of the point to the fit-lines. Diagrams are constructed for values of y between 0.09 and 0.18 and for microturbulence-values of 0, 5, 10 and 15 km s^{-1}.

The fit diagram for 10 Lac is show in figure 4.5 and a sequence of diagrams for varying y and microturbulence is shown in appendix C. The best-fit value is found by defining a grid of points that surrounds the lines on the fit diagram. For each point in the grid, the shortest distance to each line is found, and the sum of squares of these distances is calculated. The point in the grid with the smallest sum of squares is taken to be the best-fit point. There is a slight ambiguity in defining the distances between point on the fit diagrams since the axes are not in the same units. The effective temperatures will typically be of the order 30000 – 40000, whereas the surface gravities are of the order 3.0 – 4.5. Unless these values are scaled, the temperatures will dominate in the calculation of impact parameters. In an attempt at "normalising" the axes, the y-axis ($\log_{10} g$) is simply multiplied by 10 (and effective temperatures are measured in kK). Thus both axes have units which are of the same magnitude.

From the fit diagram it appears that most lines are in fairly good agreement, with none of the lines falling outside the plotted area. There do, however, appear to be some lines that lie well outside the ± 5% variations shown in figures 4.7 and 4.8 (a discussion of the uncertainties and these plots follows later). The He I lines at 4009Å and 4471Å and the He II line at 4200Å all appear to lie well outside the intersection zone of the greater number of lines. The He I lines are both among the lines in table 4.3 with the largest differences in measured equivalent widths. He I λ4009Å is a weak line, and appears to be blended in all the observed stars, and this blend could lead to the observed over-estimation of the measured equivalent width. He I λ4471Å on the other hand, is a relatively strong line, and the measured equivalent width is in this case under-estimated. This is a triplet line with a strong forbidden component. There are also several blends in the line wings. Because this line has a strong but narrow line profile, and because of the resolved forbidden component, it is very poorly fitted using ELF. The blends in the line wings make reliable measurements using EW difficult. The EW measurements (715 mÅ) are significantly larger than the ELF estimates (646 mÅ), and in the model spectrum for $T_{\rm eff}$ = 38 kK and $\log_{10} g$ = 4.2 the

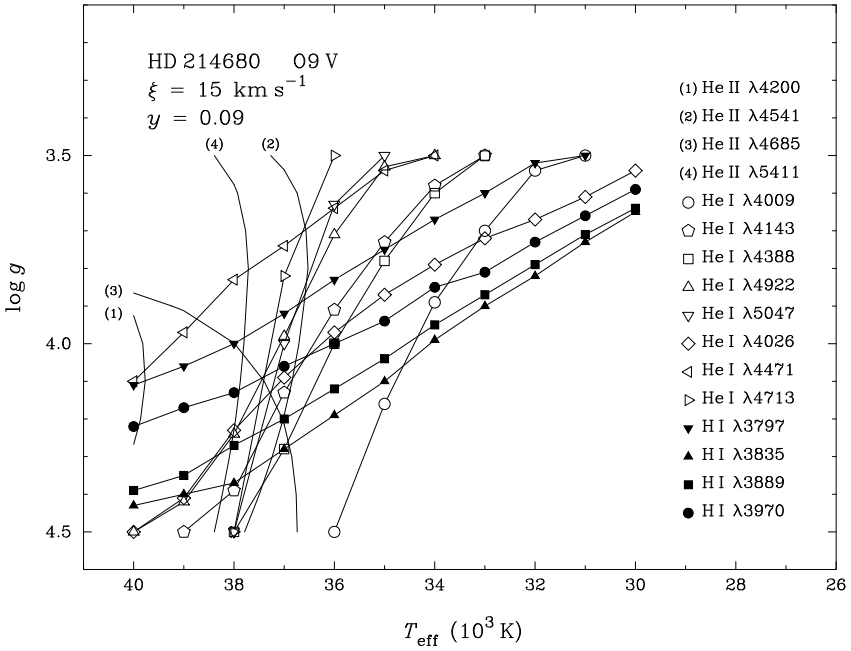

Figure 4.5: *The fit diagram for 10 Lac at* $y = 0.09$. *The diagram is plotted in the same orientation as the Hertzsprung-Russel diagram, with* $\log_{10} g$ *(≡ luminosity) increasing downwards and* $T_{\rm eff}$ *increasing to the left. Each line on the plot represents the locus of parameters for the model spectrum which best fits either the equivalent width (for the helium lines) or the line-wing profile (for the hydrogen lines).*

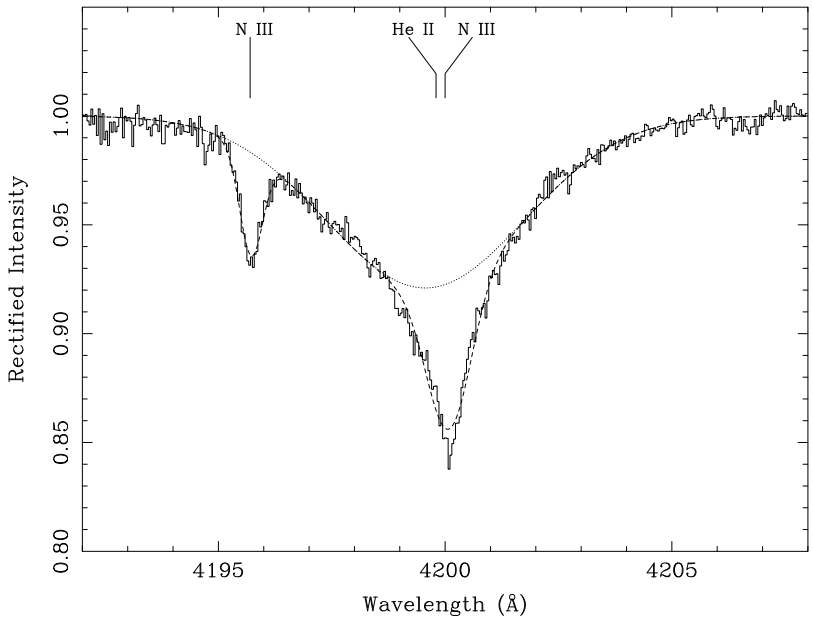

Figure 4.6: ELF *fit used to estimate equivalent width of* He II *λ4200Å. The dotted line shows the* ELF *fit to the* He II *line component, and the dashed line shows the fit to the combined line profile. The* EW *measurements included the blend with* N III *and overestimated the equivalent width of the* He II *line. Using* ELF *we can get a far better measurement, although because the line profiles are not well fitted by Gaussians it is likely that the* He II *line strength is underestimated in this figure.*

equivalent width between 4466Å and 4476Å is 766 mÅ. However in the unblended region between 4468Å and 4474Å the model equivalent width is only 663 mÅ, so it appears that the model is not in disagreement with the observations.

In the case of He II λ4200Å (4199.8Å), the disagreement between model and observations is most likely caused by a blend with a N III line at 4200.0Å. Using ELF to fit He II λ4200Å and both N III lines at 4195.7Å and 4200.0Å (see figure 4.6) yields an equivalent width of 433 mÅ which is in good agreement with the 454 mÅ predicted by the model.

It is difficult to give an accurate breakdown of the uncertainties that might be included in the analysis. Obviously the method is limited by the physics of the models and these results are difficult to quantify. It is slightly easier to look at the possible errors on the measurements. In the process of measuring the equivalent widths, the main pitfall is the determination of the continuum. For some lines this is relatively easy; however, when the lines are in a part of the spectrum with many other lines it can be very dif-

ficult. Nonetheless, by looking back at table 4.3 (where we compare equivalent widths measured independently using two different methods and repeating the steps of spectral normalisation), it seems that the uncertainties on the equivalent widths are within a few per cent for most lines, and that an error estimate of ±5% is probably quite reasonable. Figures 4.7 and 4.8 show the effects of adding these errors to the He I and He II lines respectively. The change in position of the plotted lines is more or less of the order of the minimum spread seen in the fit-diagrams (e.g. HD 195592, HD 202124; see fig 5.8). This could imply that we have underestimated the uncertainty on the equivalent width measurements, but more likely it is down to a combination of uncertainties in measurements and omissions/simplifications in the models.

4.7 Physical parameters of 10 Lac

The results of the impact parameter analysis are listed in table 4.5. From this table it appears that both temperature and gravity are well constrained by the equivalent width diagrams. It is also clear that the fits are significantly better for high microturbulent velocities of the order 10-15 km s^{-1}. The parameter p listed in the table is the root-mean-square distance to the lines as discussed in section 4.6. The smallest value of p is for $y = 09$ and $\xi = 15$ km s^{-1}, and we adopt these values, and $T_{\rm eff} = 38{,}000$ K and $\log_{10} g = 4.2$ as the best-fit parameters for 10 Lac. Comparisons of model spectra for these parameters and the observations are shown in figures 4.9 and 4.10.

The He I lines fit the observed equivalent widths very well, but for all lines apart from 4009Å and 4143Å the model line profiles are too weak in the cores. Lowering the $v_e \sin i$ by 10 – 15km s^{-1} resolves this, but the profiles then appear too narrow. The model He II lines are consistently too narrow and the line at 4200Å is also clearly blended as discussed earlier. The H I lines fit the line wings very well, but the model cores are clearly too weak and too narrow. In addition to this, the red wing of H10 λ3797Å does not fit the observations. It is possible that the normalisation at this point is poor. This line appears in the first echelle order observed and the normalisation could be affected by edge effects (see also chapter 2).

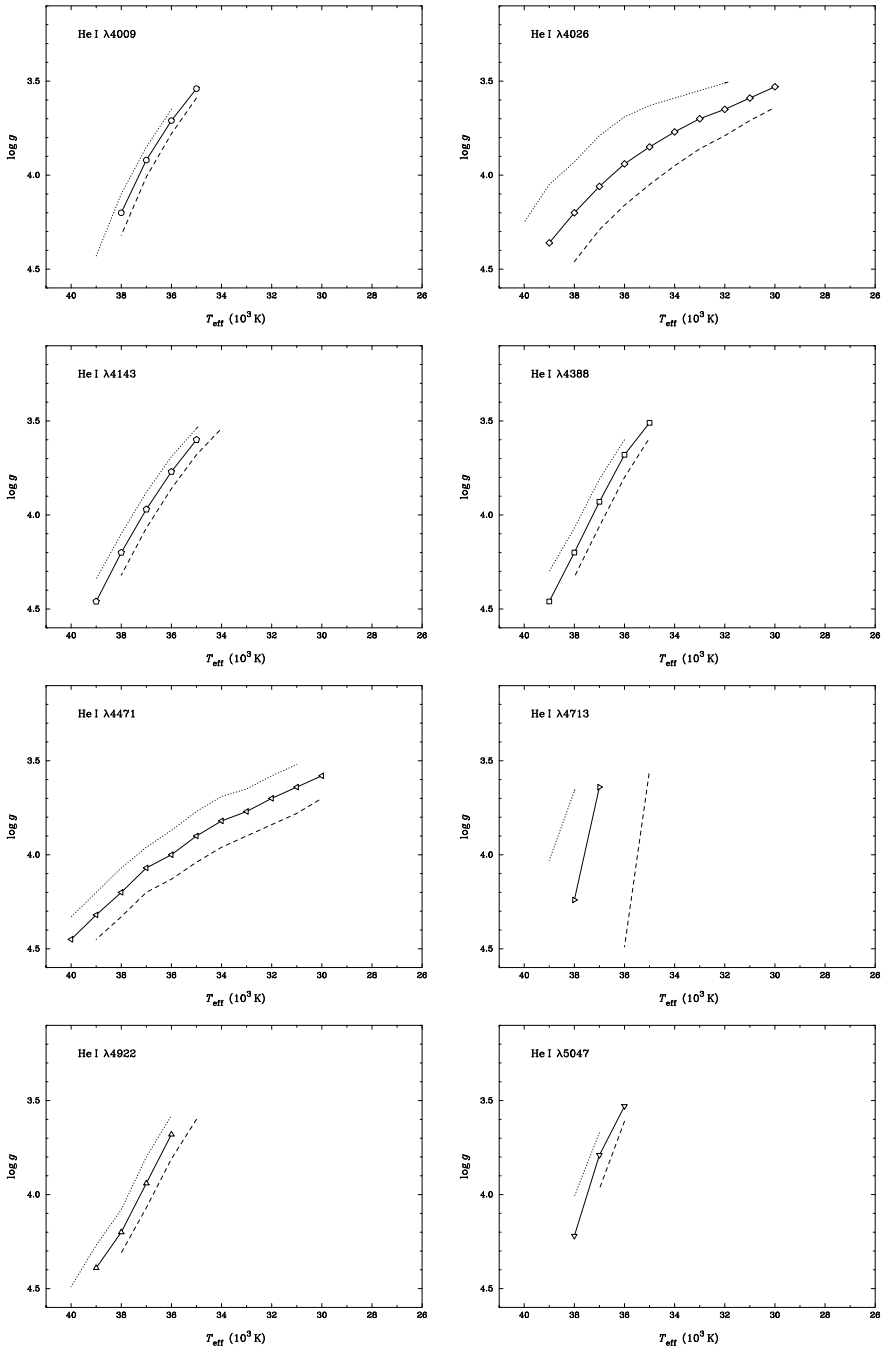

Figure 4.7: *These diagrams show the* He I *lines plotted as they would appear on a fit diagram using the equivalent widths predicted by the models for the adopted parameters of 10 Lac (solid lines). Error estimates of* ± 5 *per cent on the equivalent widths are shown as dashed lines (+5%) and dotted lines (-5%).*

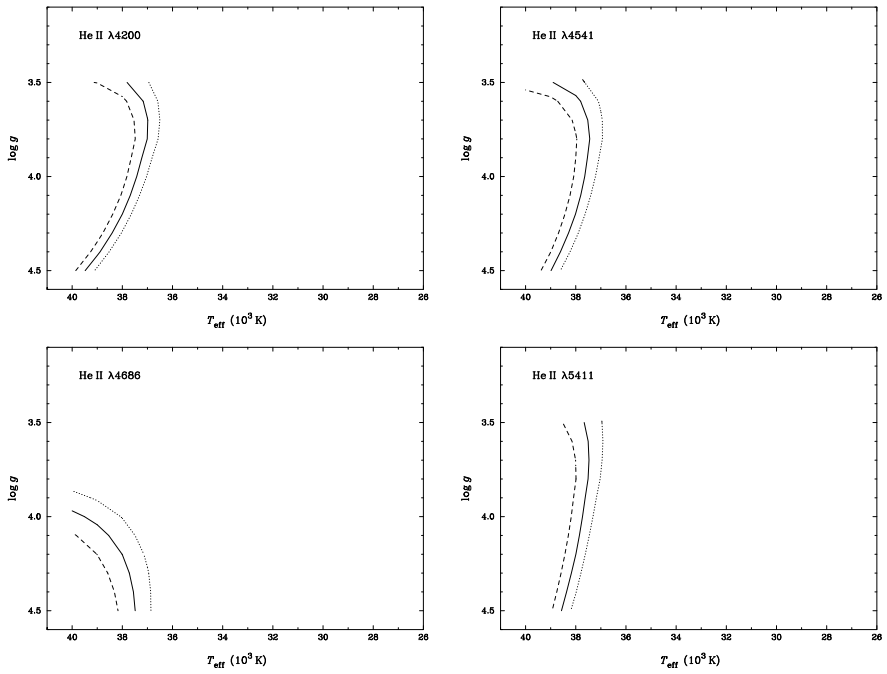

Figure 4.8: *These diagrams show the* He II *lines plotted as they would appear on a fit diagram using the equivalent widths predicted by the models for the adopted parameters of 10 Lac (solid lines). Error estimates of* ± 5 *per cent on the equivalent widths are shown as dashed lines (+5%) and dotted lines (-5%).*

Table 4.5: Impact parameter analysis for 10 Lac.

y	ξ (km s^{-1})	$T_{\rm eff}$ (kK)	$\log_{10} g$	p
09	0	37.6	4.21	1.439
	5	37.7	4.24	1.437
	10	37.7	4.22	1.376
	15	37.6	4.16	1.136
10	0	37.6	4.20	1.419
	5	37.5	4.16	1.430
	10	37.5	4.18	1.363
	15	37.5	4.09	1.142
11	0	37.8	4.20	1.459
	5	37.8	4.18	1.463
	10	37.0	4.02	1.167
	15	37.5	4.03	1.281

NOTES: *ξ is the microturbulence and p is a number representing the goodness of fit. It is given by the sum of the distances squared. A small p represents a tight clustering of the lines in the diagram, with $p = 0$ if all the lines intersect at a single point.*

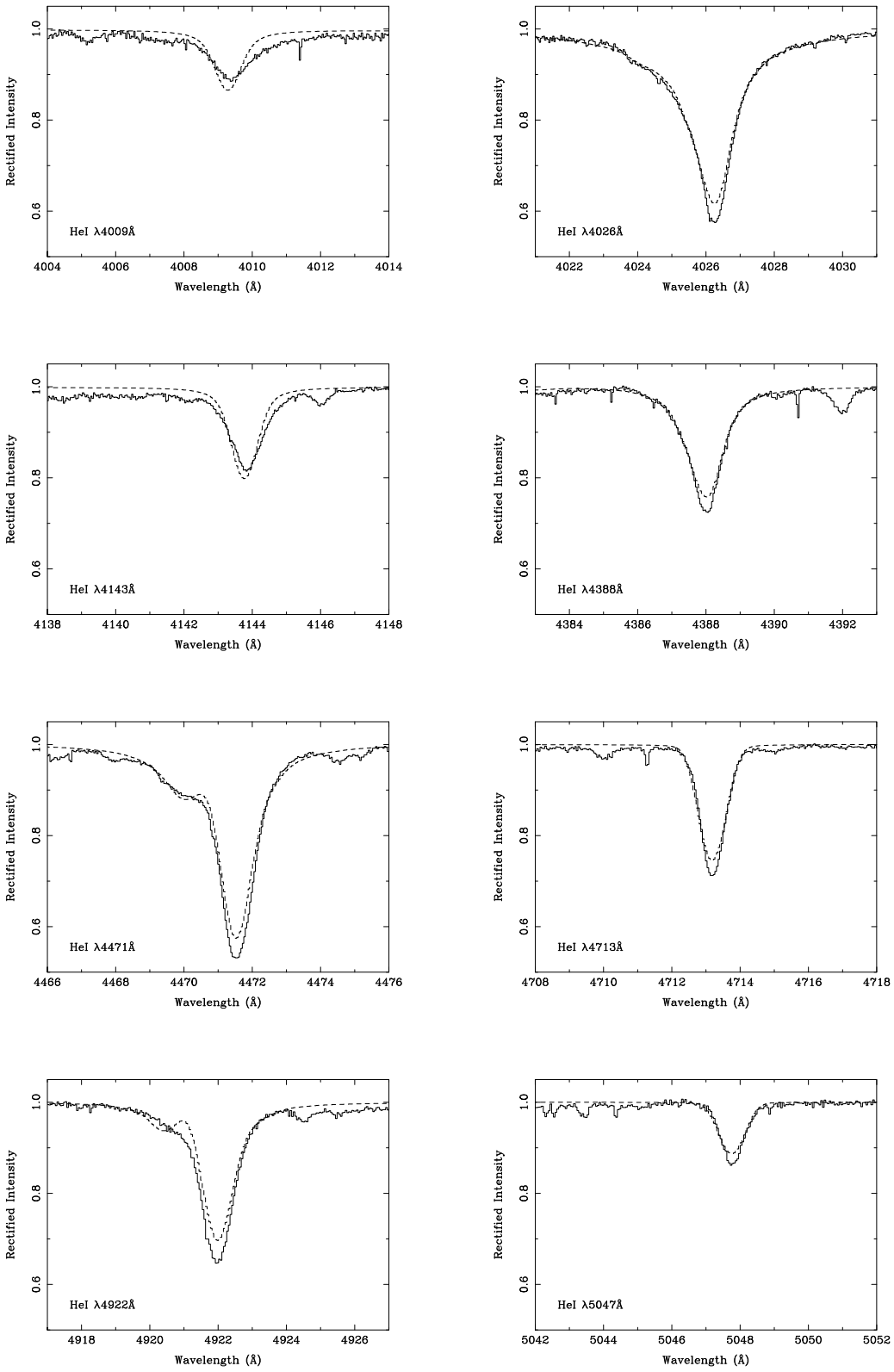

Figure 4.9: *Model fits to* He I *lines in 10 Lac.*

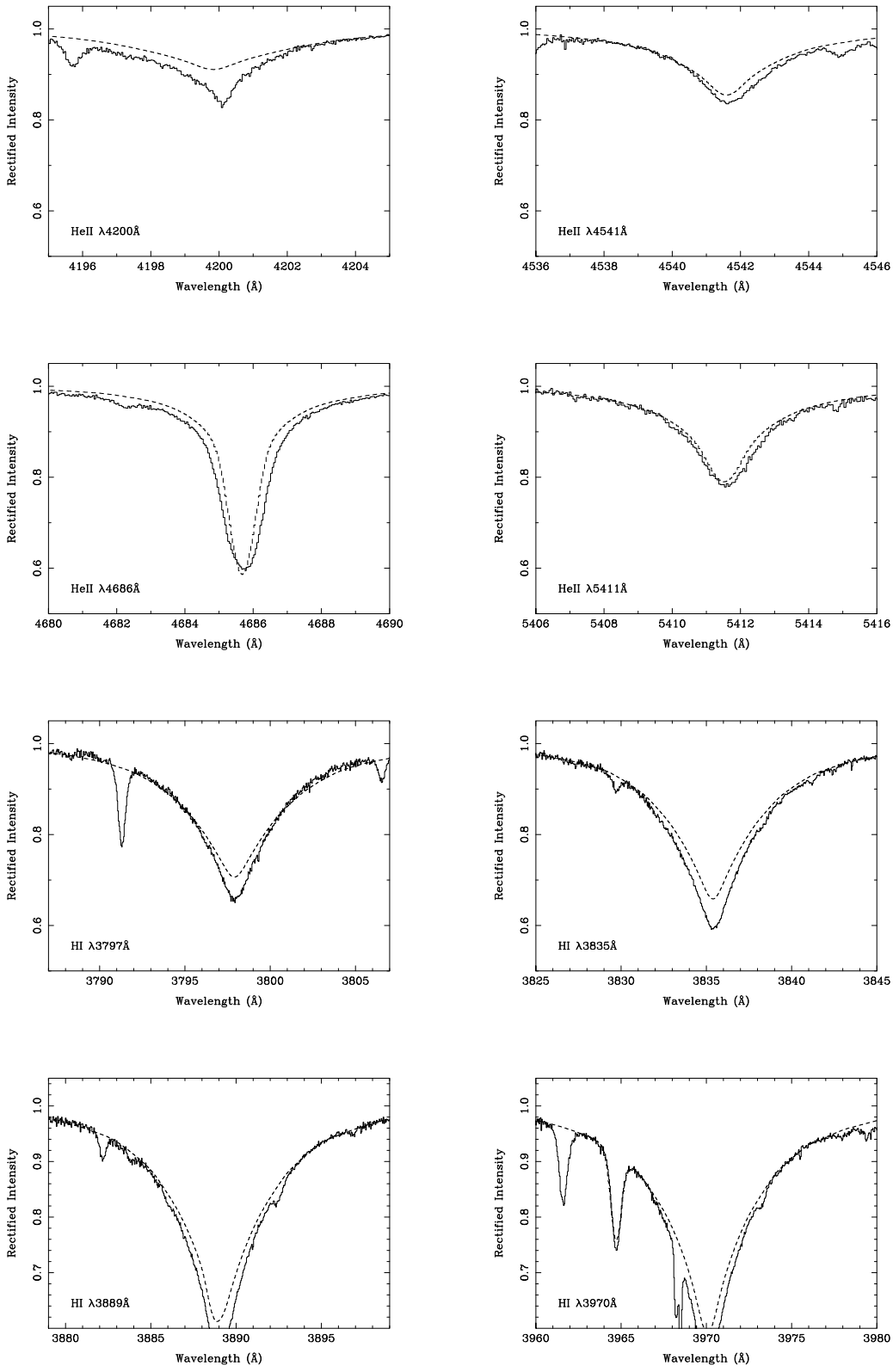

Figure 4.10: *Model fits to* He II *and* H I *lines in 10 Lac.*

4.8 Discussion

As shown in table 4.6, our results are in good agreement with Schönberner et al. (1988), but disagree with Grigsby et al. (1992). Grigsby et al. put this difference down to the inclusion of He II λ4686Å in Schönberner et al. We have also included this line; however it is in good agreement with all the other lines. Excluding this line does not appear to affect the analysis; the impact parameter results for 10 Lac exluding He I λ4686Å are $T_{\rm eff} = 37.7$ kK and $\log_{10} g = 4.16$ (for $y = 0.09$; $\xi = 15$ km s^{-1}). Including this line gave $T_{\rm eff} = 37.6$ kK. Clearly He II λ4686Å has no effect on the final results in this case.

The likely cause of the differences (also noted for other stars, see 5) must then be put down to differences in the atmospheric models and fitting methods used. In particular, Grigsby et al. used the cores of Hα, Hβ and Hγ and the He I lines λ4471Å and λ4922Å to determine temperatures. The cores of the hydrogen lines are likely to be filled-in by emission from the stellar wind, although from the plots in Grigsby et al. this would appear to have the effect of increasing the adopted effective temperatures, contrary to what would be required to bring their results into agreement with ours. The line He I λ4471Å consistently predicts lower temperature than the rest in our study. It is possible that this line could have affected their results (although Grigsby et al. note that their models also fail to reproduce the strength of this line). It is also worth noting that Grigsby et al. used line-blanketed atmospheric models, and Hubeny (1998) showed that when comparing analyses using H/He models to analyses using line-blanketed models, the H/He model analyses *overestimate* the derived temperatures. Hubeny found differences between the approaches of the order 2.5 kK, however he only 'analysed' synthetic spectra, not actual observations.

Table 4.6: Published parameters for 10 Lac

	This study	Schönberner et al.	Grigsby et al.	Herrero et al.
$T_{\rm eff}$	38,000 K	38,000 K	30,000 K	37,500 K
$\log_{10} g$	4.20	4.25	4.00	4.00
y	0.09	0.09	0.10	0.10
$v_e \sin i$	30 km s^{-1}	25 km s^{-1}	30 km s^{-1}	50 km s^{-1}

REFERENCES: *Schönberner et al. (1988); Grigsby et al. (1992); Herrero et al. (1992)*

Chapter 5

O Star Analyses

In this chapter, we apply the methods described in chapter 4 to all of the WHT O stars. Briefly, this involves estimating $T_{\rm eff}$ and $\log_{10} g$. Using model spectra computed for these parameters, we can find the line broadening velocity for each star. These results are discussed in section 5.1. Next, we measure equivalent widths and fit the hydrogen line wings using a χ^2 fitting procedure to construct fit-diagrams in the $T_{\rm eff}$ – $\log_{10} g$ plane. Series of these diagrams, constructed for different values of the helium number fraction, y, and the microturbulence, ξ, are used to find the values of these parameters that best fit all the measured lines. The appearance of the fit diagrams, model spectra and peculiarities of each star are briefly discussed in section 5.2. The fit diagrams for all the sample stars are shown in figure 5.8 at the end of this chapter.

As explained in chapter 4, the stellar parameters are found by using an automated routine to find the point of closest approach to all the lines in the fit diagrams. This routine sets up a grid surrounding the intersection zone, and calculates the sum of impact parameters for each grid point. This method works well when the intersection zone is close to the centre of the diagrams. Unfortunately, quite often the stellar parameters are towards one of the edges of the grid of models. At these points unfortunate 'edge effects' can occur. Notably, lines that fall outside the grid (for higher values of $\log_{10} g$) are treated as horizontal lines at the bottom of the diagrams. These lines are, however, easy to identify and remove from the analysis. Worse is the tendency of lines to cluster towards the low $\log_{10} g$ end of the diagrams. The grid of models goes as close to the Eddington limit as was computationally possible, and at these low values for $\log_{10} g$ the equivalent width changes rapidly with g. This effect is clearly apparent in the fit diagrams for the star BD+36 4063

(figure 5.1).

The impact parameter routines are also fairly sensitive to outlier lines, so they do include some automatic rejection routines. These routines work by first finding the point closest to all the lines, then rejecting those lines that are further than some arbitrary value from that point and re-calculating. If the first point is close to the 'correct' value, then this method usually works well. However, if the starting point is wrong, rejecting the outliers often rejects reliable lines, and the solution gets even worse. Because of this sensitivity to outliers, the lines that are more or less consistently in disagreement with the other lines, like He I λ4471Å and He II λ4686Å, have manually been excluded from the analyses where necessary.

5.1 Line broadening functions

The velocity characterising the best-fit line-broadening function in each star was found, as described in chapter 4, by creating a synthetically broadened model spectrum and using statistical methods to find the best-fit broadening function and velocity parameter. The median of the velocities found from the He I lines was adopted as the broadening velocity of the star.

Table 5.1 shows the results of the line broadening analyses for three 'typical' stars. They are representative of the complete sample, in the sense that the inferred rotational velocities are always higher than the inferred macroturbulent velocities. This effect is intrinsic to these functions; the macroturbulent function is shallower and broader than a rotational function with the same velocity (see chapter 3).

The stars in table 5.1 are also 'typical' in that the rotational broadening function fits better for the main-sequence star, and the macroturbulent broadening function fits better for all the other stars (see table 5.2 for results for the complete sample). This is true for all the stars, except AE Aur (HD 34078; O9.5 V), 10 Lac (HD 214680; O9 V) and the two stars with the broadest lines: HD 13745 (O9.7 II) and HD 16429 (O9.5 II). For the two main-sequence stars there is no real difference in the reduced χ^2 values for the two fits, and neither broadening function fits the observations particularly well. Unfortunately there are only 4 main-sequence stars in the dataset, so the sample is too small to draw any firm conclusions. However, it is not unreasonable to assume that the dominating line-broadening effect in main-sequence stars is rotation, whereas in the giants and supergiants,

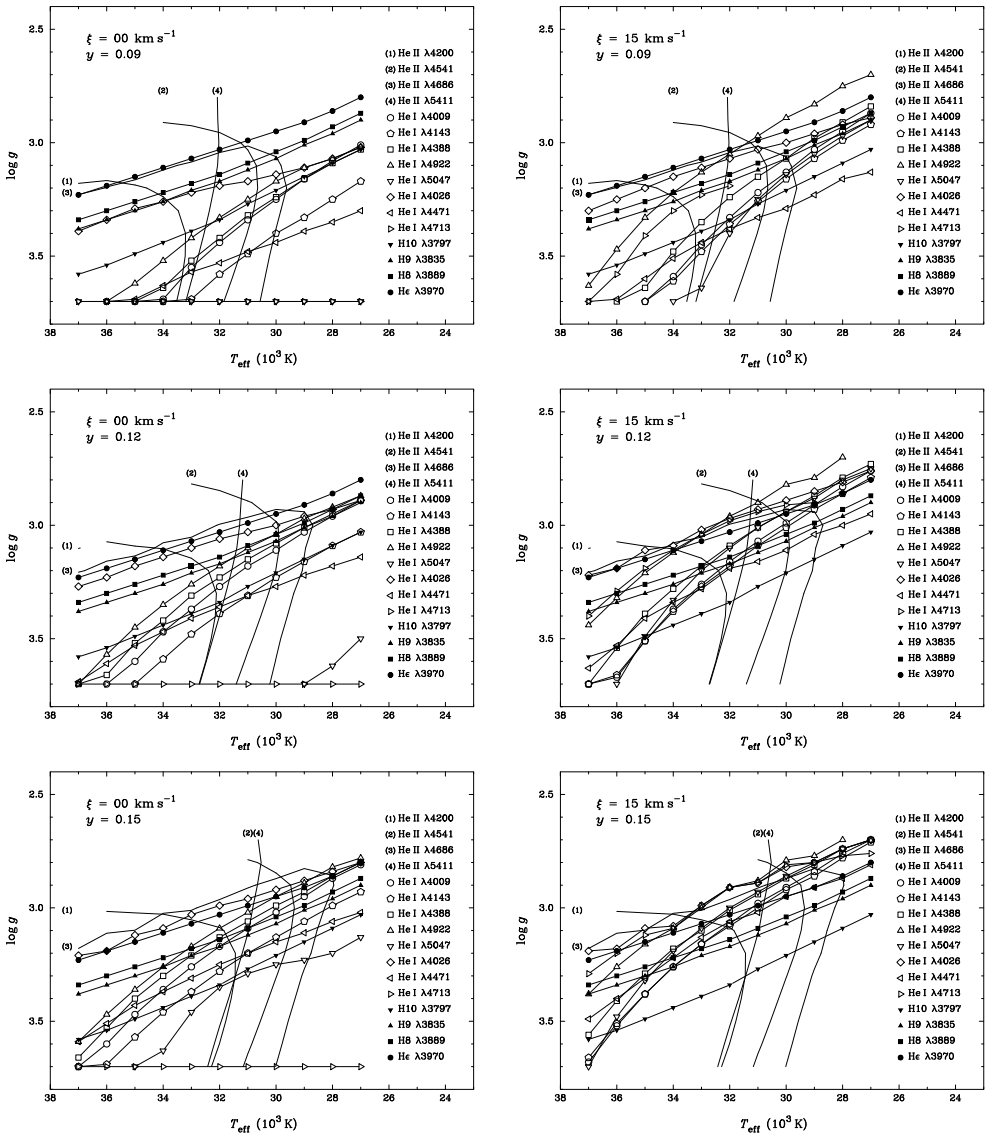

Figure 5.1: *Series of fit diagrams for BD+36 4063 for varying values of the helium number fraction, y, and the microturbulence, ξ. Note the tendency for the* He I *lines to cluster towards the lower* $\log_{10} g$ *(top) end of the grid as* y *increases. This can confuse the impact parameter calculating routines.*

Table 5.1: Example of line broadening analysis.

HD 12323 – ON9 V

He I λ	$v_e \sin i$			macroturb.		
(Å)	v (km s^{-1})	y	χ^2	v (km s^{-1})	y	χ^2
4009	153	0.12	0.491	124	0.13	0.491
4026	118	0.13	0.424	88	0.14	0.586
4143	142	0.17	0.191	115	0.20	0.179
4388	117	0.10	0.459	90	0.11	0.521
4922	128	0.13	0.373	95	0.14	0.498
5047	134	0.11	0.231	117	0.14	0.253
Median:	131		0.399	105		0.495

HD 218195 – O9 III

He I λ	$v_e \sin i$			macroturb.		
(Å)	v (km s^{-1})	y	χ^2	v (km s^{-1})	y	χ^2
4009	132	0.13	0.500	104	0.14	0.318
4026	72	0.10	1.011	53	0.10	0.986
4143	85	0.08	0.320	70	0.09	0.184
4388	78	0.08	0.493	62	0.08	0.391
4922	70	0.11	0.321	56	0.11	0.216
5047	65	0.07	0.201	54	0.07	0.181
Median:	75		0.407	59		0.267

HD 30614 – O9.5 Ia

He I λ	$v_e \sin i$			macroturb.		
(Å)	v (km s^{-1})	y	χ^2	v (km s^{-1})	y	χ^2
4009	110	0.11	0.232	94	0.12	0.190
4026	103	0.22	0.468	76	0.22	0.411
4143	108	0.11	0.249	92	0.12	0.168
4388	120	0.15	0.216	95	0.16	0.124
4922	107	0.22	0.310	88	0.24	0.199
5047	105	0.12	0.268	80	0.13	0.173
Median:	108		0.259	90		0.182

with their large, extended atmospheres, there could be other velocity fields contributing to the line broadening.

There are several theoretical reasons why an O star should slow down as it ages. Conti and Ebbets (1977) have outlined several such theories. Firstly, as a star evolves, its radius increases, and from conservation of angular momentum, it should slow down. Secondly, a star may also lose angular moment because of its stellar wind.[1] Penny (1996) has calculated the wind-related "spin-down" time of a O9 main sequence star. It turns out that this is more or less six times longer than the star's H-burning lifetime. However, there is observational and theoretical evidence that as a star evolves away from the main sequence, its mass-loss rate might increase and thus the rate of spin-down from this process should also increase.

There is also a lack of narrow-lined O supergiants. In the comprehensive survey of O stars by Howarth et al. (1997b) the slowest-rotating O supergiant had a $v_e \sin i = 68$ km s^{-1}. The narrowest-lined O supergiant in the present sample (HD 195592) has a macroturbulent velocity of 54 km s^{-1} (the best-fit rotational profile for this star is 70 km s^{-1}, in reasonable agreement with the published values shown in table 5.2). This clearly indicates that there must be some other effect apart from rotation which contributes to the line broadening in evolved O stars. We have therefore chosen to adopt rotational profiles for all main-sequence stars and macroturbulent profiles for the rest of the sample, except for the two stars with the broadest lines where it appears that rotation is dominating.

Such a generalisation might however be dangerous. Since there appears to be a total lack of zero-velocity O stars (main-sequence and evolved; see discussions in Penny, 1996 and Howarth et al.), and 10 Lac and AE Aur are both among the narrowest-lined O stars known, it is not unreasonable to assume that these stars might be rotating, but that they are seen pole-on. If this is the case, then the observed broadening can only be caused by some other broadening mechanism. It is also not unreasonable to assume that this is the same mechanism as seen in the evolved stars, only not as strong. In this case, at least for these two stars, the lines should have the shape of the macroturbulent broadening function. However, since neither profile fits well, we will use the rotational broadening functions for all main-sequence stars as discussed above. In any case, the broadening functions do not affect our derived parameters since these rely on equivalent widths for the helium lines,

[1] This is only the case if the material remains somehow bound to the photosphere, for example through a magnetic field. See discussions in Langer and Heger (1998), Maeder (1998) and Meynet (1998).

and the broadening in the hydrogen lines is dominated by the intrinsic line-width.

Estimating an uncertainty on our adopted broadening-velocities is complicated due to the lack of published velocities to compare with. No other measurements using the macroturbulent profile are available for comparison. However, several of the sample stars have a $v_e \sin i$ between 90 – 95 km s^{-1} listed in Howarth et al. (1997b). The range in our adopted macroturbulent velocities for the same stars is 65 - 85 km s^{-1}(only one of these stars has a macroturbulent velocity higher than 70 km s^{-1}). Computing a synthetic line profile with a $v_e \sin i$ of 93 km s^{-1} and then fitting this synthetic line with a macroturbulent profile, yields a macroturbulent velocity of 73 km s^{-1}, which is in very good agreement with our adopted velocities. An estimate of the errors on the macroturbulent velocities is then about $\pm$ 10 km s^{-1} (and probably the same for the rotational velocities). This spread in velocities is slightly smaller than seen in the variations between the individual lines in each spectrum, and might as such be a slightly conservative estimate.

5.2 Notes on individual stars

This section contains brief summaries of the properties of the individual stars in the sample. As mentioned earlier, the fit diagrams for all the stars are shown in figure 5.8, and fit diagrams, results, and selected regions of the optical spectra are shown in appendix C.

5.2.1 HD 10125

This star was classified O9.7 II by Walborn (1976). The spectrum of this star appears normal, with a moderate wind contamination of the H I lines typical of its spectral type. There appears to be some weak emission in the unidentified $\lambda\lambda$4465, 4505Å doublet (this doublet is briefly discussed in section 5.2.13). The fit diagram shows little scatter of the lines, and gives $T_{\rm eff}$ = 32.5 kK, $\log_{10} g$ = 3.3 for y = 0.15. None of the He I triplet lines ($\lambda\lambda$4026, 4471, 4713Å) are in very good agreement with the other lines on the fit diagrams, but the only two lines that are in great disagreement are He I λ4471Å and He I λ4713Å. He I λ4713Å, as discussed in section 4.3, is very insensitive to changes in $T_{\rm eff}$ and $\log_{10} g$, and the model spectrum fits the observations for this line well. For He I λ4471Å the synthetic spectrum is consistently too weak for most of the stars in the sample. This is undoubtedly due to the 'generalized dilution effect' which was shown by Voels et al. (1989) to be very strong for this line (see also discussion in section 4.3).

Table 5.2: Line broadening velocities

HD/BD	Spectral	$v_e \sin i$ (km s^{-1})				this thesis	
	Type	UF	CE	P96	H97	rot. v	mac. v
10125	O9.7 II	95	...	...	...	161	**132**
12323	ON9 V	130	100	113	131	**131**	105
13745	O9.7 II((n))	185	...	168	169	**176**	151
16429	O9.5 II((n))	165	140	...	...	**216**	175
30614	O9.5 Ia	80	85	115	129	108	**90**
34078	O9.5 V	25	27	25	30	**30**	41
36486	O9.5 II	145	109	...	144	153	**126**
37742	O9.7 Ib	135	110	123	124	120	**109**
188209	O9.5 Iab	80	70	87	92	79	**65**
189957	O9.5 III	90	...	89	92	106	**85**
191781	ON9.7 Iab	80	...	...	...	110	**89**
194280	OC9.7 Iab	...	...	...	...	120	**101**
195592	O9.7 Ia	85	60	...	...	68	**54**
201345	ON9 V	95	54	87	91	**109**	82
202124	O9.5 Iab	95	60	137	115	111	**93**
207198	O9 Ib-II	80	70	91	91	78	**67**
209975	O9.5 Ib	40	...	90	95	86	**69**
210809	O9 Iab	120	101	118	117	112	**89**
214680	O9 V	30	32	31	35	**30**	22
218195	O9 III	85	...	...	70	75	**59**
218915	O9.5 Iab	115	110	74	94	81	**68**
225160	O8 Ib(f)	105	95	...	...	124	**109**
+36 4063	ON9.7 I	...	...	...	...	106	**84**

NOTES: *The adopted broadening velocities are indicated by* ***bold*** *text.*

REFERENCES: *UF – Uesugi and Fukuda (1982), CE – Conti and Ebbets (1977), P96 – Penny (1996), H97 – Howarth et al. (1997b)*

5.2.2 HD 12323

HD 12323 is among the ON main-sequence (ON9 V) stars classified by Walborn (1976). The line profiles in this star are best fitted with a rotational broadening function, and we have derived a rotational velocity of 131 km s^{-1}. This corresponds well with the velocities found by other authors (see table 5.2). The fit diagrams show a fairly large scatter in the parameters predicted by the He I lines. At surface gravities higher than $\log_{10} g = 3.7$ there are models calculated only for $\log_{10} g = 4.0$ and 4.5 (below $\log_{10} g = 3.7$ the grid is calculated with a step size of 0.1 dex). This increased step-size, coupled with the fact that the lines get more sensitive to changes in equivalent width (see figures 3.3 and 3.4) is probably the cause of the large scatter. The solution, however, is well constrained by the H I and He II lines.

In this case, the impact parameter analysis has to be applied very carefully, since the automatic procedures can very easily be fooled by the horizontal appearance of lines that predict surface gravities higher than the scope of the model grid. These lines have to be removed before running the impact parameter routines. The smallest scatter is found for $y = 0.17$, and the predicted parameters are $T_{\rm eff} = 36$ kK and $\log_{10} g = 4.1$. The synthetic spectrum fits the observations well, although the H I line cores are consistently predicted to be too weak. This is the opposite of what is observed for most stars in the sample, where the observed cores are filled in by emission from the stellar wind. The only ways of matching the observed H I line profiles are by either lowering the temperature and surface gravity of the models until they fall well outside the O star range, or by lowering the rotational velocity. Neither of these options is likely to give realistic results, and they fail to reproduce the observed profiles of the He I and He II lines. Lowering the helium abundance to a solar value ($y = 0.09$) has only a negligible effect on the H I lines.

The He II line strengths are well matched by the models, but in the case of He II λ4200Å the blend with N III as discussed in chapter 4 is very obvious. He II λ4686Å is also, unlike what is noted for most other stars in the sample, predicted to be too weak.

5.2.3 HD 13745

This star is of spectral type O9.7 II((n)) (Walborn, 1976), where '((n))' indicates that the star has broad lines. The exact criterion used by Walborn (1971b) and by the same author in subsequent papers, was that the lines $\lambda\lambda$4116 and 4121Å (see appendix C) are

just merged (using spectra with a spectral dispersion of 63 Å mm^{-1}). This star has, in fact, the second highest broadening velocity of the sample, with a rotational velocity of 176 km s^{-1}. It has also the highest helium abundance of the sample. The impact parameter analysis indicates a helium abundance as high as $y = 0.20$, and also $T_{\rm eff} = 33$ kK and $\log_{10} g = 3.3$. The fit diagram is fairly well constrained, with only the He I triplet lines $\lambda\lambda$4471, 4713Å in serious disagreement. Comparisons of synthetic and observed spectra are complicated by the fast rotation of this star. At these high velocities the lines are very broad and it is difficult to identify a continuum. Of the 'problem' He I lines, λ4471Å is predicted to be too weak, whereas λ4713Å fits well. This line probably only appears to disagree with the other lines in the fit diagram, due to its low sensitivy to $T_{\rm eff}$ and $\log_{10} g$.

Of the other lines, the He II lines fit moderately well, although λ4686Å is predicted to be too strong. This could be due to wind emission contaminating this line. This is quite commonly observed in giants and supergiants in this region of the H–R diagram.

5.2.4 HD 16429

HD 16429 was noted by Walborn (1976) to be nitrogen deficient. He classified it as O9.5 II((n)) where again ((n)) denotes very broad lines. It has the broadest lines the sample with a $v_e \sin i = 216$ km s^{-1}. The H I lines show clearly asymmetric line profiles (see plots on page 200 in appendix C) where the red wing is much steeper than the blue wing, probably caused by filling-in by emission in the stellar wind.

The fit diagrams for this star shows a large scatter in the $T_{\rm eff}$ – $\log_{10} g$ plane. The helium abundance appears to be high, and the impact parameter analysis indicates that the inferred value can be higher than 0.15; however, this is probably caused by the tendency for lines to cluster by the edge of the grid – in this case the lower limit for $\log_{10} g$ which is closely related to the Eddington limit. The best estimate of y is approximately 0.12. At this value, only a few of the plots for the He I lines have reached the edge of the grid and the intersection between the H I and He II lines is centered between the He I lines. For this helium abundance, the parameters predicted by the models are $T_{\rm eff} = 35$ kK and $\log_{10} g = 3.4$.

The model spectrum reproduces the observations well. Most of the He I lines fit, with only He I λ4026Å and λ4471Å being predicted to be too strong and too weak respectively. It is not unusual for the triplet lines not to fit well, and λ4471Å is almost always predicted to be too weak.

The He II lines all fit resonably well. He II λ4200Å fits poorly in the blue wing. The λ4541Å model appears too strong. However, continuum placement is difficult with such broad lines, and λ4541Å is in a very 'crowded' part of the spectrum. He II λ4686Å could possibly show some signs of wind contamination, although it also possible that, like λ4541Å the rectification could be imperfect.

The H I lines fit very well, although they are all badly blended at these high line-broadening velocities.

5.2.5 HD 30614

Walborn (1976) classified α Camelopardalis (HD 30614) as O9.5 Ia, and included it in his list of stars with morphologically normal CNO spectra. However, Bisiacchi et al. (1982) proposed that it might be an ON star. From the line broadening analysis, we have adopted a macroturbulent broadening velocity of 90 km s^{-1} for this star, a value which falls more or less in the middle of the distribution of $v_e \sin i$ values published by other authors (see table 5.2). The spectrum is typical of a luminous star, with strong Hα emission; C III λ5696Å and the unidentified lines at $\lambda\lambda$4486, 4504Å are also in emission. The 4630 – 4640 – 4650Å CNO complex appears normal with no indication of unusually strong nitrogen lines.

The fit diagram clusters very tightly with only He I $\lambda\lambda$4471, 4713Å and He II λ4686Å giving discrepant results. He II λ4686Å is probably contaminated by emission from the wind. The fit diagrams indicate a moderately high helium fraction of 0.13. The physical parameters predicted by the models for this value of y are $T_{\rm eff} = 33$ kK and $\log_{10} g = 3.1$. The resulting model spectra fit the observations well for most lines. He I λ4471Å is predicted to be too weak, and He II λ4686Å is predicted to be too strong, in agreement with the assumption that it is contaminated by wind emission. He II λ4200Å appears to be predicted to be too weak, but this is probably due to the blend with N III.

5.2.6 HD 34078

HD 34078 (AE Aurigae), is an O9.5 V star (Walborn, 1973) with a spectrum that appears very similar to that of 10 Lac (see chapter 4). It has a rotational broadening velocity similar to that of 10 Lac (30 km s^{-1}) and consequently the problems with measuring and fitting the lines for 10 Lac discussed in chapter 4 apply to AE Aur as well.

The fit diagram shows even a bit more scatter in the predicted parameters than those for 10 Lac, although the H I lines are all in fairly good agreement. The maximum deviation

in $\log_{10} g$ predicted by the H I lines is about ± 0.15, and the spread in $T_{\rm eff}$ from the He I lines at the adopted value of $\log_{10} g = 4.2$ is about 6 kK. This is greatly reduced by the He II lines, where the spread is only 3 kK. He II λ4200Å predicts a slightly higher temperature than the other He II lines. This is probably because the equivalent width has been overestimated as a result of the blend with N III. Figure 4.8 shows that an increase in equivalent width gives a higher temperature for the He II lines, so the error on the temperature estimate caused by the spread of the lines is probably less than ± 1 kK.

For a helium fraction of $y = 0.09$ we find $T_{\rm eff} = 37$ kK and $\log_{10} g = 4.2$. For these values the model spectrum fits the observed spectrum reasonably well, and matches the observed equivalent widths more or less within the errors on the measurements, which are probably similar to those of 10 Lac (see chapter 4).

For the He I lines, most of the cores of the lines appear to weak. This could be due to a too high value for the rotational broadening velocity, or possibly due to use of a wrong broadening function. The model reproduces the He II line profiles well, with the exception of He II λ4686Å for which, like in 10 Lac, the model profile appears too narrow. The H I lines also have the same problems as in 10 Lac, where the model profile fits the wings very well, but the cores are too weak.

5.2.7 HD 36486

δ Orionis (HD 36486), one of the Orion Belt stars, is classified as O9.5 II by Walborn (1976) with a note that it shows signs of moderate morphological nitrogen deficiency. It has quite a high macroturbulent broadening velocity of 126 km s^{-1}.

The fit diagrams show an unusually large spread in the plots of the H I lines. In particular, H10 λ3797Å predicts a far higher value of the surface gravity than the rest of the H I lines. The fit diagrams suggest a helium fraction of 0.10, with $T_{\rm eff} = 34$ kK and $\log_{10} g = 3.4$. The model spectrum for these parameters fits well, with the notable exception of the H I lines. The red wing of these lines all have a very broad shape, with the wings far weaker than what is predicted by the models. This is probably also the reason why H10 λ3797Å, the line with the strongest blend in the blue wing, predicts a very different surface gravity than the rest of the H I lines. The blend makes the area that is suitable for fitting very small. It also appears that the red-wing asymmetry also could be present in some of the He I lines. The He II λ4200Å line fits far better than what is observed for most of the other stars. If we assume that this line normally appears to be

stronger than the model predictions because of the nitrogen blends, then this supports Walborn's (1976) classification of this star as nitrogen deficient.

5.2.8 HD 37742

ζ Orionis (HD 37742) is the second Orion Belt star of the sample. The third, ϵ Orionis (HD 37128), is a B0 Ia star, and falls outside the scope of this thesis. ζ Ori has, like δ Ori, relatively broad lines, and we adopt a macroturbulent velocity of 109 km s^{-1} for this star. This star is classified O9.7 Ib, and it and the other Orion Belt stars were classified and discussed in Walborn (1976). Walborn also noted that all three stars were moderately nitrogen deficient.

The fit diagram is well confined, with only He II λ4686Å diverging from the other lines. The closest clustering of the plotted lines is found for $y = 0.10$, with $T_{\rm eff} = 34$ kK and $\log_{10} g = 3.3$. The model spectra fit well. Some asymmetries like in δ Ori are possibly present in the H I lines, although they do not appear as strong. He I λ4713Å appears to have a 'bump' in the red wing, which is also possibly present in some of the other He I lines. This star shows very little absorption in He II λ4200Å from the blend with N III, consistent with Walborn's N-deficient classification.

5.2.9 HD 188209

HD 188209 was classified O9.5 Iab by Walborn (1976), and we have adopted a macroturbulent broadening velocity of 65 km s^{-1}. The fit diagrams for this star are very tight, and the impact parameter solution is at the point where the He II lines turn over from being temperature to gravity sensitive. The adopted solution for $y = 0.14$ is $T_{\rm eff} = 33.0$ kK and $\log_{10} g = 3.1$. The model spectrum fits the observations very well, with only a very few exceptions. He I λ4471Å is, as usual, predicted to be too weak, He II λ4200Å shows signs of blending and He II λ4686Å is probably contaminated by emission. Hα is not in emission (above the continuum), but it is almost entirely filled in. The model H I lines fit the observations well, with the exception of H I λ3935Å which has broader wings than predicted by the models. Usually this would be indicative of a higher surface gravity, but in this case could be caused by blends.

5.2.10 HD 189957

This star is an O9.5 III (Walborn, 1973), and the line profiles show very clearly the macroturbulent v-shape. We derived a macroturbulent broadening velocity of 85 km s^{-1}.

The fit diagrams show some scatter, especially H9 λ3835Å which predicts a higher $\log_{10} g$ than the other H I lines. The model profiles confirm this, showing that the wings of this line are predicted to be too narrow. The impact parameter analysis suggests that $y = 0.11$ with $T_{\rm eff} = 33$ kK and $\log_{10} g = 3.5$ is the best solution for this star. The model profiles are not very good, however. All the He II lines are predicted to be too weak, something that usually suggests that the temperature is estimated slightly too low. The equivalent widths match well, so it could be a matter of using a slightly too high line-broadening velocity or even that the data rectification is slightly off.

5.2.11 HD 191781

Classified ON9.7 Iab by Walborn (1976), this star shows all the signs of a 'typical' ON star. N III λ4640Å is clearly much stronger than the C blends at 4650Å (see figure 5.2). We find a macroturbulent broadening of 89 km s^{-1} for this star.

The fit diagrams are very tight with all lines in good agreement, with the exception of the He I triplet lines and the blended λ4009Å line. We find a high helium fraction of $y = 0.16$ for this star, with $T_{\rm eff} = 31$ kK and $\log_{10} g = 3.1$. The model profiles fit the observations well, and, after carefully using ELF to fit and remove the blends from He I λ4009Å, this line also fits. He I λ4143Å is, as usual, modelled too weak. For He II λ4200Å the model appears too weak, but this line is blended with a N III line, which we can expect to be quite strong in this star. The H I lines all appear weaker than the model profiles. This star has clear emission in Hα and the discrepancies between the model and observations are probably due to wind effects in these lines.

5.2.12 HD 194280

HD 194280 is the only OC star in the sample. It was classified OC9.7 Iab by Walborn (1976). Comparing the spectra of HD 191781 and HD 194280 (figure 5.2) we can see some clear differences. The N III lines at $\lambda\lambda$4634.2, 4640.6 and 4641.9Å (and possibly also the N II λ4630.5Å line) are much stronger in the ON star HD 191781, whereas the C III lines at $\lambda\lambda$4647.4 and 4650.3Å are much stronger in the OC star. Most of the other lines appear

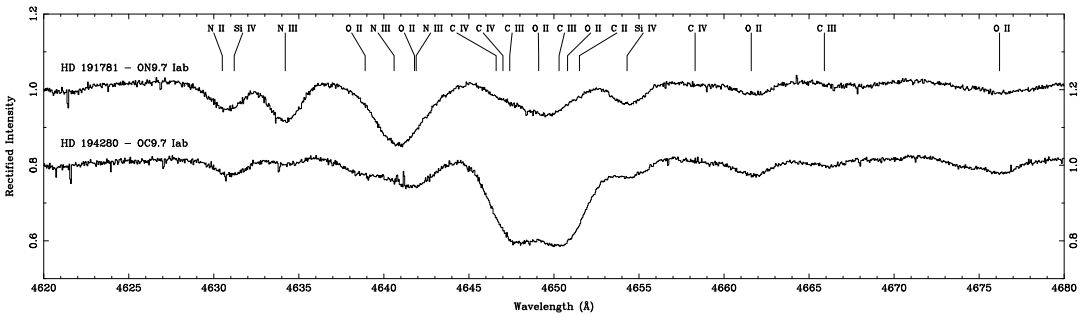

Figure 5.2: *The λ4650Å spectra of the ON star HD 191781 and the OC star HD 194280*

to be of similar strenght in the two spectra. The spectra of these two stars in the range 3800 – 6200Å are included in appendix B.

The fit diagrams for this star show a well defined solution for y=0.09 with $T_{\rm eff} = 32$ kK and $\log_{10} g = 3.2$.

5.2.13 HD 195592

This star is undoubtedly very luminous. The spectrum shows a large number of emission lines, including Si III λ3806.5Å, the unidentified lines at $\lambda\lambda$4486, 4504Å, C III λ5695.9Å, and of course several of the H I lines, including Hα. There also appear to be several other weak emission lines, some of which are shown in figure 5.3.

This star has relatively narrow lines (see also table 4.3 in chapter 4), and we have adopted a macroturbulent broadening profile of 54 km s^{-1}. The fit diagrams show a very tight clustering of the lines, and the impact parameter analysis yields a best estimate at $y = 0.12$ with $T_{\rm eff} = 31$ kK and $\log_{10} g = 3.0$. The model profiles fit well, but the H I lines show clear effects of emission filling in the cores, and He II λ4686Å is not visible as an absorption feature (there is some slight emission at the centre of the line).

5.2.14 HD 201345

This is the second ON main-sequence star in the sample. It was classified as ON9 V by Walborn (1976), and shows the same characteristic strong nitrogen and weak carbon and oxygen lines as HD 12323. It is a relatively fast rotator, with a $v_e \sin i$ of 109 km s^{-1}.

The fit diagrams show quite large scatter for the lines, possibly due to errors introduced into the measurements of the equivalent widths because of the fast rotation (like unidentified blends etc.). The impact parameter analysis suggests a helium fraction $y = 0.14$,

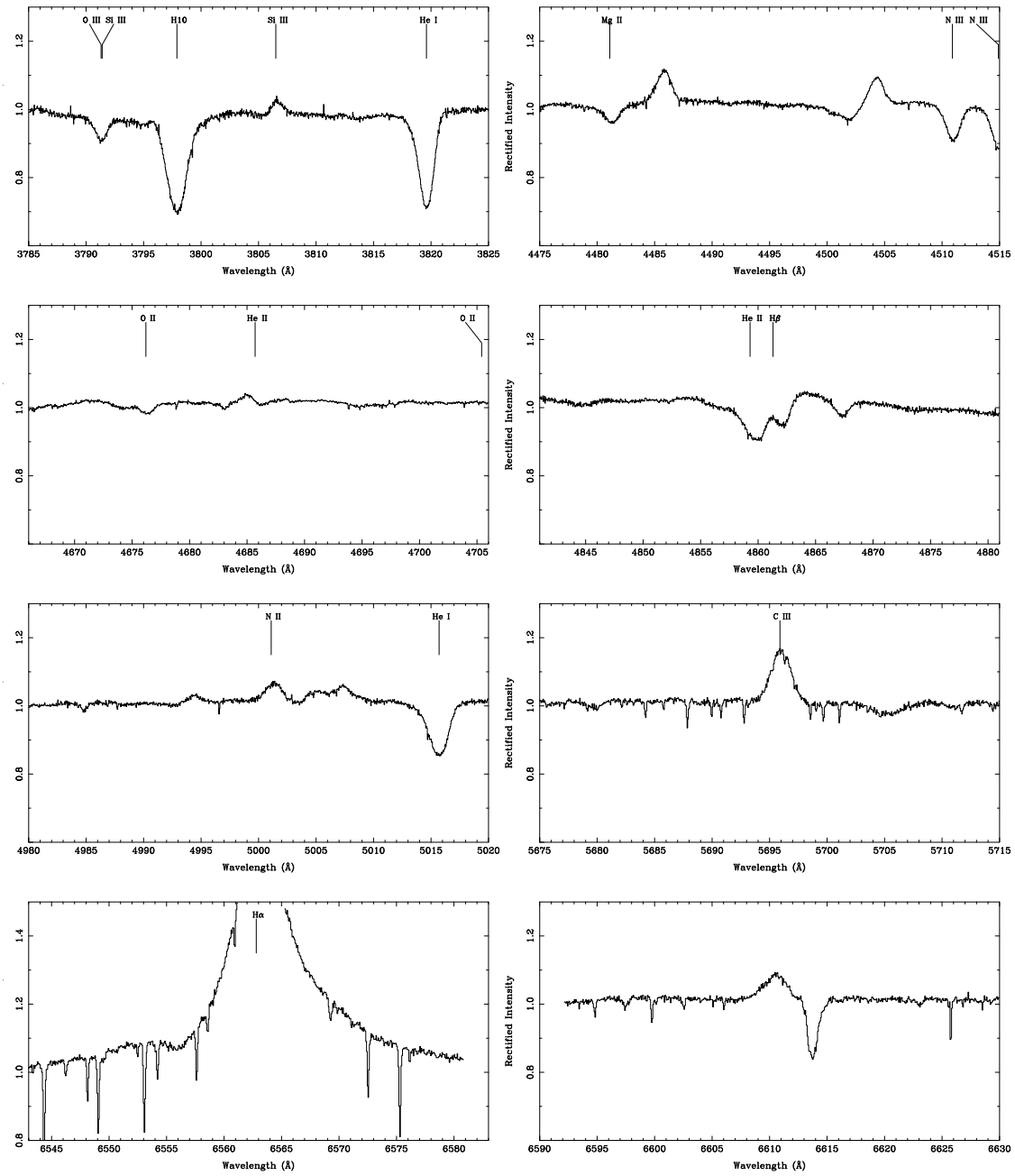

Figure 5.3: *Some lines in the optical spectrum of HD 195592. Hα has been plotted on a different scale than the other lines. To obtain good S/N we had to saturate this line (see also fig 2.5).*

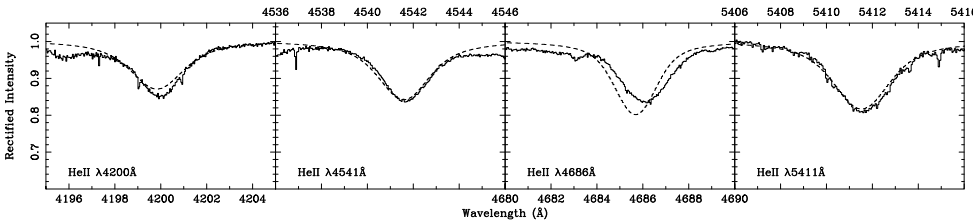

Figure 5.4: *The* He II *lines with model fits for HD 207198. The unusual apparent wavelength shift of* He II *λ4686Å is probably caused by wind contamination (see text).*

with $T_{\rm eff} = 36$ kK and $\log_{10} g = 3.9$. For these parameters, the model profiles fit well, with a few exceptions. As usual, the He I λ4471Å model line is too weak, and so is, very unusually, He II λ4686Å. This line is only modelled too weak for the main-sequence stars, and it is possible this is due to shortcomings in the models.

5.2.15 HD 202124

For HD 202124, classified O9.5 Iab by Walborn (1976), we have adopted a macroturbulent broadening velocity of 93 km s^{-1}. The lines on the fit diagrams are all in good agreement, apart from He II λ4686Å. However, this star shows emission in Hα and it is thus likely that also He II λ4686Å will be contaminated by emission. Indeed, by comparing with models for our adopted parameters of $y = 0.13$, $T_{\rm eff} = 34$ kK and $\log_{10} g = 3.2$, it is clear that this line is clearly filled-in. All other lines fit well, with the usual exception of He I λ4471Å. The H I line cores are all predicted to be too strong, probably due to wind contamination in these lines.

5.2.16 HD 207198

HD 207198 (O9 Ib–II; Walborn, 1976) has an interesting spectrum, showing emission in several lines, including the unidentified doublet at λλ4486, 4505Å and C III λ5695.9Å. There also seems to be some emission in the 4630 – 4640Å region. We find $T_{\rm eff} = 36$ kK and $\log_{10} g = 3.4$ for $y = 0.12$. Comparing the model with the observed spectrum of this star, it looks like there is a wavelength shift in He II λ4686Å between the model and the observations; however it is more likely that it just appears that way due to wind contamination in this line (figure 5.4).

5.2.17 HD 209975

HD 209975 was classified O9.5 Ib by Walborn (1976). It has a macroturbulent broadening velocity of 69 km s^{-1}, and from the fit diagrams appears to have a solar helium abundance. The fit diagrams are well confined, and most lines are in good agreement. He II λ4686Å predicts a temperature a few thousand Kelvin colder than the other He II lines. The model spectrum for $y = 0.09$, $T_{\rm eff} = 35$ kK and $\log_{10} g = 3.4$ fits well, with only He I λ4471Å and He II λ4686Å predicted to be too weak and too strong respectively. Some of the H I lines show signs of weak filling-in in the red wing.

5.2.18 HD 210809

The fit diagrams for this star show a small amount of scatter. Most of the He I singlets are in good agreement, with the exception of He I λ4009Å which predicts a slightly lower temperature/higher surface gravity. This is most likely due to an overestimation of this line's equivalent width resulting from a blend. He II λ4686Å fits at a temperature several thousand K colder than the other He II lines, which is not unexpected for a O9 Iab star. The spectrum shows clear emission in Hα and it is likely that He II λ4686Å is also contaminated by stellar wind emission. The impact parameter suggests a helium fraction of 0.13, but the results are inconclusive for the temperature and gravity. With the inclusion of He II λ4686Å we get $T_{\rm eff} = 35$ kK and $\log_{10} g = 3.4$. The model spectrum for these parameters fits reasonably well, but the He II lines are all predicted to be too weak. By ignoring λ4686Å in the analysis, we find a temperature of $T_{\rm eff} = 36$ kK and $\log_{10} g = 3.3$. This solves the problem with the weak He II lines and the overall fit is much better, althought the adopted uncertainties encompass both solutions.

5.2.19 HD 214680

This is 10 Lac, and the analysis of this star is discussed in detail in chapter 4.

5.2.20 HD 218195

This star was classified O9 III by Walborn (1976), and he also noted that the spectrum, although not an ON spectrum, shows signs of moderate nitrogen enhancement.

The fit diagram for this star is fairly well defined, and the impact parameter analysis suggests a helium number fraction, $y = 0.12$ with $T_{\rm eff} = 37$ kK and $\log_{10} g = 3.6$. The

model spectrum fits the observations well, with the usual exception of He I λ4471Å. The N III blend in He II λ4200Å appears strong, in agreement with Walborn's classification of the star as nitrogen enhanced. He II λ4686Å shows no signs of filling-in, but appears to have some extra absorption in the red wing.

5.2.21 HD 218915

HD 218195 was classified O9.5 Iab by Walborn (1976). The fit diagram appears tight, but shows quite a large scatter in the He II lines. We have adopted $y = 0.10$, $T_{\rm eff} = 34.0$ and $\log_{10} g = 3.2$ as the parameters for this stars. The model spectrum fits the observations well, although He II λ4686Å show signs of filling-in.

5.2.22 HD 225160

HD 225160 is the only O8 star in the sample (O8 Ib(f) – Walborn, 1976). The fit diagram is fairly tight, but the weak He I lines are in disagreement with the other lines. Both He I λ4009Å and λ5047Å predict lower $T_{\rm eff}$ (models underestimate the equivalent width) than the rest of the He I lines (with the exception of He I λ4471Åwhich consistently is predicted to be too weak). This star has very broad lines and we have adopted a macroturbulent broadening velocity of 109 km s^{-1}.

The model spectrum for the adopted parameters of $y = 0.15$, $T_{\rm eff} = 38$ kK and $\log_{10} g = 3.4$ appears to fit well with the exception of He II λ4686Å which is completely filled in. All the H I lines also show clear signs of filling-in, and the star has several strong emission lines. There also appears to be some emission in the 4630 – 4640Å region, possibly due to N III.

5.2.23 BD +36 4063

This star is the only star in the sample that was not originally classified by Walborn. It was first classified as ON by Mathys (1989) (ON9.7 I), and appears similar to that of HD 191781 only with even weaker carbon lines. This star is also a binary (Howarth, private communication), and unfortunately the spectrum is of quite low S/N compared to the other stars in the sample because the star is much fainter. However, the fit diagrams appear quite well confined, although the He II and H I lines show slightly larger scatter than the norm.

The model spectrum for $y = 0.11$, $T_{\rm eff} = 32$ kK and $\log_{10} g = 3.1$ fits the observations fairly well, although there appears to be some absorption in the red wing of most lines. H I lines fit poorly, although this could be due to wind contamination. This star has strong Hα emission, and He II λ4686Å is too weak in the model spectrum.

5.3 Microturbulence

In chapter 3 we saw how the inclusion of microturbulence in the line formation calculations increases the equivalent width of most He I lines, especially at low surface gravities. The effects of this on the fit diagrams can clearly been seen in figure 5.5. The strengthening of the He I lines mean that we can get consistent fits at lower y than we would for zero microturbulence. This has another interesting effect. The He II lines are relatively unaffected by microturbulence in our grid (in more recent calculations by Smith and Howarth, 1998, this is not necessarily the case). Since we have to lower the helium abundance to match equivalent widths for the He I lines, we have to increase the temperature to get consistent fits for the He II lines. From figure 5.5 (and also appendix C) it appears that the temperatures are about 1 – 2 kK higher[2] when including a microturbulence of 15 km s^{-1}.

The microturbulence is also relatively more important for the He I triplet lines $\lambda\lambda$4471 and 4713Å than the other He I lines. These two lines are typically predicted to be too weak in standard analyses not taking microturbulence into account (cf. the *generalized dilution effect*, see section 4.3). Including a microturbulence of 15 km s^{-1} does increase the strength of this line, but not enough to fit the observations. However, Smith and Howarth (1998) have shown that this line is strengthened further by treating microturbulence in both the statistical equilibrium and line formation calculations, and that this could be enough to solve the discrepancy.

The results of the impact-parameter analyses described earlier favour a microturbulent velocity, ξ, of 15 km s^{-1} for all stars except HD 207198 (O9 Ib-II; $\xi = 0$ km s^{-1}) and HD 218195 (O9 III; $\xi = 10$ km s^{-1}). However, in both of these cases this is probably caused by a slight 'defect' in the way we perform the impact-parameter calculations. As mentioned previously in this chapter, outliers are rejected before re-calculating the impact parameters. For both of these stars, more lines were included in the $\xi = 15$ km s^{-1} fits, and these probably do represent the most consistent fits. For these reasons we have chosen to

[2] All temperatures quoted previously in this chapter *do* include microturbulence unless otherwise stated

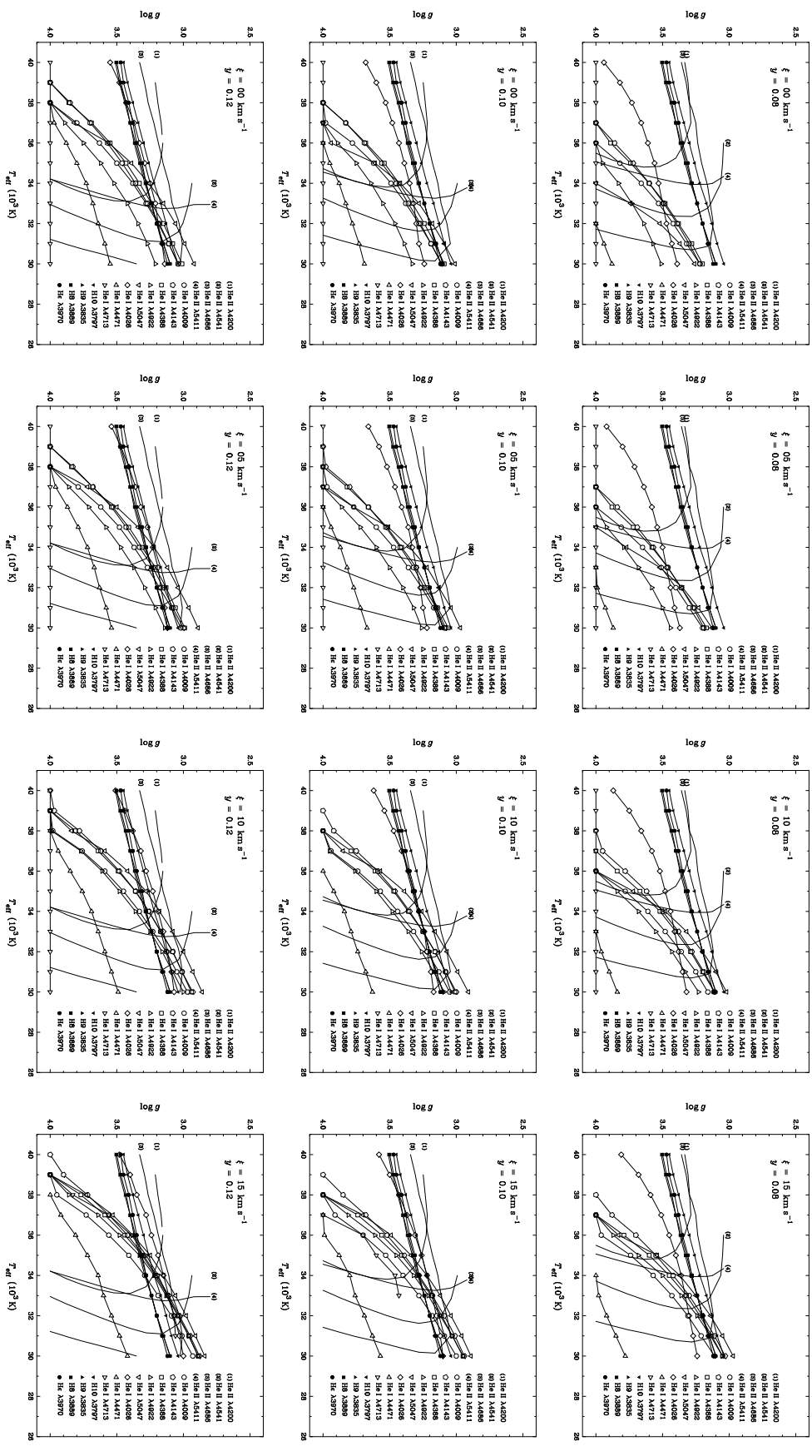

Figure 5.5: *Series of fit diagrams for HD 218915 (O9.5 Iab) showing dependence on microturbulence, ξ, and helium abundance, y. Microturbulence increases from left to right (0, 5, 10, 15 km s^{-1}) and helium abundance from top to bottom (0.08, 0.10, 0.12).*

adopt a microturbulent velocity of 15 km s^{-1} for all the stars in the sample, including the main-sequence stars, although microturbulence is relatively unimportant for these stars (see also chapter 3).

5.4 Physical parameters of the O stars

The adopted parameters for the WHT sample stars are summarised in table 5.3, and the observed and modelled equivalent widths (and their ratios) are shown in table 5.4. There are two trends of particular interest in this table:

- The He I line λ4009Å is consistently predicted to be too weak. The median ratio of $W_{\rm obs}/W_{\rm mod}$ for this line is over 1.4. This is probably due to some unidentified blending.

- The median of $W_{\rm obs}/W_{\rm mod}$ for the He I lines in each star is almost consistently larger than 1. This can probably be attributed to the impact-parameter analysis introducing a systematic bias. The effect seems to be particularly strong in stars where the fit-diagram intersection zone is close to the point where the He II lines go from being temperature sensitive to gravity sensitive (e.g. HD 188209, HD 210809 and HD 218915). It is possible that this 'pulls' the solution towards a slightly lower gravity causing an underestimation of the equivalent width of the He I lines. However this effect is likely to be small, and within the uncertainty of the results.

For HD 12323 the ratio of the He I lines to the models seem to be particularly large; the median value is 1.153. This star has a helium abundance which is very high, and the lines show a large scatter on the fit-diagrams. It is possible that we have slightly underestimated the helium abundance ($y = 0.17$), but increasing the helium abundance results in a larger scatter of the lines on the fit-diagrams. The solution for this star lies very close to the high-gravity limit of our grid of models, and it is therefore possible that unwanted 'edge-effects' caused by interpolating the models causes a higher uncertainty for all determined parameters for this star (see below).

5.4.1 Uncertainties

It is possible to obtain an estimate of the uncertainties on the results from the impact-parameter analyses. When finding the point of closest approach to all the measured

lines, the scatter of the lines will be related to the internal error on our measurements and models (not taking into account systematic effects caused by missing physics in the models etc.). Typically the RMS scatter of the lines is of the order 0.5 – 1.0 kK in effective temperature, and 0.05 – 0.09 dex in surface gravity. However, these values are only valid if we only fit on 2-D grid, i.e. have fixed values of the helium abundance and microturbulence. As discussed above, it appears that all the stars show microturbulent velocities of the order 15 km s^{-1}, and that neglecting microturbulence altogether will only lower the temperatures by 1 – 2 kK. This probably means that the uncertainty on the choice of microturbulence is likely to have only a negligible effect on the temperatures and gravities. The helium abundance, however, will probably be more important. The analyses vary the helium abundance from subsolar $y = 0.08$ to about $y = 0.20$ in steps of 0.01. It appears that the impact-parameter analysis is able to distinguish the best-fit model from its 'neighbours', so the precision of the measured helium abundance will be about ± 0.01. The implied uncertainty on temperatures and gravities (from impact-parameter solution on the neighbouring y fit-diagrams) appear to be of the order 0.5 kK in $T_{\rm eff}$ and 0.05 dex for $\log_{10} g$.

Within the context of the adopted models, good estimates of the uncertainties on the four fitted parameters are then ± 1 kK and 0.1 dex for $T_{\rm eff}$ and $\log_{10} g$ respectively, ± 0.01 for the helium number fraction, and ± 5 km s^{-1} for the microturbulence. Of course, the results may be wrong by much larger amounts. This will not be clear until dynamical, spherically extended, line-blanketed nLTE models are available for comparison (but see section 5.5).

5.4.2 Masses and radii

Using absolute visual magnitudes, M_V, from Garmany's unpublished catalogue of O stars,[3] (cf. Garmany et al., 1982) we can calculate radii and spectroscopic masses for the sample. We can find the bolometric correction using:

$$\mathrm{BC} = K - 0.08(T_{\rm eff}/\mathrm{kK}) \tag{5.1}$$

[3] For HD 34078 Garmany gives $M_V = -5.0$ (probably from Humphreys, 1978). However Humphreys based this number on the assumption that HD 34078 belongs to the Ori OB1 association. According to Gies (1987) this might not be the case. Like Herrero et al. (1992), we therefore adopt a value of $M_V = -4.0$, which approximately corresponds to a main-sequence star of this spectral type (Conti et al., 1983).

where the constant K is weakly dependent on surface gravity. We adopt the values from Howarth and Prinja (1989) with $K = -0.6$ for supergiants, and $K = -0.5$ for all other luminosity classes. We can now calculate luminosities and radii from:

$$\log(L_\star/L_\odot) = -0.4(M_{\rm BOL} - 4.75) \tag{5.2}$$

and

$$\log(R_\star/R_\odot) = 0.5\log(L_\star/L_\odot) - 2\log(T_{\rm eff}/T_\odot) \tag{5.3}$$

These derived parameters are listed in table 5.5 with internal error estimates using the uncertainties discussed in section 5.4.1 and $\pm$ 0.3 for M_V (see Herrero et al., 1992).

5.5 Comparisons with published work

Plotting the effective temperatures against 'typical' temperatures from Howarth and Prinja (1989) reveals a systematic difference (figure 5.6). The temperatures are clearly seen to increase with spectral type, and the slope of the relation appears to be the similar for our adopted values and those listed in Howarth and Prinja, however our temperatures come out systematically higher by about 2 – 5 kK for all luminosity classes.

The same plot for surface gravities (fig 5.7), reveals a much closer correlation between the values in Howarth and Prinja and those adopted here, although for the giants and supergiants there might be a slight tendency for our adopted gravities to be slightly lower than those in Howarth and Prinja.

Tables 5.6 – 5.8 compare our results to those of other authors. The results compare well within the uncertainties given above, except with the results of Grigsby et al. (1992) shown in table 5.7. Grigsby et al. consistently predict effective temperatures 6 – 8 kK lower than our adopted values. This discrepancy was also noted earlier for 10 Lac, and is discussed in section 4.8.

There appears to be a trend for our results to systematically come out slightly (about 2 kK) higher than those adopted by other authors. Most likely this is due to the inclusion of microturbulence in our study and/or the use of an objective impact parameter routine to find the best-fit solution. As discussed in section 5.3, using microturbulent velocities of about 15 km s^{-1} will increase the adopted effective temperatures with 1 – 2 kK, which is comparable to the systematic differences seen in tables 5.6 and 5.8, and could also partly

explain the disagreement with Howarth and Prinja. The surface gravities and helium abundances generally agree well.

Table 5.3: Observed parameters of the WHT O stars

HD/BD	Name	Spectral Type		$T_{\rm eff}$(kK)	$\log_{10} g$	y	L. broadening	v
10125		O9.7 II	W76	32.5	3.3	0.15	mac	132
12323		ON9 V	W76	36.0	4.1	0.17	rot	131
13745		O9.7 II((n))	W76	33.0	3.3	0.20	rot	176
16429		O9.5 II((n))	W76	35.0	3.4	0.12	rot	216
30614	α Cam	O9.5 Ia	W76	33.0	3.1	0.13	mac	90
34078	AE Aur	O9.5 V	W73	37.0	4.2	0.09	rot	30
36486	δ Ori	O9.5 II	W76	34.0	3.4	0.10	mac	126
37742	ζ Ori	O9.7 Ib	W76	34.0	3.3	0.10	mac	109
188209		O9.5 Iab	W76	33.0	3.1	0.14	mac	65
189957		O9.5 III	W73	33.0	3.5	0.11	mac	85
191781		ON9.7 Iab	W76	31.0	3.1	0.16	mac	89
194280		OC9.7 Iab	W76	32.0	3.2	0.09	mac	101
195592		O9.7 Ia	W76	31.0	3.0	0.12	mac	54
201345		ON9 V	W76	36.0	3.9	0.14	rot	109
202124		O9.5 Iab	W76	34.0	3.2	0.13	mac	93
207198		O9 Ib-II	W76	36.0	3.4	0.12	mac	67
209975	19 Cep	O9.5 Ib	W76	35.0	3.4	0.09	mac	69
210809		O9 Iab	W76	36.0	3.3	0.13	mac	89
214680	10 Lac	O9 V	W73	38.0	4.2	0.09	rot	30
218195		O9 III	W76	37.0	3.6	0.12	mac	59
218915		O9.5 Iab	W76	34.0	3.2	0.10	mac	68
225160		O8 Ib(f)	W71	38.0	3.4	0.15	mac	109
+36 4063		ON9.7 I	M89	32.0	3.1	0.11	mac	84

Table 5.4: Measured and calculated equivalent widths

HD/BD		He I equivalent widths (mÅ)								He II equivalent widths (mÅ)				Median	
		λ4009Å	λ4026Å	λ4143Å	λ4388Å	λ4471Å	λ4713Å	λ4922Å	λ5047Å	λ4200Å	λ4541Å	λ4686Å	λ5411Å	He I	He II
10125	obs	268.0	736.0	294.0	488.0	965.0	325.0	598.0	179.0	395.0	351.0	484.0	480.0		
	mod	241.0	817.3	302.5	489.7	742.9	318.6	606.9	189.8	336.8	389.0	510.6	436.8		
	obs/mod	1.112	0.901	0.972	0.997	1.299	1.020	0.985	0.943	1.173	0.902	0.948	1.099	0.991	1.023
12323	obs	390.0	1062.0	451.0	626.0	1043.0	306.0	836.0	233.0	532.0	592.0	842.0	730.0		
	mod	301.1	1004.7	383.3	553.9	999.8	333.8	707.5	188.4	497.5	603.7	826.7	684.8		
	obs/mod	1.295	1.057	1.177	1.130	1.043	0.917	1.182	1.237	1.069	0.981	1.019	1.066	1.153	1.042
13745	obs	310.0	842.0	322.0	545.0	1073.0	377.0	584.0	205.0	399.0	398.0	409.0	527.0		
	mod	266.5	883.7	326.9	525.7	804.5	336.3	648.4	209.6	410.3	469.6	582.8	531.5		
	obs/mod	1.163	0.953	0.985	1.037	1.334	1.121	0.901	0.978	0.972	0.848	0.702	0.992	1.011	0.910
16429	obs	259.0	677.0	330.0	453.0	822.0	257.0	497.0	60.0	480.0	490.0	542.0	630.0		
	mod	164.9	765.7	228.2	383.0	664.1	298.5	493.5	141.1	411.1	491.6	542.7	601.6		
	obs/mod	1.571	0.884	1.446	1.183	1.238	0.861	1.007	0.425	1.168	0.997	0.999	1.047	1.095	1.023
30614	obs	187.0	709.0	181.0	333.0	920.0	335.0	469.0	124.0	333.0	367.0	199.0	485.0		
	mod	147.5	669.1	208.2	351.0	635.7	291.9	466.9	136.7	287.6	351.3	364.1	473.4		
	obs/mod	1.268	1.060	0.869	0.949	1.447	1.148	1.004	0.907	1.158	1.045	0.547	1.025	1.032	1.035
34078	obs	256.0	823.0	275.0	488.0	680.0	246.0	477.0	133.0	540.0	438.0	705.0	660.0		
	mod	179.1	809.8	254.5	388.9	804.5	267.6	505.7	121.3	389.7	502.8	755.3	606.1		
	obs/mod	1.429	1.016	1.081	1.255	0.845	0.919	0.943	1.096	1.386	0.871	0.933	1.089	1.048	1.011
36486	obs	317.0	642.0	201.0	396.0	737.0	231.0	490.0	167.0	432.0	403.0	425.0	458.0		
	mod	168.6	726.4	229.7	379.5	645.5	285.4	491.4	139.2	334.8	401.2	499.6	478.8		
	obs/mod	1.880	0.884	0.875	1.043	1.142	0.809	0.997	1.200	1.290	1.004	0.851	0.957	1.020	0.981
37742	obs	195.0	746.0	171.0	371.0	834.0	251.0	499.0	129.0	366.0	350.0	263.0	551.0		
	mod	146.9	691.3	206.3	348.7	619.0	280.0	460.5	128.5	322.0	390.0	451.6	488.2		
	obs/mod	1.327	1.079	0.829	1.064	1.347	0.896	1.084	1.004	1.137	0.897	0.582	1.129	1.072	1.013

Table 5.4: *continued*

HD/BD		He I equivalent widths (mÅ)								He II equivalent widths (mÅ)				Median	
		λ4009Å	λ4026Å	λ4143Å	λ4388Å	λ4471Å	λ4713Å	λ4922Å	λ5047Å	λ4200Å	λ4541Å	λ4686Å	λ5411Å	He I	He II
188209	obs	225.0	749.0	250.0	406.0	855.0	330.0	550.0	147.0	307.0	362.0	360.0	487.0		
	mod	156.7	687.8	218.2	366.2	647.8	298.9	482.2	144.5	299.6	364.0	382.0	487.1		
	obs/mod	1.436	1.089	1.146	1.109	1.320	1.104	1.141	1.017	1.025	0.995	0.942	1.000	1.125	0.997
189957	obs	295.0	768.0	313.0	465.0	814.0	260.0	576.0	141.0	301.0	277.0	560.0	440.0		
	mod	224.9	788.8	287.2	452.3	741.2	297.0	570.3	165.5	303.1	356.7	507.9	392.1		
	obs/mod	1.312	0.974	1.090	1.028	1.098	0.875	1.010	0.852	0.993	0.777	1.103	1.122	1.019	1.048
191781	obs	365.0	732.0	291.0	483.0	850.0	352.0	586.0	232.0	263.0	264.0	389.0	339.0		
	mod	234.7	763.7	293.3	477.9	707.8	311.4	595.2	191.8	269.2	309.8	427.4	350.4		
	obs/mod	1.555	0.958	0.992	1.011	1.201	1.130	0.985	1.210	0.977	0.852	0.910	0.967	1.071	0.939
194280	obs	318.0	675.0	231.0	430.0	810.0	270.0	550.0	135.0	234.0	284.0	384.0	350.0		
	mod	159.8	648.4	217.3	363.7	611.7	269.5	479.2	135.5	231.3	276.9	375.4	327.9		
	obs/mod	1.990	1.041	1.063	1.182	1.324	1.002	1.148	0.996	1.012	1.026	1.023	1.067	1.105	1.024
195592	obs	215.0	641.0	207.0	386.0	811.0	309.0	500.0	145.0	202.0	263.0	...	364.0		
	mod	163.9	631.3	222.8	370.1	626.0	280.6	490.5	147.2	211.0	253.9	314.7	323.4		
	obs/mod	1.312	1.015	0.929	1.043	1.296	1.101	1.019	0.985	0.957	1.036	...	1.126	1.031	1.036
201345	obs	313.0	925.0	355.0	546.0	910.0	300.0	629.0	170.0	419.0	481.0	768.0	624.0		
	mod	242.6	910.7	316.8	482.0	868.5	315.5	610.9	167.0	492.9	591.2	758.7	674.8		
	obs/mod	1.290	1.016	1.121	1.133	1.048	0.951	1.030	1.018	0.850	0.814	1.012	0.925	1.039	0.887
202124	obs	182.0	641.0	188.0	339.0	747.0	283.0	429.0	141.0	346.0	382.0	211.0	582.0		
	mod	150.7	710.8	212.3	358.8	634.7	297.3	471.7	137.5	346.1	419.4	430.9	548.2		
	obs/mod	1.208	0.902	0.886	0.945	1.177	0.952	0.909	1.025	1.000	0.911	0.490	1.062	0.948	0.955
207198	obs	186.0	745.0	188.0	369.0	817.0	281.0	457.0	122.0	440.0	479.0	488.0	658.0		
	mod	134.3	748.1	195.1	334.0	622.3	288.2	443.3	119.5	446.9	538.5	548.3	674.1		
	obs/mod	1.385	0.996	0.964	1.105	1.313	0.975	1.031	1.021	0.985	0.890	0.890	0.976	1.026	0.933

Table 5.4: *continued*

HD/BD		He I equivalent widths (mÅ)								He II equivalent widths (mÅ)				Median	
		λ4009Å	λ4026Å	λ4143Å	λ4388Å	λ4471Å	λ4713Å	λ4922Å	λ5047Å	λ4200Å	λ4541Å	λ4686Å	λ5411Å	He I	He II
209975	obs	210.0	700.0	179.0	362.0	814.0	273.0	441.0	114.0	330.0	377.0	364.0	512.0		
	mod	130.6	686.1	188.2	322.0	605.0	268.2	431.9	113.5	350.3	428.0	489.9	534.6		
	obs/mod	1.608	1.020	0.951	1.124	1.345	1.018	1.021	1.004	0.942	0.881	0.743	0.958	1.021	0.911
210809	obs	223.0	700.0	206.0	368.0	870.0	310.0	474.0	135.0	416.0	472.0	214.0	666.0		
	mod	111.7	715.5	169.0	296.5	602.1	281.6	408.6	104.0	428.9	520.9	477.8	679.0		
	obs/mod	1.996	0.978	1.219	1.241	1.445	1.101	1.160	1.298	0.970	0.906	0.448	0.981	1.230	0.938
214680	obs	224.0	791.0	247.0	399.0	646.0	265.0	466.0	117.0	632.0	562.0	797.0	764.0		
	mod	155.6	786.1	227.7	352.4	766.4	260.6	458.5	109.6	453.9	581.1	802.8	699.4		
	obs/mod	1.440	1.006	1.085	1.132	0.843	1.017	1.016	1.068	1.392	0.967	0.993	1.092	1.042	1.043
218195	obs	281.0	777.0	204.0	407.0	788.0	270.0	470.0	121.0	509.0	552.0	728.0	740.0		
	mod	146.9	792.1	210.5	348.5	655.1	289.7	454.5	123.1	522.5	624.0	662.4	746.0		
	obs/mod	1.913	0.981	0.969	1.168	1.203	0.932	1.034	0.983	0.974	0.885	1.099	0.992	1.009	0.983
218915	obs	168.0	653.0	201.0	346.0	794.0	287.0	467.0	115.0	346.0	288.0	317.0	456.0		
	mod	119.1	640.6	175.4	302.7	592.5	268.8	416.5	110.7	297.9	368.2	381.0	492.3		
	obs/mod	1.411	1.019	1.146	1.143	1.340	1.068	1.121	1.039	1.161	0.782	0.832	0.926	1.132	0.879
225160	obs	196.0	650.0	129.0	256.0	773.0	253.0	343.0	143.0	506.0	620.0	...	798.0		
	mod	86.2	749.1	136.4	246.6	581.7	264.8	354.1	80.3	548.1	651.1	565.5	824.5		
	obs/mod	2.274	0.868	0.946	1.038	1.329	0.955	0.969	1.781	0.923	0.952	...	0.968	1.003	0.952
+36 4063	obs	187.0	580.0	252.0	378.0	666.0	269.0	406.0	150.0	296.0	227.0	275.0	356.0		
	mod	158.4	651.9	217.5	363.6	621.5	281.8	481.0	141.4	244.4	294.5	360.7	373.0		
	obs/mod	1.181	0.890	1.159	1.040	1.072	0.955	0.844	1.061	1.211	0.771	0.762	0.954	1.050	0.863
Median	obs/mod	1.411	0.996	0.992	1.105	1.296	0.975	1.016	1.018	1.012	0.902	0.933	1.000		

Table 5.5: Derived parameters for the WHT O stars

HD/BD	Sp. Type	$T_{\rm eff}$ (kK)	$\log_{10} g$	M_V	$\log_{10} L/L_\odot$	$R/R_\odot$	$M/M_\odot$
10125	O9.7 II	32.5	3.3	-5.8	5.5 ± 0.2	17 ± 3	21 ± 12
12323	ON9 V	36.0	4.1	-3.5	4.7 ± 0.1	5 ± 1	14 ± 8
13745	O9.7 II((n))	33.0	3.3	-5.3	5.3 ± 0.2	13 ± 2	13 ± 8
16429	O9.5 II((n))	35.0	3.4	-6.8	5.9 ± 0.1	25 ± 4	59 ± 34
30614	O9.5 Ia	33.0	3.1	-6.1	5.6 ± 0.2	20 ± 3	19 ± 11
34078	O9.5 V	37.0	4.2	-4.0^*	4.9 ± 0.2	7 ± 1	26 ± 15
36486	O9.5 II	34.0	3.4	-6.6	5.8 ± 0.2	24 ± 4	51 ± 30
37742	O9.7 Ib	34.0	3.3	-7.0	6.0 ± 0.1	30 ± 5	64 ± 37
188209	O9.5 Iab	33.0	3.1	-6.0	5.6 ± 0.2	19 ± 3	17 ± 10
189957	O9.5 III	33.0	3.5	-5.0	5.2 ± 0.2	12 ± 2	15 ± 9
191781	ON9.7 Iab	31.0	3.1	-6.0	5.5 ± 0.1	20 ± 3	19 ± 11
194280	OC9.7 Iab	32.0	3.2	-6.1	5.6 ± 0.2	21 ± 3	25 ± 14
195592	O9.7 Ia	31.0	3.0	-6.0	5.5 ± 0.1	20 ± 3	15 ± 9
201345	ON9 V	36.0	3.9	-4.2	4.9 ± 0.1	8 ± 1	16 ± 9
202124	O9.5 Iab	34.0	3.2	-6.0	5.6 ± 0.1	19 ± 3	20 ± 12
207198	O9 Ib-II	36.0	3.4	-5.5	5.5 ± 0.1	14 ± 2	19 ± 11
209975	O9.5 Ib	35.0	3.4	-5.7	5.5 ± 0.2	16 ± 3	23 ± 14
210809	O9 Iab	36.0	3.3	-6.2	5.8 ± 0.1	20 ± 3	28 ± 16
214680	O9 V	38.0	4.2	-4.4	5.1 ± 0.2	8 ± 1	37 ± 21
218195	O9 III	37.0	3.6	-5.1	5.3 ± 0.2	11 ± 2	18 ± 10
218915	O9.5 Iab	34.0	3.2	-6.0	5.6 ± 0.1	19 ± 3	20 ± 12
225160	O8 Ib(f)	38.0	3.4	-6.6	6.0 ± 0.2	23 ± 4	48 ± 27
+36 4063	ON9.7 I	32.0	3.1	-5.9	5.5 ± 0.2	19 ± 3	16 ± 10

NOTES: * – *See discussion in text*

Table 5.6: Physical parameters in Voels et al. (1989)

	This thesis			Voels et al.		
HD	$T_{\rm eff}$(kK)	$\log_{10} g$	y	$T_{\rm eff}$(kK)	$\log_{10} g$	y
30614	33.0	3.1	0.13	30.0	2.90	0.18
34078	37.0	4.2	0.09	35.5	3.95	0.10
36486	34.0	3.4	0.10	33.0	3.45	0.10
37742	34.0	3.3	0.10	32.0	3.20	0.10

Table 5.7: Physical parameters in Grigsby et al. (1992)

	This thesis			Grigsby et al.	
HD	$T_{\rm eff}$(kK)	$\log_{10} g$	y	$T_{\rm eff}$(kK)	$\log_{10} g$
12323	36.0	4.1	0.17	29.0	4.00
201345	36.0	3.9	0.14	29.0	4.00
214680	38.0	4.2	0.09	30.0	4.00
218195	37.0	3.6	0.12	31.5	3.60

Table 5.8: Physical parameters in Herrero et al. (1992)

	This thesis			Herrero et al.		
HD	$T_{\rm eff}$(kK)	$\log_{10} g$	y	$T_{\rm eff}$(kK)	$\log_{10} g$	y
34078	37.0	4.2	0.09	36.5	4.05	0.09
207198	36.0	3.4	0.12	34.0	3.30	0.12
209975	35.0	3.4	0.09	32.5	3.20	0.09
210809	36.0	3.3	0.13	33.0	3.10	0.12
214680	38.0	4.2	0.09	37.5	4.00	0.10

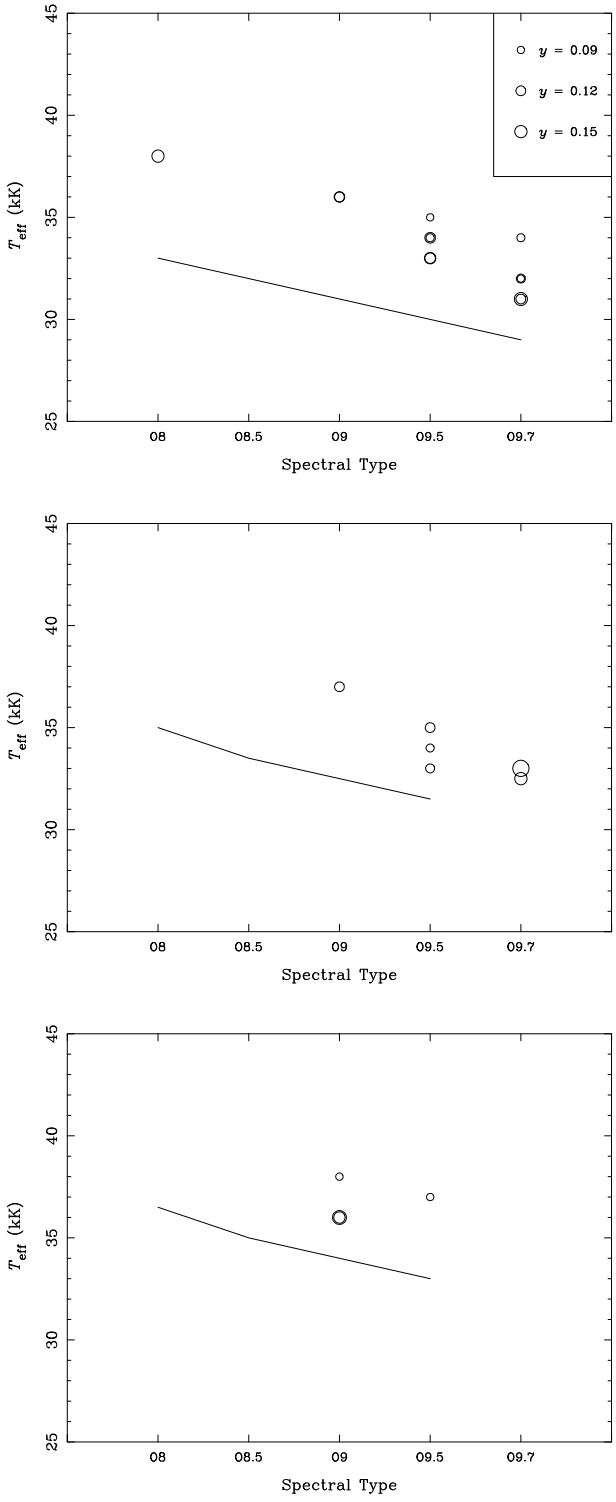

Figure 5.6: *Effective temperatures against spectral types for sample stars.* ***top*** *– luminosity class I,* ***middle*** *– luminosity classes II and III,* ***bottom*** *– luminosity classes IV and V. The size of the symbols refers to the helium number fraction, y (see top diagram for key). 'Typical' parameters for O stars from Howarth and Prinja (1989) are drawn as lines.*

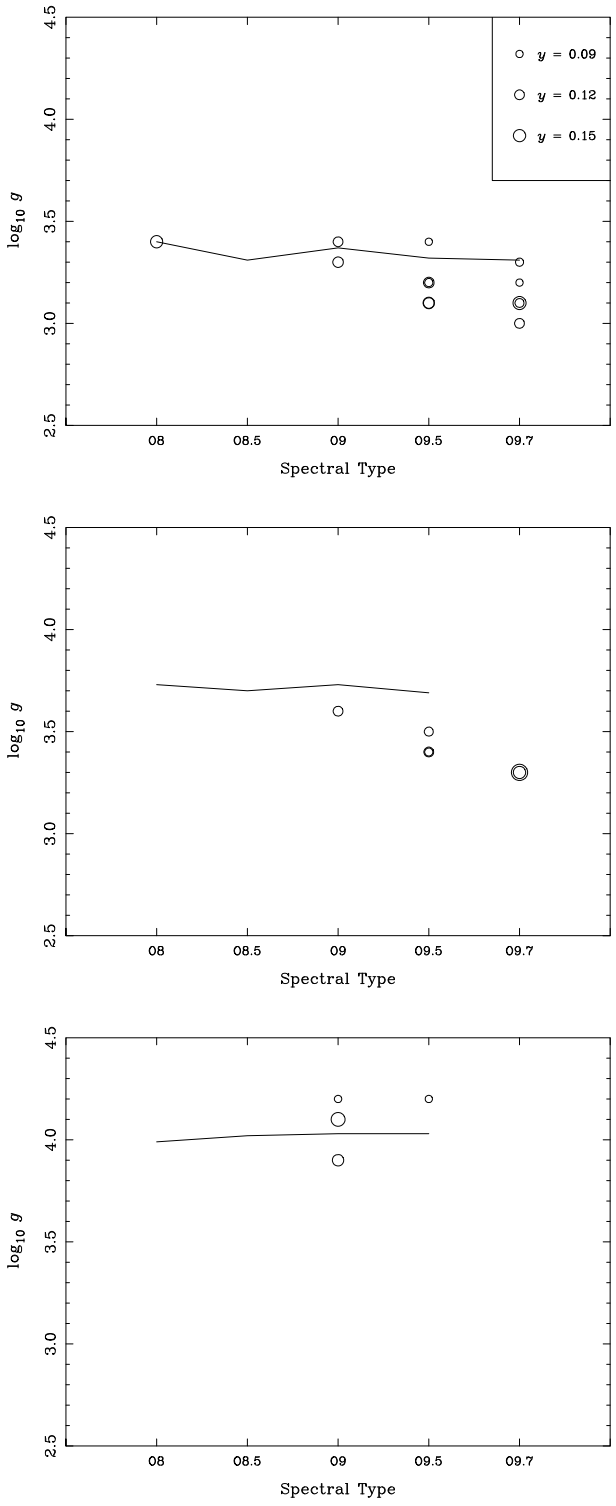

Figure 5.7: *Surface gravity against spectral types for sample stars.* ***top*** *– luminosity class I,* ***middle*** *– luminosity classes II and III,* ***bottom*** *– luminosity classes IV and V. The size of the symbols refers to the helium number fraction, y (see top diagram for key). 'Typical' parameters for O stars from Howarth and Prinja (1989) are drawn as lines.*

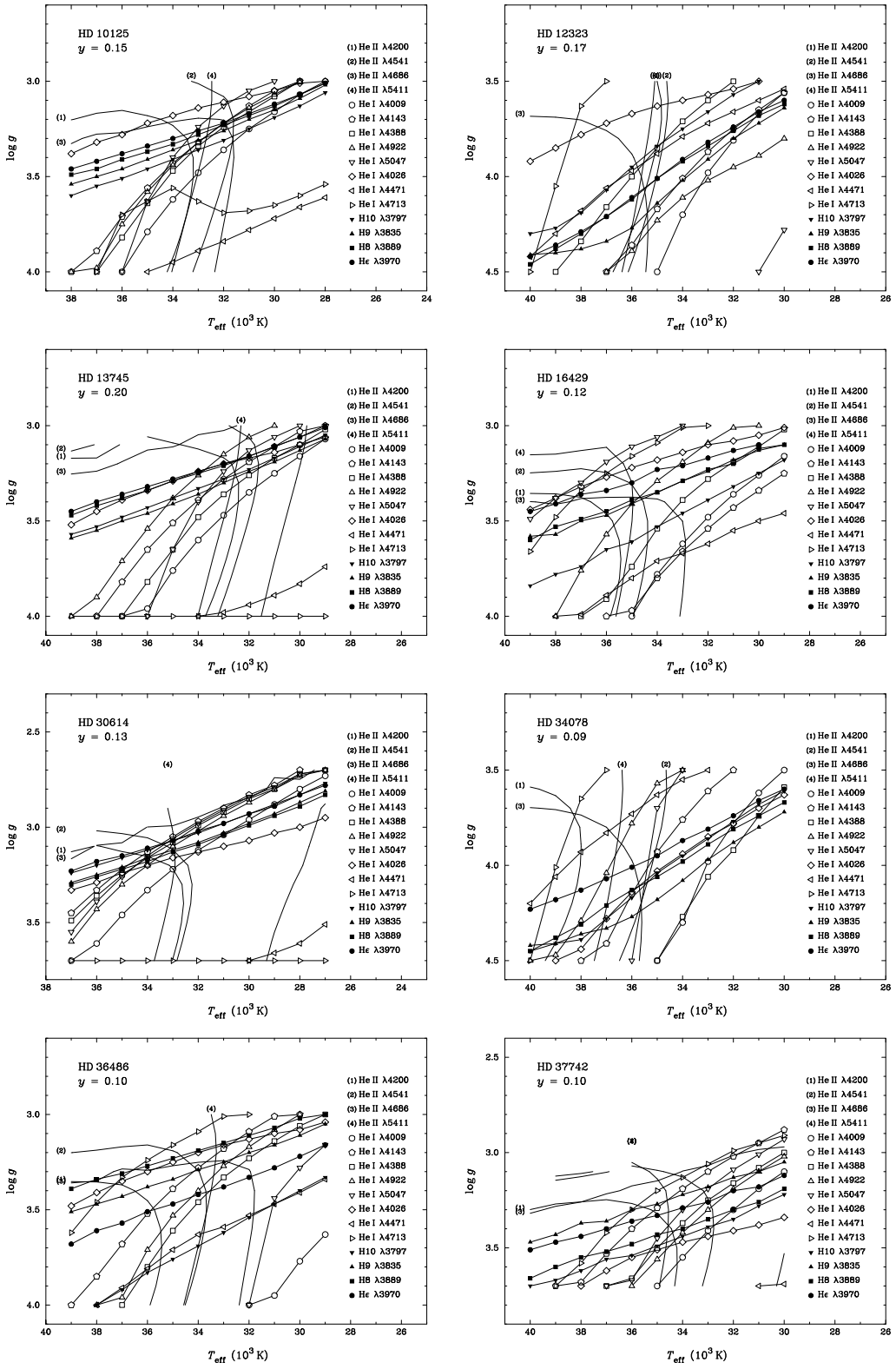

Figure 5.8: *Fit diagrams for all sample stars. Catalogue number and adopted value of y shown in upper left-hand corner of each diagram. Lines that appear horizontal at the bottom of the diagrams fall outside the plotted area.*

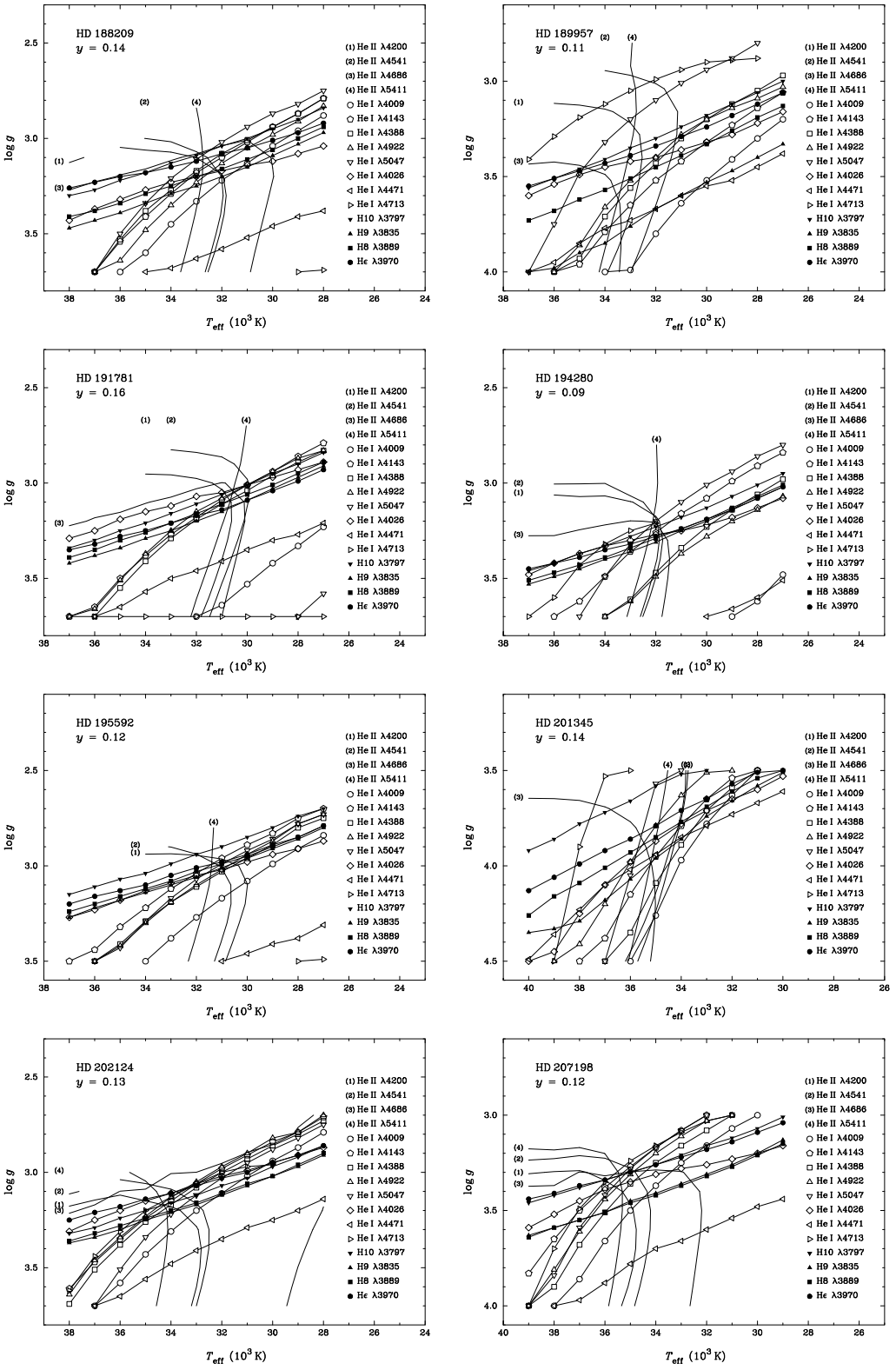

Figure 5.8: – *continued*

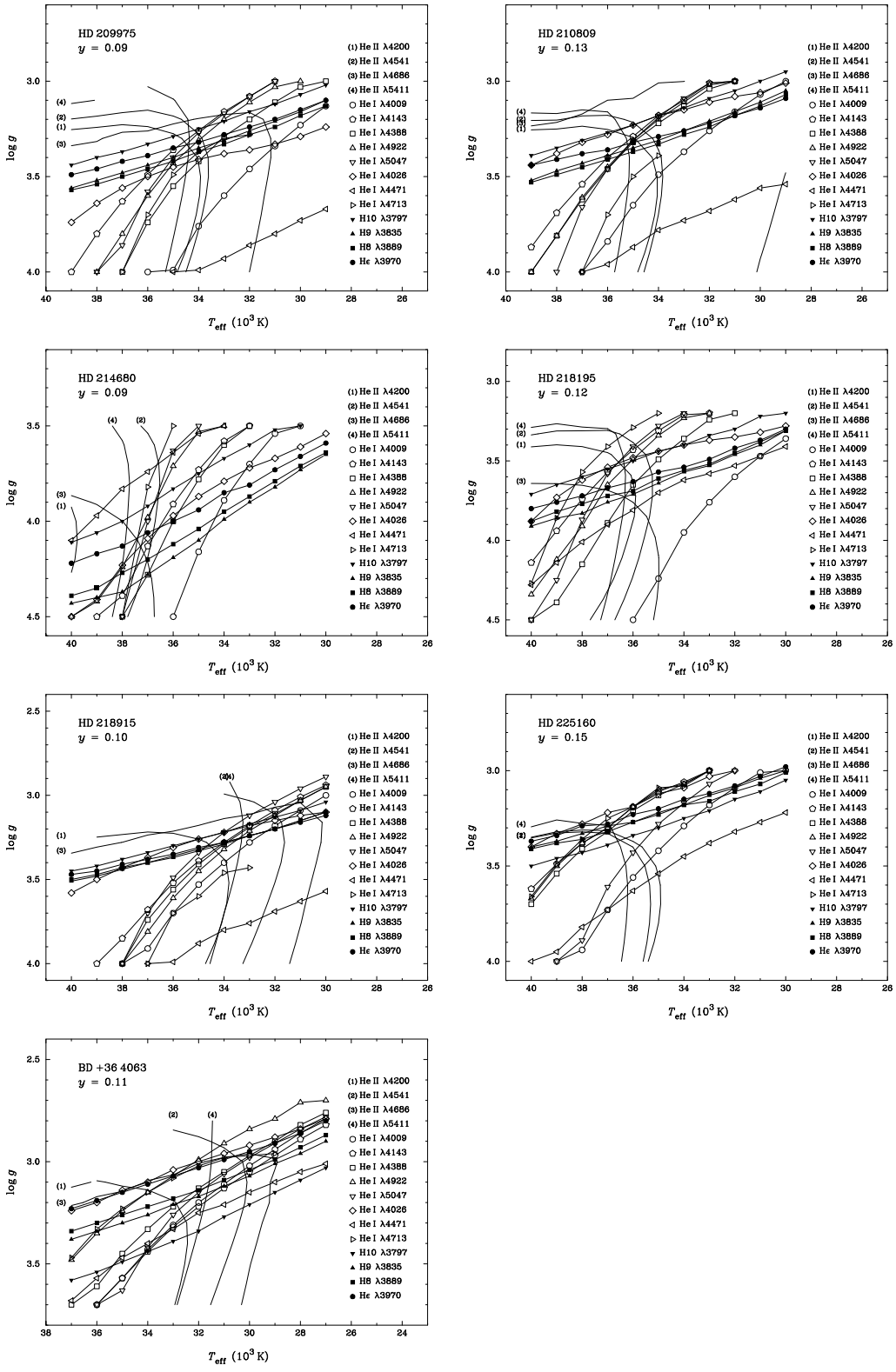

Figure 5.8: – *continued*

Chapter 6

Properties of the O stars

In chapter 5 we derived physical parameters for a large sample of O stars. There are obvious shortcomings to the models, as is clearly seen in the case of He I λ4471Å, for which the models consistently fail to reproduce the observed spectra. However, even with important physics left out or approximated, we believe the stellar models of today are good enough to give us a reasonable representation of the stellar atmosphere and a unique insight into the processes that might take place in, on and around the star. In this chapter we will look at the stellar parameters derived in chapters 4 and 5, and try to interpret some of the observed properties.

Chapter conventions

Several of the figures shown in this chapter will use a set of 'standard' symbols used throughout this chapter (and also in some diagrams appearing in earlier chapters). Table 6.1 summarises the different symbols. In addition to use of different symbols for different subgroups of stars, the symbols are also sometimes scaled according to some other parameter, e.g. the inferred helium number fraction. In these cases the scaling will be explained, either in the caption, or in the figure itself.

When the figures are there to investigate a relationship between two parameters, rank correlation coefficients are calculated and shown in the figure. Two such correlation coefficients are calculated; the Spearman Rank-Order Correlation Coefficient, $r_{\rm s}$, and Kendall's τ. Both of these are shown with their respective significance levels, p. A small value of p indicates a significant correlation. The properties of these correlation coefficients are described in *Numerical Recipes* (Press et al., 1992).

Table 6.1: Symbols used in this chapter

	Luminosity Class	
	I, II, III	IV, V
Morphologically normal	○	□
OC classified	●	
ON classified	●	■

NOTES: *There are no known OC main-sequence stars.*

H–R diagrams and evolutionary tracks

Figure 6.1 shows the sample stars on the H–R diagram, with evolutionary tracks from Schaller et al. (1992). Also indicated on the diagram is the Zero Age Main Sequence (ZAMS) and the Terminal Age Main Sequence (TAMS). The latter is taken here to be the most redward point the stars reach during their core hydrogen burning lifetimes. One of the ON main sequence stars, the binary star HD 12323, falls below the ZAMS (although the ZAMS is well within the error box surrounding this star; see figure for typical uncertainties).

After the core hydrogen is exhausted, the stars make a long trip redwards in the H–R diagram before they return again (only for stars with a ZAMS mass, $M_0 \gtrsim 40 M_\odot$) to the O star region, as shown in figure 6.2; this time the models predict nuclear processed material on the surface, and the star are tens of per cent lighter than they were on the ZAMS. On the return trip to the O-star region, the stars are very evolved and have a high mass-loss. The atmospheres are predicted to show large amounts of CNO processed materials, and much higher helium fractions than we observe.

6.1 The helium abundance

From looking at the results listed in table 5.3 we see than one of the most noticeable trends is that a large number of the stars show a higher-than-solar helium abundance. This has also been found by several other authors. Kudritzki et al. (1983) and Bohannan et al. (1986) both found increased helium abundances for the O4 If star ζ Pup ($y = 0.14$ and 0.17 respectively). Schönberner et al. (1988) analysed a sample of OBN class V stars and

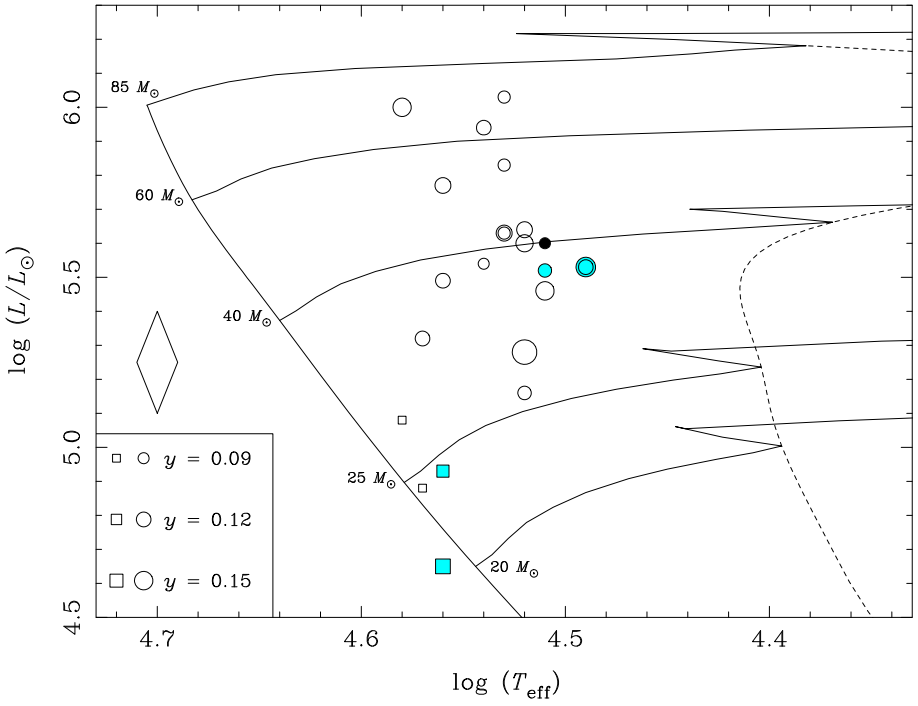

Figure 6.1: *H–R diagram showing O star parameters and evolutionary tracks. Main sequence stars are shown as squares, all other stars as circles (see table 6.1 for description of symbols). The size of the symbols depends on the helium number fraction, y (see key in lower left-hand corner). Evolutionary tracks for 20, 25, 40, 60 and 85 $M_\odot$ from Schaller et al. (1992) are shown, with the predicted ZAMS and TAMS (dashed line). Typical error box (assuming an error of 0.3 on M_V; see Herrero et al. 1992) is shown to the left of the ZAMS.*

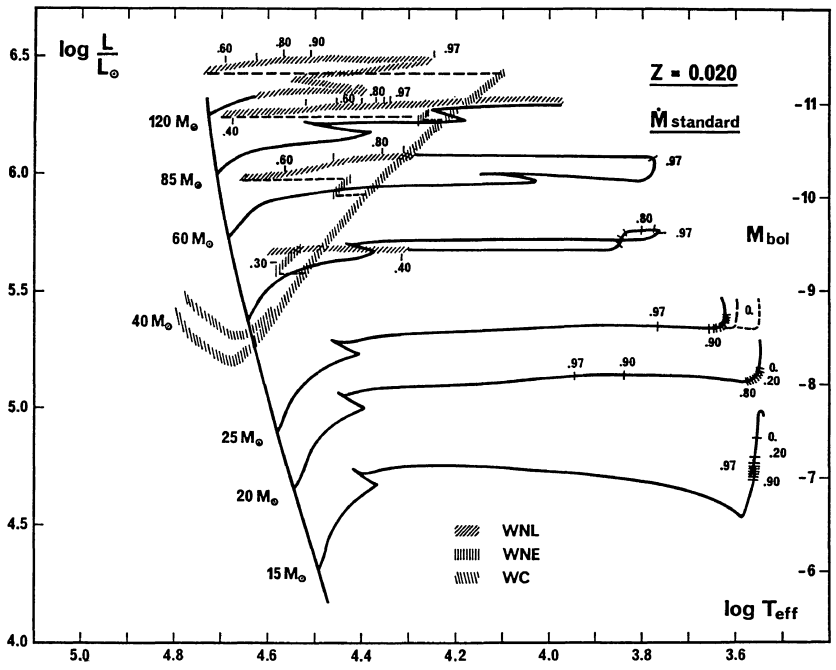

Figure 6.2: *H–R diagram including post-MS evolutionary tracks from Schaller et al. (1992).*

compared them to the normal OB stars 10 Lac and τ Sco. All the nitrogen-rich stars also came out with high helium abundances, whereas the normal stars had solar composition. Voels et al. (1989) performed a study of stars of spectral type O9.5 and found helium enrichment only in the Ia star α Cam. All other luminosity classes showed normal helium abundances. Along the same lines, Herrero et al. (1992) studied a sample of OB stars and came to the conclusions that all main sequence stars (if not fast rotators) have normal helium abundances; almost all stars with a $v_e \sin i$ faster than 200 km s^{-1} or classified as Ia, Iab, f or (f) show helium enhancement ($y \geq 0.12$; most of the sample $y \geq 0.15$); and that all other objects show normal helium fractions ($y \leq 0.12$). From this they deduce that most O giants and supergiants show CNO enrichment which is "apparently the only explanation for helium enrichment", and further that the enrichment is reinforced when the star has a high $v_e \sin i$ or a low gravity and high luminosity. More recently, Smith and Howarth (1994) studied three supergiants of approximately the same spectral type and luminosity class, one of which was an OC star, one was classified as ON, and the third was a normal O star. They found that both the ON and the O star showed enhanced helium abundances (0.17 and 0.13 respectively), and that the OC had a solar composition.

6.1.1 Evolutionary effects

All these effects could be explained as evolutionary effects. Hot stars experience a large mass loss through stellar wind during their lifetimes, and this will slowly strip off the outer layers of the stars, exposing deeper layers. These layers might contain the products of nuclear burning brought up from the core through some deep convective process. The evolutionary models by Schaller et al. (1992) discussed above, taking into account mass loss and convective overshooting, do reveal nuclear processed materials on the surface of the stars. This happens, however, at a much later evolutionary stage (i.e., post red supergiant) than that which these stars appear to be in, and the helium abundances predicted by the evolutionary models are far larger than observed. Only the very high-mass evolutionary tracks predict an increase in surface helium abundance while the star is still core hydrogen burning. Figure 6.3 shows the predicted surface helium number fraction of the evolutionary tracks, and figure 6.4 shows the same diagram as figure 6.1, with the inclusion of the model helium fractions. To make the diagram easier to read, all stars are here shown as identical symbols. It appears that the predicted increase in y is roughly the same as observed. However, only stars at a higher luminosity and lower temperature than those analysed in this study, are predicted to show this increased helium abundance.

Walborn (1976) proposed several scenarios to explain the observed carbon, nitrogen and sometimes oxygen anomalies in the OBN and OBC stars, and it is probable that these are very closely related to the observed variations in helium abundances (see section 6.3). Apart from the evolutionary effects discussed above, it is also possible that the observed abundance anomalies (C, N or He) could reflect initial abundance differences. The main (if not only) evidence supporting this theory is the existence of the three nitrogen deficient Orion Belt stars (HD 36486, HD 37128, HD 37742). HD 37128 is a B0 Ia star, and as such is not covered by this study. The other two are, and both are found to have a normal helium abundance ($y = 0.10$). In a recent study, McErlean et al. (1998) analysed HD 37128 using models very similar to the ones used in this thesis, and they derived $y = 0.10$.

To return to Herrero's conclusions; they notice that all their main sequence stars, except the fast rotators ($v_e \sin i \geq 200$ km s^{-1}), have normal helium abundances. Figure 6.5 shows y against $\log_{10} g$ and luminosity class. Unlike Herrero et al., we have no main sequence stars with a $v_e \sin i$ faster than 200 km s^{-1}, but we do observe that two (out

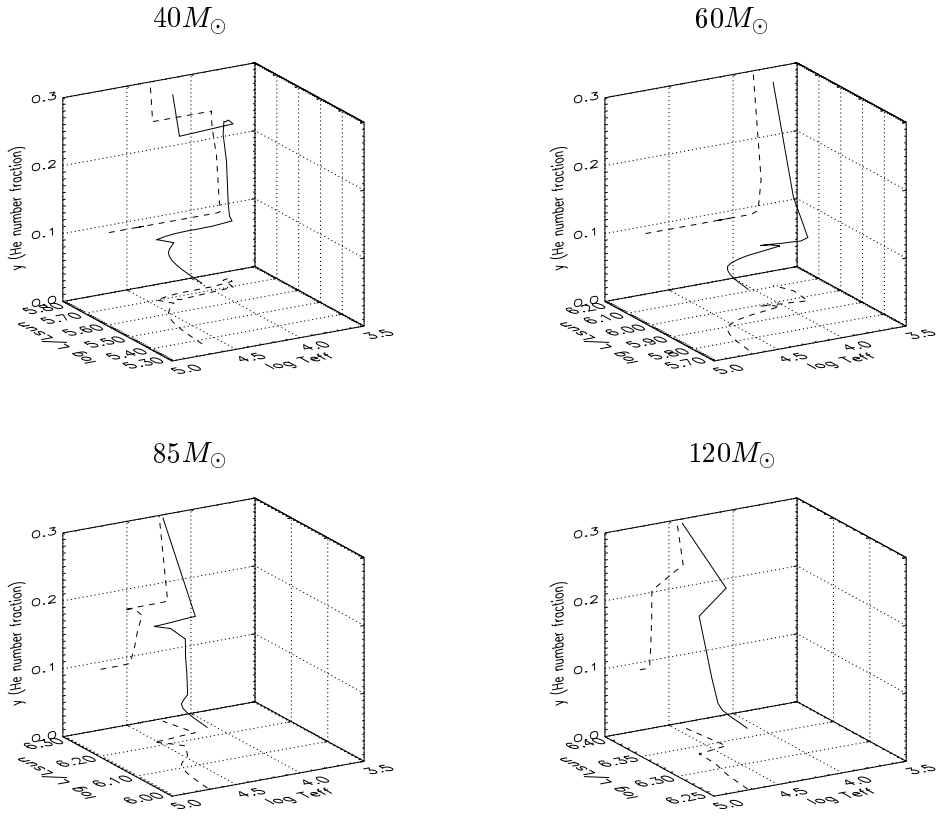

Figure 6.3: *Helium number fractions, y, predicted by evolutionary tracks. The dashed lines show the 3D models (solid lines) projected onto the plane described by the axes. The* $\log L/\log T_{\rm eff}$ *plane is the familiar H-R diagram (as shown in figures 6.1 and 6.2). The models are from Schaller et al. (1992).*

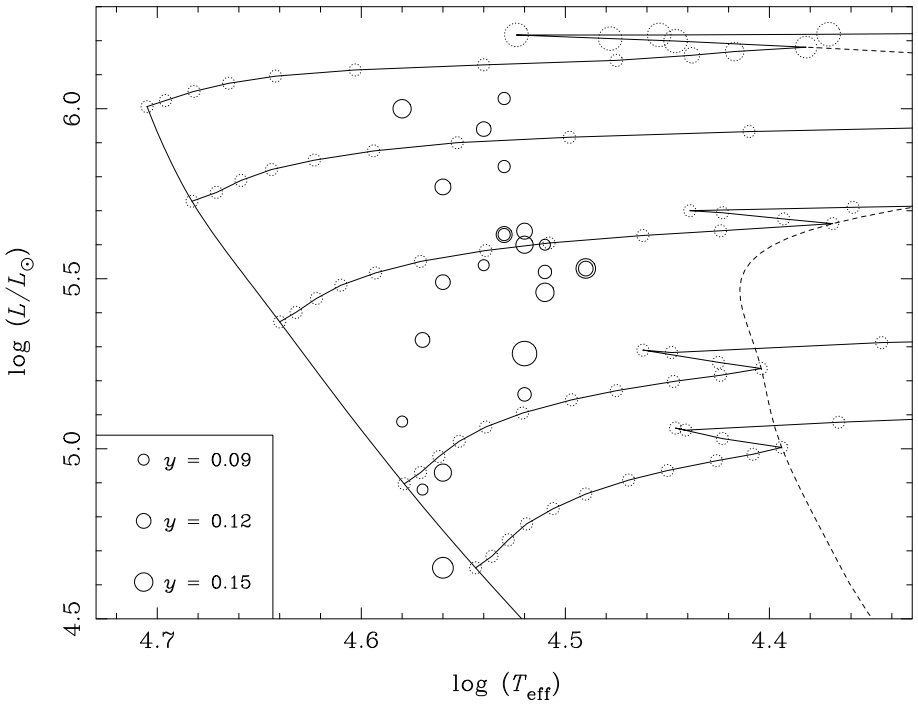

Figure 6.4: *H–R diagram showing O star parameters and evolutionary tracks (as in figure 6.1). The predicted surface helium number fractions are shown as 'ghost' stars on the evolutionary tracks. The size of the symbols depends on the helium number fraction, y (see key in lower left-hand corner). All stars are shown as circles to simplify diagram.*

of four) of the MS stars do show enhanced helium. Both of these stars were classified as ON stars by Walborn, and both are possibly binaries[1]. Although 50 % of the MS sample show helium enhancement, there is a strong bias towards stars classified as either ON or OC in our sample (there are no known OC main sequence stars) so this is certainly not a representative percentage of helium enhanced O main-sequence stars.

Our supergiants also show a much larger spread in helium abundances than those studied by Herrero et al. Roughly half the luminosity class I objects have a helium abundance of 0.12 or below, but only two have a y of 0.15 or higher, whereas Herrero et al. found that all but one of their Ia, Iab, f or (f) classified stars had abundances of 0.15 or higher. In our sample, only five stars appear to have a helium abundance this high, and two of these are classified as ON (one is the ON main-sequence binary HD 12323).

Comparing the position in the H–R diagram to evolutionary models allows us to estimate the mass of the star, and also its age. Interpolating between the models by Schaller et al. (1992) we can find the evolutionary track that passes through a given point on the H–R diagram (by supplying a $T_{\rm eff}$ and L). Mapping this evolutionary track onto a $T_{\rm eff}$ – $\log_{10}(L/L_{\odot})$ grid we can find the current mass (see section 6.2) and age from the spectroscopic $T_{\rm eff}$. Figure 6.6 shows the helium abundance as a function of age and fractional age (age / MS lifetime). Neither shows a clear relation, but the rank correlation coefficients r_s and τ shown in upper right-hand corner of figures, suggest that there is possibly some correlation between age and y. The probability that there is no correlation is only 12 – 17%, but there is no conclusive evidence to suggest that the helium abundance increases with age, especially since there appears to be very small probability of a correlation between the fractional age and y.

6.1.2 Rotation

As mentioned above, Herrero et al. (1992) found that their fast rotators, arbitrarily defined as those stars with a $v_e \sin i \geq 200$ km s^{-1}, showed high ($y \geq 0.15$) helium abundances. We have only one star with a broadening velocity higher than 200 km s^{-1}. Figure 6.7 shows y as a function of broadening velocity. Notice that the MS stars (marked as squares) and the two fastest rotators belong to a separate distribution from the other stars due to the use of different profiles to estimate the broadening velocity. We have, however, treated

[1] HD 12323 is a binary according to Garmany et al. (1980); HD 201345 was listed as binary according to Bolton and Rogers (1978), but single by Gies and Bolton (1986) and Mason et al. (1998)

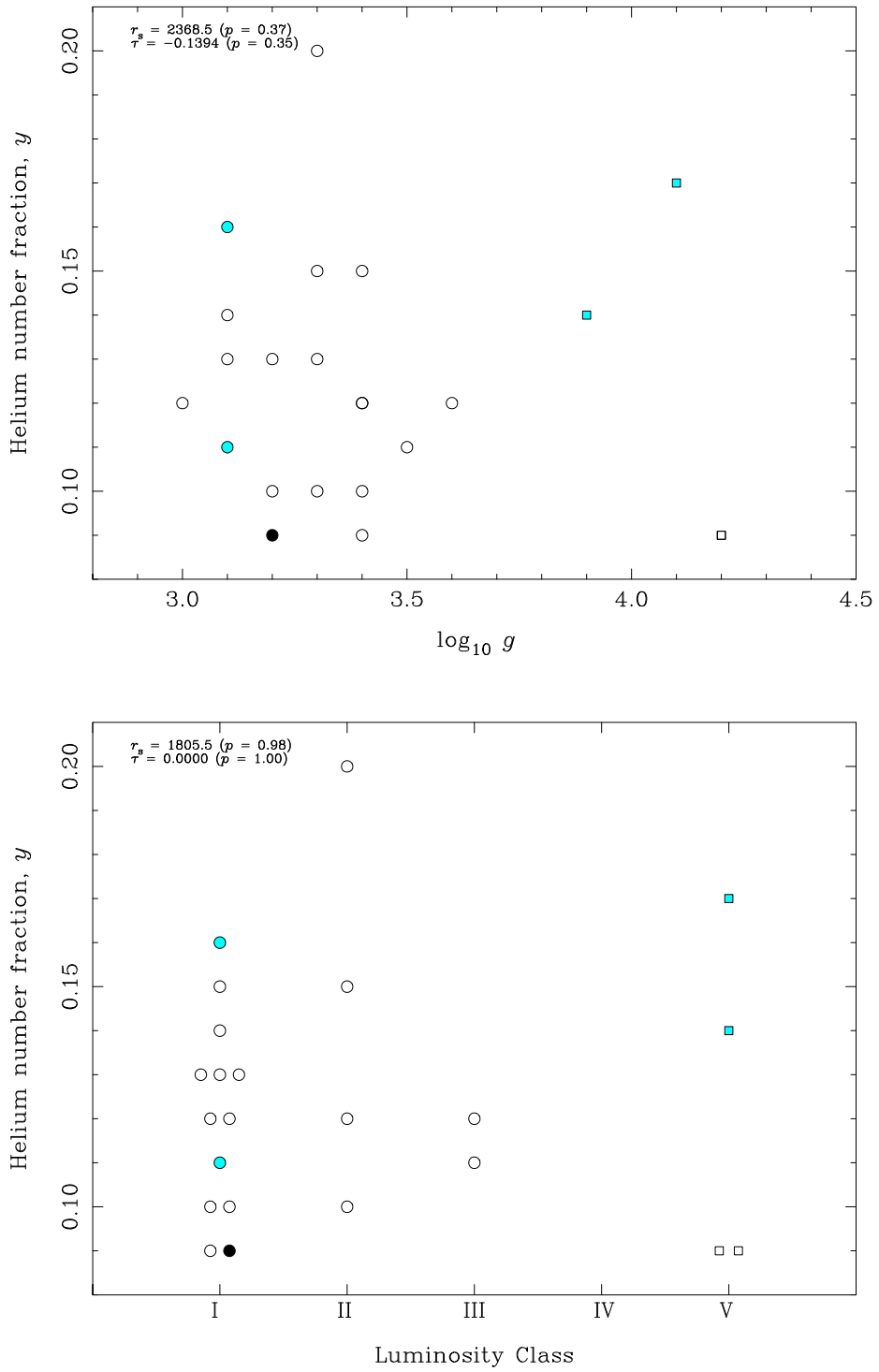

Figure 6.5: *Helium number fractions for different* $\log_{10} g$ (***top panel***) *and luminosity classes* (***bottom panel***). r_s *is the Spearman rank-order correlation coefficient, and* τ *is Kendall's* τ. *The numbers in brackets indicate the probabilities that the points belong to a random distribution, ie no correlation.*

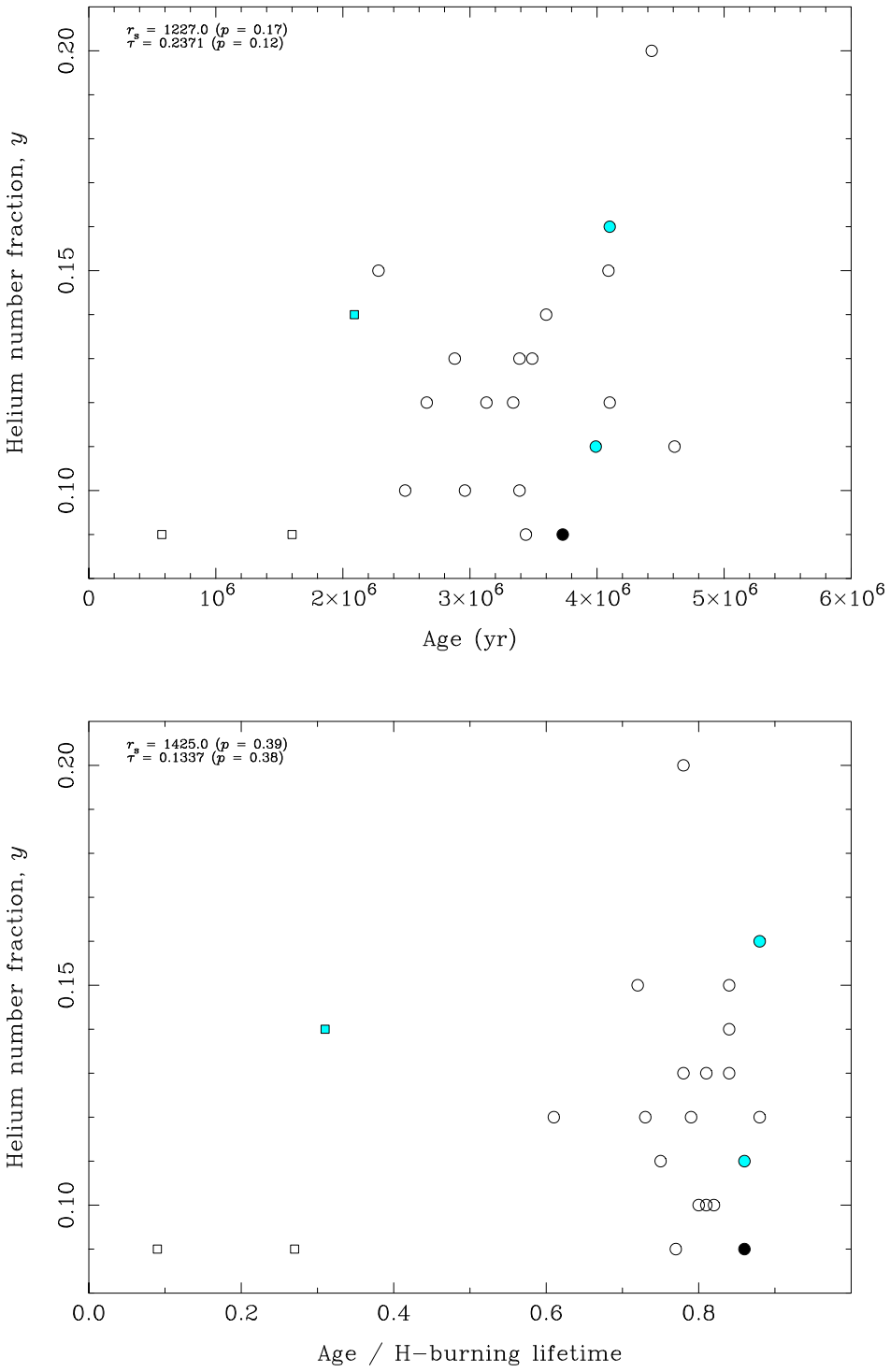

Figure 6.6: *Helium number fractions against the stellar age predicted by evolutionary models (Schaller et al. 1992).* ***Top panel*** *shows y vs. the evolutionary age, and the* ***bottom panel*** *shows y vs. fractional age (age / core hydrogen burning lifetime). HD 12323 is not plotted due to its position below the main-sequence. r_s and τ are the correlation coefficients as for figure 6.5.*

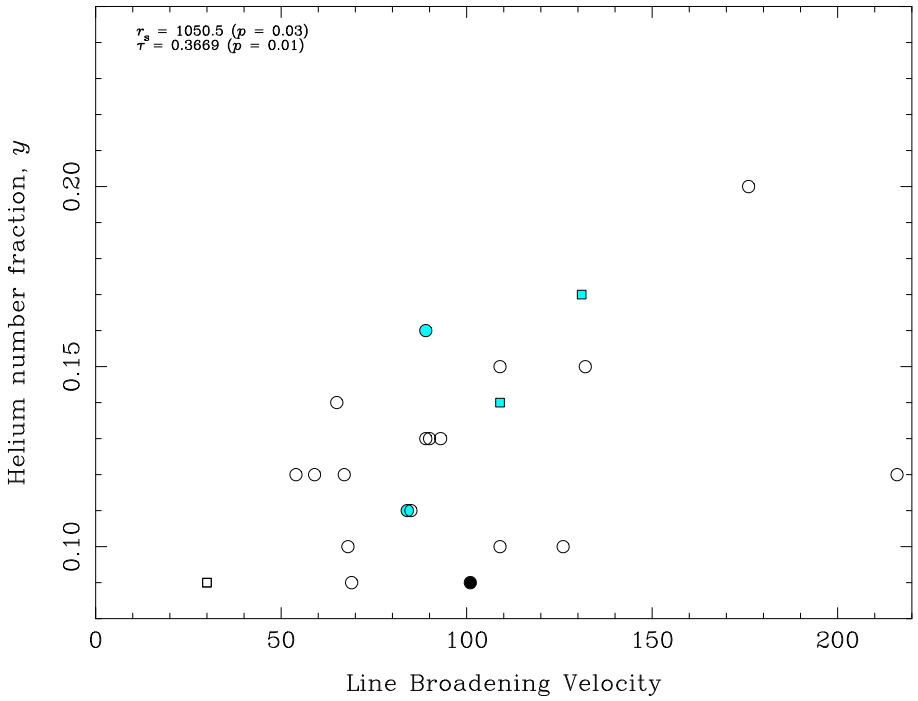

Figure 6.7: *Helium number fractions against the stellar broadening velocity. Symbols are as shown in table 6.1.*

them as one dataset when calculating the correlation coefficient, r, shown in the upper right-hand corner. Although the star with the broadest absorption lines shows only a moderately high helium abundance, there appears to be a clear trend between the width of the spectral lines and the helium abundance. From the correlation coefficients we find a low probability that these parameters are not correlated.

If we assume that the main broadening mechanism in all O-stars is rotation, then the implication of this would be that there is some turbulent mixing of the stellar interior caused by the rotation that brings processed material up to the surface. There is, however, extensive evidence to suggest that this is not the case. The almost total absence of sharp-lined O stars (as would be expected in the case of rotational broadening, considering a number of the stars would be seen pole-on) could imply that the broadening must, at least partly, be caused by other mechanisms (see discussion in chapter 7). That the dependence of y on the line broadening velocity is apparently the same for both main-sequence and giant stars implies that the broadening mechanism could be the same. However, there are only 4 main-sequence stars in the sample, and two of these have very narrow lines, so the

sample is too small to draw any firm conclusions.

There is of course the possibility that the increases in helium abundance are not real. It is easy to imagine that for stars with broad lines, it is difficult to detect blends, and the measured equivalent widths might be overestimated. Figure 6.8 shows a simulation of this effect. The left hand column of the figures shows the fit diagrams for the measured equivalent widths of 10 Lac (HD 21460). This star has very narrow lines, and a 'normal' helium abundance. The right hand column shows equivalent widths measured after artificially spinning this star up to 250 km s^{-1} by convolving the spectrum with equation 3.11 discussed in chapter 3. The star now appears to have a helium abundance of roughly 0.12, compared to the 'original' adopted value of 0.09. However, we made no attempts at using multiple gaussians to fit irregular looking lines, and it is quite likely that, in a careful study, these errors could be reduced by careful fitting of the lines. It is therefore possible that blending effects could cause a *slight* increase in the adopted helium fractions, but not enough to explain the enhanced helium abundances observed in this study.

Another factor that might be contributing to the increase in helium abundances observed by Herrero et al. for the very fastest rotators, could be caused by rotational distortion. For stars that rotate very fast, close to their break-up angular velocity, ω_c, the equatorial radius will be significantly larger than the polar radius, and similarly the gravity at the equator will be lower than at the pole. From the 'law of gravity darkening' (von Zeipel, 1924) we have $T_{\rm eff}^4 \propto |\mathbf{g}|$. This will lead to differences in atmospheric structure at the poles and equator, and differing contributions from different elements (it will also lead to different line profiles for lines that form predominantly near the equator and those that form predominantly at the poles).

Ian Howarth (private communication) has generated synthetic spectra for stars with ω/ω_c near 1. At these high velocities the stars 'bulge' around the equator, and consequently have lower effective temperature and gravity at the equator. The synthetic spectra are generated by dividing the stellar surface into sections, and calculating an average $T_{\rm eff}$ and $\log_{10} g$ for each section. Spectra from the grid of models are then co-added to generate a synthetic spectrum of the star. We have fitted a random sample of these synthetic spectra as if they were actual observed stars (the 'true' atmospheric parameters were not revealed until after the analyses). Table 6.2 summarises the results of the analysis. The models closest to their breakup-velocity appear to have a slightly increased helium abundance. The effect is very small, however, and probably too small to be observed in real stellar

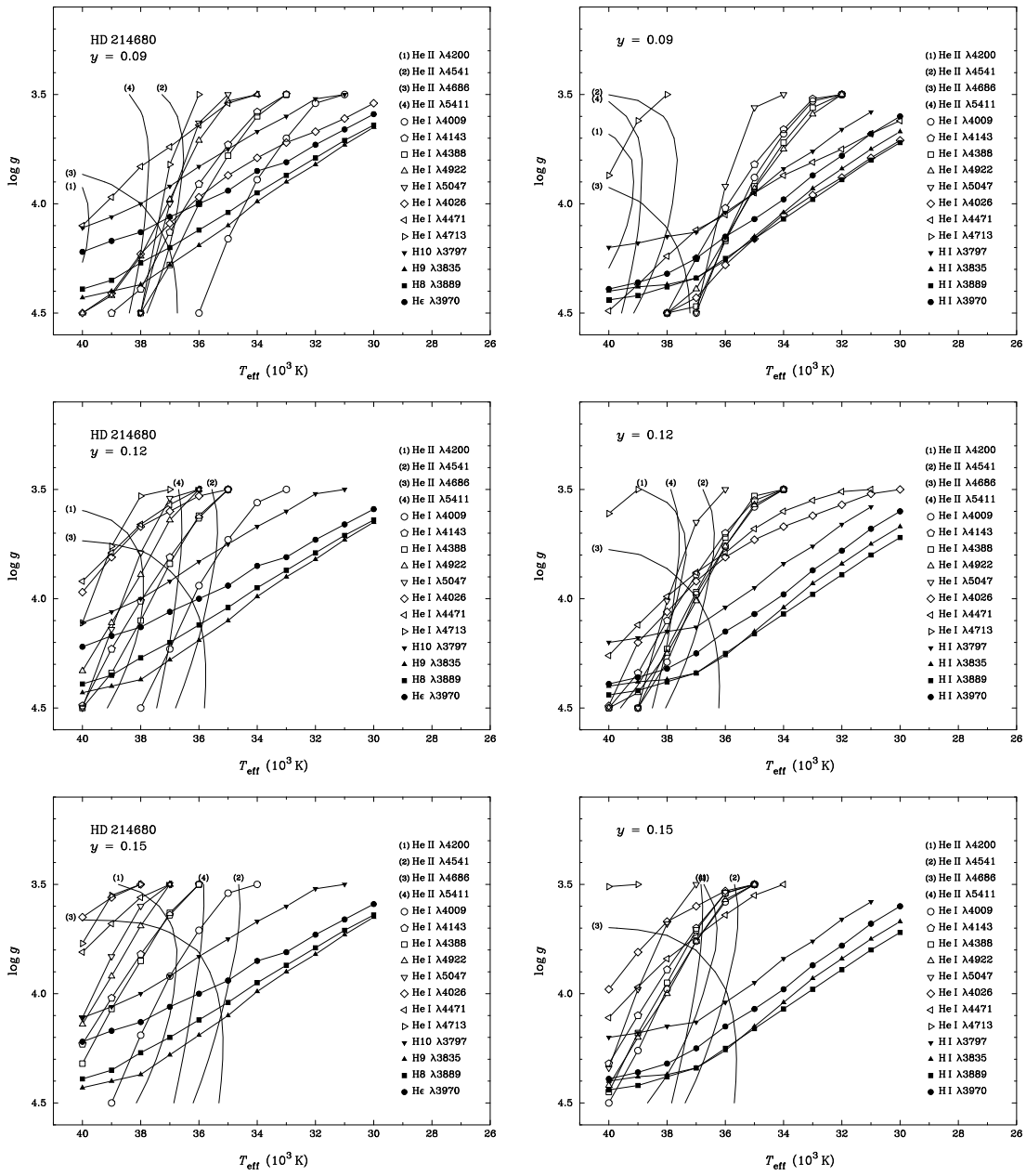

Figure 6.8: *Fit diagrams for artificially 'spun-up' 10 Lac. The left-hand column shows the real fit diagrams for 10 Lac (HD 214680) with an adopted helium fraction of 0.09. The right-hand column shows fit diagrams from equivalent widths measured after artificially 'spinning-up' the spectrum of 10 Lac to 250 km s^{-1}. The star now appears to have a helium fraction of 0.12.*

Table 6.2: Results of high ω/ω_c analyses

Input spectrum					Fit parameters			
ω/ω_c	T_p (kK)	T_e (kK)	$\log_{10} g_p$	$\log_{10} g_e$	T_{eff} (kK)	$\log_{10} g$	y	$v_e \sin i$ (km s^{-1})
0.10	32.00	31.95	3.50	3.50	32.0	3.5	0.09	440
0.10	40.00	39.94	3.90	3.90	39.0	3.9	0.09	440
0.90	32.00	25.21	3.50	3.09	27.0	3.2	0.10	435
0.90	40.00	31.51	3.90	3.49	35.0	3.8	0.09	444
0.95	32.00	23.00	3.50	2.93	27.0	3.3	0.09	435
0.95	40.00	28.74	3.90	3.33	33.0	3.5	0.10	442
0.98	32.00	20.37	3.50	2.72	27.0	3.1	0.10	428
0.98	40.00	25.46	3.90	3.12	31.0	3.5	0.10	436

NOTES: *The velocity of all input spectra were 438 km s^{-1}. The velocities listed are those found from the* He I *lines.* He II *line broadening velocities are lower, at about 350 km s^{-1}, because the main contribution is from closer to the hot poles. The subscripted letters* p *and* e *denote polar and equatorial values respectively.*

spectra. For the low ω/ω_c models, we find values of T_{eff} and $\log_{10} g$ very close to the input parameters. However, as ω/ω_c increases, we find values that appear to lie about half-way between the polar and equatorial values. Adopting these values and computing synthetic spectra, we find that the He I lines are predicted to be too strong and the He II lines too broad and weak. It would be very difficult to fit the observed line profiles using just one value of $v_e \sin i$ since the He I lines are mainly formed closer to the hot poles (He II is very temperature sensitive) where the star rotates slower. From table 6.2 it appears that the effects of rotational distortion are unable to account for the observed enhanced helium abundances.

6.2 The 'mass discrepancy'

Using exactly the same method as we described earlier to find the stellar ages, we can also find their 'evolutionary masses'. The evolutionary mass is the mass predicted by the

(model) evolutionary track that passes through a star's position on the H–R diagram. Table 6.3 lists the spectroscopic mass (derived in chapter 5), the ZAMS mass, and the 'current' evolutionary mass for each target. For the main sequence stars the two 'evolutionary' masses are similar, but it is apparent from the table that the stars lose a significant amount of mass during their core H-burning lifetime.

Groenewegen et al. (1989) and Herrero et al. (1992) both noticed that there was a discrepancy between the spectroscopic and evolutionary masses in O and B stars. Herrero et al. suggested that this discrepancy could be made smaller by assuming the stars were no longer core H-burning, and on their way back to the blue after the red supergiant stage. However, at this stage the stars are expected to be at a highly evolved stage with very different properties than those observed (different surface abundances, mass-loss etc.), so this is unlikely to be the case. Herrero et al. also derive masses from radiation driven wind theory, and find that these masses agree within the errors on the spectroscopic masses. This probably rules out any large systematic errors in the spectroscopic masses (however, see discussion below about the impact of recent evolutionary models).

Table 6.3 clearly shows that the mass discrepancy is also significant for our data, and that the distribution of values is very similar to that found by Herrero et al. Although we only have a very small sample of main-sequence stars, we clearly see that the mass discrepancy is significantly smaller for these objects. Figures 6.9 and 6.10 show the mass discrepancy against $\log_{10} g$ and age. These two parameters are clearly related, so it is no big surprise to see that the distribution of values is similar in the two figures. What *is* striking however is a small clustering of three stars with near zero mass discrepancy. These are clearly not main-sequence stars, as they both show a higher age and lower surface gravity than the luminosity class V objects. These three stars are the two Orion Belt stars (HD 36486 and HD 37742) and HD 16429 (which is the broad-lined star, with a relatively low helium abundance). It is very interesting that these three stars are the only stars in the sample which appear on Walborn's list of normal O stars with moderate N deficiencies. The third Orion Belt star, ϵ Ori (HD 37128; B0 Ia), which also appears on Walborn's list, has recently been studied by McErlean et al., 1998. For their adopted parameters, and $M_V = -7.0$ from Groenewegen et al. (1989), we find that this star has a $M_s = 48.5$ and $M_e = 49.9$; so it appears that this star also belongs to the group with $\delta M \sim 0$.

Recent evolutionary models that also take into account the effects of stellar rotation

could partly help resolve the problem of the mass discrepancy. Rotating stars evolve towards higher luminosity than predicted by non-rotating models (Maeder, 1998; Meynet, 1998). This is mainly caused by two processes:

- Rotational mixing 'erodes' the molecular-weight gradient at the outer edge of the convective core, leading to a mass enhancement of the convective core.

- The mixing brings hydrogen-burning products (such as helium) to the surface. The surface helium enhancement decreases opacity.

Since the evolutionary masses are derived by comparing the evolutionary tracks with observed luminosities and temperatures, the effect of the overluminous models is to lower the evolutionary masses, which would bring them more in line with the spectroscopic masses.

6.3 Carbon and nitrogen abundance anomalies

Carbon and nitrogen, and sometimes oxygen, abundance anomalies in the O and B stars have been known since 1967 when Jaschek and Jaschek observed nitrogen deficiencies in two early-type supergiants. In the years following, several more objects were discovered and there existed a certain amount of confusion as to exactly which objects were anomalous (e.g. ζ Ori or HD 188209; see Jaschek and Jaschek, 1974). Walborn (1976) re-examined the classification criteria and reviewed the material and we have mostly adopted classifications from his papers, with the exception of BD+36 4063.

There are some problems in understanding the actual cause of the anomalies, not so much in the case of the OBNs[2], where the strong nitrogen enhancement is probably caused by mixing of CNO processed material into the atmosphere of the star, but there is no obvious way of creating a nitrogen deficiency in a star at early evolutionary stages. This led Walborn to propose that the morphologically normal O and B stars, which are by definition the largest groups, are not necessarily *chemically* normal. The sequence would then be that the nitrogen deficient OBC stars correspond to the natal abundances, while the morphological normal OB stars are in fact slightly chemically evolved, and the OBN stars are the extreme cases.

[2]OBN is a collective term for BN and ON stars. Similarly, OBC includes both BC and OC.

Table 6.3: Spectroscopic and evolutionary masses for the O stars

HD/BD	Sp. Type	$T_{\rm eff}$(kK)	$\log_{10} g$	y	M_s	M_0	M_e	δM
10125	O9.7 II	32.5	3.3	0.15	20.9	34.2	32.8	11.9
12323	ON9 V	36.0	4.1	0.17	13.6	20.7	20.6	7.0
13745	O9.7 II((n))	33.0	3.3	0.20	12.9	29.0	28.1	15.2
16429	O9.5 II((n))	35.0	3.4	0.12	59.0	62.8	58.0	−1.0
30614	O9.5 Ia	33.0	3.1	0.13	18.6	42.0	39.6	21.0
34078	O9.5 V	37.0	4.2	0.09	26.2	24.1	24.1	−2.2
36486	O9.5 II	34.0	3.4	0.10	51.2	54.2	49.8	−1.4
37742	O9.7 Ib	34.0	3.3	0.10	64.5	69.7	64.3	−0.1
188209	O9.5 Iab	33.0	3.1	0.14	16.9	40.1	38.0	21.1
189957	O9.5 III	33.0	3.5	0.11	15.5	26.1	25.4	9.9
191781	ON9.7 Iab	31.0	3.1	0.16	18.8	36.3	34.4	15.6
194280	OC9.7 Iab	32.0	3.2	0.09	24.6	39.7	37.5	12.9
195592	O9.7 Ia	31.0	3.0	0.12	14.9	36.3	34.4	19.5
201345	ON9 V	36.0	3.9	0.14	16.4	23.9	23.7	7.4
202124	O9.5 Iab	34.0	3.2	0.13	20.4	41.9	39.7	19.4
207198	O9 Ib-II	36.0	3.4	0.12	18.8	36.9	35.8	17.0
209975	O9.5 Ib	35.0	3.4	0.09	23.5	38.4	36.9	13.4
210809	O9 Iab	36.0	3.3	0.13	28.4	50.8	47.5	19.1
214680	O9 V	38.0	4.2	0.09	36.6	27.9	27.7	−8.9
218195	O9 III	37.0	3.6	0.12	18.1	32.2	31.6	13.5
218915	O9.5 Iab	34.0	3.2	0.10	20.4	41.9	39.7	19.4
225160	O8 Ib(f)	38.0	3.4	0.15	48.3	68.5	65.5	17.2
+36 4063	ON9.7 I	32.0	3.1	0.11	16.2	36.2	34.5	18.2

NOTES: *M_s – spectroscopic mass; M_0 – evolutionary ZAMS mass; M_e – evolutionary mass; $\delta M = M_e - M_s$*

All masses are in units of solar mass ($M_\odot$).

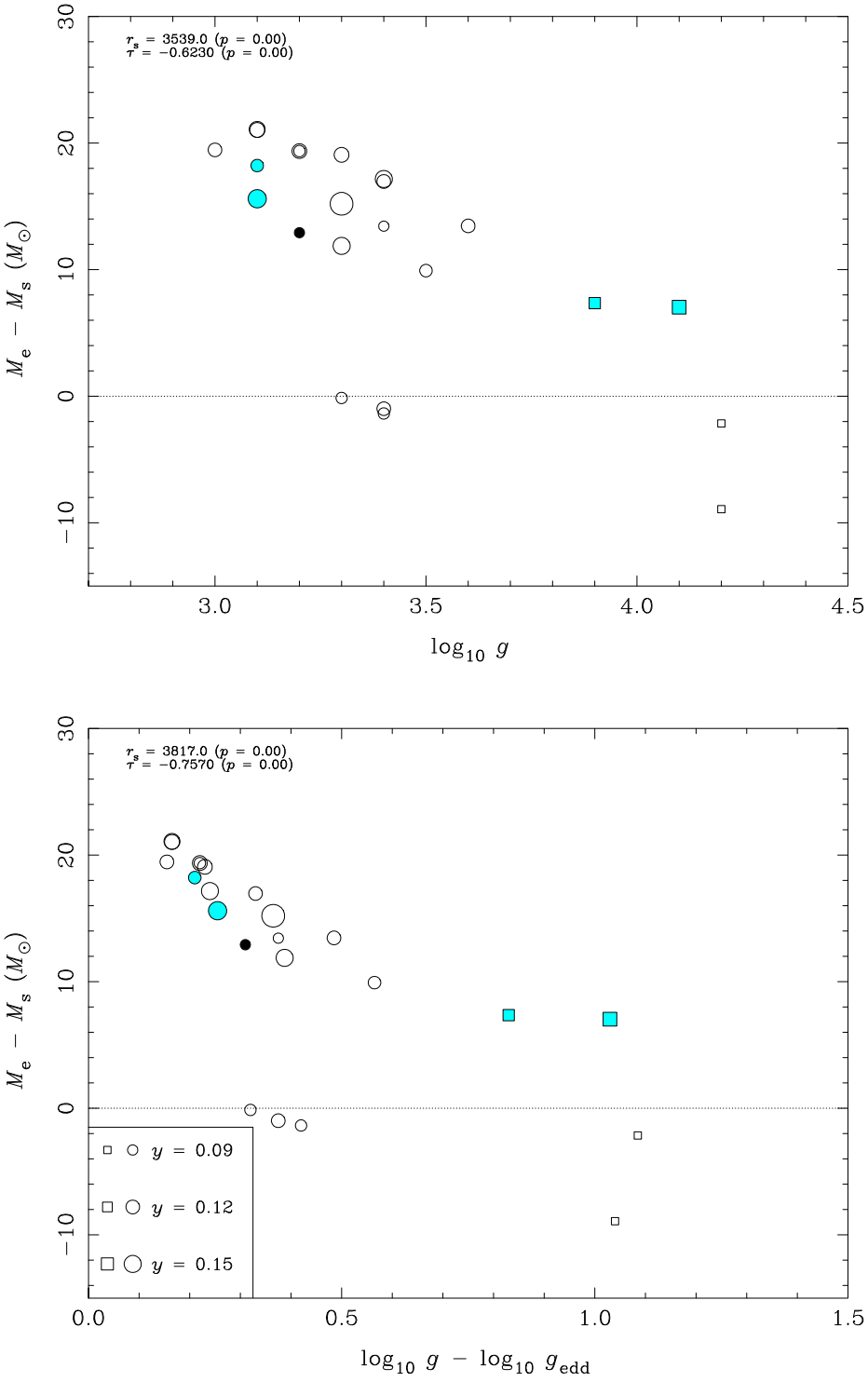

Figure 6.9: *Mass discrepancy against* $\log_{10} g$. *Symbols are as shown in table 6.1.*

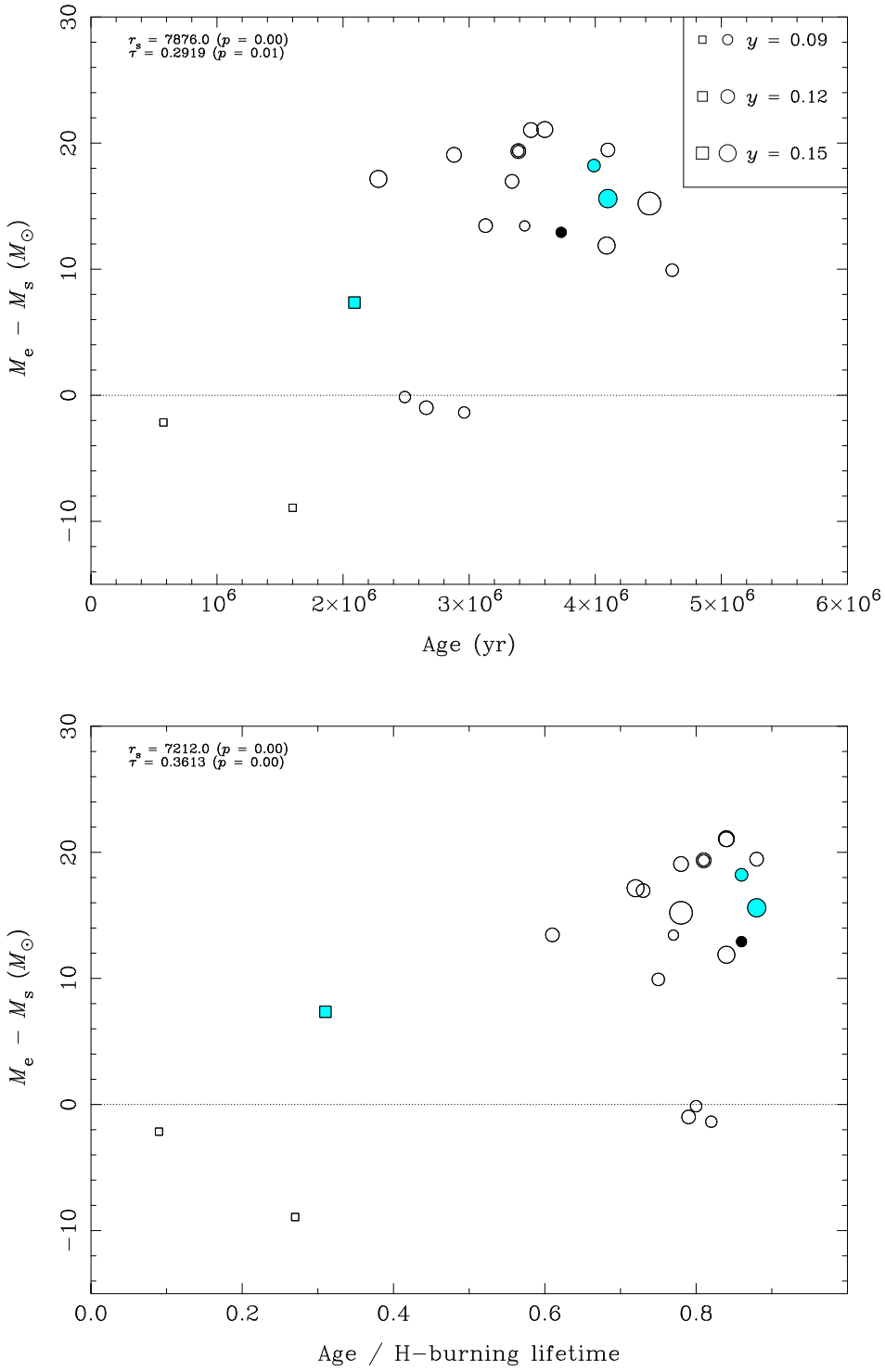

Figure 6.10: *Mass discrepancy against age.*

This picture is very pleasing and simple; it does, however, have some major shortcomings. The existence of both main-sequence and supergiant OBN stars, objects that should be highly evolved if the above theory is correct, suggests that other mechanisms also exist for bringing processed material onto the surface of the stars. There is also the problem that all known OBC stars are supergiants (and are evolved objects — see e.g. figure 6.6) but show no chemical evolution. So the chemical enrichment cannot solely be an evolutionary process.

Even considering all these problems, the evolutionary theory is still probably one of the strongest candidates, although current models do not predict any abundance enhancements until a later evolutionary stage than that which is observed (see section 6.1). These results are constantly being revised, however, and recent calculations, including rotation (which we know to be very important in O and B stars), clearly show a much earlier mixing than previous models (cf. Meynet, 1998). It is also clear that there are other factors that might influence the stars' surface abundaces. There is some evidence to suggest that the anomalies reflect the natal abundances. All three Orion Belt stars (of which only two are analysed here) were found by Walborn to be nitrogen deficient, and we also find that both stars have relatively low (ie. solar) helium abundances. Interestingly enough, these two stars, and HD 16429, seem to form a little subgroup of evolved stars with near-zero mass discrepancy (see section 6.2).

A number (possibly all) of the OBN stars are also binaries, and it is possible that, at least for some objects, the nature of the anomalies could be caused by the binary nature of these stars. Mass transfer, either active or past, by an evolved companion has been suggested as a method of bringing CNO processed material onto the surface of the stars. Of the two ON main-sequence stars in our sample, both have been proposed as binaries by Bolton and Rogers (1978). They also derived orbital elements for HD 12323, but could only say that the line profiles for HD 201345 varied in a way as to suggest that it might be a binary. This star was later regarded as single by Gies and Bolton (1986). Of the other ON stars in our sample, Bolton and Rogers found variability in the spectrum of HD 191781, but they did not have enough data to confirm that it is a binary. Finally, BD+36 4063 has been confirmed as a single-lined spectroscopic binary by I. D. Howarth (private communication).

6.3.1 Carbon and nitrogen line strengths

As we lack good model predictions for the strengths of carbon and nitrogen lines, we cannot directly determine abundances for these elements in our data. We can, however, try to identify anomalous objects by looking at the ratio of equivalents widths for these two elements. There is a lack of strong, unblended carbon and nitrogen lines, and the only two unblended candidates are N II λ4630Å and C II λ4267Å. These lines are very weak and difficult to measure, so we can expect large errors on these measurements. The equivalent widths were measured at least 4 times using the data analysis package DIPSO (Howarth et al., 1997a), and the results are shown in table 6.3.1. The uncertainties quoted are based on the standard deviation of repeated measurements of the equivalent widths.

Since we do not know the expected behaviour of this ratio, we have plotted the N/C line ratio as functions of both $T_{\rm eff}$ and $\log_{10} g$ in figure 6.11. What we can clearly see from these figures are that the ON stars all have far larger N/C line ratios than the other stars. There also appears to be a subgroup of slightly higher (≈ 5) ratios, but by comparing with figure 6.12 it appears that this might be a luminosity effect. Most of these stars seem to be at the low-$\log_{10} g$ end of the distribution for their temperature. The only exception to this is possibly HD 10125 at 32.5 kK, although these data have to be taken as they were intended; simply as an illustration of the OBN/OBC anomaly.

Table 6.4: C & N equivalent widths

HD/BD	N II λ4630Å EW (mÅ)	C II λ4267Å EW (mÅ)	N II / C II ratio
BD +36 4063	133.5 ± 2.4	4.4 ± 2.2	30.1 ± 14.9
HD 10125	159.4 ± 9.8	25.8 ± 3.9	6.2 ± 1.0
HD 12323	88.6 ± 4.7	6.0 ± 2.1	14.7 ± 5.3
HD 13745	166.0 ± 7.0	53.6 ± 2.7	3.1 ± 0.2
HD 16429	102.6 ± 15.3	21.0 ± 4.2	4.9 ± 1.2
HD 30614	91.7 ± 6.2	37.8 ± 3.3	2.4 ± 0.3
HD 34078	105.8 ± 1.3	65.2 ± 0.8	1.6 ± 0.0
HD 36486	95.2 ± 13.1	35.5 ± 4.5	2.7 ± 0.5
HD 37742	97.4 ± 5.6	44.2 ± 5.4	2.2 ± 0.3
HD 188209	123.5 ± 4.0	39.0 ± 3.5	3.2 ± 0.3
HD 189957	137.7 ± 8.8	73.2 ± 3.0	1.9 ± 0.1
HD 191781	211.2 ± 9.1	9.5 ± 6.1	22.3 ± 14.5
HD 194280	176.2 ± 6.5	81.2 ± 10.7	2.2 ± 0.3
HD 195592	198.0 ± 7.0	18.8 ± 2.6	10.5 ± 1.5
HD 201345	103.8 ± 2.7	6.1 ± 2.2	16.9 ± 6.2
HD 202124	74.8 ± 8.1	13.7 ± 2.9	5.5 ± 1.3
HD 207198	55.8 ± 4.6	32.0 ± 5.9	1.7 ± 0.4
HD 209975	91.0 ± 7.3	42.2 ± 4.3	2.2 ± 0.3
HD 210809	73.2 ± 3.8	8.7 ± 2.7	8.4 ± 2.6
HD 214680	66.2 ± 1.6	38.5 ± 2.4	1.7 ± 0.1
HD 218195	47.0 ± 3.6	31.3 ± 3.0	1.5 ± 0.2
HD 218915	114.8 ± 2.5	20.6 ± 4.7	5.6 ± 1.3
HD 225160	11.5 ± 3.1	6.7 ± 3.1	1.7 ± 0.9

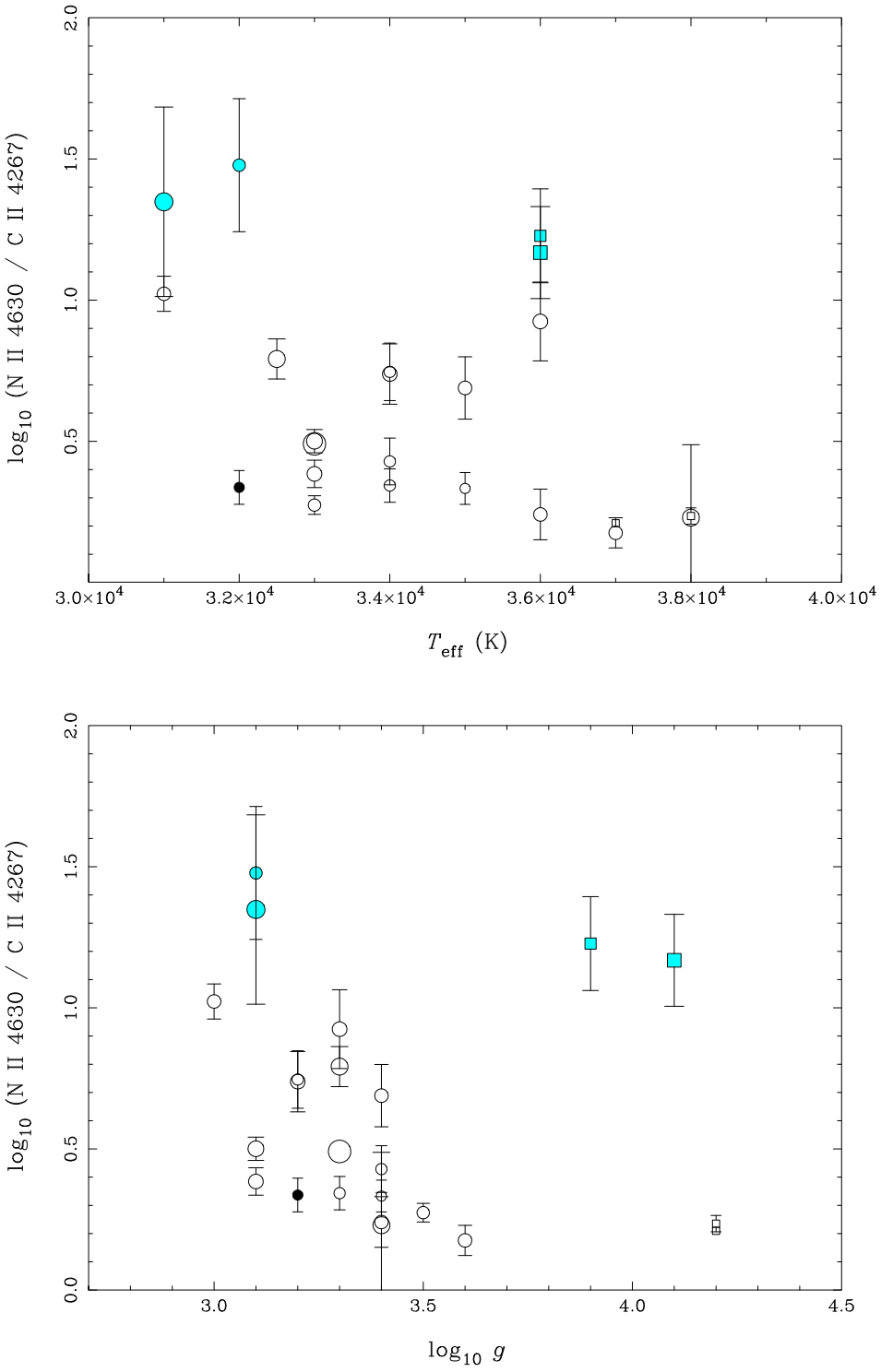

Figure 6.11: *N*II *λ4630Å / C*II *λ4267Å against* $T_{\rm eff}$ ***(top)*** *and* $\log_{10} g$ ***(bottom)***

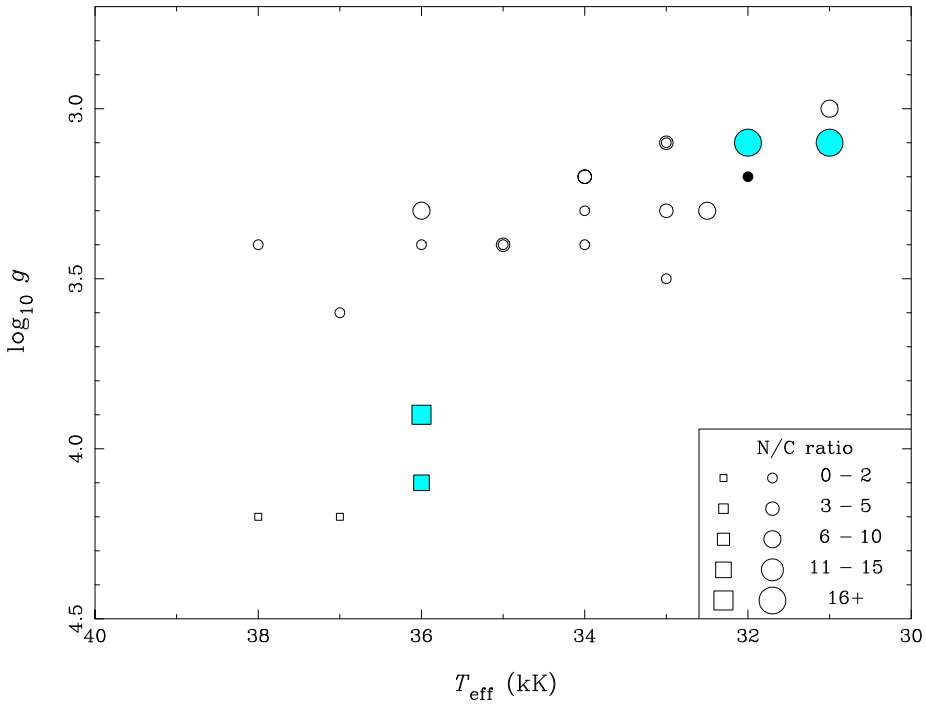

Figure 6.12: *Dependence of* N II *λ4630Å / C* II *λ4267Å ratio on stellar parameters* $T_{\rm eff}$ *and* $\log_{10} g$. *Symbols are scaled to represent the line-strength ratio as shown in lower right-hand corner. The N to C ratio seems to be higher at the low-*$\log_{10} g$ *end of the distribution for each temperature (except in the case of the ON stars).*

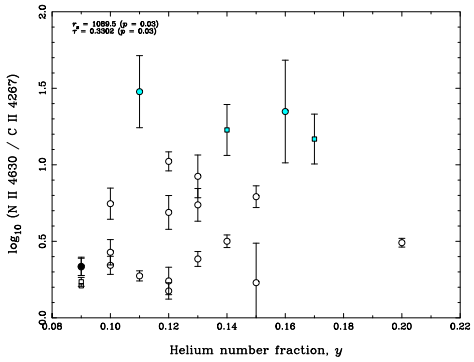

Figure 6.13: *N*II *λ4630Å / C*II *λ4267Å against y*

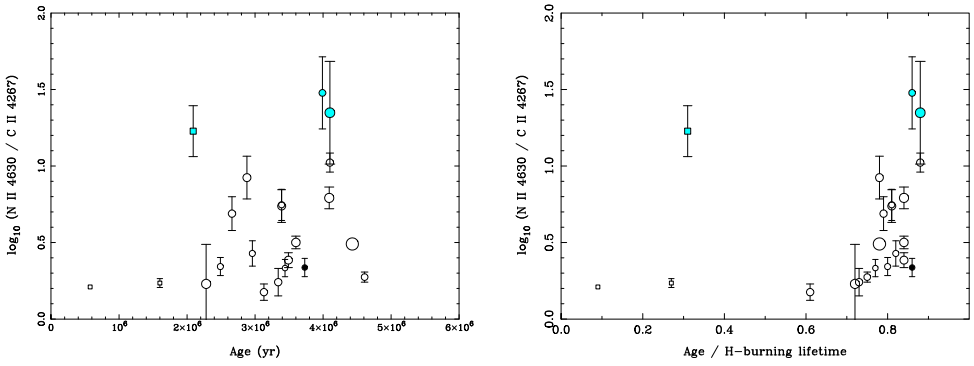

Figure 6.14: *N*II *λ4630Å / C* II *λ4267Å against evolutionary age*

Chapter 7

A survey of rotational velocities

There is a small mystery about the rotational properties of early-type stars. The apparent deficit of narrow-lined O stars suggests that some type of 'turbulence' might be contributing to the overall line broadening (e.g. Conti and Ebbets, 1977). The exact nature of this turbulence is unknown, although it appears that it is more important in evolved stars (Penny, 1996; Howarth et al., 1997b and chapters 4 to 6 in this thesis).

Recent evolutionary models show that rotation is important not only for the stars' physical properties, in terms of temperature and luminosity, but also for the surface element abundances (Langer and Heger, 1998; Maeder, 1998; Meynet, 1998). This could help solve many discrepancies between observations and evolutionary models (e.g. the *mass discrepancy* discussed in section 6.2) and the chemical anomalies seen in the OBC/OBN stars (section 6.3). A better understanding of the rotational properties of early-type stars would indicate if rotation is important in the evolution of most OB-stars.

Rotation has also been connected with several types of variability in early-type stars. Rapidly rotating OB stars appear to be particularly prone to absorption-line variability (Fullerton et al., 1996) and rotation is expected to be related to the emission mechanism in Be stars (see section 1.2.4).

A cross-correlation analysis of line widths in O and supergiant B stars was performed by Howarth et al. (1997b). The cross-correlation routines developed for that project have since been automated to the point where large scale surveys are possible. To test the routines, and expand the sample from Howarth et al., we measured a large sample of B stars of all luminosity classes.

7.1 The sample

To obtain an unbiased sample of stars, all the B stars from the Bright Star Catalogue (Hoffleit and Warren Jr., 1991) were cross-checked with the IUE observing logs. Usually, the newest observations of a given star were used, unless these were noted to be of poor quality or to have a low number of peak counts. Because we initially did not have access to the complete IUE logs, some stars were observed more recently than we were first aware of. In these cases, we have also tried to include analyses of the new observations. Also, when the quality of the observations was questionable, several spectra were analysed. Some stars from Howarth et al. (1997b) were included to test the accuracy of the automatic measurements.

Little or no care was taken to exclude peculiar or non-related objects (e.g. mis-identified stars in the observing logs or stars with erroneous spectral types in the Bright Star Catalogue) from the analysis. We expect some of these objects to reveal themselves subsequently by failing to give a strong cross-correlation peak with the template stars used.

Since Bright Star Catalogue (hereafter BSC) spectral types are sometimes inaccurate and are usually of uncertain provenance, better documented spectral types were adopted from the references listed in appendix D. The data were reduced as explained in chapter 2, using essentially the same routines as those described in Howarth and Prinja (1989).

7.2 Cross-correlation analysis

The analyses were performed by using a C-shell wrapper for DIPSO. The wrapper script would launch DIPSO, select an appropriate template and mask (see below), perform the cross-correlation, gaussian fitting, and then extract the fit-data and the cross-correlation functions (CCFs) for future reference. All the information was stored in a machine readable format[1] to simplify the statistical analysis.

The cross-correlation was performed by first masking out P Cygni profiles, very strong photospheric lines (dependent on spectral type), and interstellar lines in the target and template spectra. The very strong photospheric lines will dominate the cross-correlation

[1] The cross-correlation script would itself create another script for each star with the analysis results in it. Thus all that is required to access the data is to 'source' this data-script. A relatively slow and arguably inefficient, but very flexible and easy to use, way of storing data.

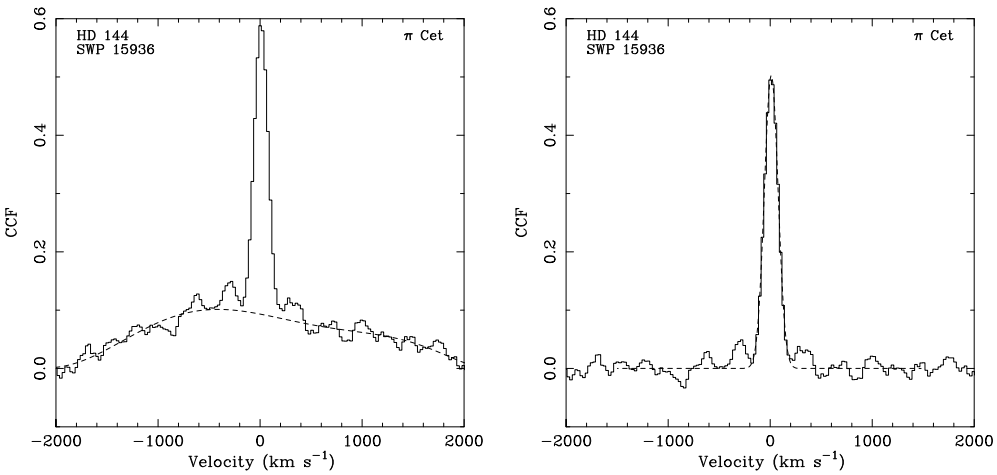

Figure 7.1: *Figure shows a typical CCF (HD 144 cross-correlated against π Cet) and the fits. Left panel shows polynomial fitting to low-level background correlations, and right panel shows the gaussian fit used to find values of full-width half-maximum (FWHM).*

function and may be significantly Stark broadened in addition to being rotationally broadened; any irregular effects in these lines will dilute the influence of the many weaker lines. More reliable results are obtained by masking out these lines.

Next, the spectra were normalised to a zero-level continuum by dividing by polynomial fits and subtracting unity. The masked out regions were then filled with zeros to make sure they would not give false correlations, and finally the spectra were cross-correlated.

The cross-correlation functions (CCFs) could then be measured. This is slightly complicated by random correlations (which will always occur) giving 'background noise'. This causes the CCF peak to sit on top of a 'shoulder' caused by these random correlations (which are dependent on the template used). To simplify the measurements of the CCFs this shoulder was removed by fitting a polynomial to the CCF (see figure 7.1)[2] in the regions with a velocity-shift of more than ± 500 km s^{-1}. This 'flattens' most of the CCF caused by random correlations but still leaves the peak. The cross-correlation functions were then fitted with gaussians (by the DIPSO subroutine ELF) using a least-squares fitting method in order to obtain the widths and strengths (the latter represented by the peak intensity and integrated area of the CCF).

[2]Including the cross-correlation functions for all the analysed stars would unfortunately take up far too much space to be included in the printed version of this thesis, but they are available in HTML format on the attached CD-ROM (see appendix E).

Table 7.1: Template Stars

Name	HD	Spectral Type	$v_e \sin i$ (km s^{-1})
τ Sco	149438	B0.2 IV [1]	< 10 [3]; 13 [4]
ι Her	160762	B3 IV [2]	17 [4]
π Cet	17081	B7 V [2]	18 [4]
α Lyr	172167	A0 V [3]	23 [3]

REFERENCES: *(1) – Walborn (1971b); (2) – Lesh (1968); (3) – Hauck and Slettebak (1989); (4) – Day and Warner (1975)*

Every star was cross-correlated against four different template spectra, as listed in table 7.2, to ensure that at least one strong CCF was obtained across the entire spectral range investigated. Although it is more customary to use the area to represent the strength of a CCF, the CCF with the strongest peak intensity was picked as the one best representing the star. Since all the template stars are narrow-lined, there should be very small width variations when a single star is cross-correlated against the four templates. However, the polynomial flattening of the CCF discussed above is not perfect, and can sometimes leave a significant bump around the base of the CCF peak. This bump can 'fool' the gaussian fitting routines into using a much broader function. This will increase the area of the function but leave the peak intensity relatively unchanged.

In this preliminary, automated run of the routines, no other quality control was performed (apart from visual inspection to check for obvious binaries). However work is underway to develop automatic detection of possible double lined spectroscopic binaries, and a measure of the 'goodness-of-fit' of the gaussians.

7.3 Calibration

This chapter is titled a survey of rotational velocities; however, what we measure is the line width and not the rotational velocity. This chapter is based on the assumption that these two parameters are the same, although as seen in Penny (1996), Howarth et al. (1997b) and also chapters 4–6 in this thesis, this assumption is probably not correct. There is now extensive evidence to suggest that rotation is not the only process contributing to absorption-line broadening in early type stars. We will, however, still work on the

assumption that the quantity $v_e \sin i$ is closely related to the true projected equatorial rotation velocity.

The usual way of determining rotational velocities (e.g. Slettebak et al., 1975 and Conti and Ebbets, 1977) is by comparing observations with rotationally broadened synthetic spectra. Unfortunately models are not yet up to accurately reproducing the line-blanketed UV spectra of hot stars, and we need a different approach of constructing a FWHM to $v_e \sin i$ calibration. As shown in Howarth et al. (1997b), reliable calibrations can be found by creating artificially 'spun up' versions of the template spectra (created by convolving the template spectra with the rotational broadening function given by Gray, 1992) and measuring these in the same way as for the sample stars. These calibrations are shown in figures 7.2 and 7.3 together with a comparisons of CCF peak widths (FWHM) and velocities measured using different templates.

There appear to be some systematic differences between measured widths (and derived velocities) found using different templates. This is almost certainly caused by the CCF background correlations discussed in section 7.2. Although the actual width of the CCF peak should not change, the gaussian fits might be slightly different. Since the background correlations are dependent on the spectral type of the template used (and also on the spectral type of the target star, but since we only usually consider stars that are within a couple of subtypes of the template it is relatively unaffected by the target star) the effect is fairly systematic and can be corrected for.

We thus want to 'force' all the templates to follow the same velocity scale. One way to do this would be to quantify the differences in measured widths found by using the different templates. However, since the background CCF 'shoulder' also appears to be a function of velocity (as can be seen by the variations in FWHM–$v_e \sin i$ calibrations for the different templates), the correction would also have to be a function of velocity.

It appears, though, that after applying the "raw" velocity calibrations (which remove the principal dependence on velocity) the problem reduces to an approximately linear relation. We fit (by least-squares) straight lines of the form $y = bx$ to the plots as shown in figure 7.3. This gives us (from the gradients) the typical ratios between measured velocities found from the different templates. If we assume that the smallest and largest velocities are off by approximately the same factors we can adopt the 'best' velocity as

Table 7.2: Velocity corrections

$v_{\rm best} = 1.094 \times v_\tau$
$v_{\rm best} = 0.871 \times v_\iota$
$v_{\rm best} = 0.954 \times v_\pi$
$v_{\rm best} = 1.100 \times v_\alpha$

the geometric mean of the 'typical' velocities:

$$v_{\rm best} = \sqrt[4]{v_\tau \times v_\iota \times v_\pi \times v_\alpha}$$

where v_τ, v_ι, v_π, v_α are the velocities found by using the τ Sco, ι Her, π Cet and α Lyr templates respectively. For any given star, we only need to have measured one of these velocities, which can then be corrected to the common scale. Table 7.2 lists the velocity corrections applied to bring the velocities to the common scale, and figure 7.4 shows the plots of measured velocities after applying the velocity corrections and the 'corrected' FWHM–$v_e \sin i$ calibrations.

So, just to summarise briefly, the steps involved in finding the adopted velocities are:

- Convert FWHM to $v_e \sin i$ using 'theoretical' calibration for each template
- Find template-to-template differences
- Apply linear correction

If more than one spectrum for any given star is measured, we adopt the median of the corrected velocities for each spectrum.

7.4 Comparison with previous work

Using the FWHM – $v_e \sin i$ calibrations discussed above we can now derive values of $v_e \sin i$ for each star. The corrected velocities for each star and template are listed in appendix D. The table there also lists the adopted velocity, which is the velocity obtained from the 'strongest' cross-correlation function. Where more than one spectrum for a given star has been analysed, the adopted velocity is the mean of the velocities from the strongest CCFs.

Since our approach is fully automatic, and because the decision of what is the "best" $v_e \sin i$ was ad hoc, it is important to compare it to previous measurements to see if there

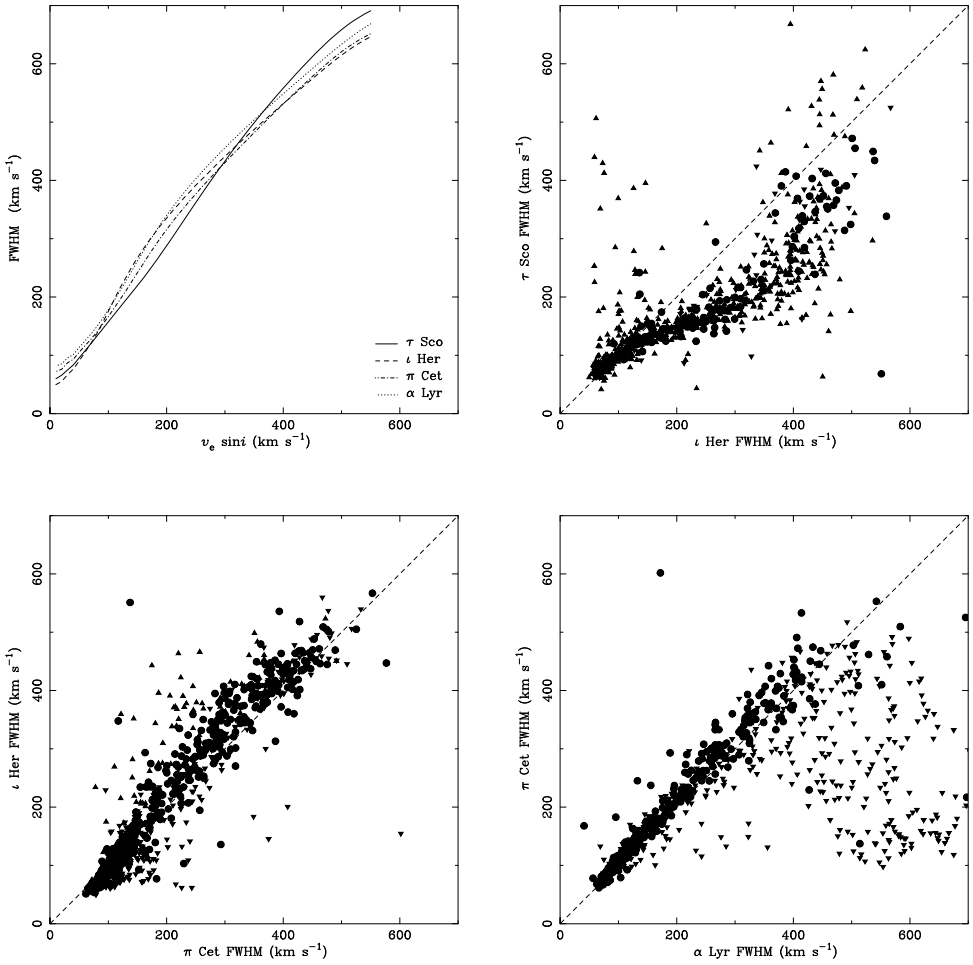

Figure 7.2: *The top left-hand panel shows calibrations between the linewidth parameter* $v_e \sin i$ *and the width of the CCFs for the different template spectra. The other panels compare full-width half-maxima measured for each star using the different templates. The different symbols represents the ratio of CCF strengths (the strengths of the abscissa star CCF divided by the ordinate star CFF). A ratio close to one is indicated by circles, whereas ratios larger than* $\frac{3}{2}$ *is shown as triangles pointing upwards, and ratios less than* $\frac{2}{3}$ *by triangles pointing downwards.*

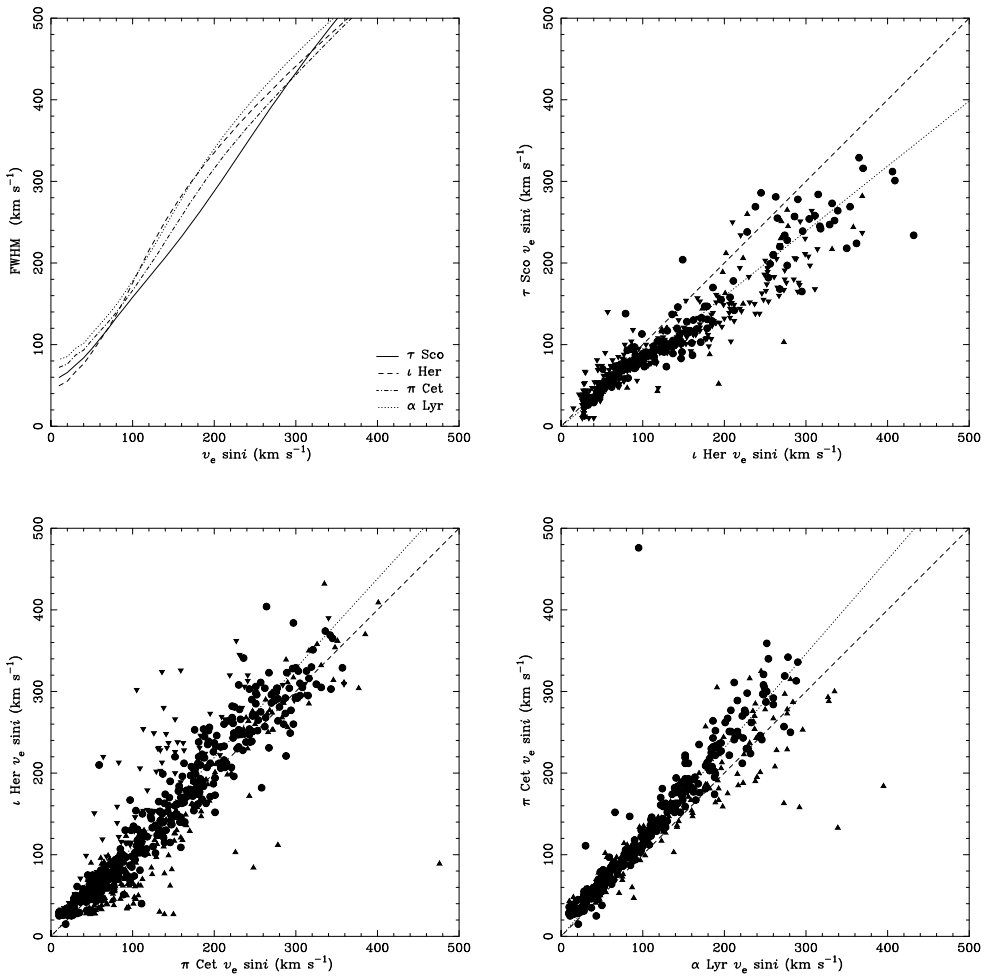

Figure 7.3: *Comparisons of cross-correlation width measurements after applying velocity calibrations (shown in upper left-hand corner; same as in previous figure but shown on a different scale). Also shown are straight-line fits discussed in text (dotted lines). This diagram shows fewer stars than in the previous figure, since some have been filtered out by the velocity calibrations if the CCF peak intensity is too low.*

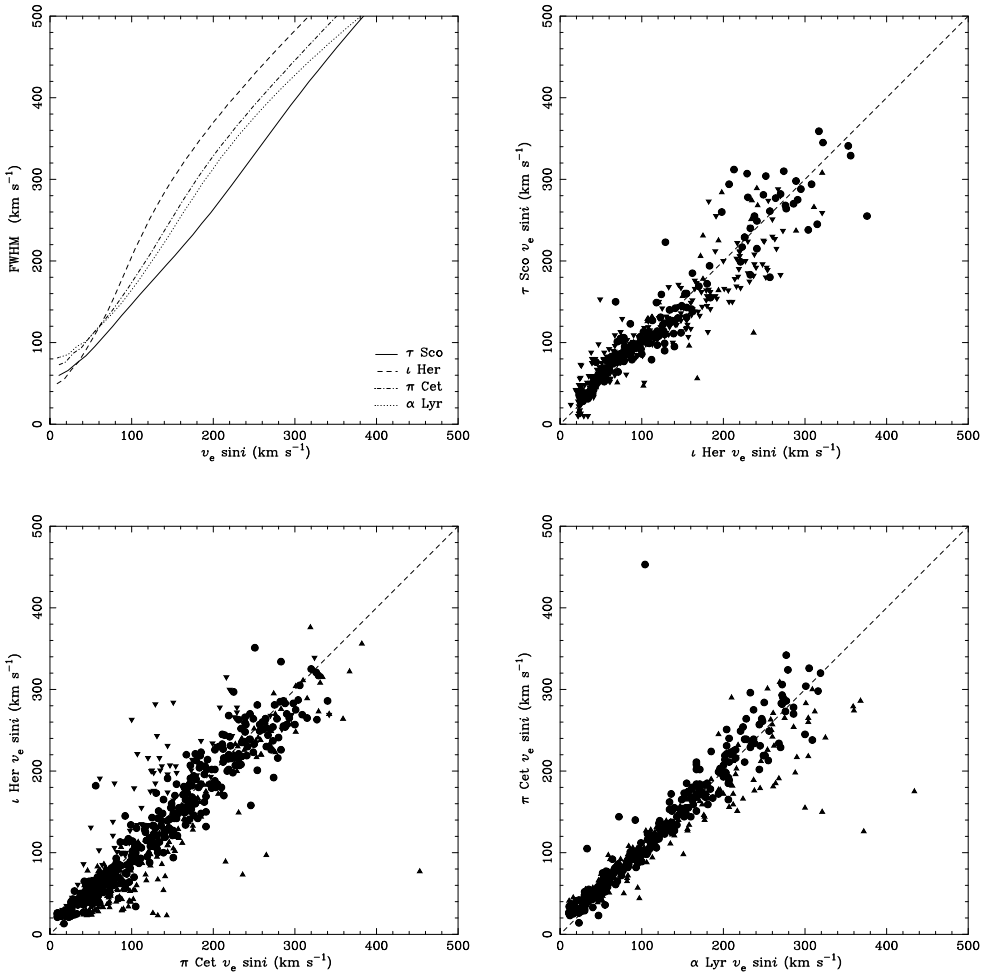

Figure 7.4: *Velocity comparisons after applying linear velocity corrections. Symbols are the same as in the previous figures. Velocity calibrations are also shown with 'corrected' velocities.*

are any systematic differences. Figure 7.5 shows the values derived in this thesis compared to those published in Howarth et al. (1997b) (these values are also presented in table 7.6). Indeed there does appear to be some systematic differences. Plotting the ratio of the MNRAS results to the new values (lower panel) it appears that the the current τ Sco velocities come out slightly higher than before, and the ι Her results are lower. This is exactly what is expected taking into consideration the new velocity corrections applied to each template's measured velocities. Also shown on the figure are the velocities for τ Sco and ι Her, and it appears that the measured velocities scatter evenly around these lines, with a couple of exceptions.

The most notable of these exceptions is HD 75759. Looking at the CCF for this star, it appears to have a double peak (see figure 7.6). This star is listed as a double-lined spectroscopic binary in Mason et al. (1998). In the case of the other discrepant star, HD 219188, it is not so clear why the results are in disagreement. The CCF for this star is single-peaked, although it appears to be weak and slightly irregular in shape (figure 7.7). The spectrum appears very noisy, and it could be the case of a low S/N exposure or problems during data reduction.

The comparison above only covers the early-type B supergiants (and a couple of O stars) since these were the only stars covered in Howarth et al. To investigate the full range of spectral types covered, we compare with the list of standard velocity stars by Slettebak et al. (figure 7.8). Here the velocities are in good agreement. The rms dispersion about the mean offset is only 11.3 km s^{-1}(9 per cent of the cross-correlation velocities).These values exclude the only star for which the velocity estimates are in clear disagreement. Slettebak et al. found a velocity of 400 kms for HD 142983 (48 Lib), whereas the cross-correlation analysis suggests a relatively narrow-lined star with a velocity of only about 40 km s^{-1} (see figure 7.9). 48 Lib is a well known shell star (e.g. Underhill, 1953) and the narrow cross-correlation function is probably from correlations with the narrow shell absorption lines present in the UV spectrum of this star (e.g. Ringuelet et al., 1981) rather than from photospheric lines.

7.5 Discussion

Figure 7.10 show velocity distributions for the B stars. It is fairly clear from the diagrams that there are very different distributions of velocities for main-sequence stars (luminosity

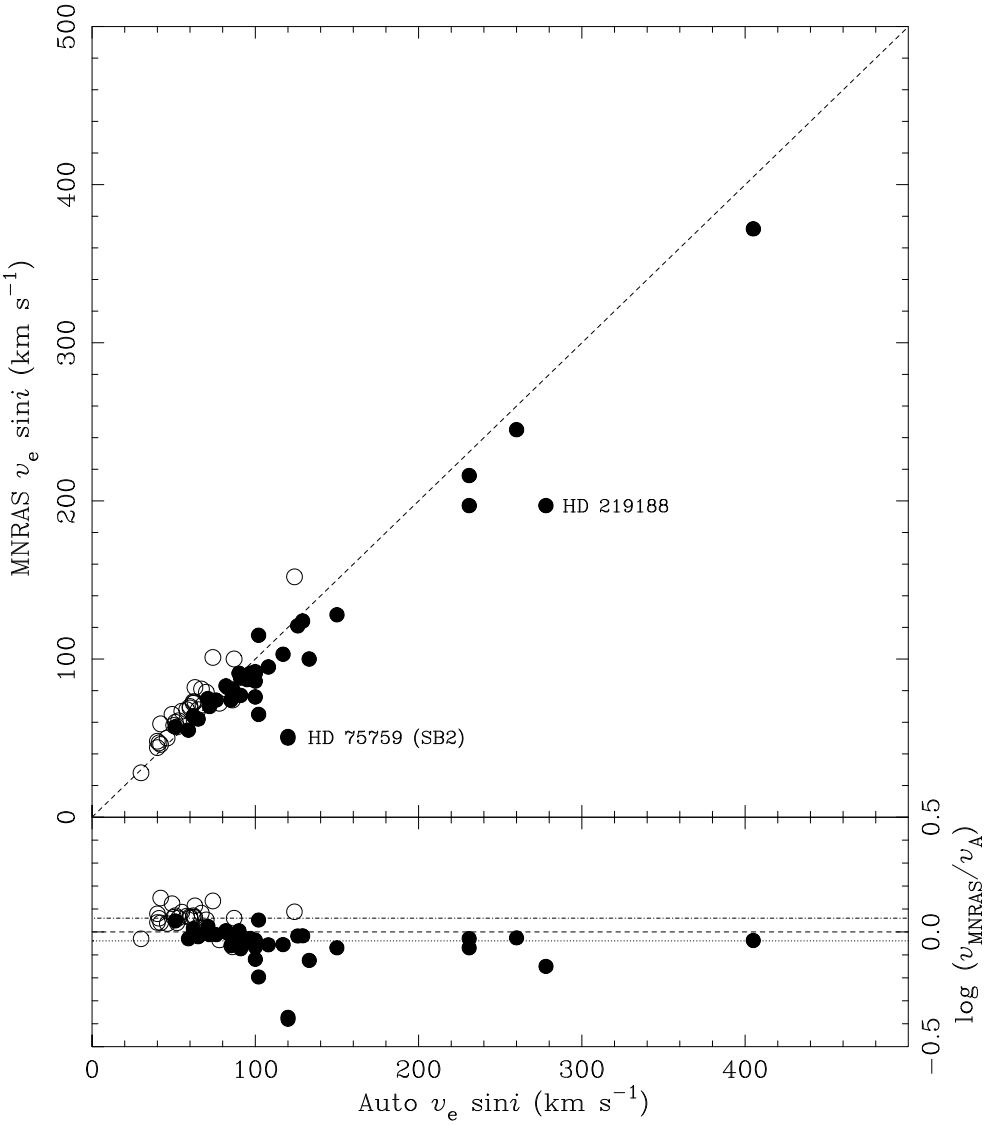

Figure 7.5: *Comparison of $v_e \sin i$ from Howarth et al. (MNRAS) and this work using the automatic routines discussed in the text (Auto). Filled circles are cross-correlated using τSco as the template, open circles using ιHer. The dotted and dashed-dotted lines are the velocity corrections applied to the τ Sco and ι Her velocities respectively.*

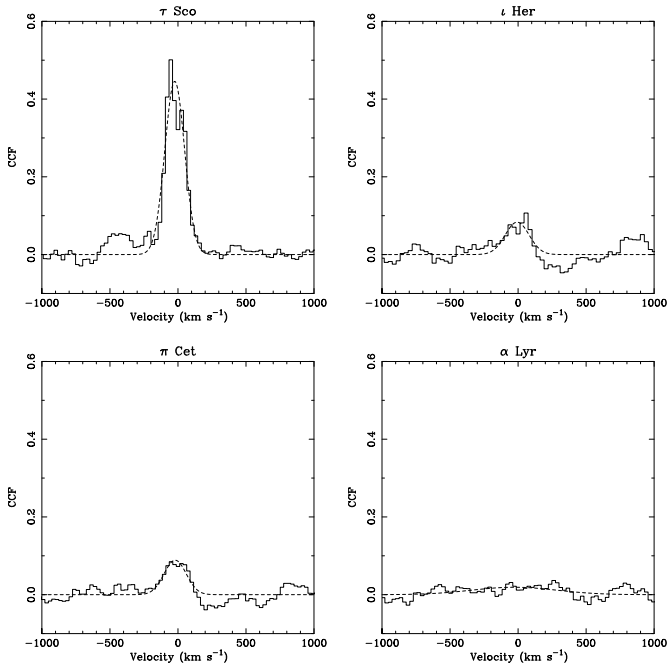

Figure 7.6: *The cross-correlation function (CCF) of HD 75759. This is a double-lined spectroscopic binary, and the CCF appears to have two peaks separated by about 100 km s^{-1}.*

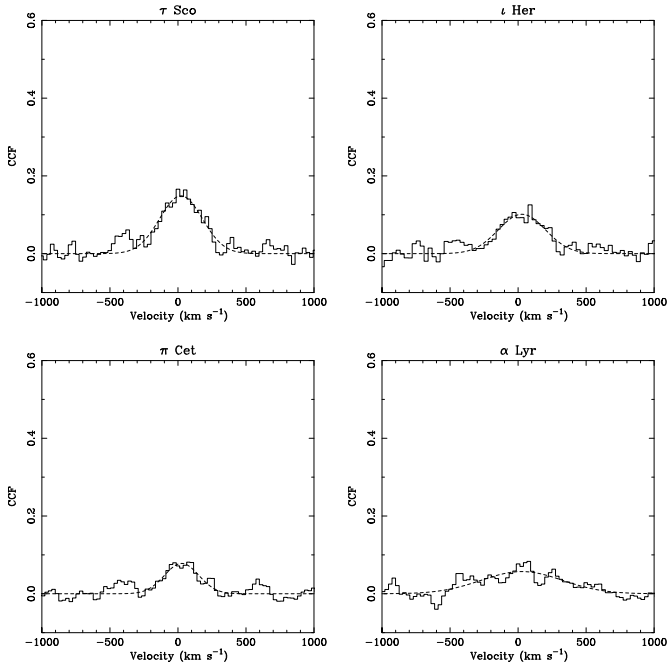

Figure 7.7: *The cross-correlation function of HD 219188.*

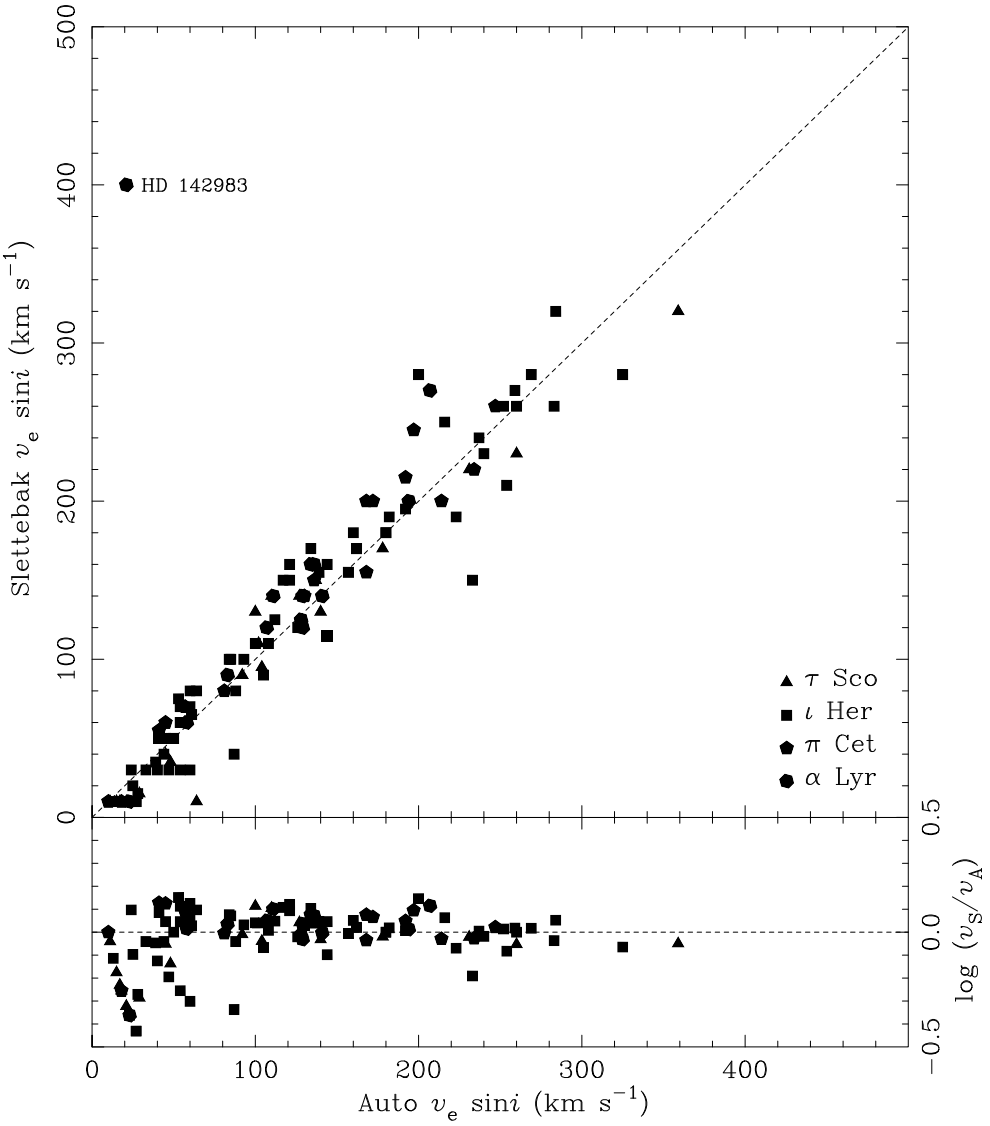

Figure 7.8: *Comparison of $v_e \sin i$ from Slettebak et al. (1975) and this work using the automatic routines discussed in the text (Auto). The template used is indicated by the different symbols (see key).*

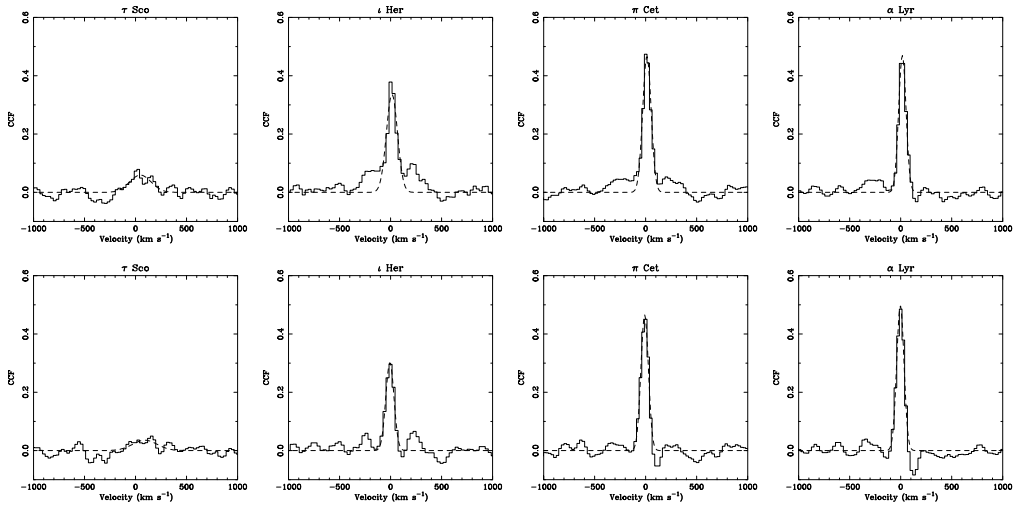

Figure 7.9: *The cross-correlation functions of HD 142983. Two spectra were examined: SWP 8810 (top) and SWP 54091 (bottom).*

classes IV and V) and supergiants (I and II), and also that there appears to be some difference between the early-type supergiants and late-type supergiants. The lower panel in this figure shows the velocity distributions for the stars grouped by their BSC catalogue spectral types, while the stars in the top panel have spectral types from the references listed in appendix D (most of these stars also have BSC spectral types).

7.5.1 Supergiant velocity distributions

Comparing the cumulative distributions with those in Howarth et al., it appears there is a sequence of increasing $v_e \sin i$ with spectral type for the supergiants. In fact, extending table 4 from Howarth et al. (table 7.3) we see the median velocities for each spectral subtype slowly increase from about 40 km s^{-1} at B9.5 to approximately 90 km s^{-1} at B0 and further to more than 100 km s^{-1} for the early O-stars. Similarly the lowest $v_e \sin i$ in each group also seems to increase uniformly with spectral type. The only exceptions to this are HD 202124 (B0 II) with a $v_e \sin i$ = 38 km s^{-1}and HD 44743 (B1 II-III; $v_e \sin i$ = 38 km s^{-1}). The second slowest rotators in the same group as each of these stars have rotational velocities of 72 and 55 km s^{-1}respectively. This is in good agreement with Conti and Ebbets (1977) who suggest that the observed line broadening in O stars is caused both by rotation and by some other broadening factor (some sort of 'turbulence') which might contribute to the broadening with about 50 km s^{-1} for a late O-star and even more for earlier types. It appears that this effect is less important for the B stars, and

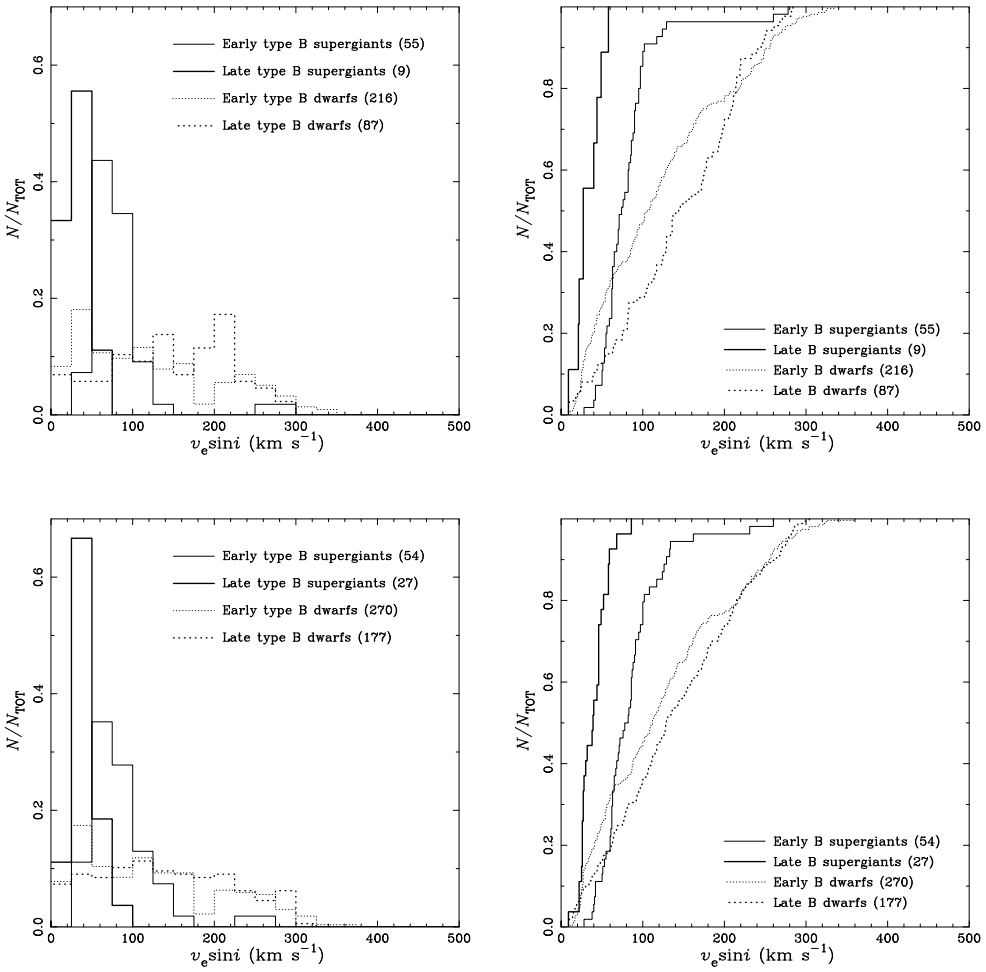

Figure 7.10: *Velocity distributions (binned and cumulative) showing the distributions for early (earlier than B5) types and late (later than B5 inclusive) with spectral types from individually referenced sources (**top** panels) and from the Bright Star Catalogue (**bottom** panels).*

trails off towards the late-Bs.

7.5.2 Kolmogorov-Smirnoff test

The Kolmogorov-Smirnoff (or K-S) test allows us to compare two data sets and find the statistical probability that they are drawn from the same distribution. The test works by finding the maximum distance between two cumulative probability distributions (like our velocity distributions):

$$D = \max_{-\infty<x<\infty} |S_{N_1}(x) - S_{N_2}(x)|$$

where $S_{N_1}(x)$ and $S_{N_2}(x)$ are the respective cumulative distribution functions to be compared. See Numerical Recipes (Press et al., 1992) for a more general discussion about the K-S test and how to find the probability P that the two data sets are drawn from the same distribution.

We can use the K-S test, first to check if our two sources of spectral types can be used to split the complete sample into subgroups which are in good agreement. Table 7.4 compare samples of stars, grouped by their individually references spectral types, or the BSC spectral types (figure 7.10). Although there are differences between the two samples, each of the subgroups[3] does appear to be drawn from the same distributions.

Next we want to see how the subgroups compare with each other (table 7.5). The only groups that appear to be at all similar are the early and late type main-sequence stars (although at a very low probability; but see section 7.5.3). The two supergiant groups vary significantly in their distributions, and it is unlikely that these are part of a common distribution of rotational velocities.

7.5.3 Main-sequence velocity distributions and Be stars

The main-sequence distributions (figures 7.10 and 7.11) show a much larger spread in velocities than the supergiants. The distribution for all luminosity class IV and V objects, including Be stars (figure 7.10) shows an almost linear cumulative distribution, meaning there is an almost identical number of stars at all velocities up to a maximum of just above 300 km s^{-1}. However, plotting the Be stars separately (figure 7.11), there appears

[3] The stellar sample was divided into early-type (earlier than B5) and late-type (later than B5 inclusive) stars. These were then divided into supergiants (SG; luminosity classes I and II) and main-sequence (MS; luminosity classes III–V) stars.

Table 7.3: Supergiant $v_e \sin i$ distribution

	MNRAS			MNRAS corrected		Auto		
Spectral Type	N	Median	Range	Median	Range	N	Median	Range
		(km s^{-1})					(km s^{-1})	
O3-6.5	8	127	71–219	138	77–239			
O7-8.5	8	100	77–176	109	84–192			
O9	6	97	78–117	106	85–127			
O9.5	7	95	78–129	103	85–141			
O9.7	12	88	68–169	96	74–184			
B0	12	89	68–180	97	74–196	8	96	38–133
B0.5	17	83	70–216	90	76–236	9	100	72–231
B0.7*	6	80	64–132	87	70–144			
B1	26	82	54–245	89	59–268	16	85	28–260
B1.5	6	75	68–81	82	74–88	3	67	60–70
B2	10	74	60–100	80	65–109	8	62	40–134
B2.5	4	70	61–73	76	66–79	2	65	62–68
B3	9	68	46–81	74	50–88	7	53	42–162
B4						1	60	60–60
B5	6	47	28–57	51	30–62	8	45	22–58
B6						2	36	26–46
B7						1	46	46–46
B8						11	38	9–86
B9						5	27	22–59

NOTES: * – *The Bright Star Catalogue does not use the B0.7 subtype.*

Columns 2–4 list the results from Howarth et al. (1997b), and columns 5 and 6 show these values 'corrected' using the τ Sco correction discussed in the text. Columns 7–9 show the results from this work.

Table 7.4: K-S test of velocity distributions using different spectral type sources

Type		$N_{\rm ind}$	$N_{\rm BSC}$	D	P
SG	early	55	54	0.11	0.85
SG	late	9	27	0.26	0.69
MS	early	216	270	0.03	1.00
MS	late	87	177	0.09	0.65

NOTES: *Group one (ind) contains the stars with individual spectral types from reliable references, and group two (BSC) are the stars with BSC spectral types. D is the K-S statistic, and P is the significance level. There are no large differences between the two groups.*

Table 7.5: K-S test highlighting differences between different groups

Individual referenced spectral types

	SG early	SG late	MS early	MS late
SG early		$D = 0.8162$	$D = 0.4276$	$D = 0.6102$
SG late	$P = 0.0000$		$D = 0.6898$	$D = 0.8506$
MS early	$P = 0.0000$	$P = 0.0002$		$D = 0.2040$
MS late	$P = 0.0000$	$P = 0.0000$	$P = 0.0096$	

BSC spectral types

	SG early	SG late	MS early	MS late
SG early		$D = 0.7407$	$D = 0.3593$	$D = 0.4476$
SG late	$P = 0.0000$		$D = 0.6185$	$D = 0.7395$
MS early	$P = 0.0000$	$P = 0.0000$		$D = 0.1338$
MS late	$P = 0.0000$	$P = 0.0000$	$P = 0.0394$	

NOTES: *This table summarises the K-S test applied to the groups of stars shown in figure 7.10. For each comparison between two groups, both the K-S statistic D and its significance level P are shown. A value of P close to zero signifies a low probability that the two data sets are drawn from the same distribution.*

to be a significantly different distribution of velocities for the two groups, with the Be stars appearing to belong to a group with high rotational velocities, peaking at about 250 km s^{-1}. This fits in well with the theories that the emission mechanism in Be stars is somehow connected to rotation, e.g. through the formation of a 'disk'-like dense wind around the equator (see section 1.2.4).

The trend of increasing $v_e \sin i$ with spectral type, seen for the supergiants, is not evident for the main-sequence stars. Although there do appear to be some differences between the different groups (because of the larger sample of main-sequence stars, split into four groups in figure 7.11), there do not appear to be any clear trends. The group containing stars of spectral types B2–B3 appears to rotate slightly slower than the other stars, and the latest-type stars (B7–B9) appear to be rotating slightly faster. However, it is probably more likely that these represent the extremes of a random distribution of errors in the measurements. Even small errors in the measurements are quite visible when plotted as a cumulative distribution, since they tend to shift the entire distribution one way or the other. Applying the K-S test to these datasets, we get a probability of one that groups 1 and 3 (B0–B1.5 and B4–B6) are drawn from the same distribution, and a probability of 0.1 that group 1 or 3 is drawn from the same distributions as both group 2 and 4 (B2–B3 and B7–B9). This probably means that they all belong to the same distribution.

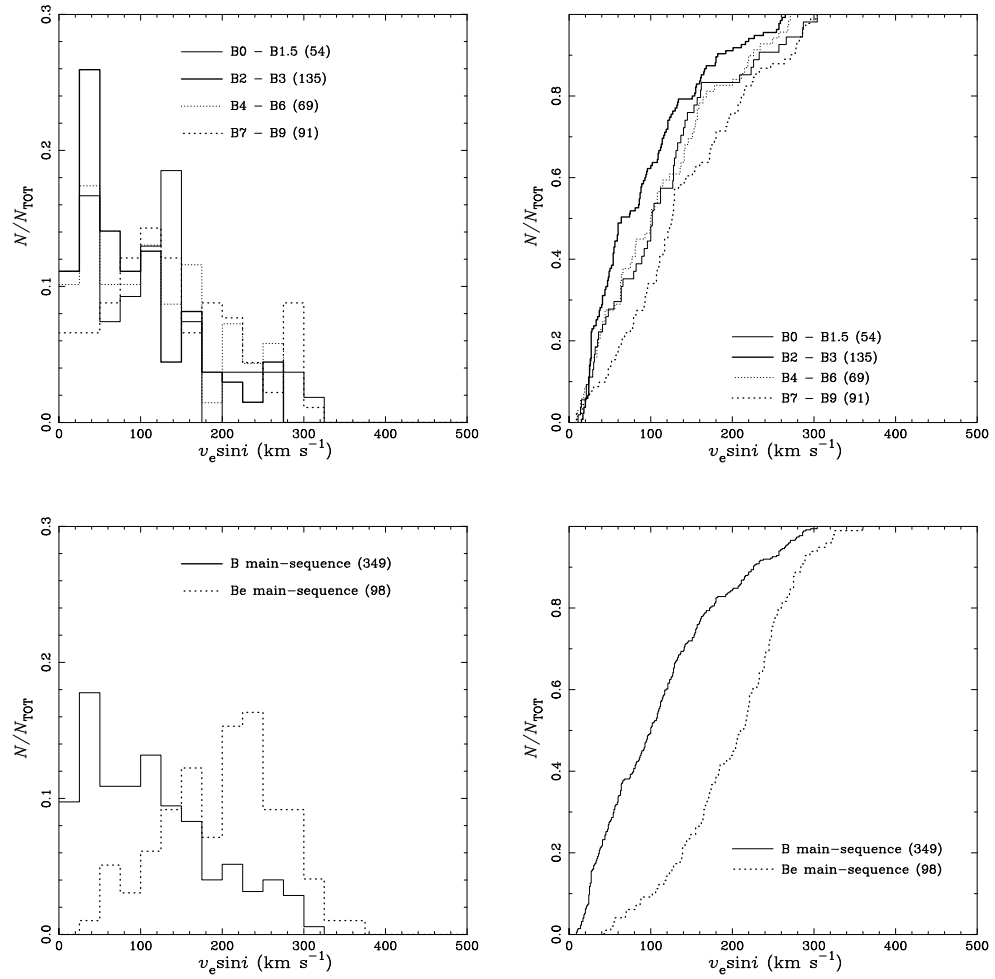

Figure 7.11: *Main-sequence and Be velocity distributions. Top figure shows velocity distributions for main-sequence (luminosity classes V and IV) B subtypes as indicated (not including Be). Lower figure compares all the 'normal' main-sequence stars to main-sequence Be stars. The Be stars clearly belong to a group that is, on average, rotating faster. Note that the figures show the normalised distributions and there that are far more stars in the group not showing emission.*

Table 7.6: Broadening parameters from Howarth et al. (1997)

Howarth et al.			$v_e \sin i$ (this thesis)					
HD	Spectral Type	$v_e \sin i$	SWP	τSco	ιHer	πCet	αLyr	Adopted
2905	BC0.7 Ia var	91	14939	**87**	91	65	...	90
			40359	**82**	95	72	...	
			54038	**80**	96	61	...	
14818	B2 Ia	82	9416	76	**73**	48	...	63
24398	B1 Ib	67	6454	59	**64**	76	...	55
24534	OBe	197	2082	**206**	223	...	...	231
			10789	**217**	332	...	...	
31327	B2 Ib	60	21280	69	**59**	52	31	51
36371	B4 Ib	65	2945	60	**57**	46	43	49
37128	B0 Ia	91	8110	**91**	108	...	...	97
			8130	**87**	106	...	...	
38771	B0.5 Ia	83	6736	**81**	97	101	...	82
			8259	**72**	90	88	...	
			30267	**74**	92	100	...	
40111	B1 Ib	124	4235	**118**	123	116	...	129
41117	B2 Ia	72	6471	74	**69**	45	...	62
			40669	69	**74**	61	...	
42087	B2.5 Ib	71	8646	70	**79**	66	...	68
43384	B3 Iab	59	4656	52	**49**	55	50	42
46485	O7 V n(e)	...	9913	**289**	...	...	...	316
47240	B1 Ib	103	4704	**117**	130	114	...	118
			48909	**99**	123	92	...	
48279	O8 V	128	11299	**138**	...	...	...	150
51309	B3 Ib	46	13937	50	**49**	42	28	42
52089	B1.5 II	48	54337	43	**47**	66	...	40
52382	B1 Ib	74	33293	**78**	90	73	...	85
53138	B3 Ia	58	30169	58	**58**	44	28	50
55879	O9.5 II-III	57	8852	**47**	81	109	...	51

continues next page ...

Table 7.6: *continued*

Howarth et al.				$v_e \sin i$ (this thesis)				
HD	Spectral Type	$v_e \sin i$	SWP	τSco	ιHer	πCet	αLyr	Adopted
58350	B5 Ia	50	7704	57	**55**	47	34	46
			30198	57	**53**	43	28	
64760	B0.5 Ib	216	53781	**212**	202	...	...	231
79186	B5 Ia	57	37499	59	**60**	48	35	52
86440	B5 Ib	28	6323	29	**35**	27	...	30
86606	B1 Ib	55	38784	**54**	55	78	...	59
91316	B1 Iab	75	4553	70	**77**	92	...	72
			8651	**71**	79	86	...	
			11312	70	**80**	84	...	
			53059	**67**	72	85	...	
106343	B1.5 Ia	81	6320	78	**78**	60	...	67
109867	B0.7 Ib	82	44494	**76**	85	85	...	83
111973	B3 Ia	68	46847	72	**67**	48	45	58
116084	B2.5 Ib	73	44795	76	**72**	49	31	62
122879	B0 Ia	92	40897	**92**	104	...	...	100
141318	B2 II	47	39022	47	**48**	57	43	41
148379	B2 Iap	70	4349	71	**69**	48	...	60
148688	B1 Ia	72	1871	97	**90**	49	...	78
149038	O9.7 Iab	86	36166	**92**	91	...	...	100
149757	O9.5 V	372	15137	**371**	...	...	...	405
150168	B1 Ia	121	47256	**116**	123	107	...	126
150898	B0.5 Ia	95	50552	**99**	87	84	...	108
152234	B0.5 Ia	76	16206	**92**	88	73	...	100
152235	B0.7 Ia	81	33294	**79**	86	67	...	86
152236	B0.5 Ia+	74	54152	113	**99**	70	...	86
154090	B0.7 Ia	78	14828	**81**	89	62	...	88
157038	B3 Iap	69	30759	85	**70**	47	89	60
157246	B1 Ib	245	54241	**238**	228	...	...	260

continues next page ...

Table 7.6: *continued*

	Howarth et al.		$v_e \sin i$ (this thesis)					
HD	Spectral Type	$v_e \sin i$	SWP	τSco	ιHer	πCet	αLyr	Adopted
164353	B5 Ib	44	4267	52	**47**	36	26	40
164402	B0 Ib	77	54242	**84**	103	84	...	91
164637	B0 II	64	42280	**57**	60	77	...	62
165024	B2 Ib	100	6020	89	**101**	119	...	87
165516	B0.5 Ib	70	48276	**66**	74	90	...	72
167264	O9.7 Iab	88	24190	**84**	110	...	...	91
167756	B0.5 Ia	79	30452	**79**	86	82	...	86
185859	B0.5 Ia	74	14207	**70**	73	83	...	76
190603	B1.5 Ia+	79	14942	75	**81**	86	...	70
191877	B1 Ib	152	14825	146	**143**	141	...	124
198478	B2.5 Ia	61	13907	71	**64**	49	42	53
			38688	64	**59**	41	42	
201345	ON9 V	91	15004	**92**	110	125	...	100
204172	B0 Ib	87	6481	**87**	90	91	...	95
			48946	**87**	102	88	...	
205139	B1 II	62	46540	**60**	59	78	...	65
206165	B2 Ib	73	6336	72	**73**	55	...	63
219188	B0.5 II-III (n)	197	7711	**255**	265	...	...	278
223987	B1 II-III	101	13763	96	**86**	71	...	74
225094	B3 Ia	68	9415	104	**86**	66	58	65
			18688	72	**65**	55	47	

NOTES: *Column 3 shows the results from Howarth et al. (1997b), columns 5–8 show the uncorrected measurements for each star and template, and column 9 shows the adopted velocity. This adopted velocity is the corrected velocity from the 'strongest' CCF (indicated in* ***bold****). When there several analysed spectra, the adopted velocity is taken to be the mean of the individual velocities. All velocities are in km* s^{-1}.

Chapter 8

Summary

8.1 Physical parameters of O stars

Modern computer models are probably sufficiently advanced for reliable — or, at least, consistent — surface parameters to be derived by comparing observations to models over much of the H–R diagram. In any case, the choice of stars over a very limited part of the H–R diagram allows us to derive good differential parameters for these objects. In chapters 3 and 4 we developed methods to find the 'best-fit' model spectrum from a four-dimensional grid of models. By comparing equivalent widths of helium lines (both He I and He II) and fitting the wings of hydrogen lines, fit-diagrams were constructed that gave possible values for the physical parameters of the stars. Series of such diagrams were used to constrain the solution in all four model dimensions, namely effective temperature, surface gravity, helium number fraction and microturbulence.

8.1.1 Temperatures and surface gravities

Effective temperatures and surface gravities were derived for the 23 WHT/UES O-star sample (chapter 5). Table 8.1 lists the derived temperatures and gravities for each spectral type. Comparisons with other studies using non-LTE models show good agreement, but it appears that the inclusion of microturbulence together with an objective procedure to locate the 'best' parameters, causes us to derive temperatures that are slightly higher than in other studies.

Using the derived surface parameters and observed/estimated absolute magnitudes, M_V, it is possible to calculate the stars' luminosities, masses and radii. These values have

Table 8.1: Summary of observed parameters

	I			II – III			IV – V		
Sp. type	N	$T_{\rm eff}$	$\log_{10} g$	N	$T_{\rm eff}$	$\log_{10} g$	N	$T_{\rm eff}$	$\log_{10} g$
O8	1	38.0	3.4						
O9	2	36.0	3.3	1	37.0	3.6	3	36.7	4.1
O9.5	5	33.8	3.2	3	34.0	3.4	1	37.0	4.2
O9.7	5	32.0	3.1	2	32.8	3.3			

NOTES: *The table shows the average (mean)* $T_{\rm eff}$ *and* $\log_{10} g$ *for each spectral type and luminosity class.* N *is the number of stars observed in each group. Effective temperatures are in kK.*

been compared to 'traditional' theoretical evolutionary models, and 'evolutionary masses' derived. There appears to be a discrepancy between evolutionary predictions and masses derived, except for a small subgroup of nitrogen deficient stars that all are in good agreement with theoretical models (section 6.2). Recent models (Maeder, 1998; Meynet, 1998) including the effects of stellar rotation, go some way towards resolving this 'mass discrepancy'. They predict that rotating stars will show an increase in luminosity, which would in turn reduce the masses derived using the above method. This, coupled with advances in stellar atmospheric modelling, will probably bring evolutionary and spectroscopic masses into better agreement.

8.1.2 Helium abundances and the evolutionary connection

Helium abundances have also been derived, and although it is difficult to evaluate the accuracy of the absolute values, the differential results should be accurate to about 0.02. A link between the morphologically peculiar ON/OC stars and the helium abundance was found (section 6.3), suggesting the unusual surface composition is caused by the exposure of CNO processed material on the surface of the stars. Estimates of the stellar ages from comparisons with evolutionary models suggest there could be a link between age and observed increased abundances; however the OC supergiants and ON main-sequence stars do not appear to follow such trends.

A relation was also found between the line broadening velocity ($v_e \sin i$ or macro-

turbulence) and the helium abundance (section 6.1.2). Several different theories which could explain these enhanced abundances as 'illusions' caused by blending effects or stellar asymmetries have been explored, but none was found that is able to reproduce the observed abundances. It therefore appears that rotation and surface chemistry are linked, something which is also indicated by the new evolutionary models mentioned above.

8.1.3 Microturbulence

The inclusion of microturbulence in the detailed line-formation calculations has several implications on the derived results. The strengthening of the helium lines when microturbulence is included leads to derived helium abundances that are closer to solar values. The lower helium abundances lead to slightly higher temperatures, since the increase in equivalent width predicted for the He II lines, which are the main temperature indicators, is less than that predicted for the He I lines. A lower helium abundance leads to weaker He II lines, and the model temperatures have to be increased (typically by about 1 – 2 kK) to match the observed equivalent widths (see also section 5.3).

Microturbulence is more important in some He I lines than others. This relative strengthening improves the model fits in the lines that are affected by the so-called *generalized dilution effect*, although the models, in general, still underestimate the equivalent widths of these lines.

We find high microturbulence values ($\sim$ 15 km s^{-1}) for all the stars in the sample, including the main-sequence stars (although, for the main-sequence stars, the models including microturbulence only fit marginally better than the zero microturbulence models). It is probably worth pointing out again that microturbulence has only been treated very simply in the model calculations. It is not clear exactly what *physical* processes (if any) contribute to the microturbulence and how they should be treated. The model grid has been calculated only for four values of microturbulent velocities up to 15 km s^{-1}. Although it would be possible to calculate models of higher microturbulent velocities, it would be difficult to justify this physically, since these velocities would greatly exceed the local sound speed. Also, K. C. Smith (private communication) has found that microturbulent velocities of 15 km s^{-1} largely desaturate the intrinsic line profiles, so larger velocities are unlikely to greatly affect the equivalent-widths. It is also possible that by treating the microturbulence in both statistical-equilibrium and line-formation calculations, the need for microturbulent velocities close to (or exceeding) the speed of sound could be relaxed.

8.2 Line broadening properties

8.2.1 B-star survey

An automated survey of the cross-correlation characteristics of a large sample (> 700) B-stars was undertaken (chapter 7). Line-broadening velocities were calculated and the velocity distributions of subsamples of the dataset examined. The velocity distributions for main-sequence stars and supergiants appear to differ significantly. The main-sequence stars have a broad velocity distribution, containing both the slowest and the fastest rotators of the sample. The supergiants were found to have a much smaller range of velocities, with a lack of slow rotators among the early-type stars. The minimum velocity for the supergiants appears to be a function of spectral type, increasing towards earlier types. This is consistent with the existence of macroturbulent velocity fields in early-type supergiants. These velocity fields (of unknown origin) would not show the same inclination dependence as rotational velocity ($v_e \sin i$), and would therefore be the lower limit to the velocity distributions.

8.2.2 Rotation vs. macroturbulence

As part of the spectroscopic analyses of the 23 O-stars, the model spectra were convolved with two different functions (section 4.4), one being the theoretical function for a line broadened by stellar rotation, and the other the broadening caused by a Gaussian velocity field in the stellar atmosphere (simulating macroturbulence). These convolved models were compared to the observations using a χ^2 method to estimate the goodness-of-fit. The results for the main-sequence stars were inconclusive, due to the low number of stars, but tentatively suggest that rotation is the dominant source of line broadening in these stars. For the supergiants, all but the two very fastest rotators have line profiles which are better fit with a macroturbulent broadening function than a rotational broadening function. We conclude that in early-type stars there appears to be some process, apart from rotation, that contributes to the line broadening. Although this has been suggested before from statistical analyses similar to that of chapter 7 (e.g. Howarth et al., 1997b), only recently has the quality of observations become good enough to measure the effect on the observed line profiles. As instrumentation is further improved even more detailed analyses of the line profiles should be possible (see section 8.3.3 below).

8.2.3 Origin of line broadening

Having established that there appears to be an additional line broadening mechanism in the OB stars, we are no closer to actually determining what this mechanism is. The 'macroturbulent' function used in the line-profile study, is equivalent to those used to model the line profiles of cooler stars, like the Sun, that show photospheric convection. According to current models of hot-star photospheres, such convection is not expected to take place (e.g. Kippenhahn and Weigert, 1990, p. 213). K. C. Smith, R. Townsend and I. D. Howarth (private communication) have experimented with high-order non-radial pulsations. They found that if a sufficiently high number of these exist at small amplitudes, the line profiles can appear macroturbulent. It is also possible that stars might not rotate as solid bodies. Differential rotation might distort the line profiles to give a macroturbulent 'look'. Finally, stellar winds and mass-loss have also been suggested as possible 'culprits' of additional line broadening in early-type stars (see discussion in Howarth et al., 1997b).

8.3 Looking forward – future work

During the course of this work, several interesting possible directions of work opened up. Unfortunately time did not allow all of these to be explored in detail.

8.3.1 Microturbulence

We have discussed above how the inclusion of microturbulence in the line-formation calculations can help partially resolve some discrepancies between observations and theoretical models. However, it is clear that our simple treatment of microturbulence is, if anything, only a first approximation of what physical processes might actually be taking place. Work is already underway to calculate a grid of models that treat microturbulence in both statistical-equilibrium and line-formation calculations, and it is hoped that these models will yield more realistic results. The first predictions by these models have already been described by Smith and Howarth (1998) in an analysis of the O9.7 Iab star HD 152003, and it is apparent that microturbulence can affect derived values of $T_{\rm eff}$, $\log_{10} g$ and the helium abundance, y. Having developed methods and routines to derive consistent results for a large number of lines in a large number of stars, we hope to use these routines with the new grid of models, when it is completed, to evaluate the effects of a more detailed treatment of microturbulence on the sample stars.

8.3.2 Larger sample

One of the major aims of this study was to look for any clear trends to explain the large variations in surface properties (like abundances, line profiles etc.) observed in early-type stars, and thus look for possible physical processes to explain them. Although several trends were found and discussed in chapter 6, no single process appears to be able to account for the abundance variations, and observation/model discrepancies like the so-called *mass discrepancy*.

Expanding the sample of stars is an obvious way of trying to get a larger statistical significance and narrowing down the possible explanations of these observed trends. Although an analysis of a huge number of stars would obviously give some very interesting results, it would be prohibitively expensive in terms of observing and analysis time. A careful selection of targets could probably give just as interesting results. Some of the possible selection criteria for an expanded sample of stars could be:

- **More chemically 'divergent' stars.** To further investigate the OC $\rightarrow$ O $\rightarrow$ ON sequence, it would be interesting to expand the sample to include more ON and especially more OC stars. The current sample, which includes two ON main-sequence stars, two ON supergiants and only one OC supergiant, showed that the helium abundance, y, is clearly linked to the OC/ON anomalies. However, there didn't appear to be any other clear relationships between the OC/ON stars in the sample. Increasing the sample with more anomalous stars would allow investigation of similar properties of these stars.

- **Stars with moderate nitrogen deficiencies.** Of the three stars in the current sample which were on Walborn's list of stars with moderate nitrogen deficiencies, all showed an unusually low mass-discrepancy compared to the other sample stars. It would be worth seeing if this is something in common for the stars with moderate N deficiencies, and, if that is the case, have a closer look at the other properties of these stars. If the mass-discrepancy is partially due to rotation being neglected in evolutionary models, then a detailed study of the rotational/line-broadening properties of these stars would be interesting.

- **An O star survey?** We have shown that it is possible to obtain good quality spectra of 20 – 30 stars in a four night observing run. Having now established which lines are

good indicators, and also that results are obtainable even for a S/N ratio of less than 200 (BD+36 4063) it is possible that even more stars could be observed in a similar time. Possible targets could then include more narrow temperature/classification bands like in this study, or a more general study of, say, an OB association.

8.3.3 Line profile analyses

We have discussed the evidence that there might be other processes that contribute to line broadening in O and early-B type stars. By using statistical methods to compare artificially broadened model spectra with observations, we have shown that we sometimes get better 'fits' by using model spectra broadened with a 'macroturbulent' function instead of a rotational function. Further to this study it would be very interesting to study more carefully the observed line profiles, and try to fit them using more sophisticated functions. The study should include comparisons of combinations of rotational and macroturbulent functions of different strengths, and it would also be worth investigating the importance of the value of the limb-darkening coefficient, ϵ, in equation 3.11, and the effects of differential rotation.

Appendix A

The spectrum of 10 Lacertae

The following pages contain plots of the entire WHT/UES merged spectrum of 10 Lac (HD 214680; O9 V). Each panel shows a 110Å section of the spectrum, and there is a 5Å overlap between panels. Details about the data reduction can be found in chapter 2. Line identifications are a subset of those given by Scholtz (1972). Interstellar lines are labelled in *italics*. Spectra of the other sample O-stars are included on the CD-ROM (see appendix E).

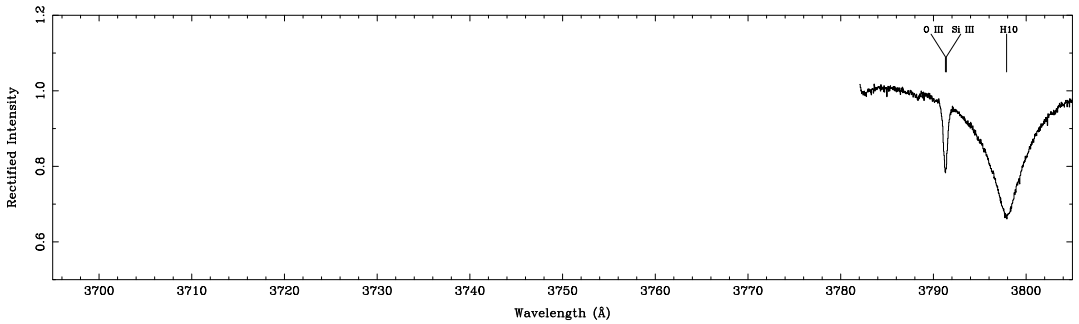
O III
Si III
H10
Rectified Intensity
Wavelength (Å)

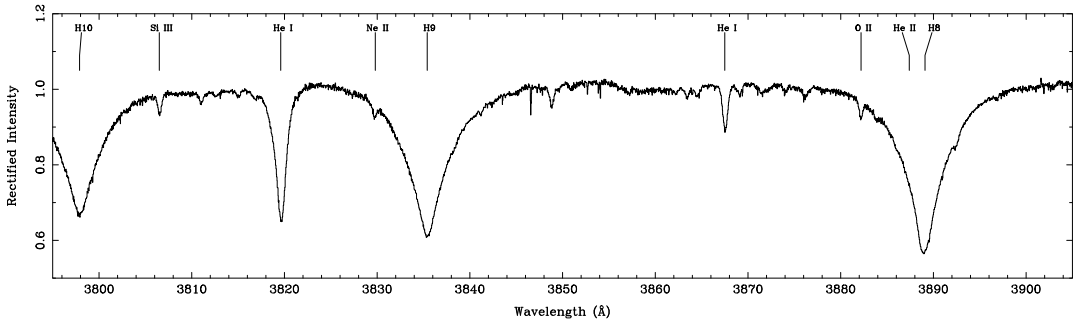
H10
Si III
He I
Ne II
H9
He I
O II
He II
H8
Rectified Intensity
Wavelength (Å)

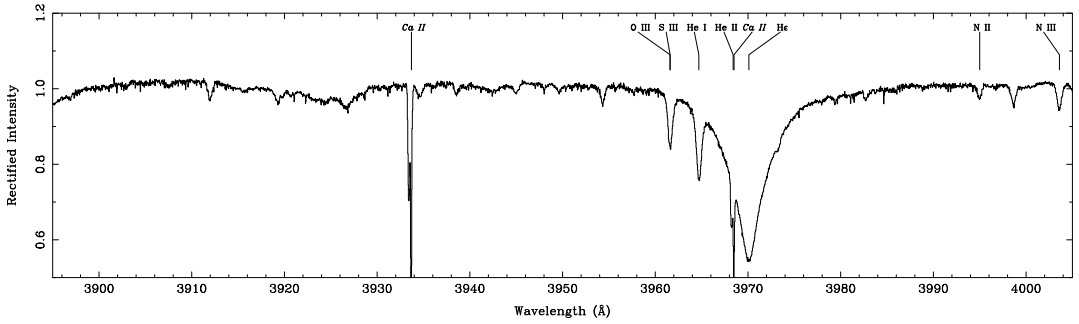
Ca II
O III
S III
He I
He II
Ca II
Hε
N II
N III
Rectified Intensity
Wavelength (Å)

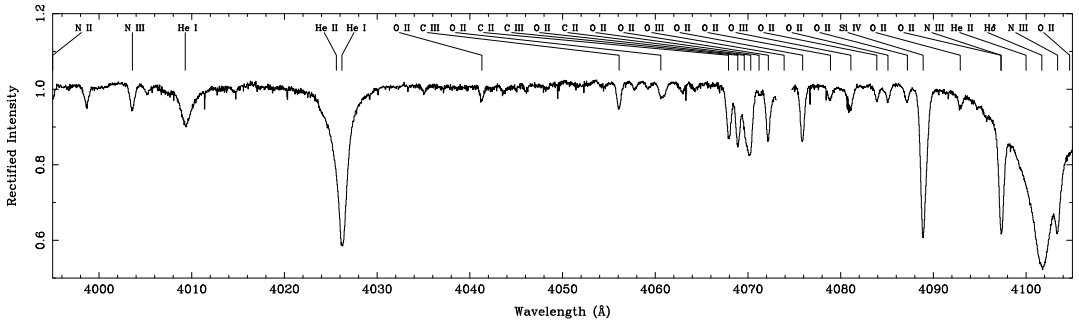
N II
N III
He I
He II
He I
O II
C III
Si IV
He II
Hδ
Rectified Intensity
Wavelength (Å)

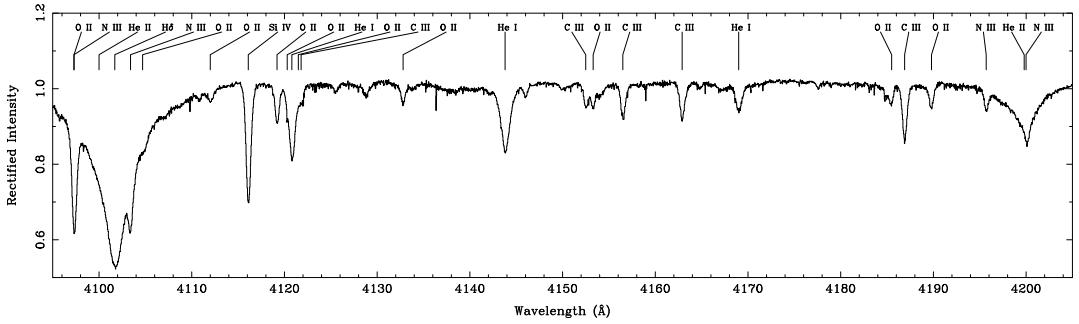
O II
N III
He II
Hδ
Si IV
He I
C III
Rectified Intensity
Wavelength (Å)

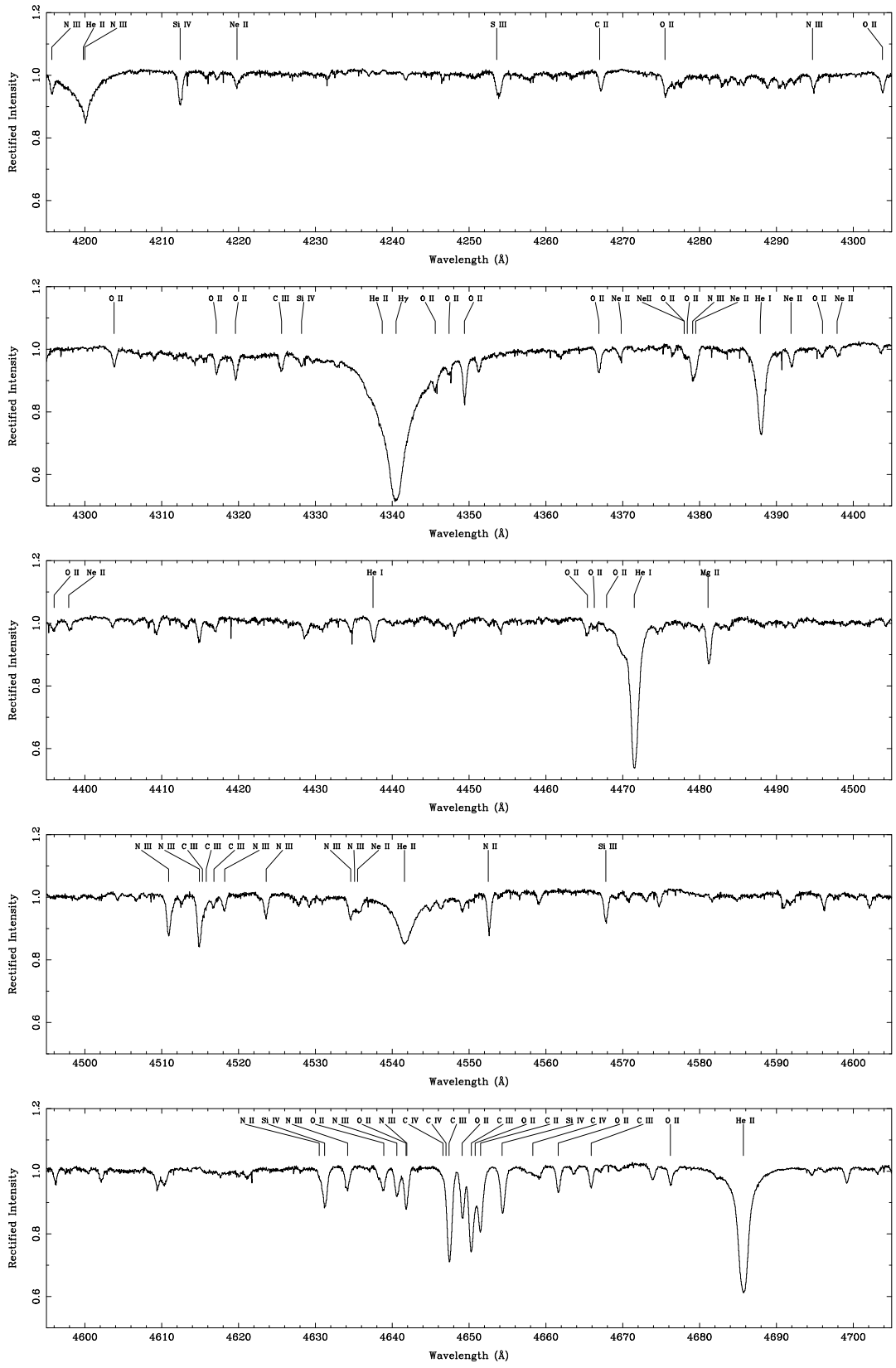
N III
He II
N III
Si IV
Ne II
S III
C II
O II
N III
O II
O II
O II
O II
C III
Si IV
He II
Hγ
O II
O II
O II
O II
Ne II
NeII
O II
O II
N III
Ne II
He I
Ne II
O II
Ne II
O II
Ne II
He I
O II
O II
O II
He I
Mg II
N III
N III
C III
C III
C III
N III
N III
N III
N III
Ne II
He II
N II
Si III
N II
Si IV
N III
O II
N III
O II
N III
C IV
C IV
C III
O II
C III
O II
C II
Si IV
C IV
O II
C III
O II
He II
Rectified Intensity
Wavelength (Å)

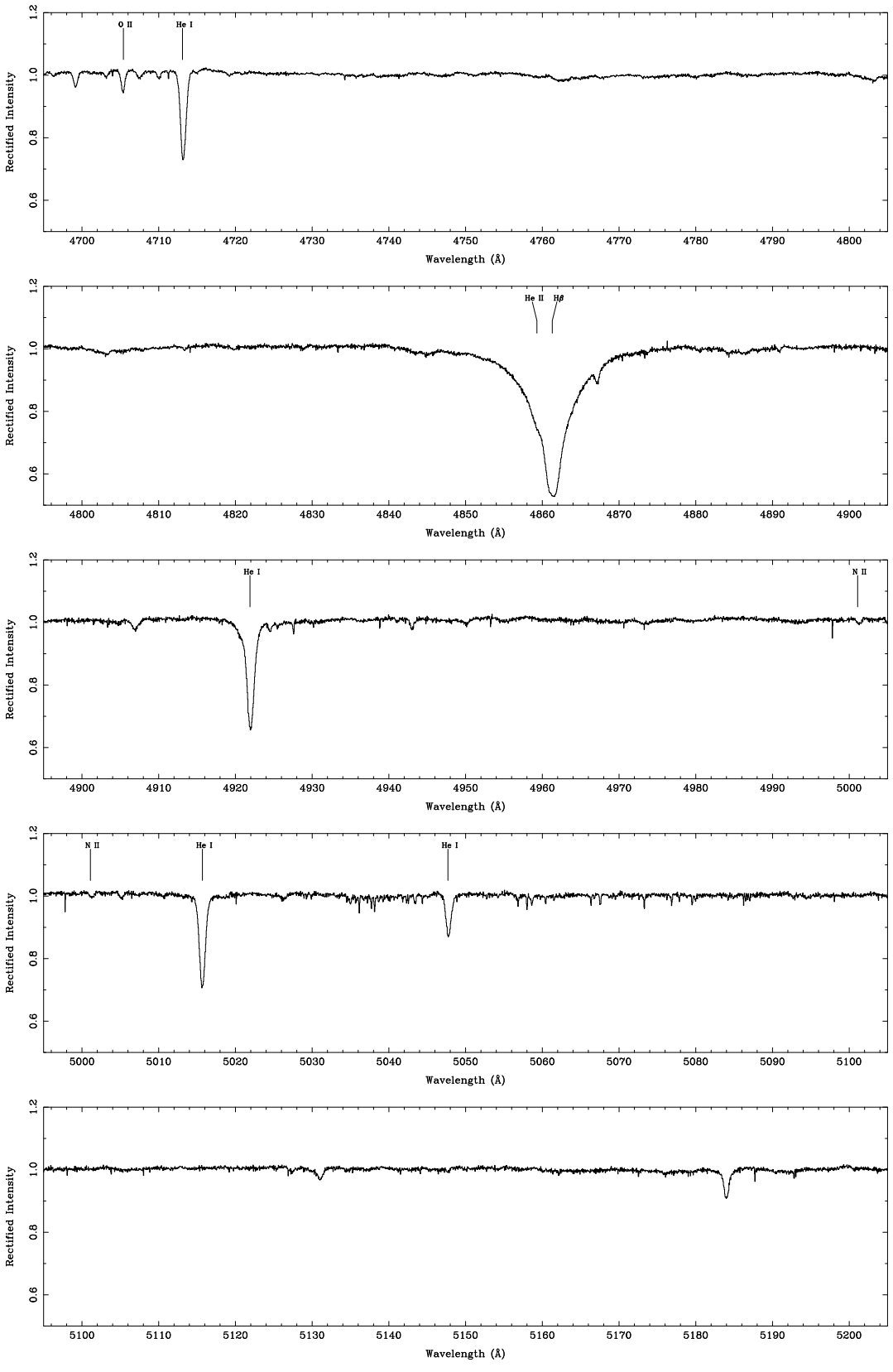
O II
He I
He II
Hδ
He I
N II
N II
He I
He I
Rectified Intensity
Wavelength (Å)

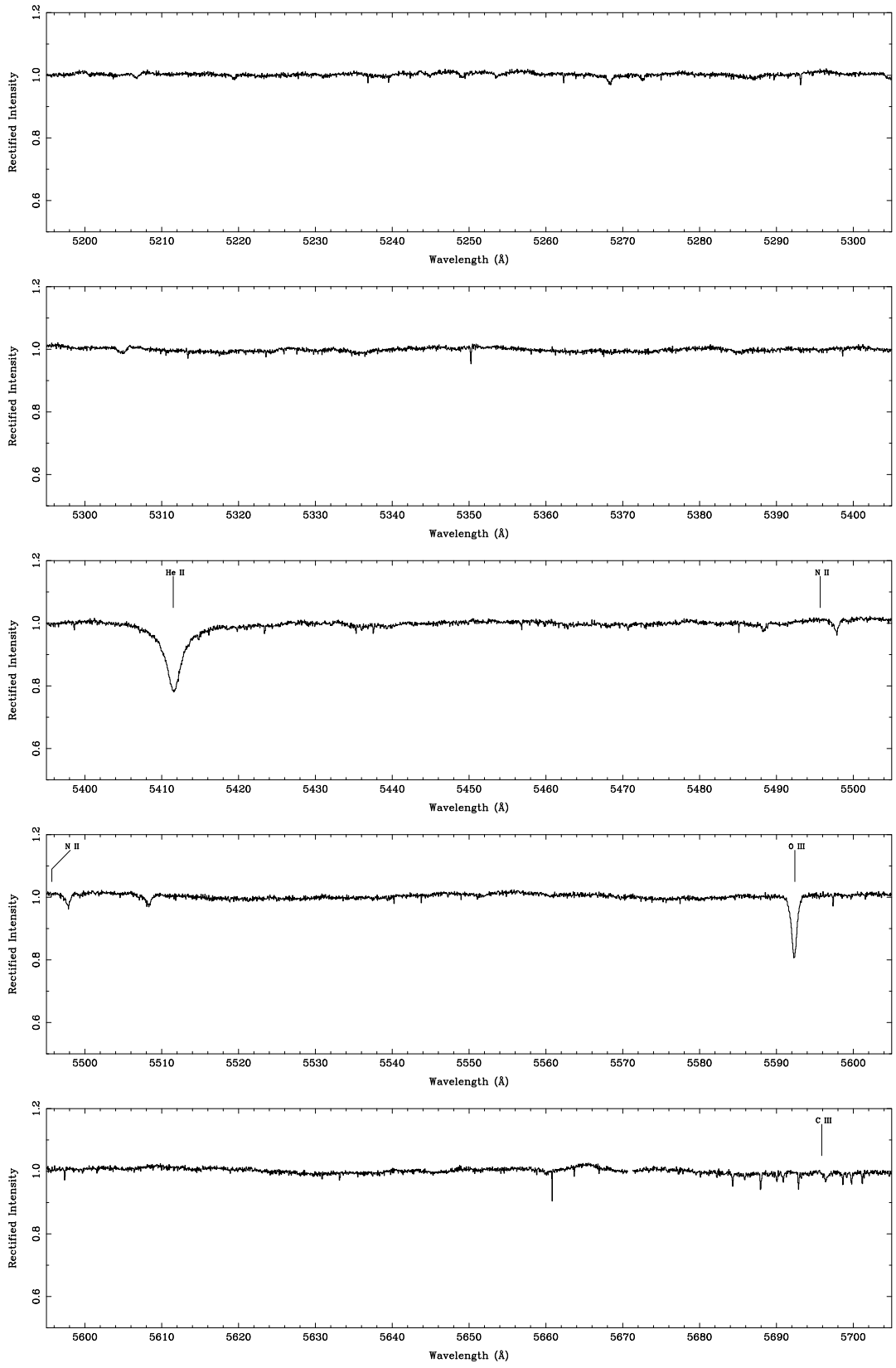
Rectified Intensity
Wavelength (Å)
He II
N II
N II
O III
C III

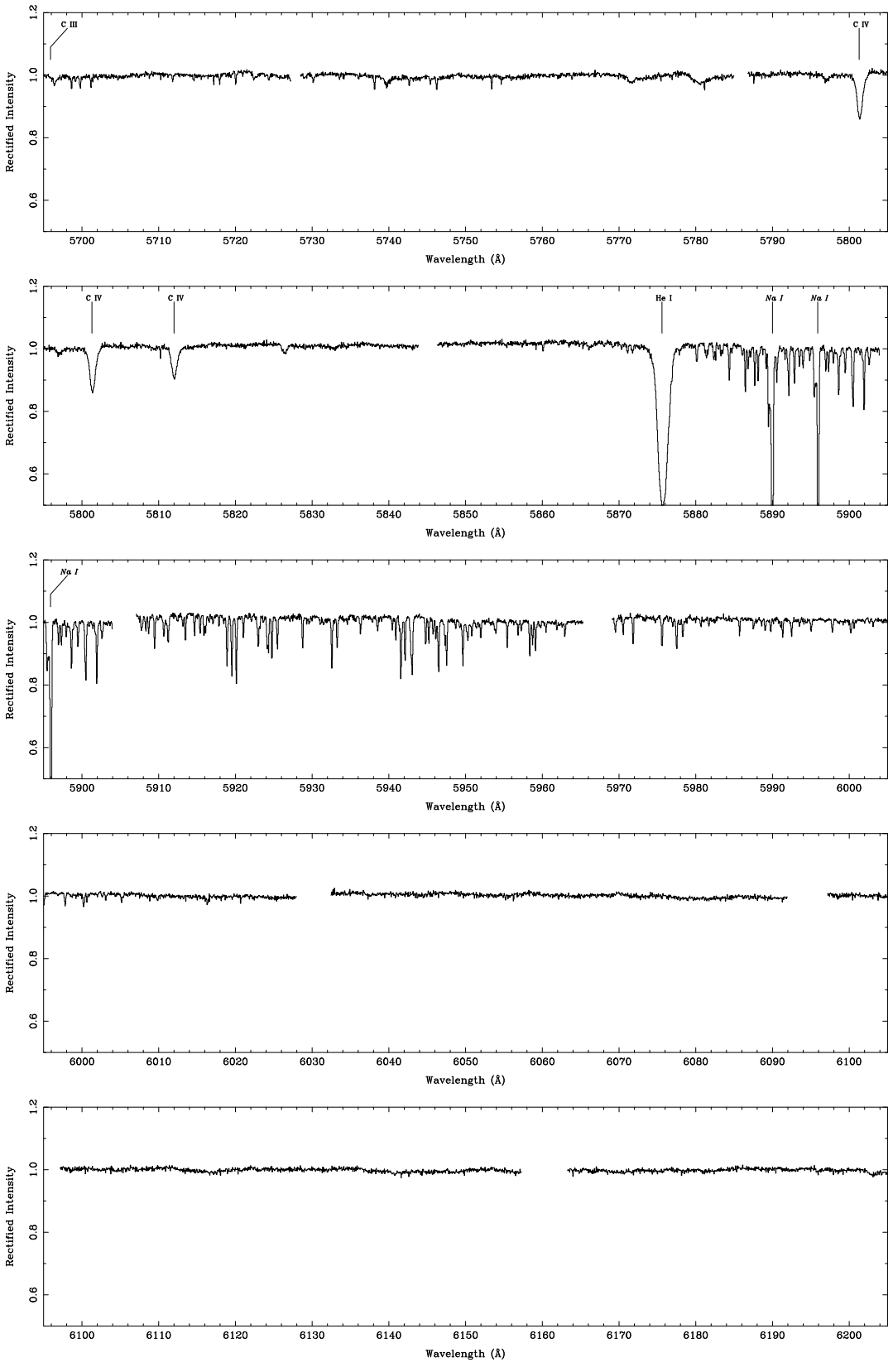
C III
C IV
C IV
C IV
He I
Na I
Na I
Na I
Rectified Intensity
Wavelength (Å)

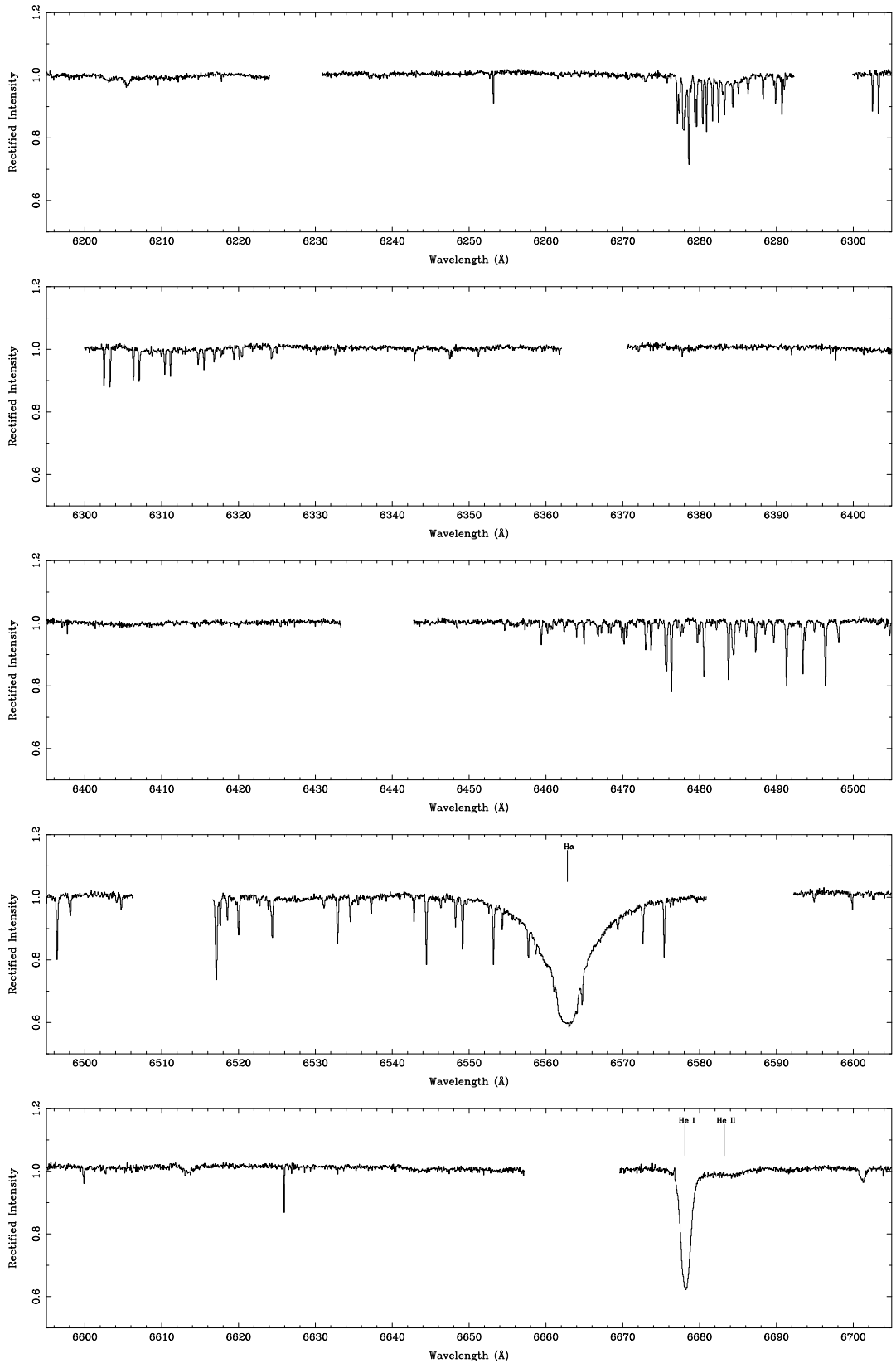
Rectified Intensity
Wavelength (Å)
Hα
He I
He II

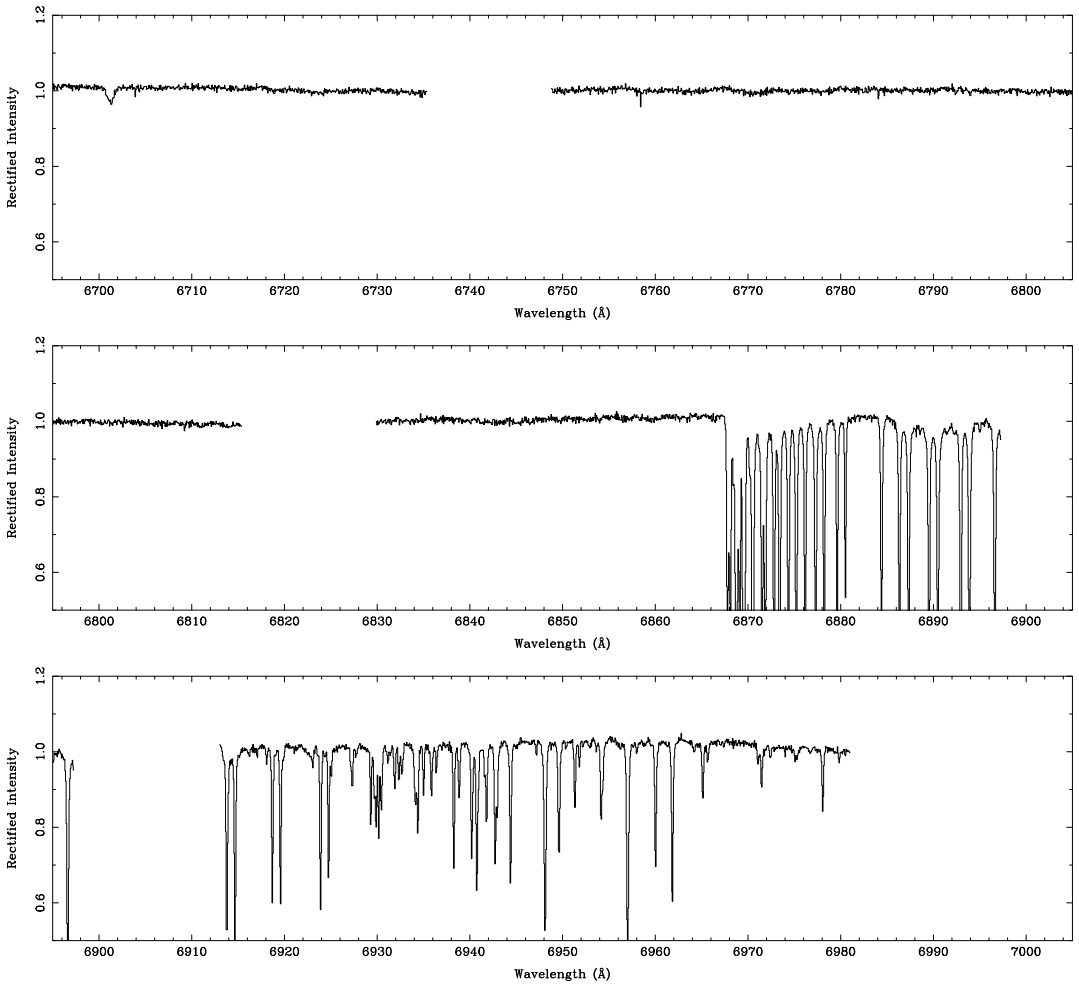
Rectified Intensity
Wavelength (Å)
6700
6710
6720
6730
6740
6750
6760
6770
6780
6790
6800
6810
6820
6830
6840
6850
6860
6870
6880
6890
6900
6910
6920
6930
6940
6950
6960
6970
6980
6990
7000
0.6
0.8
1.0
1.2

Appendix B

Comparison of ON and OC supergiant spectra

The following pages show a comparison of the WHT/UES spectra of HD 191781 (ON9.7 Iab) and HD 194280 (OC9.7 Iab) in the range $\lambda\lambda$3780 – 6210Å. Details of the diagrams are the same as for appendix A.

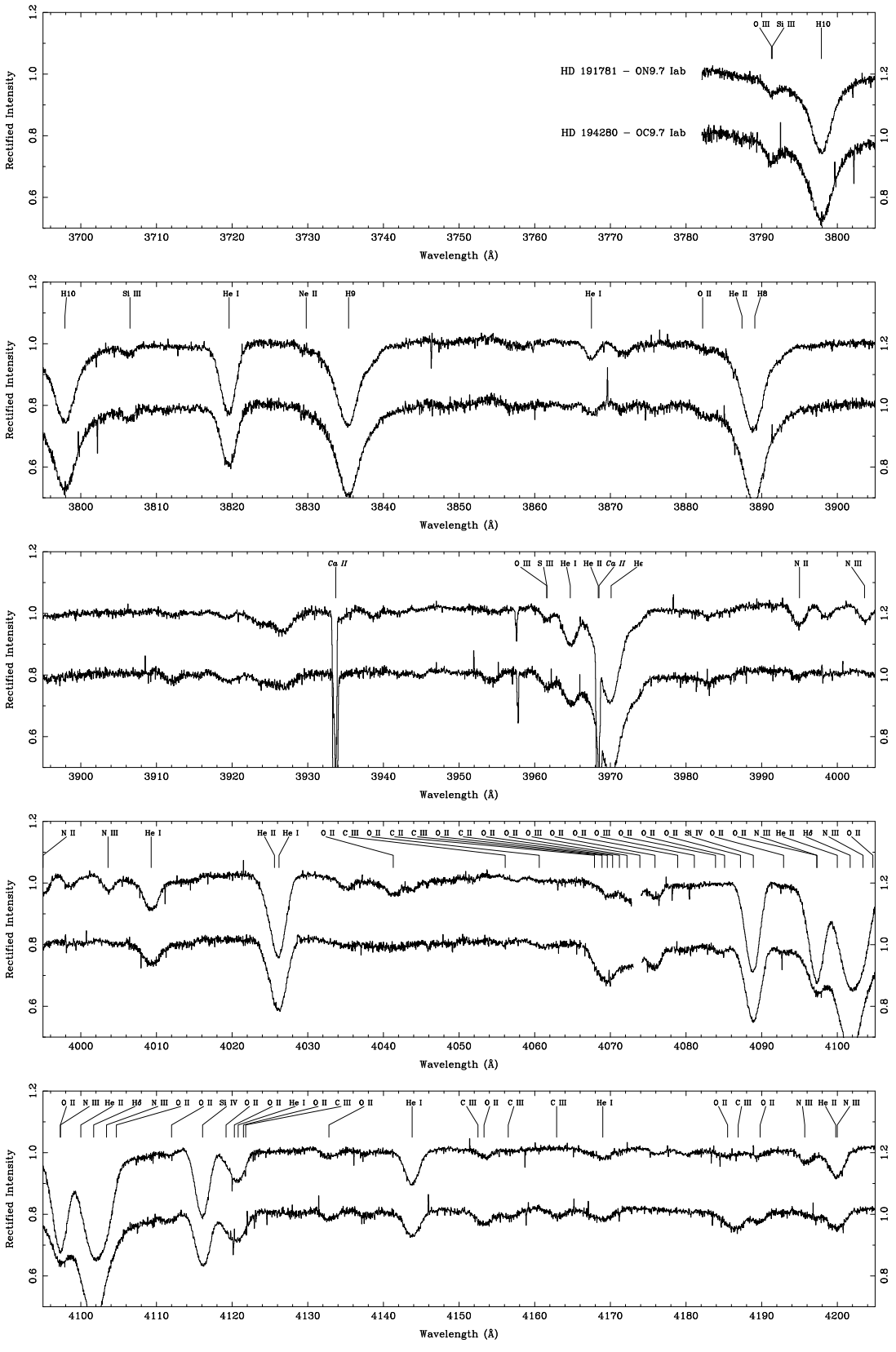
HD 191781 – ON9.7 Iab
HD 194280 – OC9.7 Iab
Rectified Intensity
Wavelength (Å)
O III
Si III
H10
H9
H8
He I
Ne II
O II
He II
Ca II
S III
N II
N III
C III
Si IV

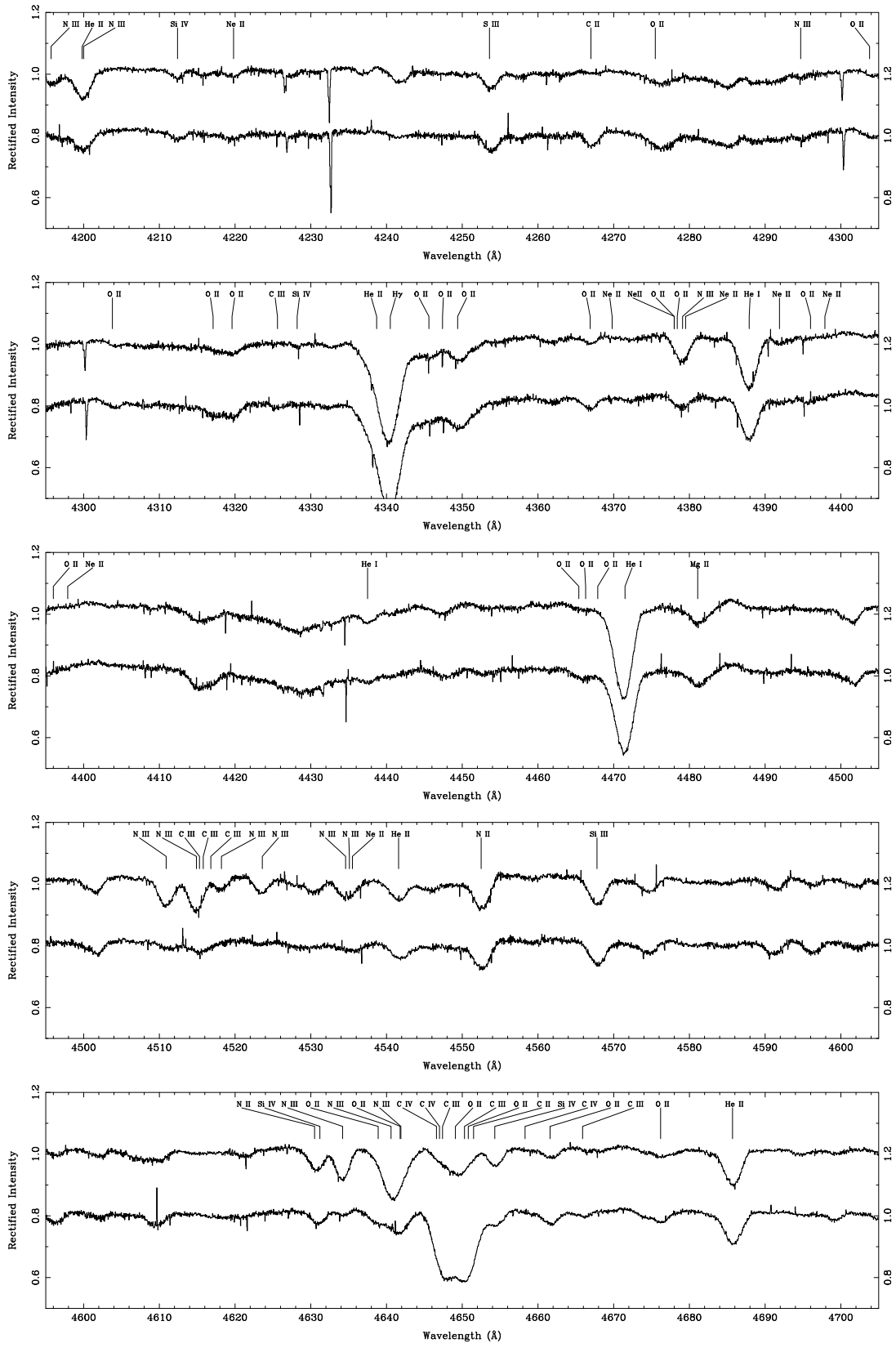
N III
He II
N III
Si IV
Ne II
S III
C II
O II
N III
O II
O II
O II
O II
C III
Si IV
He II
Hγ
O II
O II
O II
O II
Ne II
NeII
O II
O II
N III
Ne II
He I
Ne II
O II
Ne II
O II
Ne II
He I
He I
Mg II
N III
N III
C III
C III
C III
N III
N III
N III
N III
Ne II
He II
N II
Si III
N II
Si IV
N III
O II
N III
O II
N III
C IV
C IV
C III
O II
C III
O II
C II
Si IV
C IV
O II
C III
O II
He II
Rectified Intensity
Wavelength (Å)

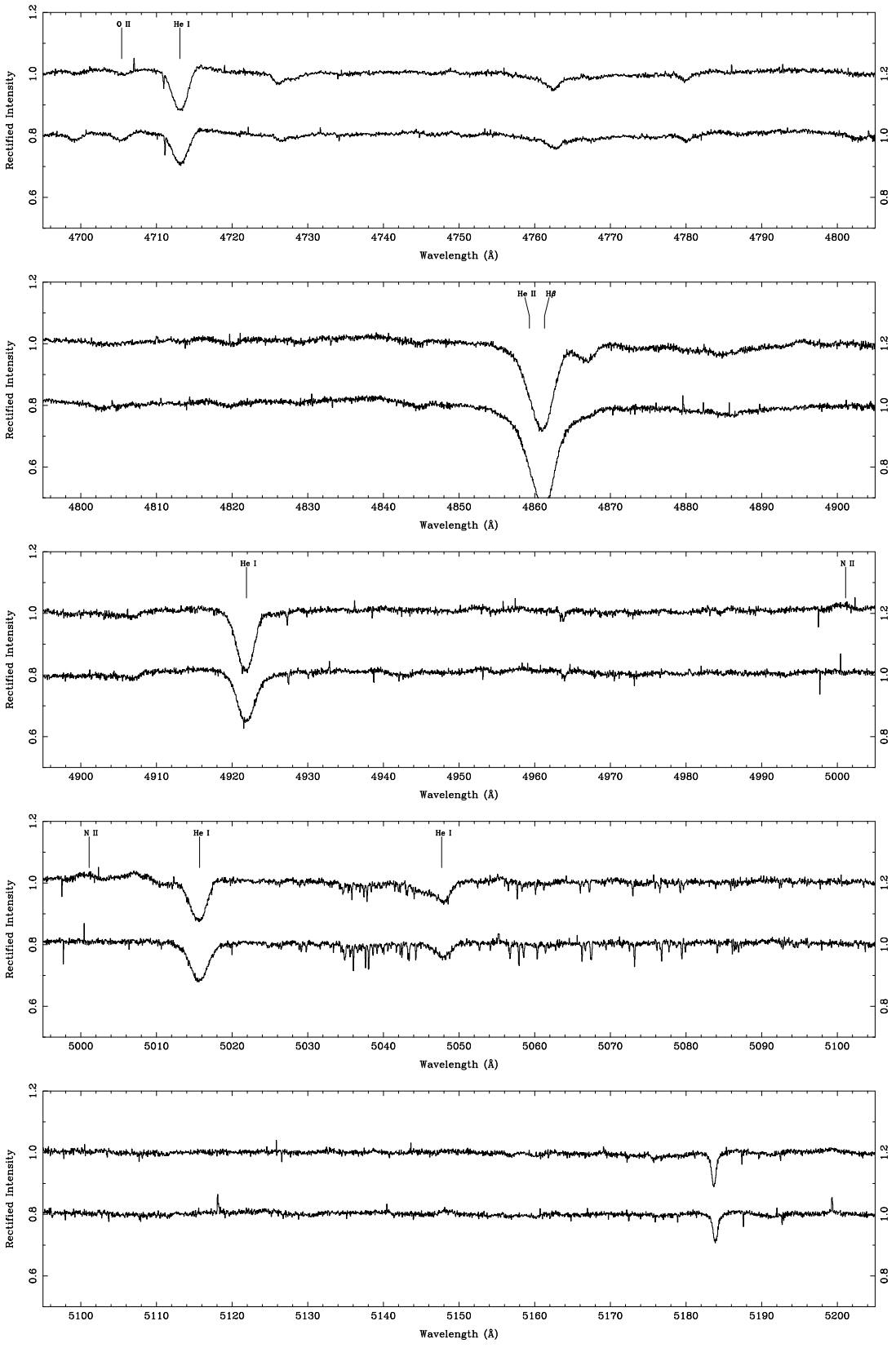
O II
He I
He II
Hδ
He I
N II
N II
He I
He I
Rectified Intensity
Wavelength (Å)

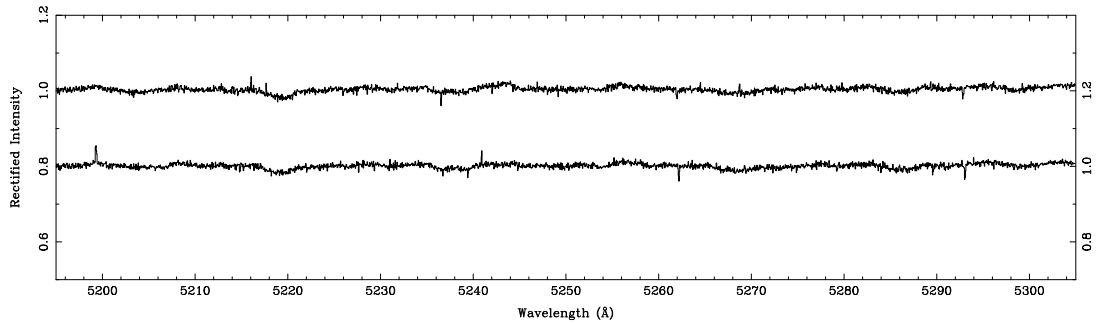
Rectified Intensity
Wavelength (Å)

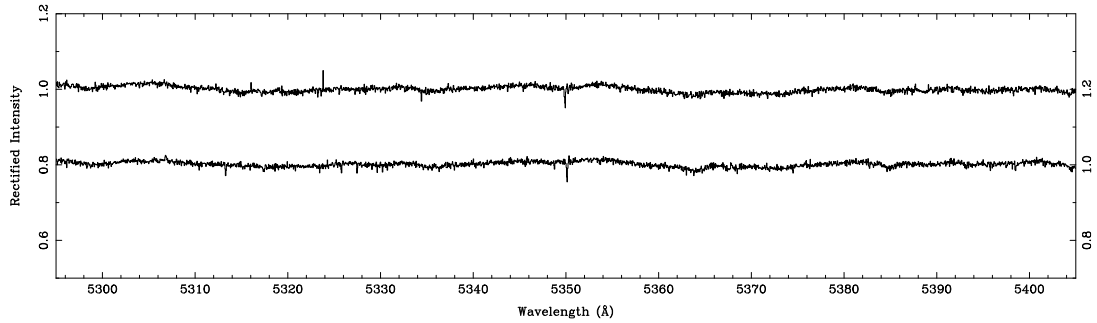
Rectified Intensity
Wavelength (Å)

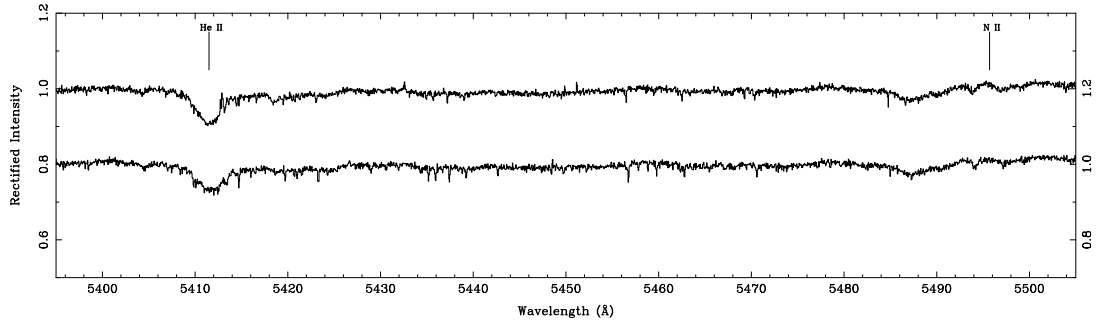
He II
N II
Rectified Intensity
Wavelength (Å)

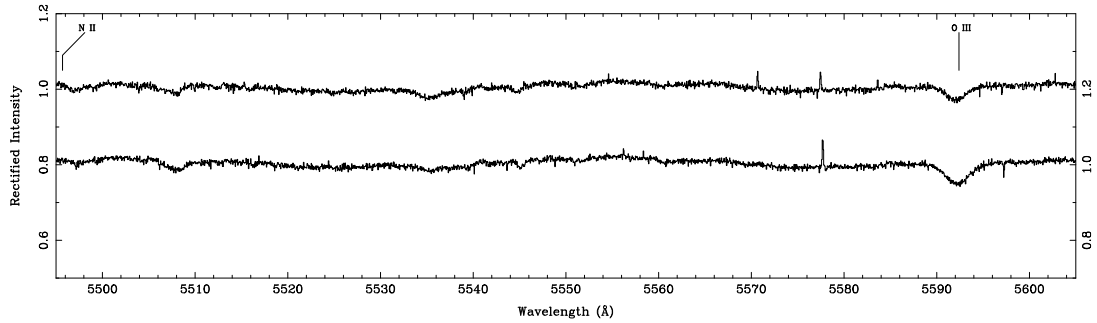
N II
O III
Rectified Intensity
Wavelength (Å)

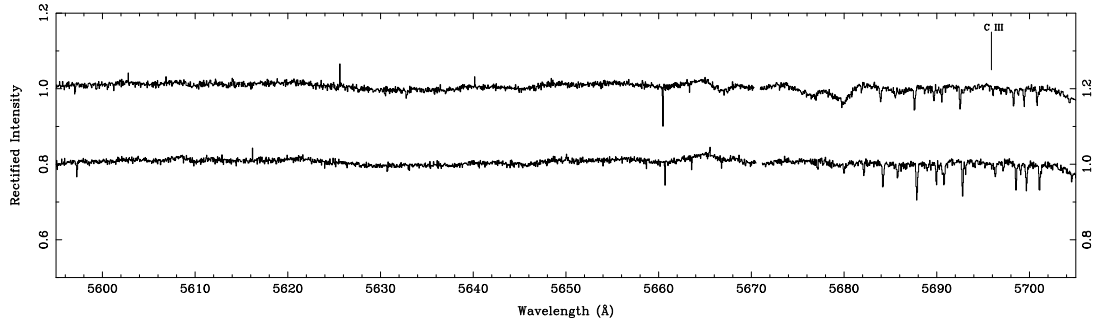
C III
Rectified Intensity
Wavelength (Å)

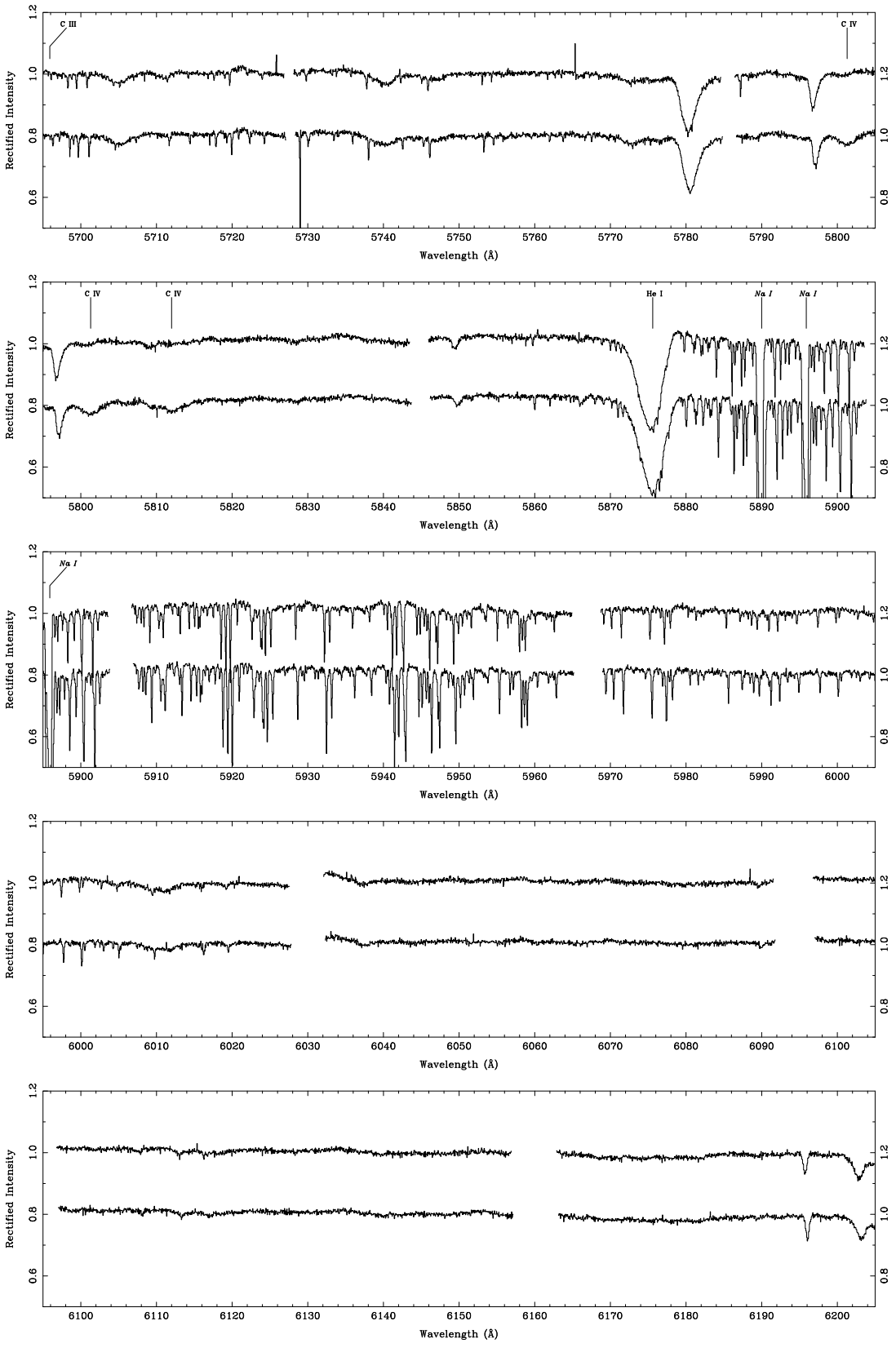
C III
C IV
C IV
C IV
He I
Na I
Na I
Na I
Rectified Intensity
Wavelength (Å)

Appendix C

Summary of O star results and spectra

This appendix summarises the adopted parameters and shows fit-diagrams and model fits for each WHT/UES star derived in chapter 5. The results for each star are shown on two pages, the first page lists the adopted parameters and shows the fit diagrams in two columns. The left-hand column shows the diagrams for a microturbulent velocity, $\xi = 0$ km s^{-1}, and the right-hand column for $\xi = 15$ km s^{-1}. Three values of the helium number fraction, $y = 0.09$, 0.12 and 0.15 are shown, with y increasing downwards. The 'best-fit' diagram for each star is shown at the end of chapter 5.

The second page for each star shows comparisons of model spectra and observations for the lines used in the analyses. Also included are selected wavelength regions, including $\lambda\lambda$4000–4200Å which includes many of the lines used in the analyses, $\lambda\lambda$4400–4600Å which includes the strong He I λ4471Å line, the He II λ4541Å line, several lines of C, N and O, and the diffuse interstellar band at λ4430Å. Also sometimes visible are the unidentified emission lines at $\lambda\lambda$4465 and 4505Å. The $\lambda\lambda$4600–4700Å region contains a wealth of C, N and O lines which often reveal carbon and nitrogen abundance anomalies (cf. appendix B), and the strong He II λ4686Å line which is very sensitive to stellar wind and mass loss. Finally the plots also include Hα. Line identifications for the strong lines and blends are taken from Scholtz (1972). For a more complete list of identifications, see appendix A or the attached CD-ROM.

C.1 HD 10125

Spectral Type:	O9.7 II
$T_{\rm eff}$:	32500 K
$\log_{10} g$:	3.3
y:	0.15
Broadening function:	macroturbulent
Broadening velocity:	132 km s^{-1}

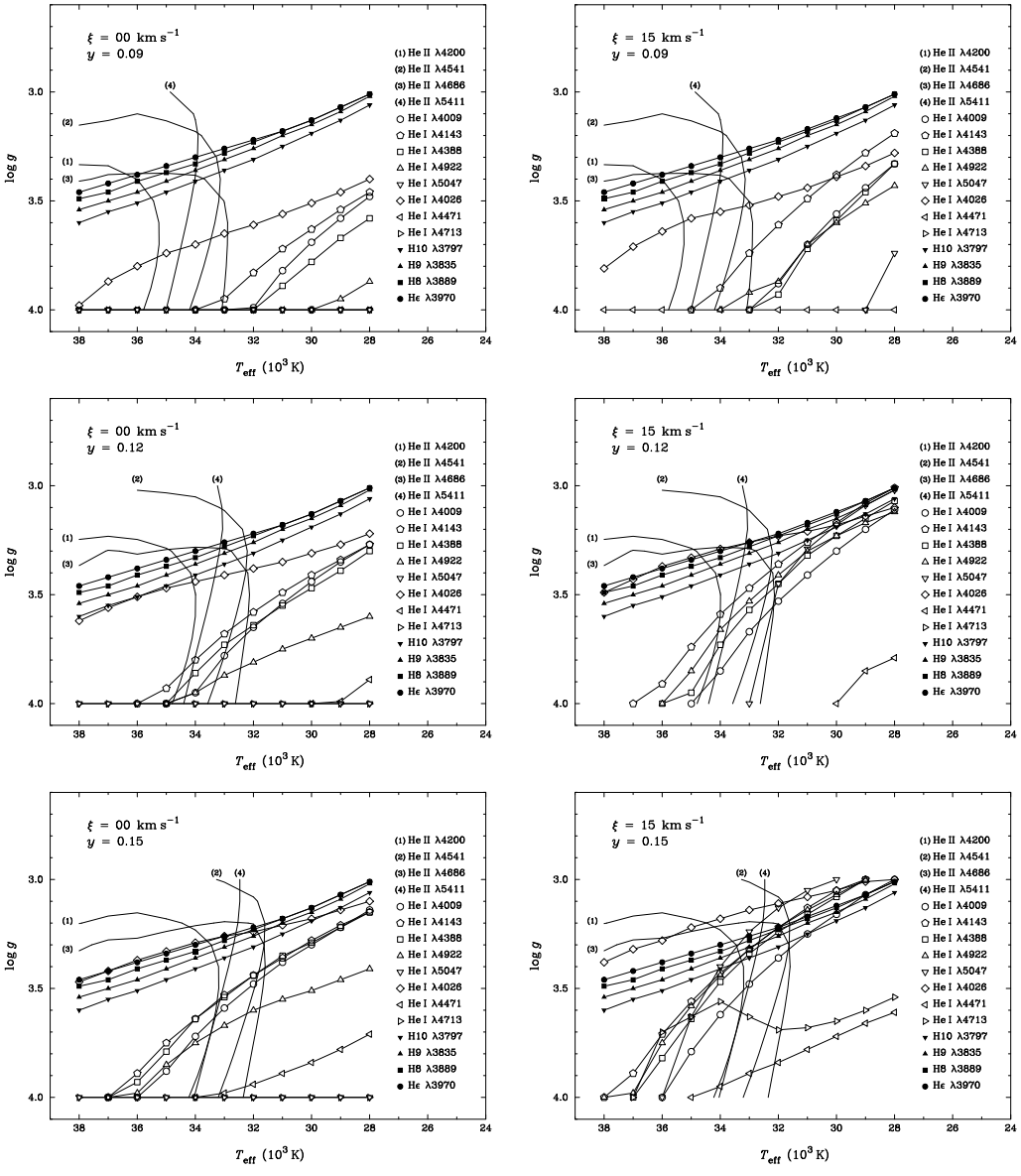

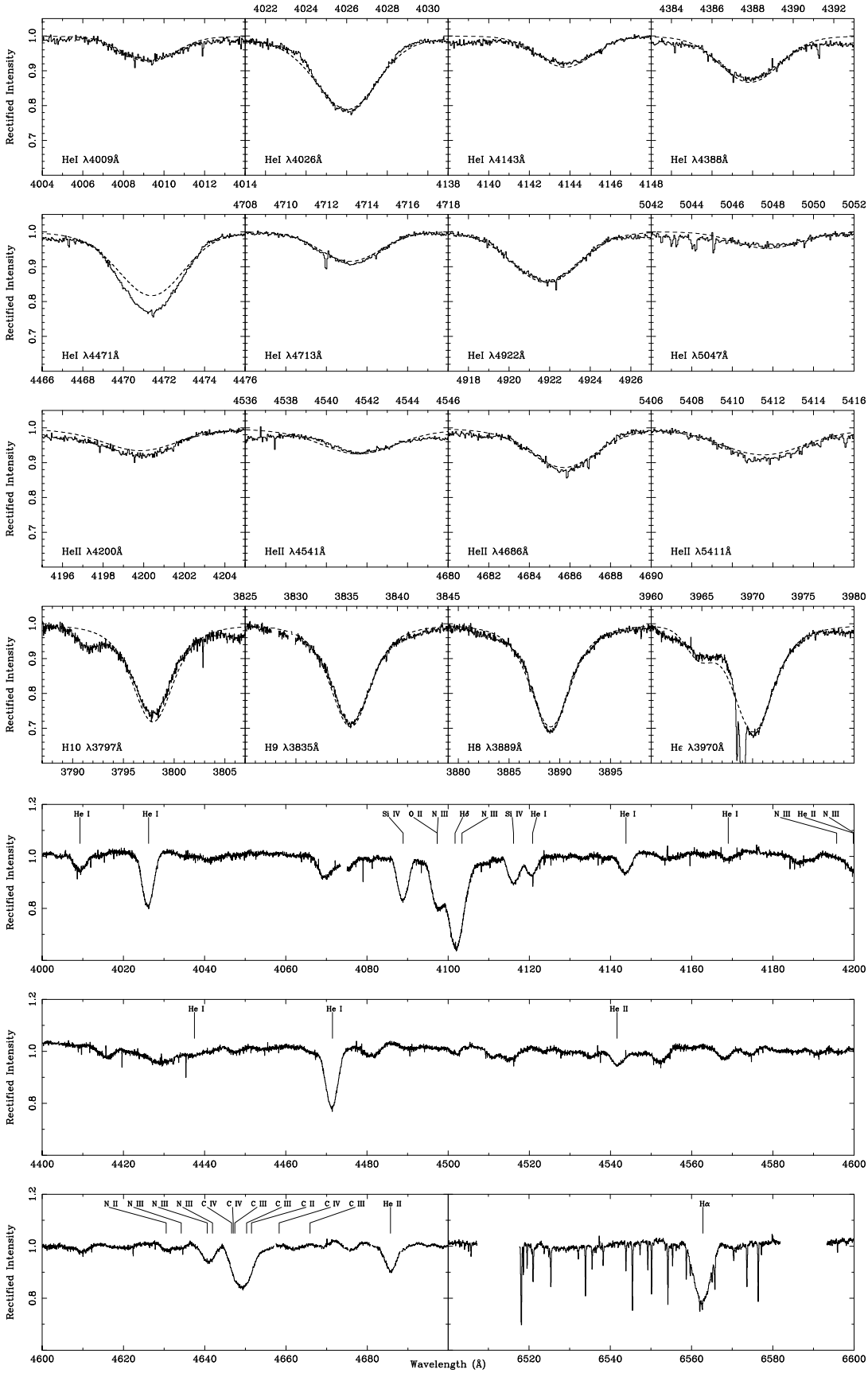
HeI λ4009Å
HeI λ4026Å
HeI λ4143Å
HeI λ4388Å
HeI λ4471Å
HeI λ4713Å
HeI λ4922Å
HeI λ5047Å
HeII λ4200Å
HeII λ4541Å
HeII λ4686Å
HeII λ5411Å
H10 λ3797Å
H9 λ3835Å
H8 λ3889Å
Hε λ3970Å
Rectified Intensity
Wavelength (Å)

C.2 HD 12323

Spectral Type:	ON9 V
$T_{\rm eff}$:	36000 K
$\log_{10} g$:	4.1
y:	0.17
Broadening function:	rotational
Broadening velocity:	131 km s^{-1}

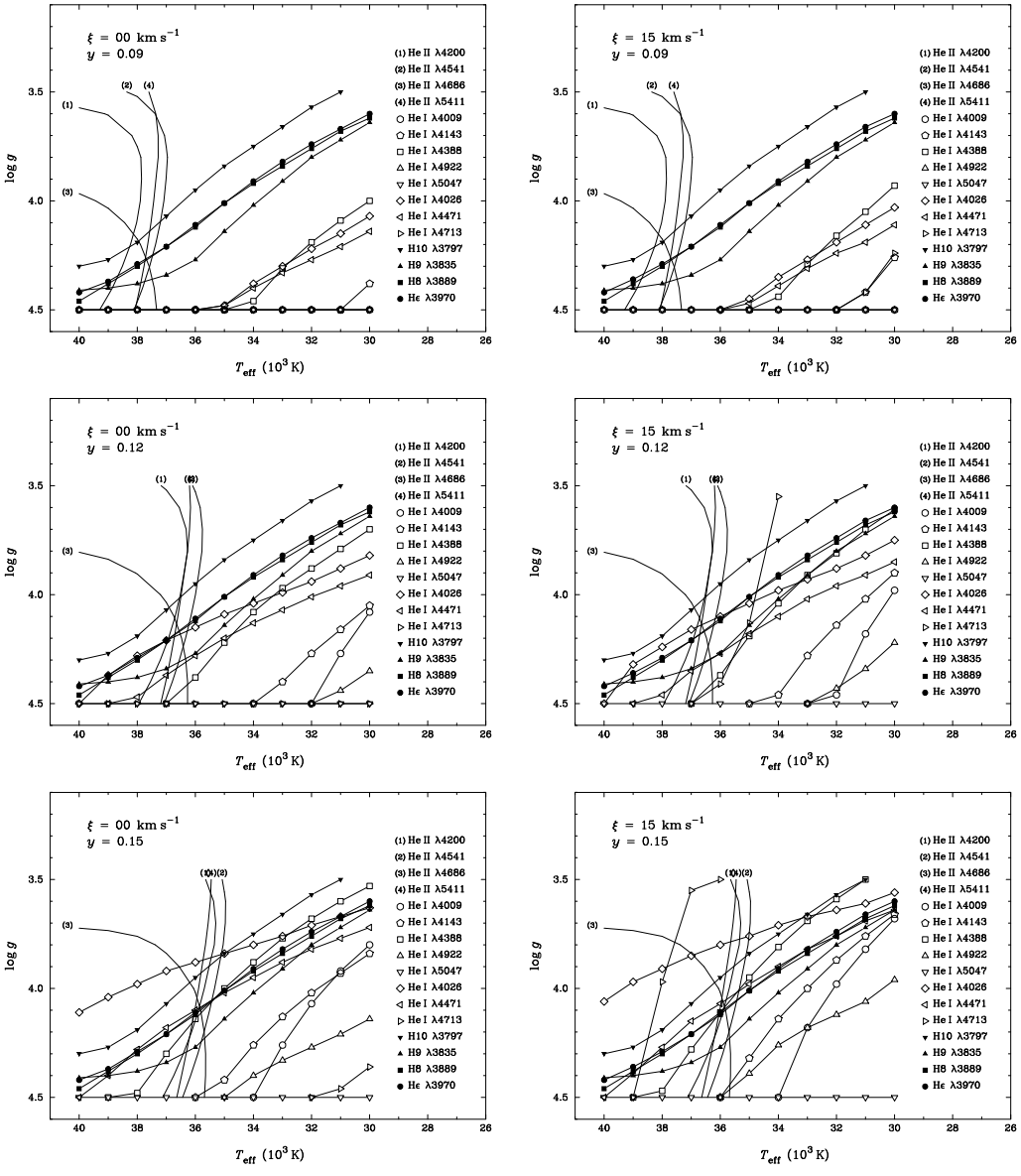

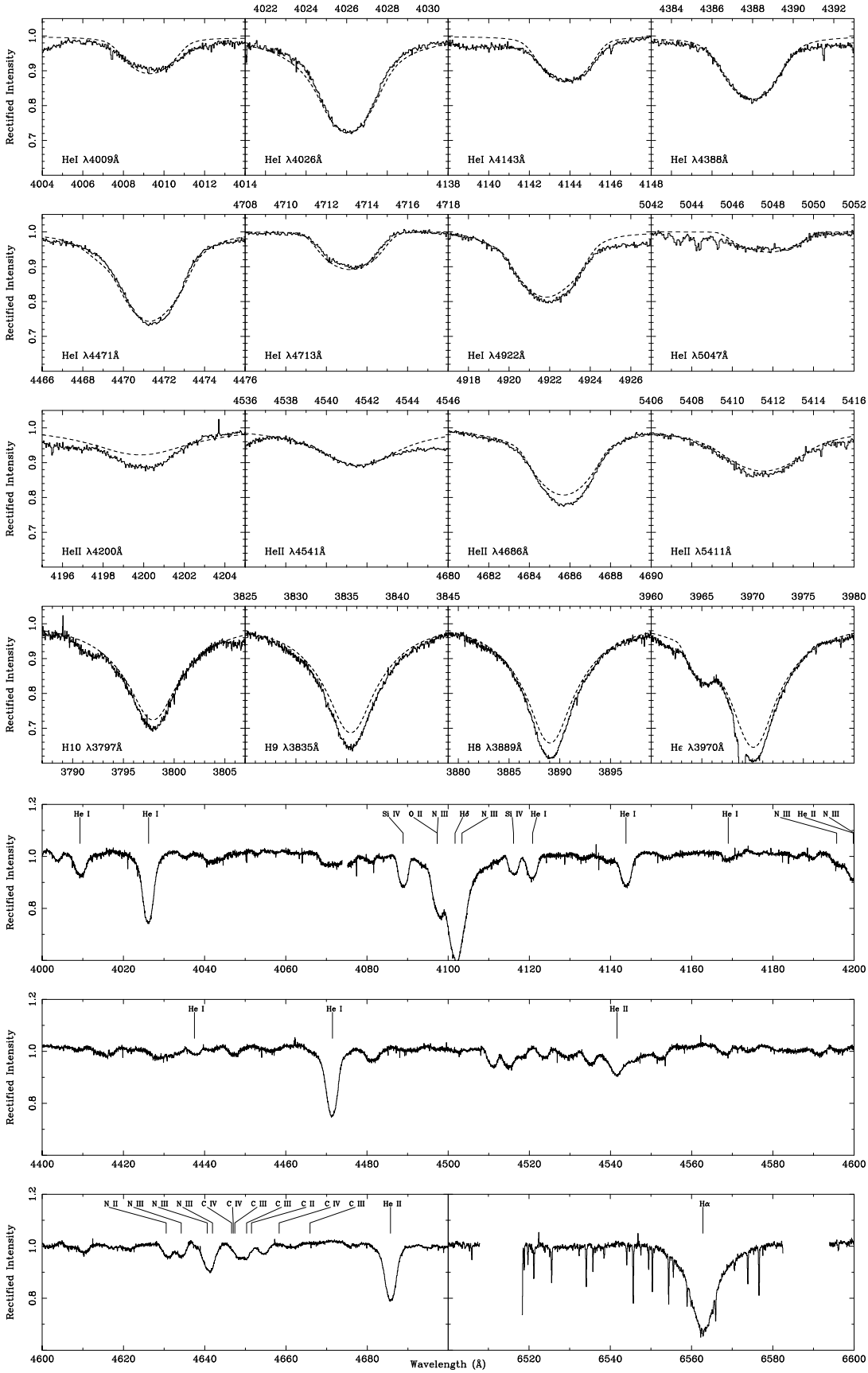
Rectified Intensity
HeI λ4009Å
HeI λ4026Å
HeI λ4143Å
HeI λ4388Å
HeI λ4471Å
HeI λ4713Å
HeI λ4922Å
HeI λ5047Å
HeII λ4200Å
HeII λ4541Å
HeII λ4686Å
HeII λ5411Å
H10 λ3797Å
H9 λ3835Å
H8 λ3889Å
Hε λ3970Å
He I
Si IV
O II
N III
Hδ
Si IV
He II
Hα
Wavelength (Å)

C.3 HD 13745

Spectral Type:	O9.7 II ((n))
$T_{\rm eff}$:	33000 K
$\log_{10} g$:	3.3
y:	0.20
Broadening function:	rotational
Broadening velocity:	176 km s^{-1}

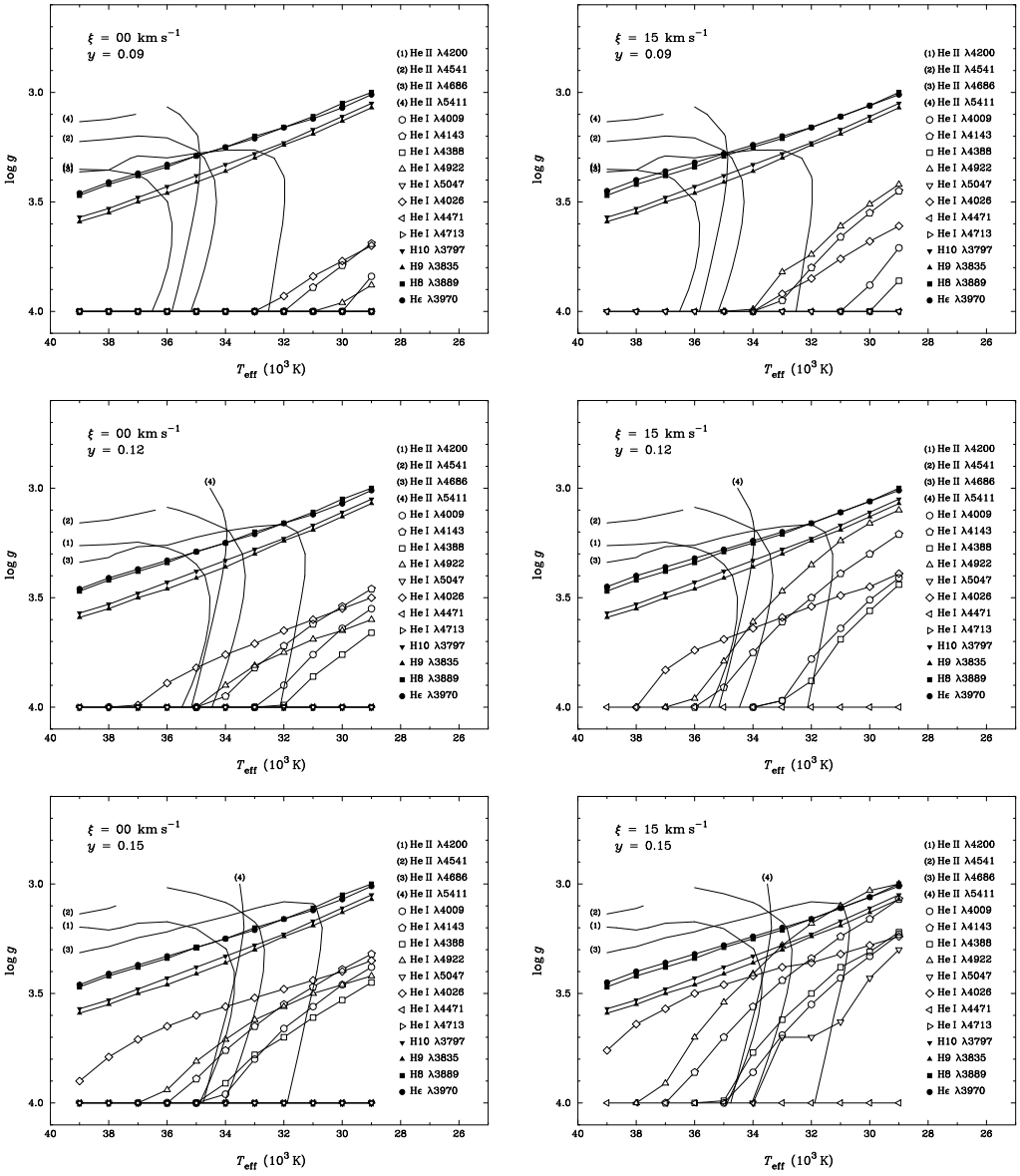

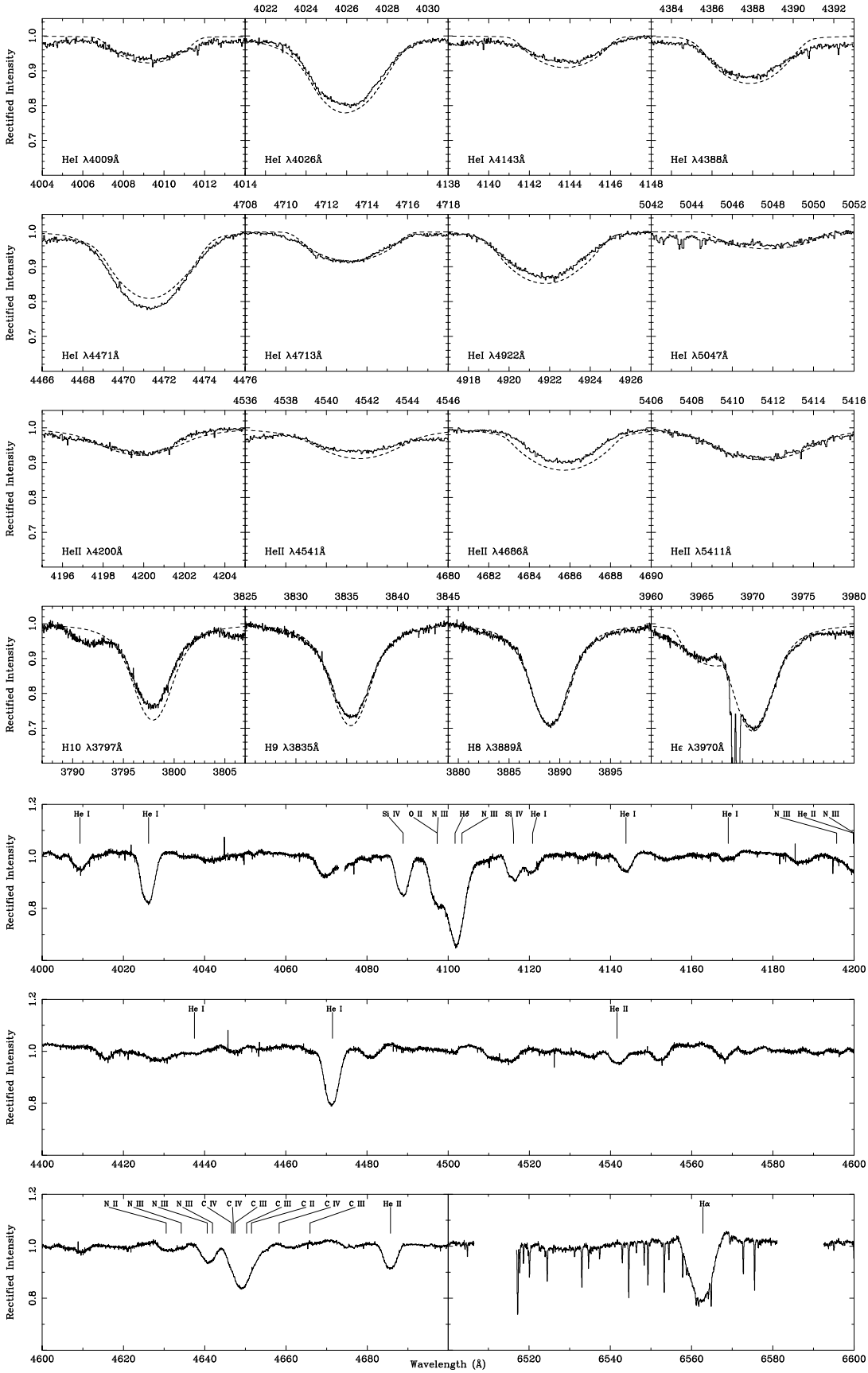
Rectified Intensity
HeI λ4009Å
HeI λ4026Å
HeI λ4143Å
HeI λ4388Å
HeI λ4471Å
HeI λ4713Å
HeI λ4922Å
HeI λ5047Å
HeII λ4200Å
HeII λ4541Å
HeII λ4686Å
HeII λ5411Å
H10 λ3797Å
H9 λ3835Å
H8 λ3889Å
Hε λ3970Å
He I
Si IV
O II
N III
Hδ
He II
Hα
Wavelength (Å)

C.4 HD 16429

Spectral Type:	O9.5 II ((n))
$T_{\rm eff}$:	35000 K
$\log_{10} g$:	3.4
y:	0.12
Broadening function:	rotational
Broadening velocity:	216 km s^{-1}

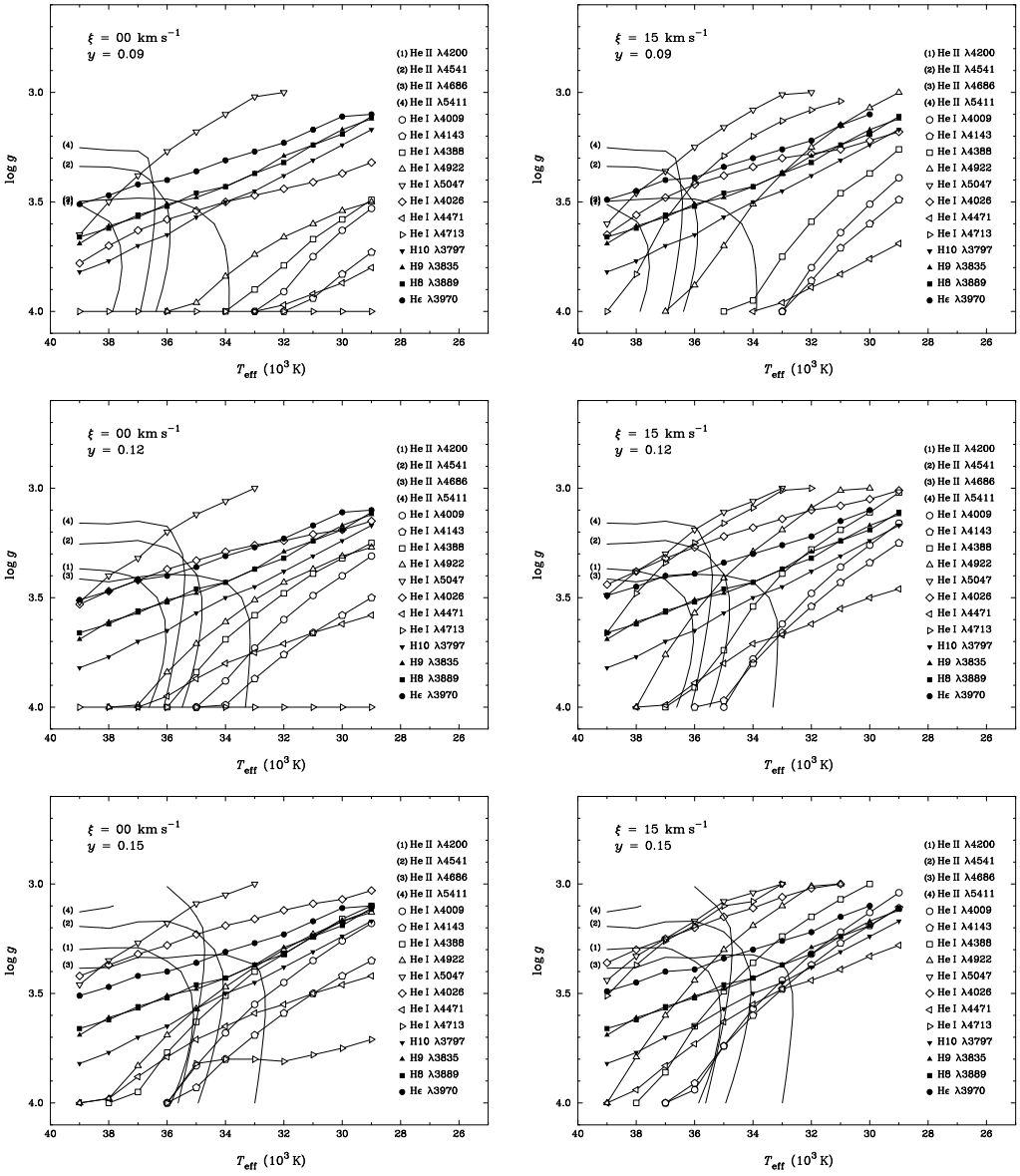

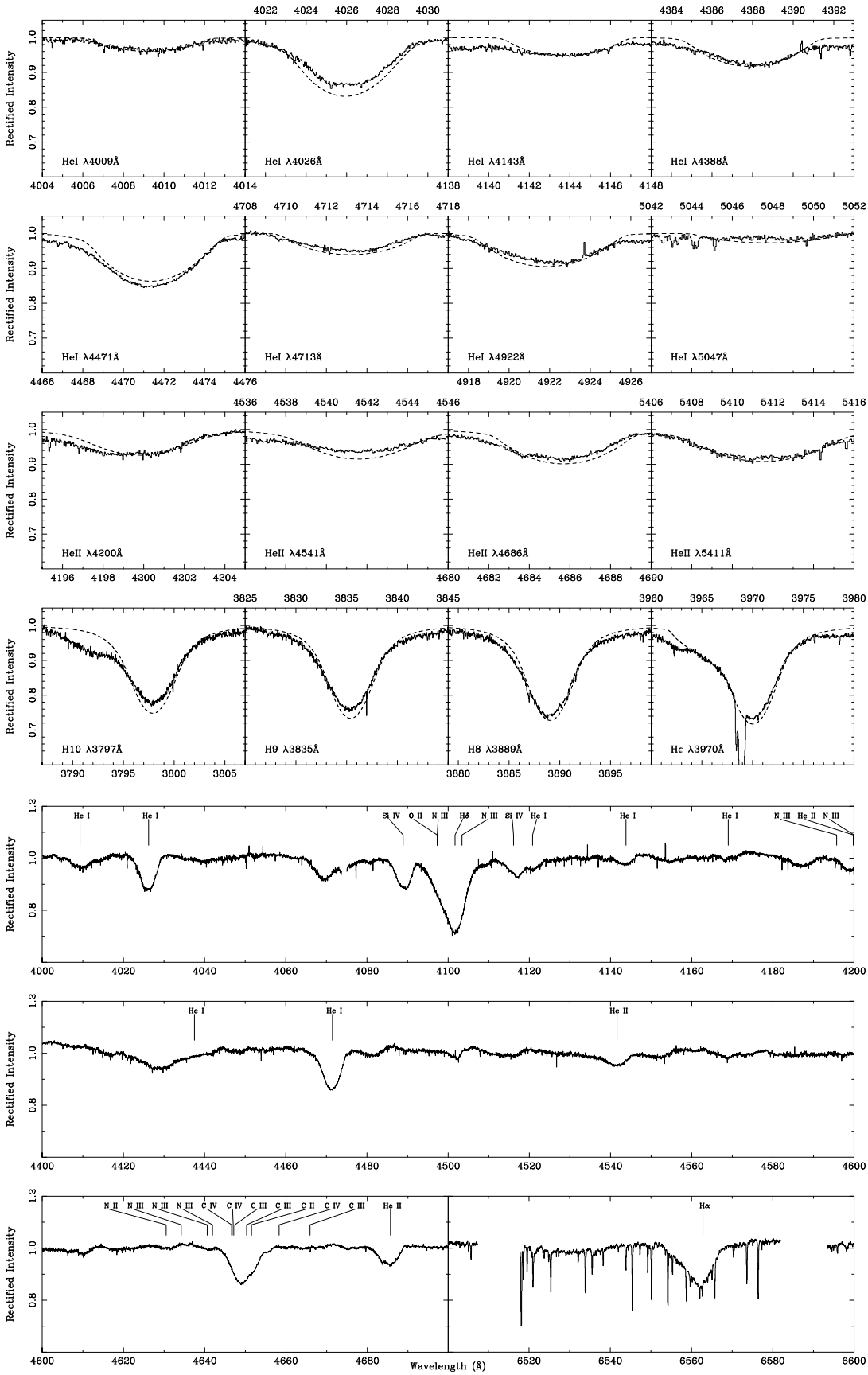
Rectified Intensity
HeI λ4009Å
HeI λ4026Å
HeI λ4143Å
HeI λ4388Å
HeI λ4471Å
HeI λ4713Å
HeI λ4922Å
HeI λ5047Å
HeII λ4200Å
HeII λ4541Å
HeII λ4686Å
HeII λ5411Å
H10 λ3797Å
H9 λ3835Å
H8 λ3889Å
Hε λ3970Å
He I
Si IV
O II
N III
Hδ
Si IV
He II
Hα
Wavelength (Å)

C.5 HD 30614

Spectral Type:	O9.5 Ia
$T_{\rm eff}$:	33000 K
$\log_{10} g$:	3.1
y:	0.13
Broadening function:	macroturbulent
Broadening velocity:	90 km s^{-1}

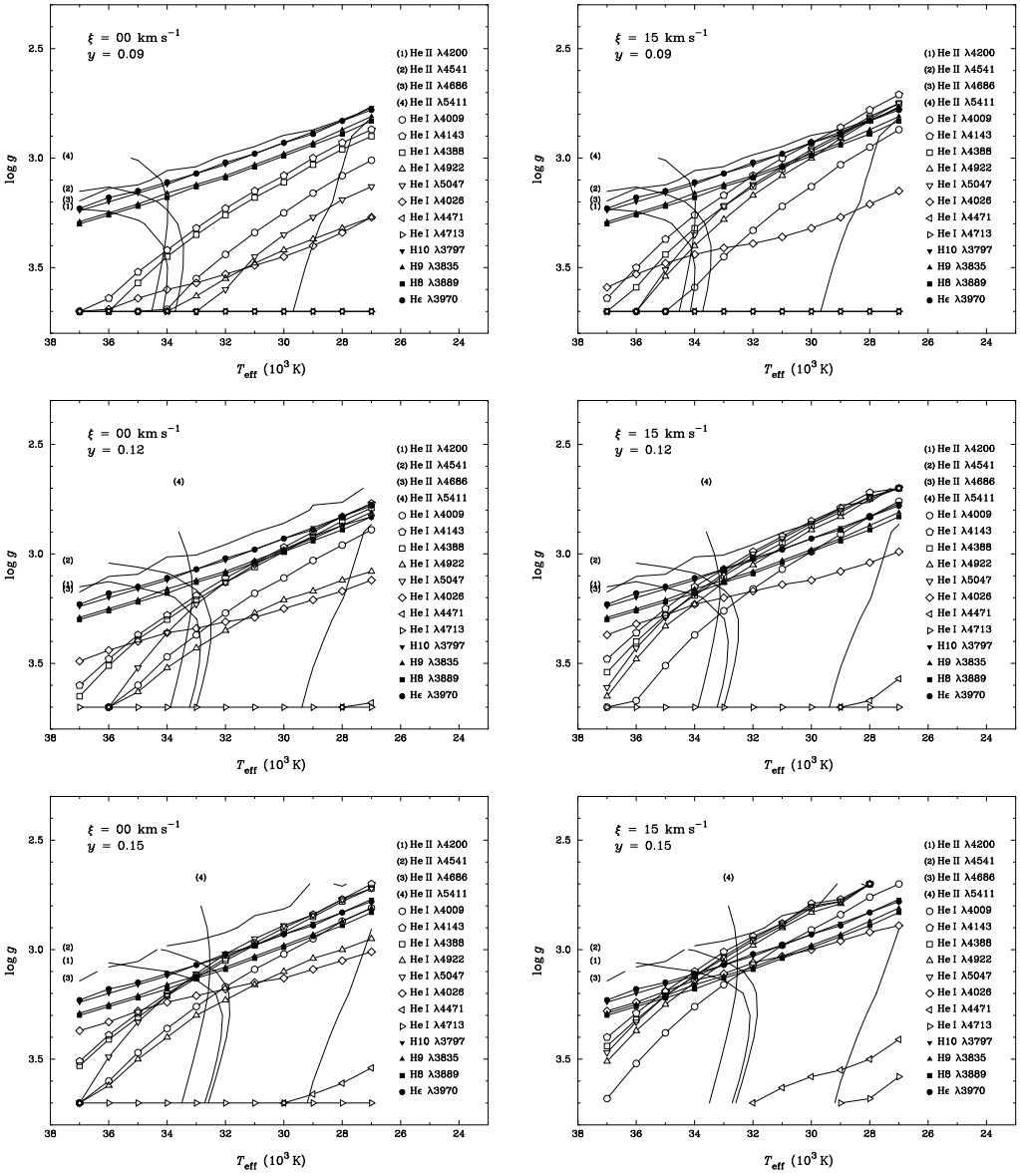

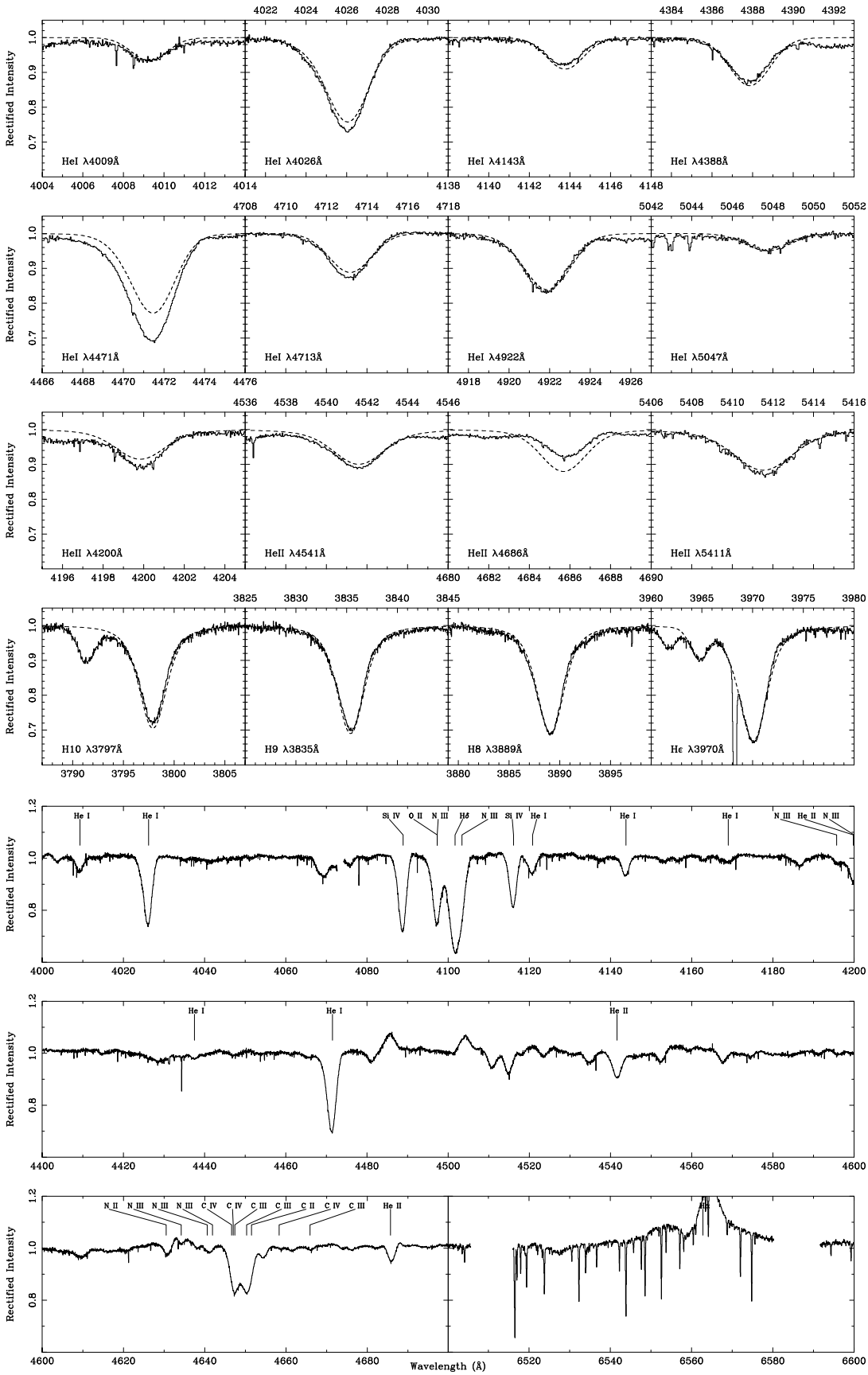
HeI λ4009Å
HeI λ4026Å
HeI λ4143Å
HeI λ4388Å
HeI λ4471Å
HeI λ4713Å
HeI λ4922Å
HeI λ5047Å
HeII λ4200Å
HeII λ4541Å
HeII λ4686Å
HeII λ5411Å
H10 λ3797Å
H9 λ3835Å
H8 λ3889Å
Hε λ3970Å
Rectified Intensity
Wavelength (Å)

C.6 HD 34078

Spectral Type:	O9.5 V
$T_{\rm eff}$:	37000 K
$\log_{10} g$:	4.2
y:	0.09
Broadening function:	rotational
Broadening velocity:	30 km s^{-1}

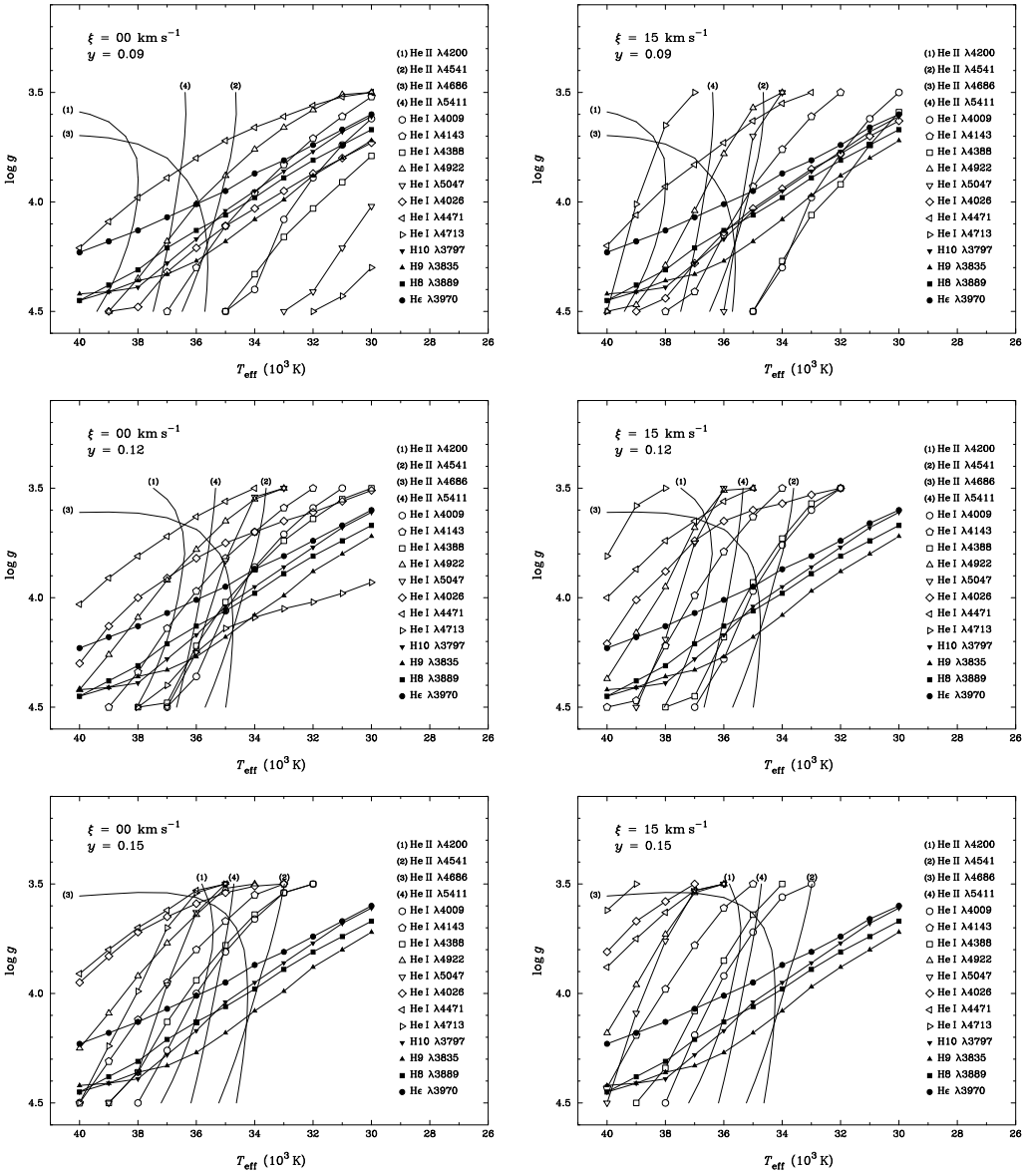

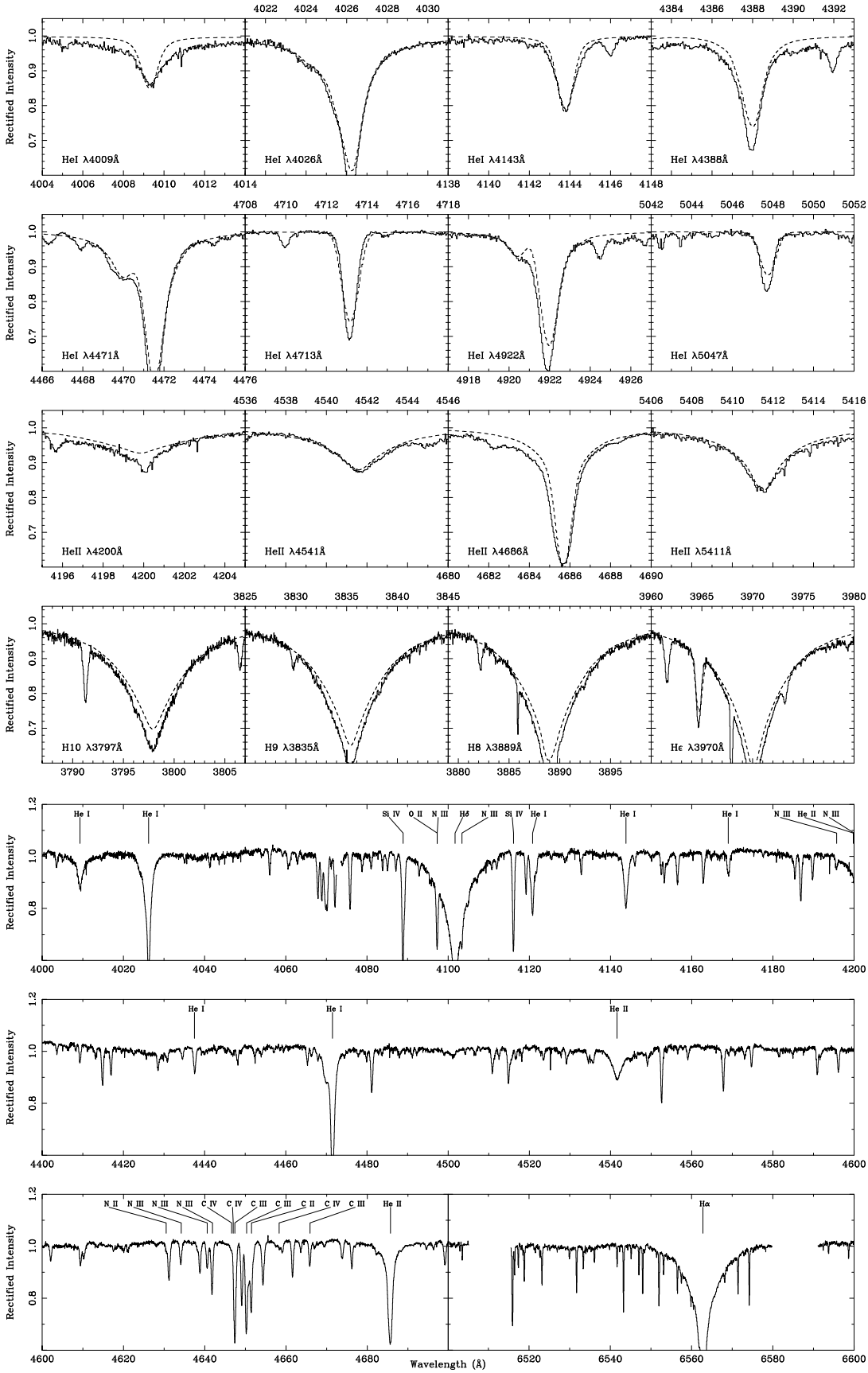
HeI λ4009Å
HeI λ4026Å
HeI λ4143Å
HeI λ4388Å
HeI λ4471Å
HeI λ4713Å
HeI λ4922Å
HeI λ5047Å
HeII λ4200Å
HeII λ4541Å
HeII λ4686Å
HeII λ5411Å
H10 λ3797Å
H9 λ3835Å
H8 λ3889Å
Hε λ3970Å
Rectified Intensity
Wavelength (Å)

C.7 HD 36486

Spectral Type:	O9.5 II
$T_{\rm eff}$:	34000 K
$\log_{10} g$:	3.4
y:	0.10
Broadening function:	macroturbulent
Broadening velocity:	126 km s^{-1}

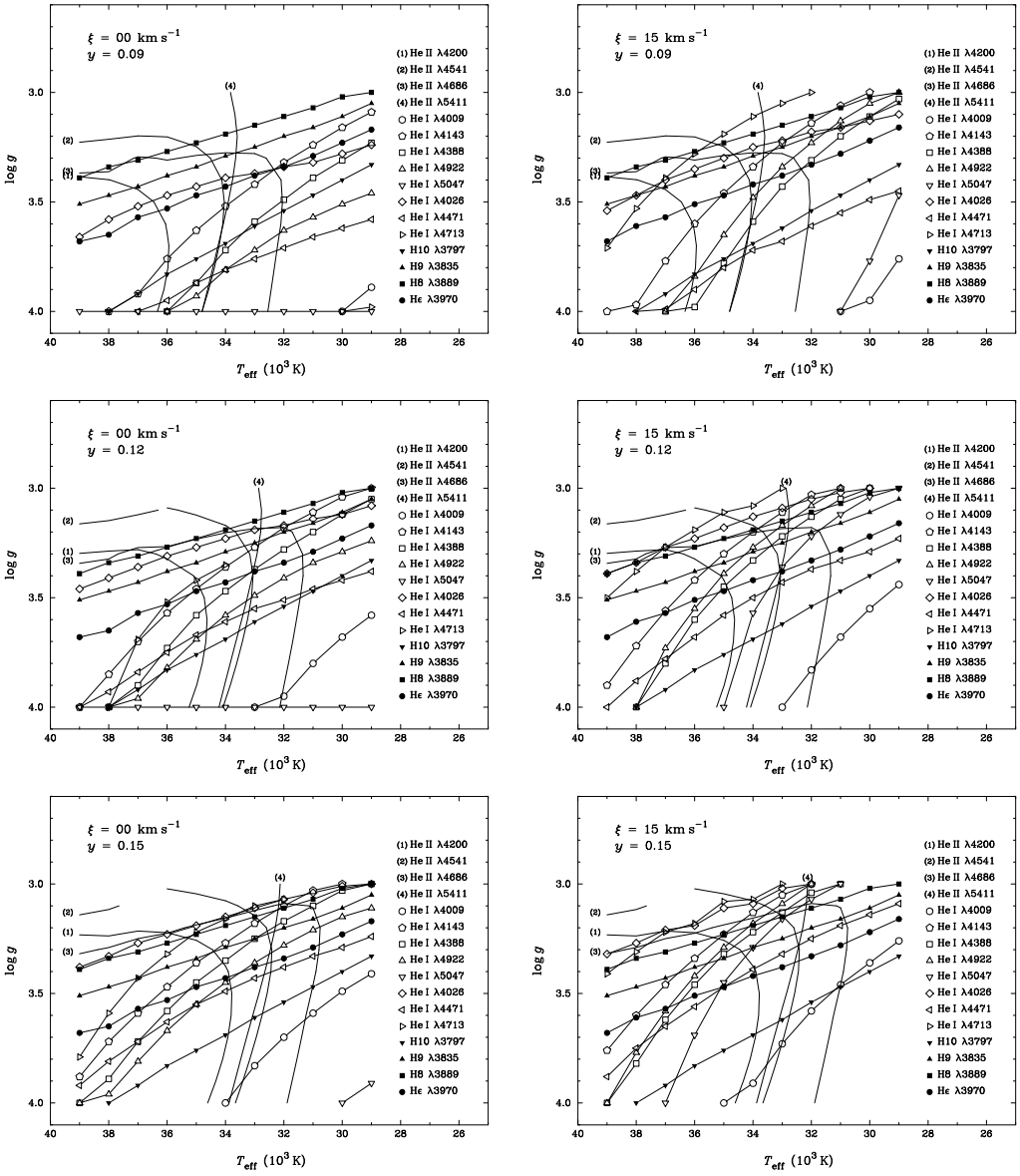

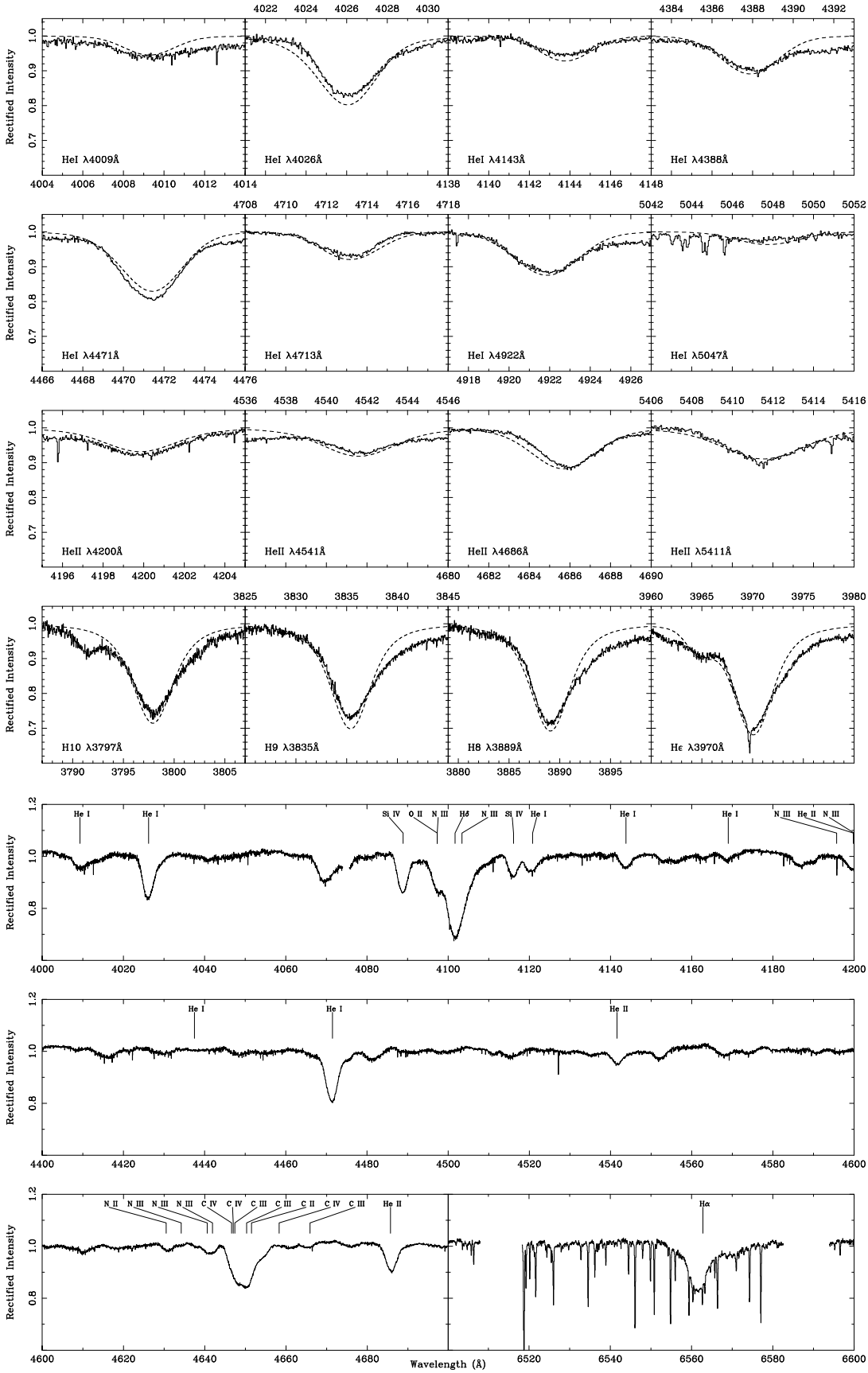
Rectified Intensity
HeI λ4009Å
HeI λ4026Å
HeI λ4143Å
HeI λ4388Å
HeI λ4471Å
HeI λ4713Å
HeI λ4922Å
HeI λ5047Å
HeII λ4200Å
HeII λ4541Å
HeII λ4686Å
HeII λ5411Å
H10 λ3797Å
H9 λ3835Å
H8 λ3889Å
Hε λ3970Å
He I
Si IV
O II
N III
Hδ
Si IV
He II
Hα
Wavelength (Å)

C.8 HD 37742

Spectral Type:	O9.7 Ib
$T_{\rm eff}$:	34000 K
$\log_{10} g$:	3.3
y:	0.10
Broadening function:	macroturbulent
Broadening velocity:	109 km s^{-1}

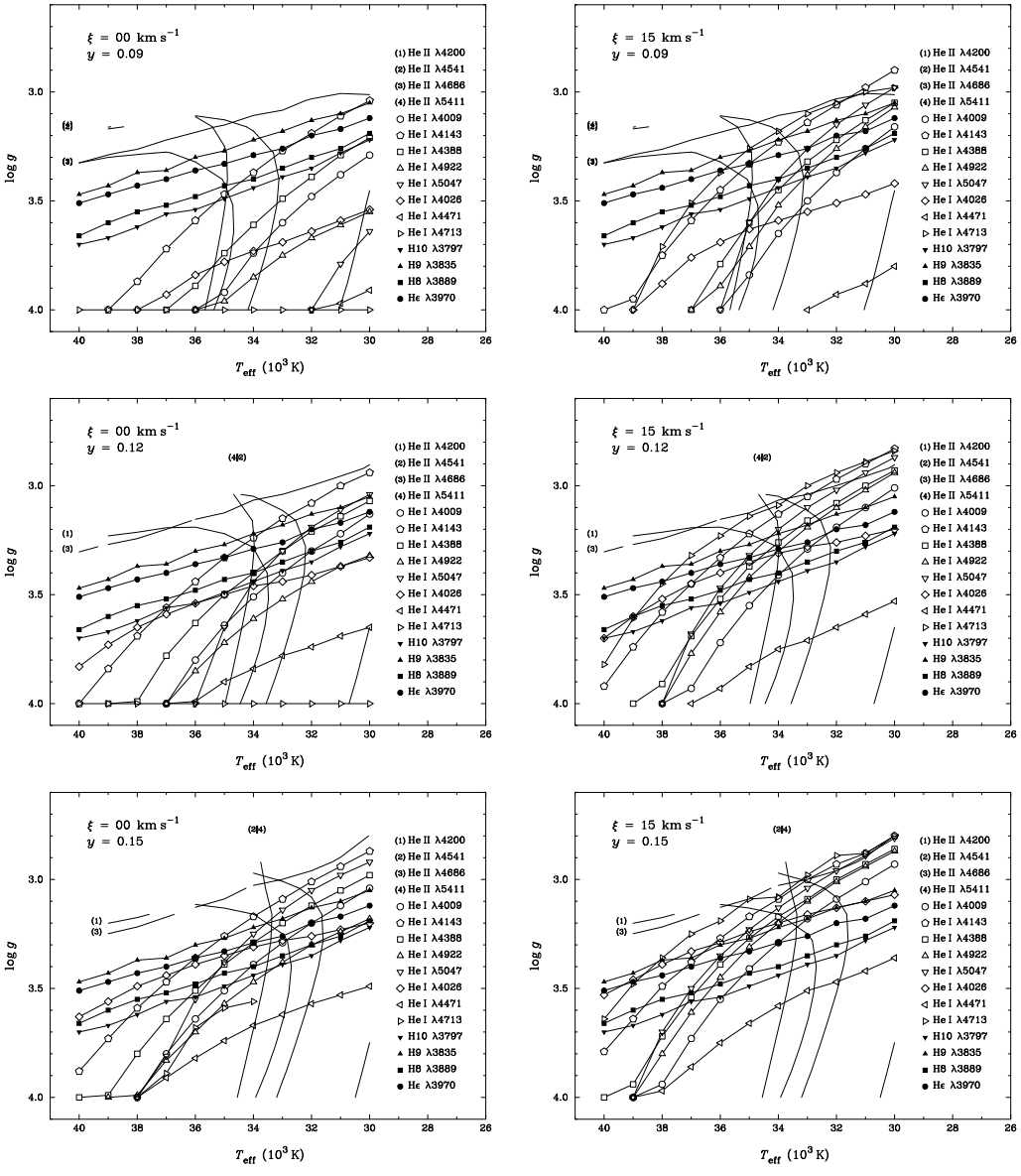

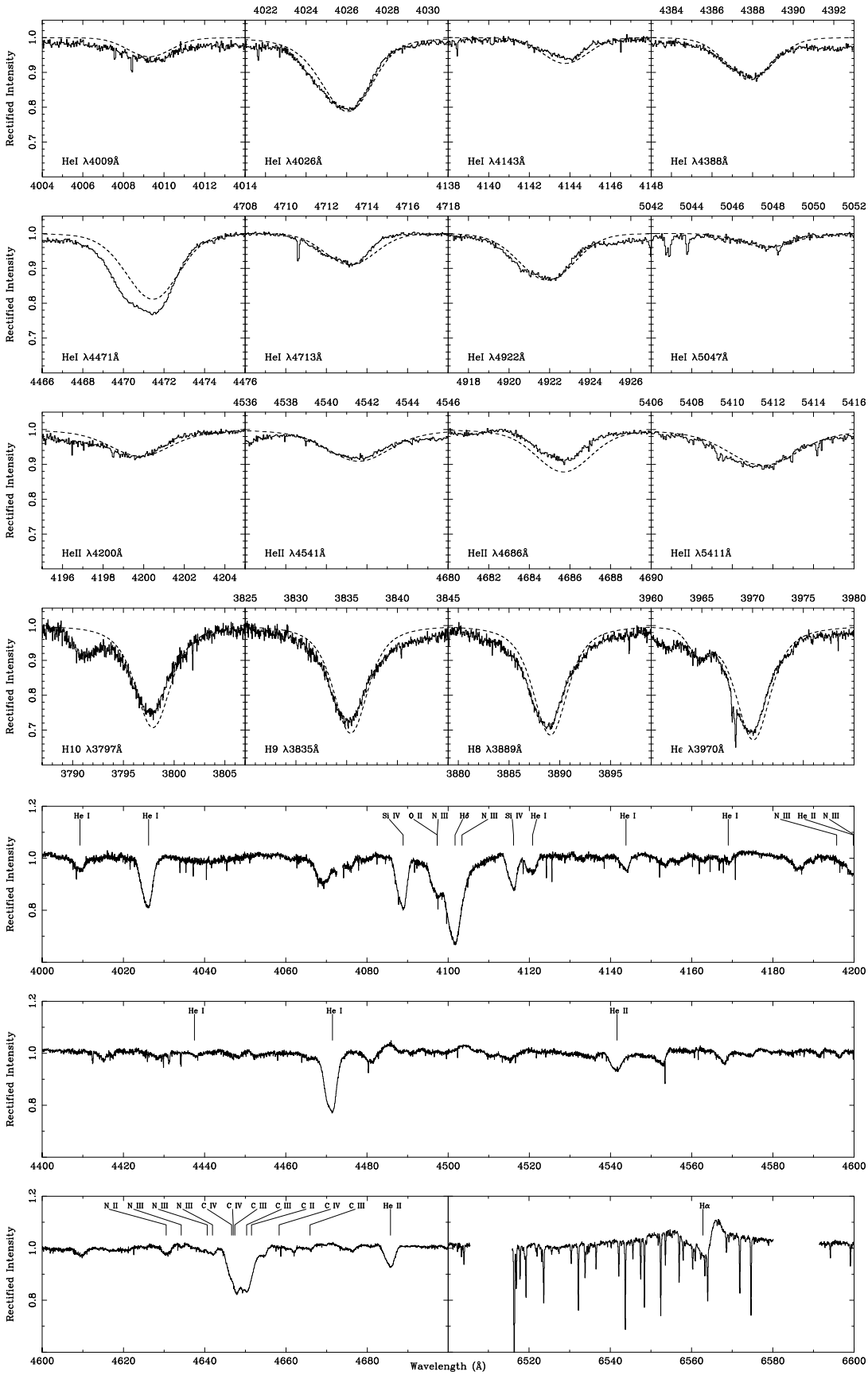
HeI λ4009Å
HeI λ4026Å
HeI λ4143Å
HeI λ4388Å
HeI λ4471Å
HeI λ4713Å
HeI λ4922Å
HeI λ5047Å
HeII λ4200Å
HeII λ4541Å
HeII λ4686Å
HeII λ5411Å
H10 λ3797Å
H9 λ3835Å
H8 λ3889Å
Hε λ3970Å
Rectified Intensity
Wavelength (Å)

C.9 HD 188209

Spectral Type:	O9.5 Iab
$T_{\rm eff}$:	33000 K
$\log_{10} g$:	3.1
y:	0.14
Broadening function:	macroturbulent
Broadening velocity:	65 km s^{-1}

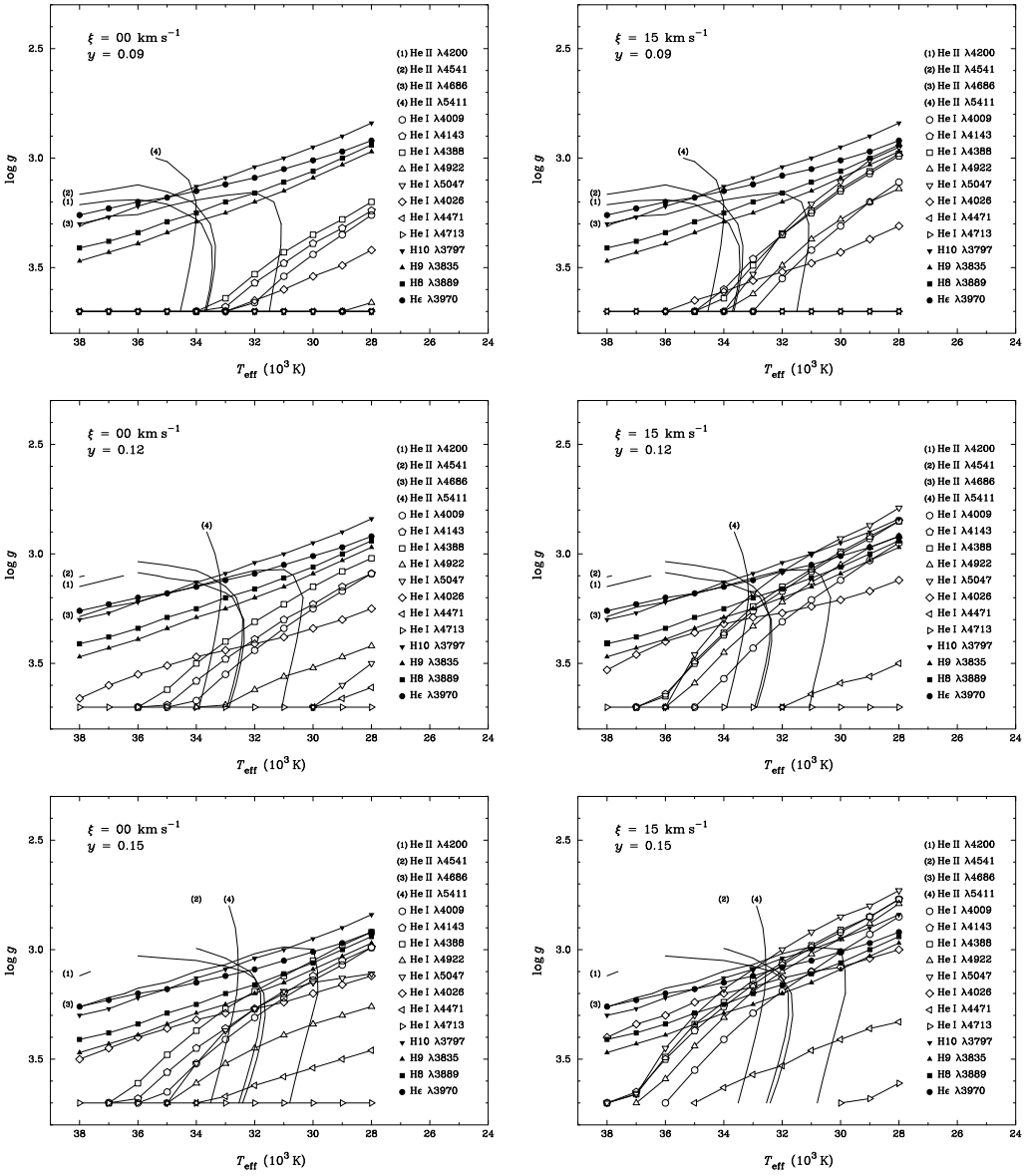

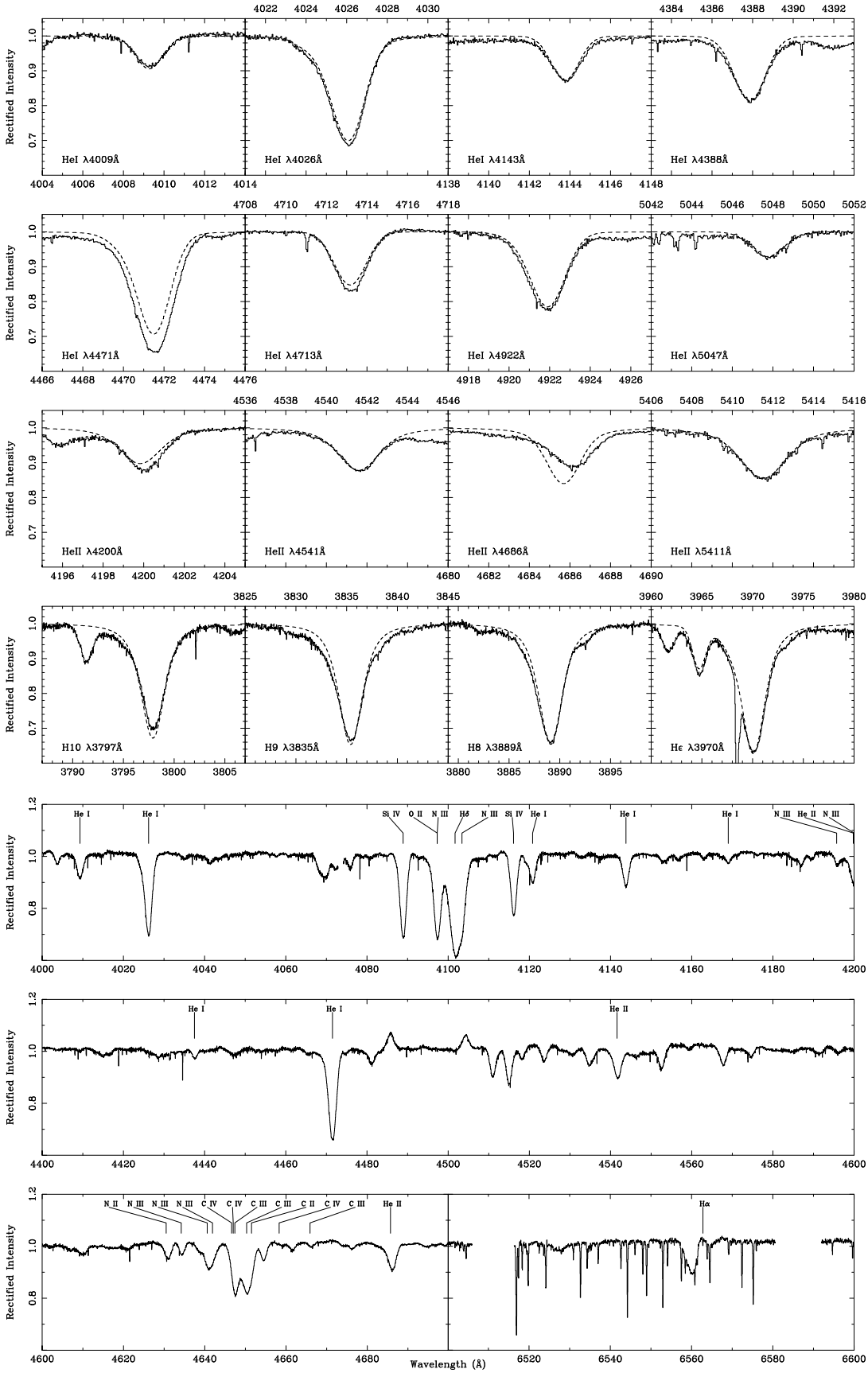
HeI λ4009Å
HeI λ4026Å
HeI λ4143Å
HeI λ4388Å
HeI λ4471Å
HeI λ4713Å
HeI λ4922Å
HeI λ5047Å
HeII λ4200Å
HeII λ4541Å
HeII λ4686Å
HeII λ5411Å
H10 λ3797Å
H9 λ3835Å
H8 λ3889Å
Hε λ3970Å
Rectified Intensity
Wavelength (Å)

C.10 HD 189957

Spectral Type:	O9.5 III
$T_{\rm eff}$:	33000 K
$\log_{10} g$:	3.5
y:	0.11
Broadening function:	macroturbulent
Broadening velocity:	85 km s^{-1}

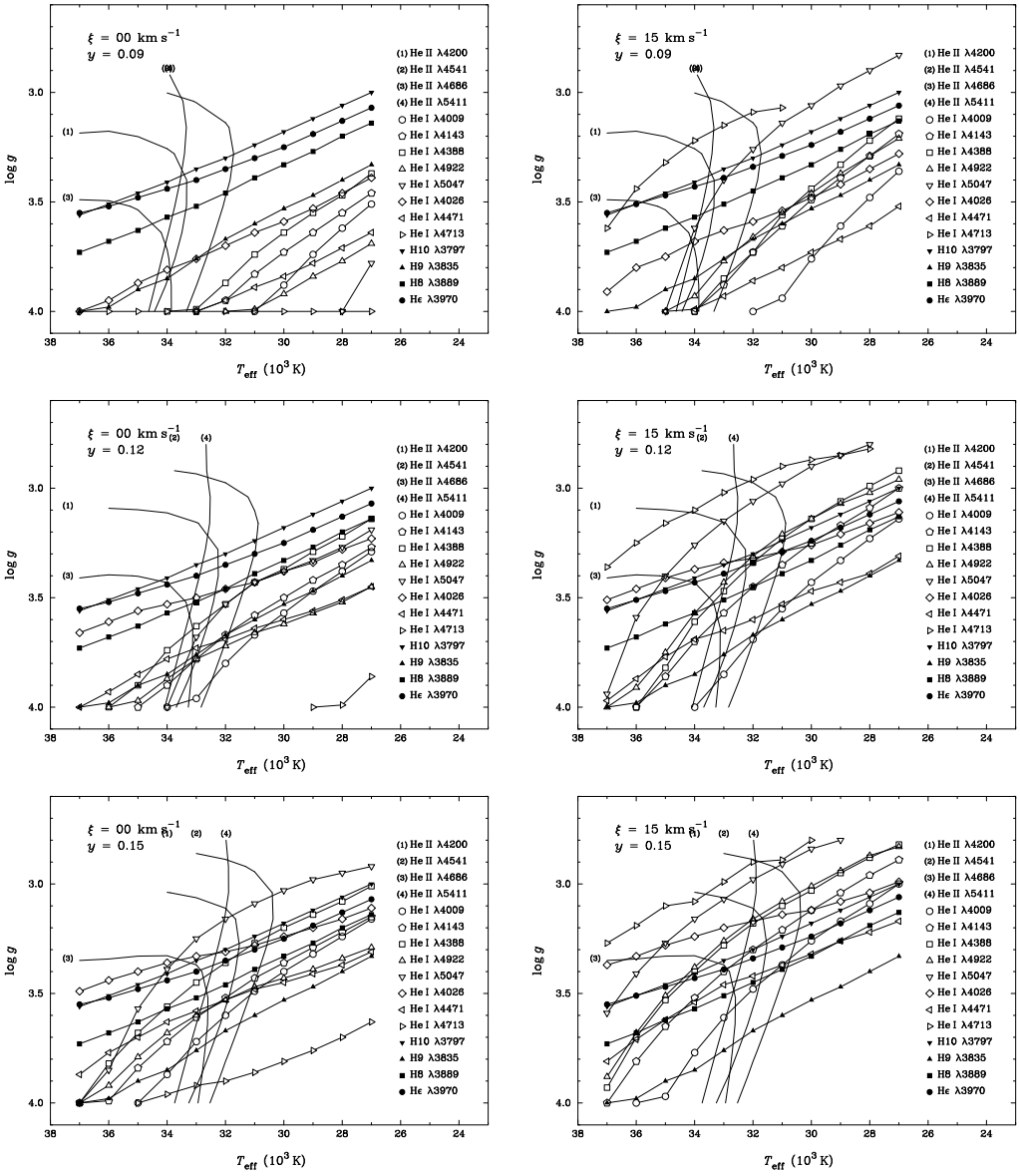

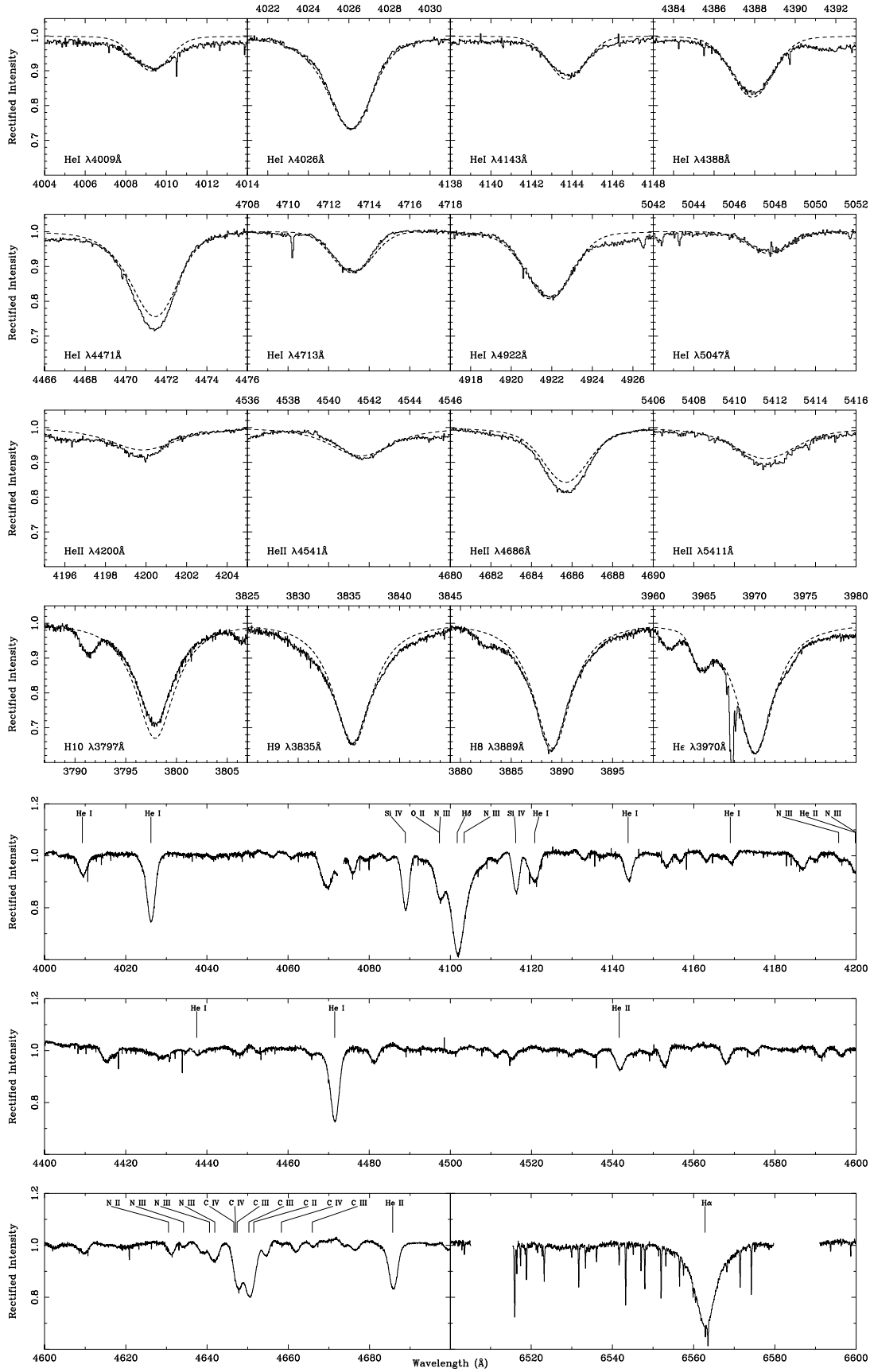
HeI λ4009Å
HeI λ4026Å
HeI λ4143Å
HeI λ4388Å
HeI λ4471Å
HeI λ4713Å
HeI λ4922Å
HeI λ5047Å
HeII λ4200Å
HeII λ4541Å
HeII λ4686Å
HeII λ5411Å
H10 λ3797Å
H9 λ3835Å
H8 λ3889Å
Hε λ3970Å
Rectified Intensity
Wavelength (Å)

C.11 HD 191781

Spectral Type:	ON9.7 Iab
$T_{\rm eff}$:	31000 K
$\log_{10} g$:	3.1
y:	0.16
Broadening function:	macroturbulent
Broadening velocity:	89 km s^{-1}

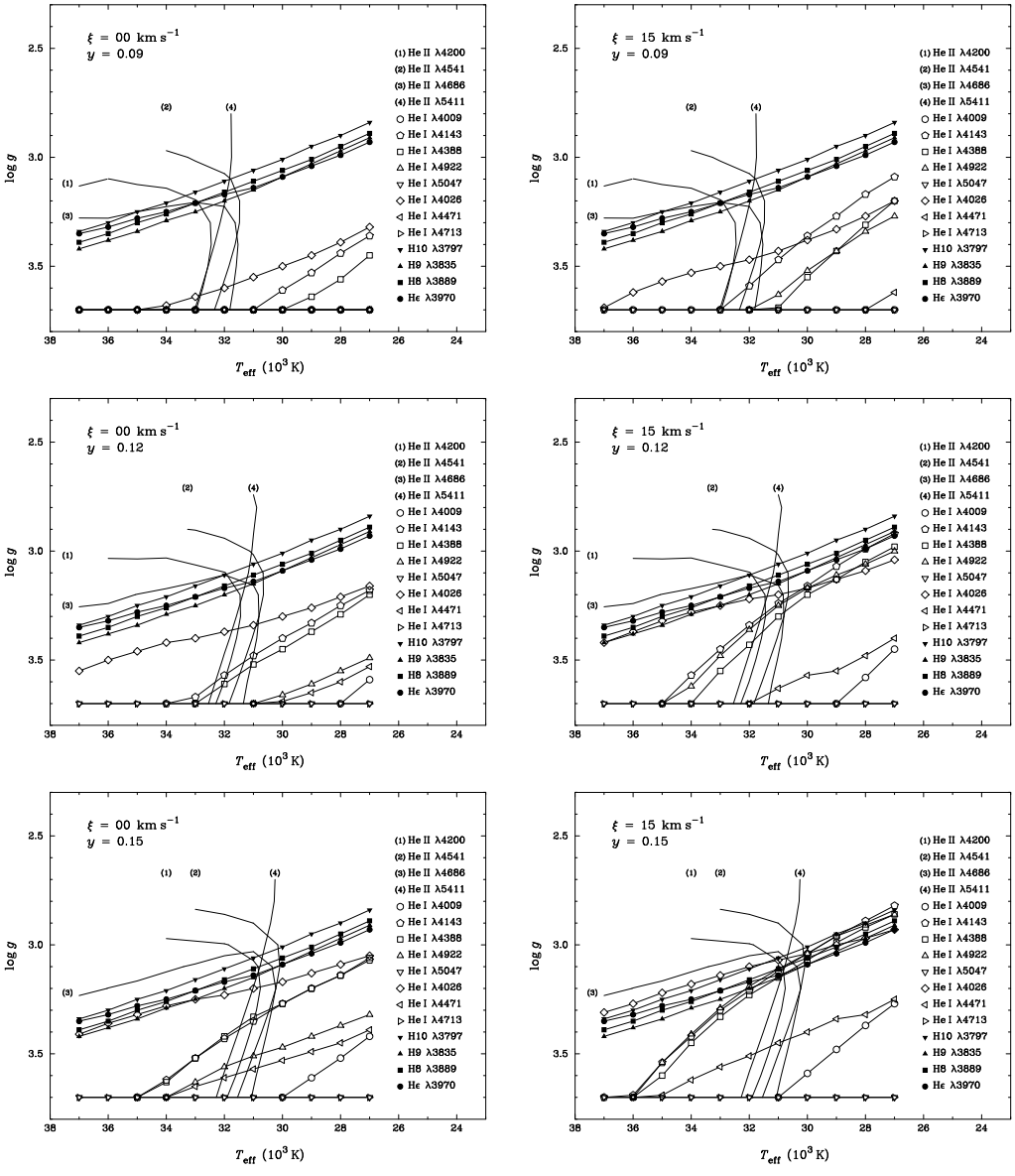

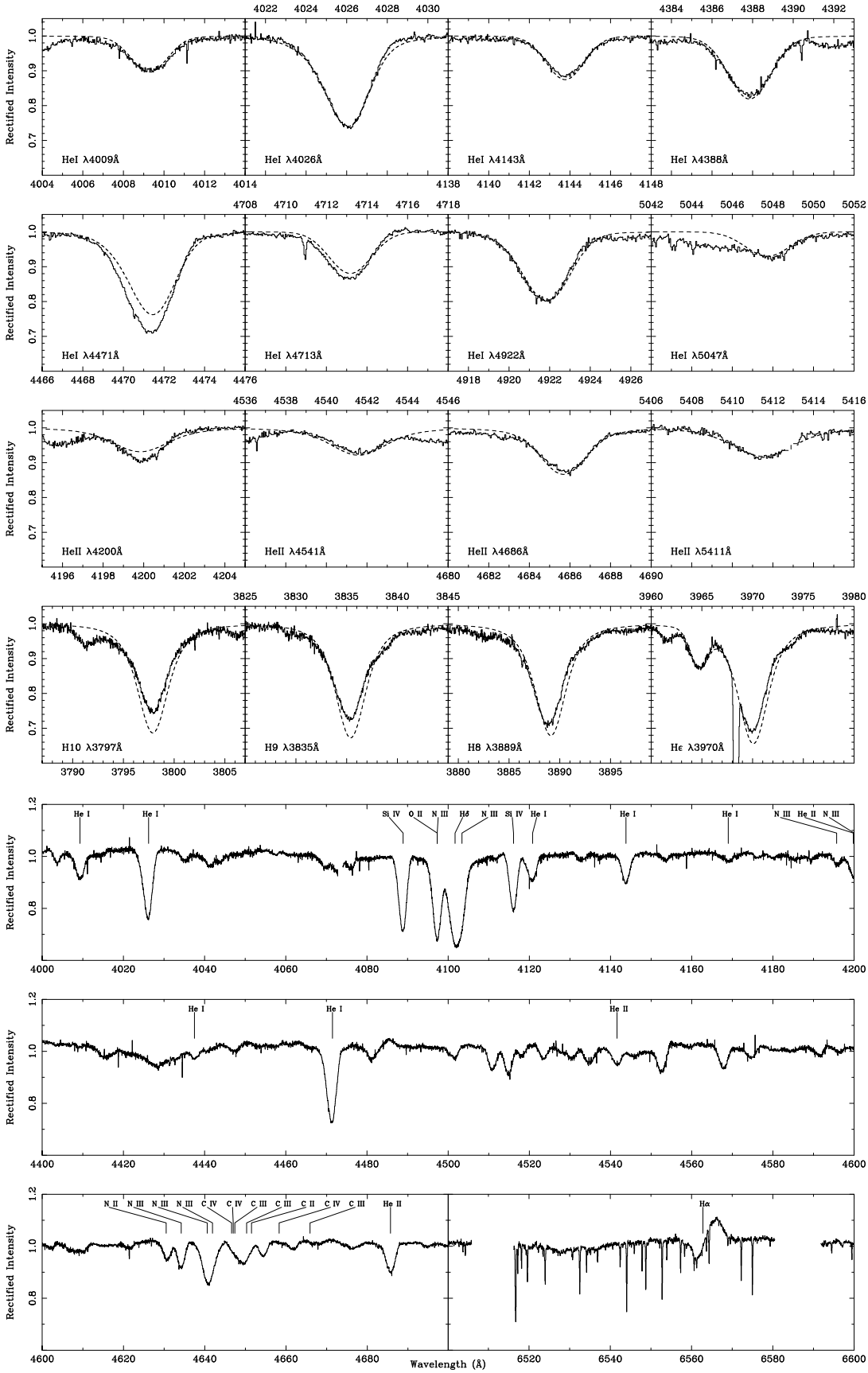
HeI λ4009Å
HeI λ4026Å
HeI λ4143Å
HeI λ4388Å
HeI λ4471Å
HeI λ4713Å
HeI λ4922Å
HeI λ5047Å
HeII λ4200Å
HeII λ4541Å
HeII λ4686Å
HeII λ5411Å
H10 λ3797Å
H9 λ3835Å
H8 λ3889Å
Hε λ3970Å
Rectified Intensity
Wavelength (Å)

C.12 HD 194280

Spectral Type:	OC9.7 Iab
$T_{\rm eff}$:	32000 K
$\log_{10} g$:	3.2
y:	0.09
Broadening function:	macroturbulent
Broadening velocity:	101 km s^{-1}

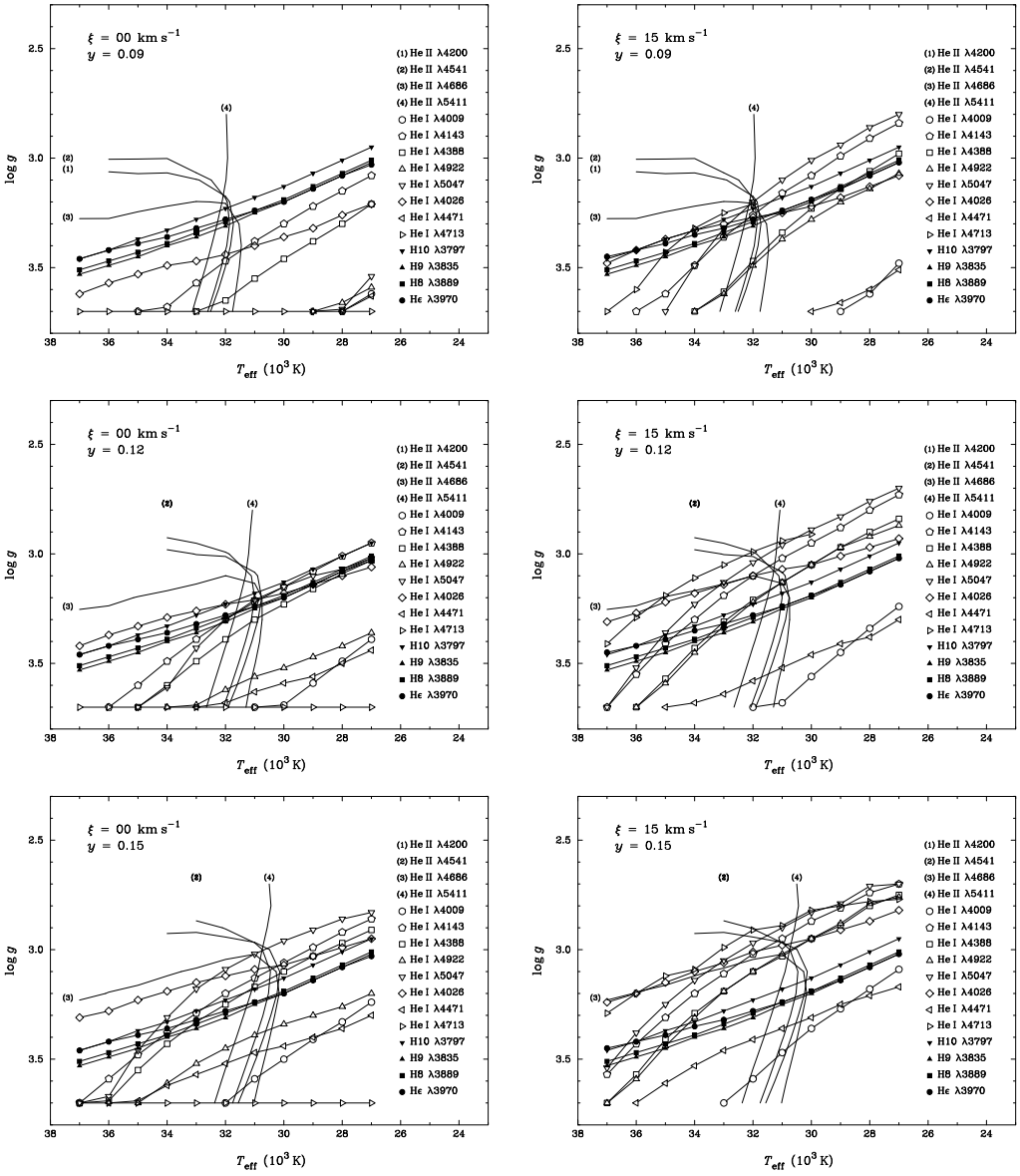

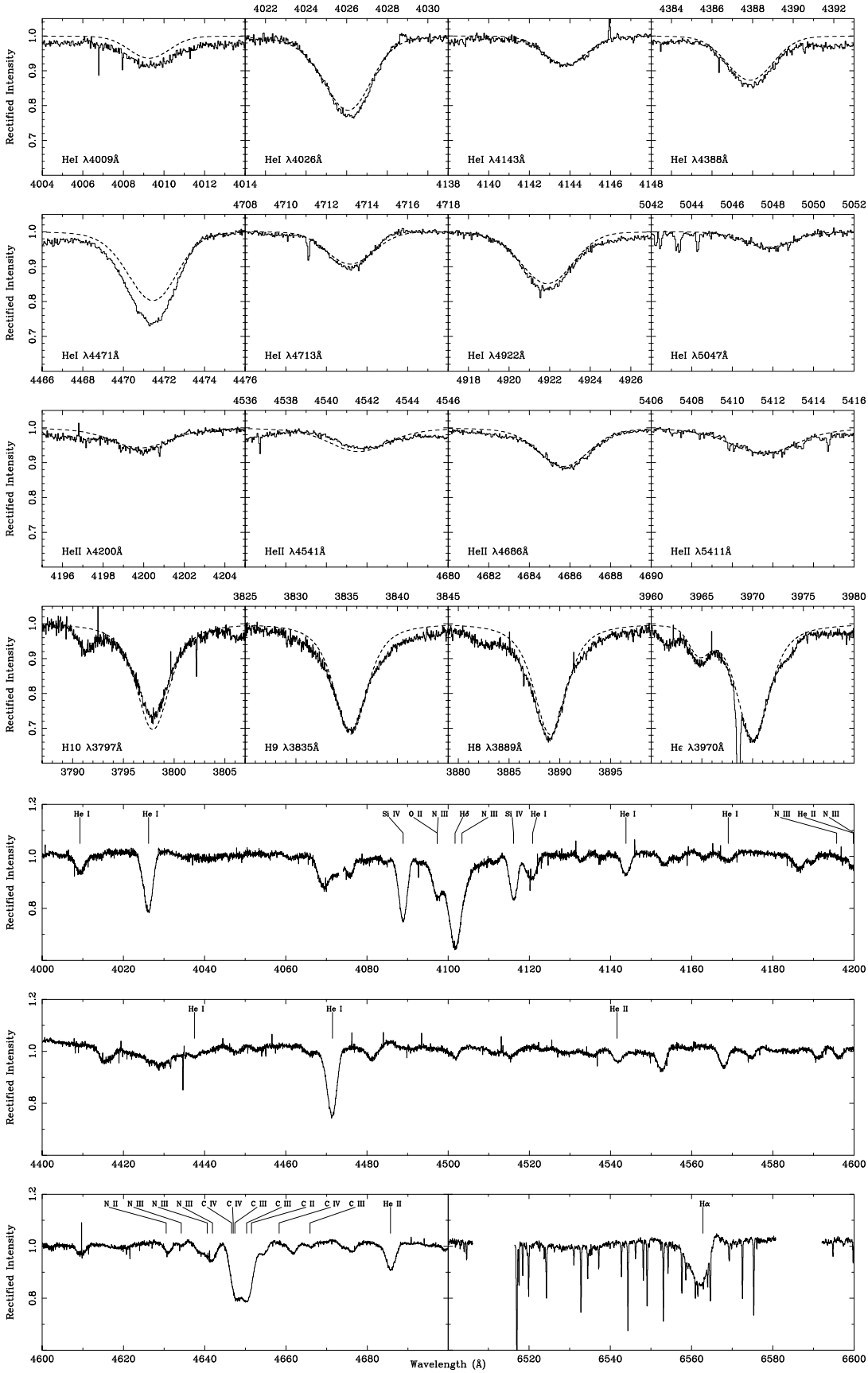
HeI λ4009Å
HeI λ4026Å
HeI λ4143Å
HeI λ4388Å
HeI λ4471Å
HeI λ4713Å
HeI λ4922Å
HeI λ5047Å
HeII λ4200Å
HeII λ4541Å
HeII λ4686Å
HeII λ5411Å
H10 λ3797Å
H9 λ3835Å
H8 λ3889Å
Hε λ3970Å
Rectified Intensity
Wavelength (Å)

C.13 HD 195592

Spectral Type:	O9.7 Ia
$T_{\rm eff}$:	31000 K
$\log_{10} g$:	3.0
y:	0.12
Broadening function:	macroturbulent
Broadening velocity:	54 km s^{-1}

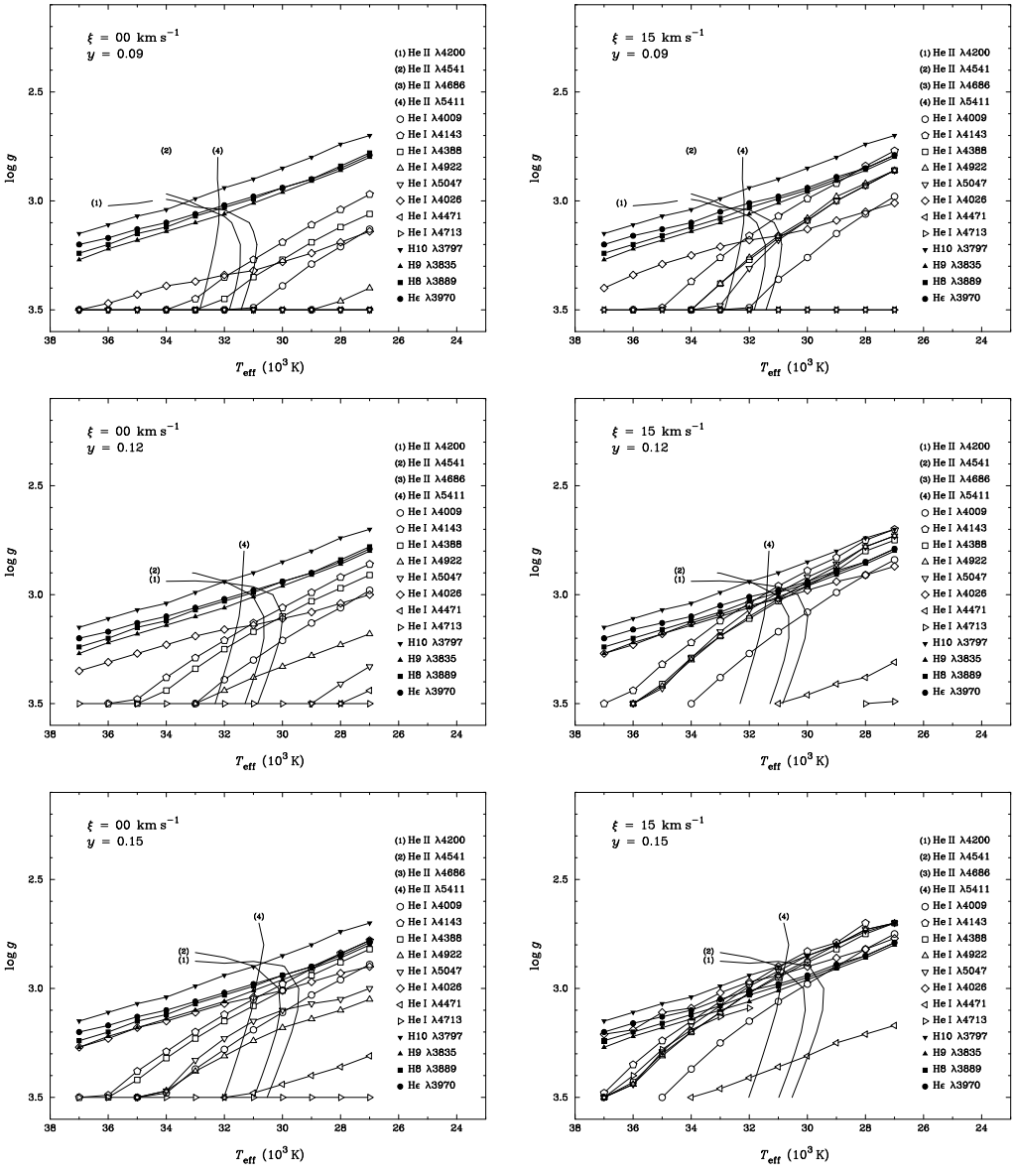

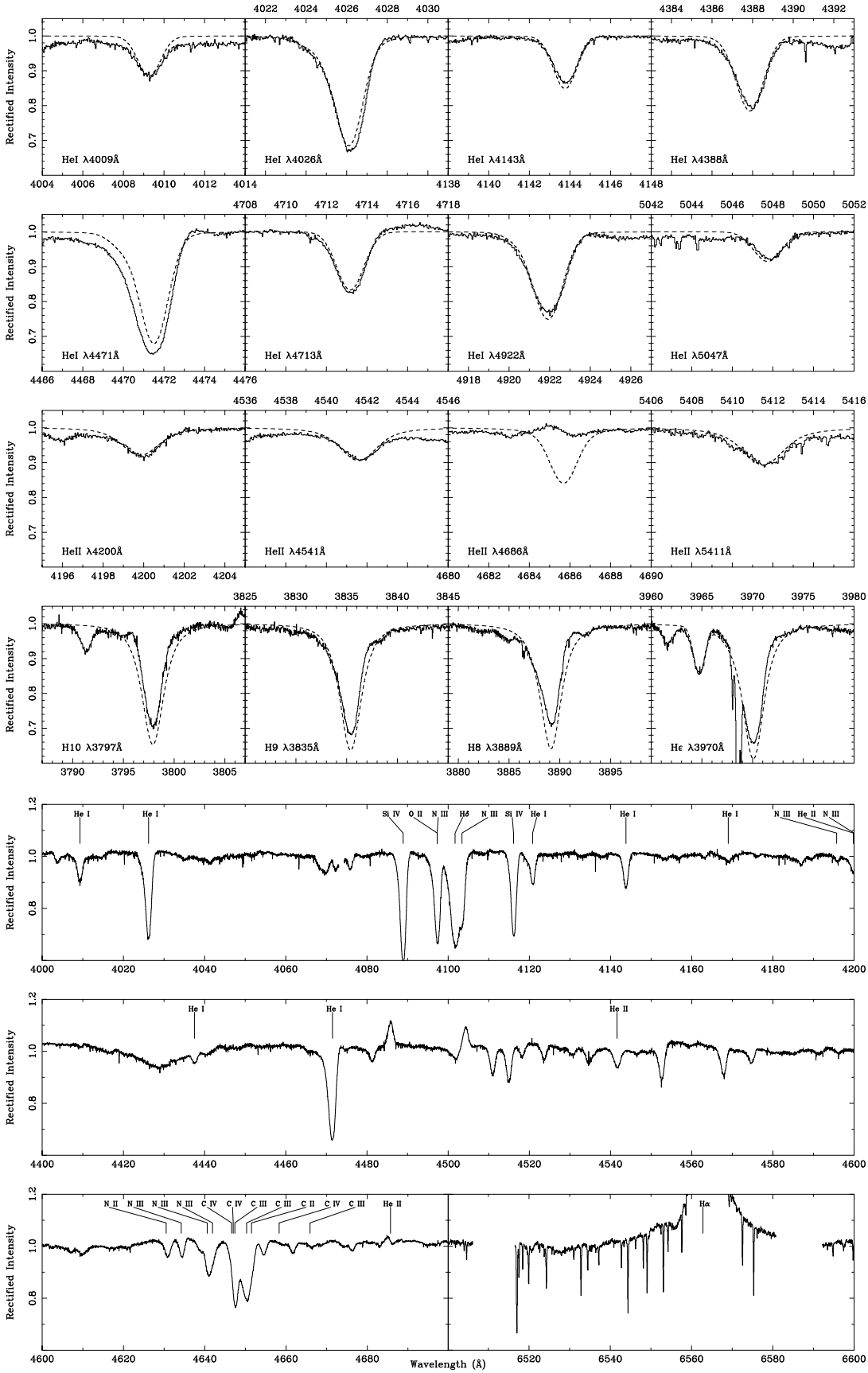
HeI λ4009Å
HeI λ4026Å
HeI λ4143Å
HeI λ4388Å
HeI λ4471Å
HeI λ4713Å
HeI λ4922Å
HeI λ5047Å
HeII λ4200Å
HeII λ4541Å
HeII λ4686Å
HeII λ5411Å
H10 λ3797Å
H9 λ3835Å
H8 λ3889Å
Hε λ3970Å
Rectified Intensity
Wavelength (Å)

C.14 HD 201345

Spectral Type:	ON9 V
$T_{\rm eff}$:	36000 K
$\log_{10} g$:	3.9
y:	0.14
Broadening function:	rotational
Broadening velocity:	109 km s^{-1}

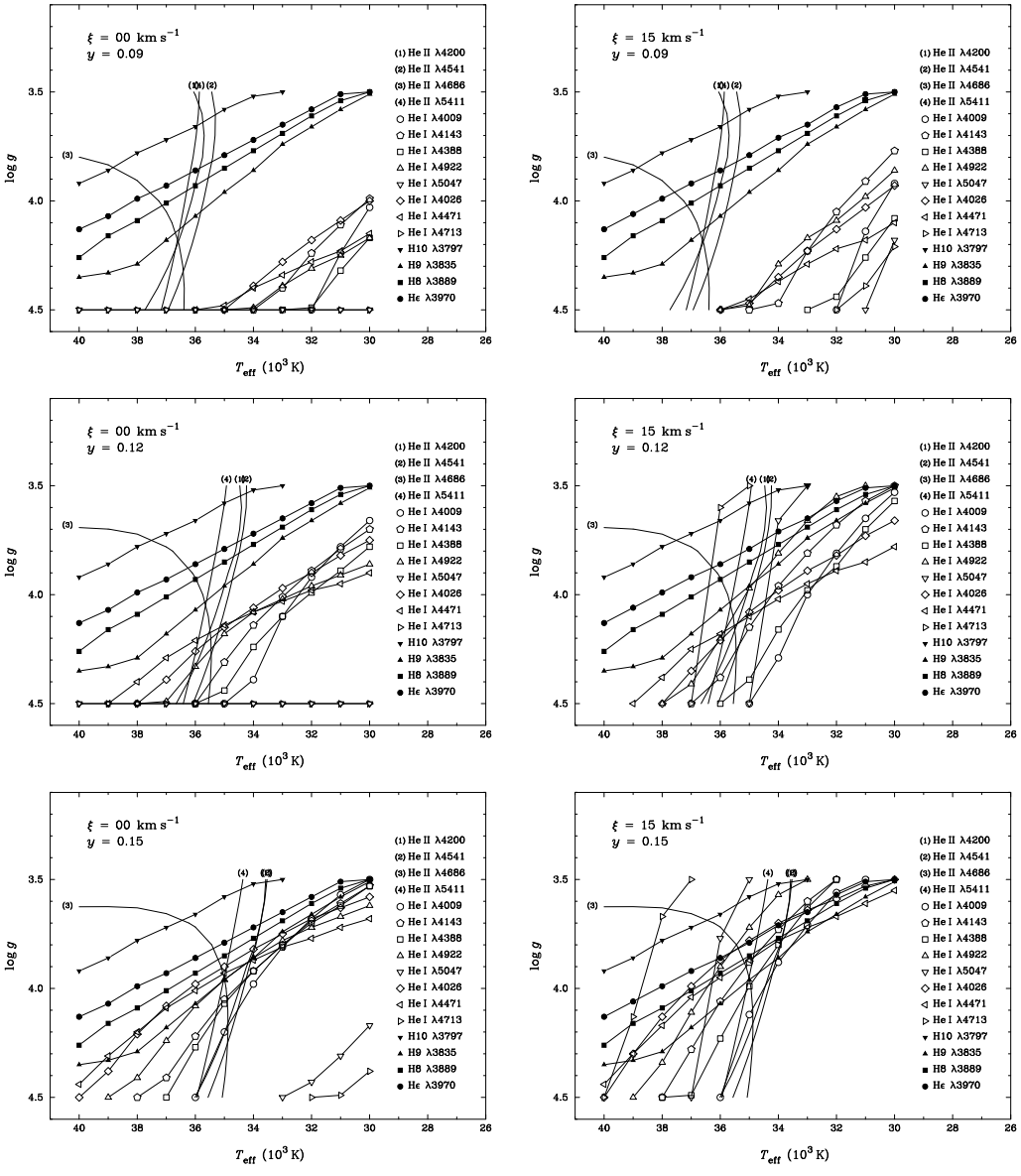

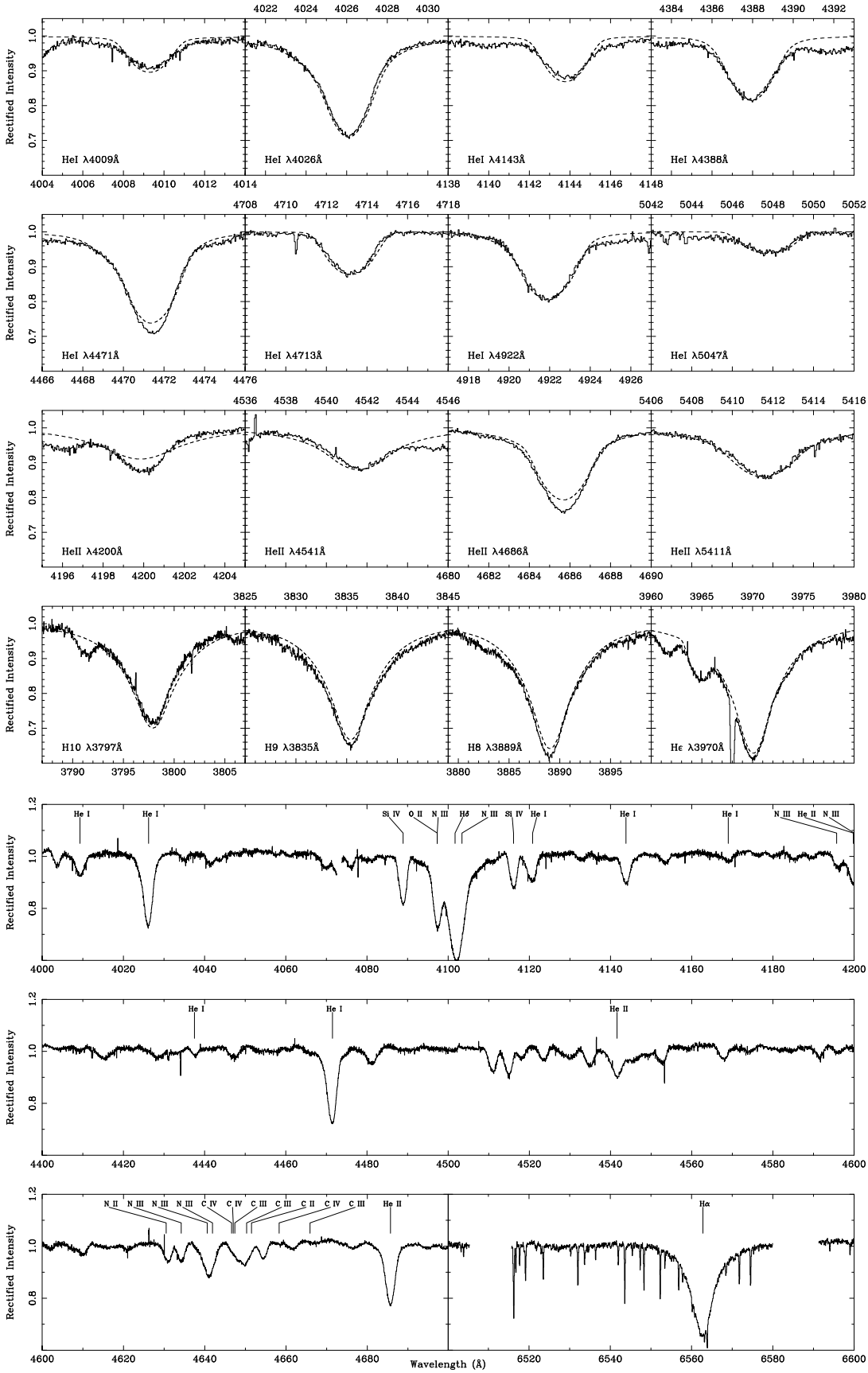
HeI λ4009Å
HeI λ4026Å
HeI λ4143Å
HeI λ4388Å
HeI λ4471Å
HeI λ4713Å
HeI λ4922Å
HeI λ5047Å
HeII λ4200Å
HeII λ4541Å
HeII λ4686Å
HeII λ5411Å
H10 λ3797Å
H9 λ3835Å
H8 λ3889Å
Hε λ3970Å
Rectified Intensity
Wavelength (Å)

C.15 HD 202124

Spectral Type:	O9.5 Iab
$T_{\rm eff}$:	34000 K
$\log_{10} g$:	3.2
y:	0.13
Broadening function:	macroturbulent
Broadening velocity:	93 km s^{-1}

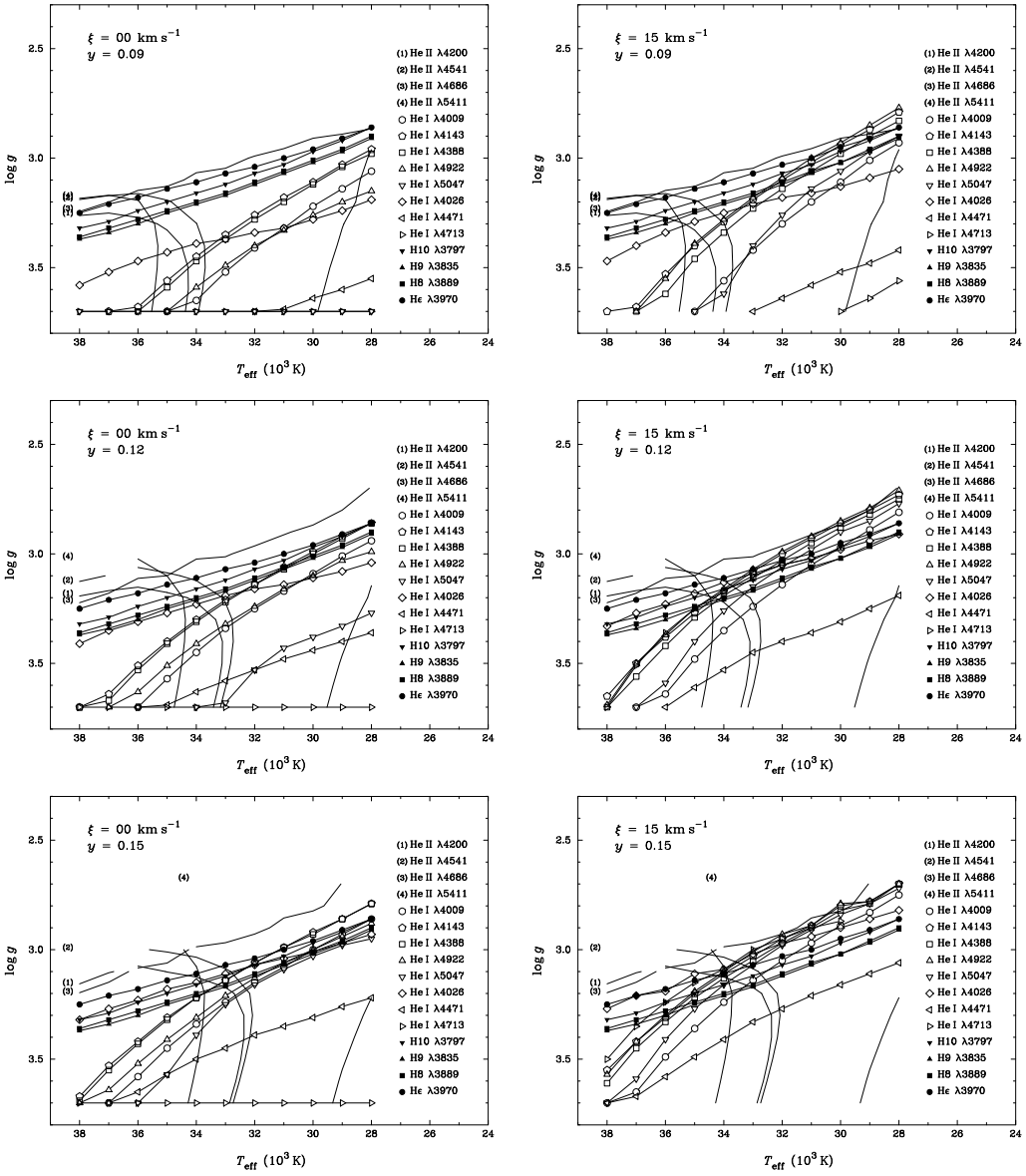

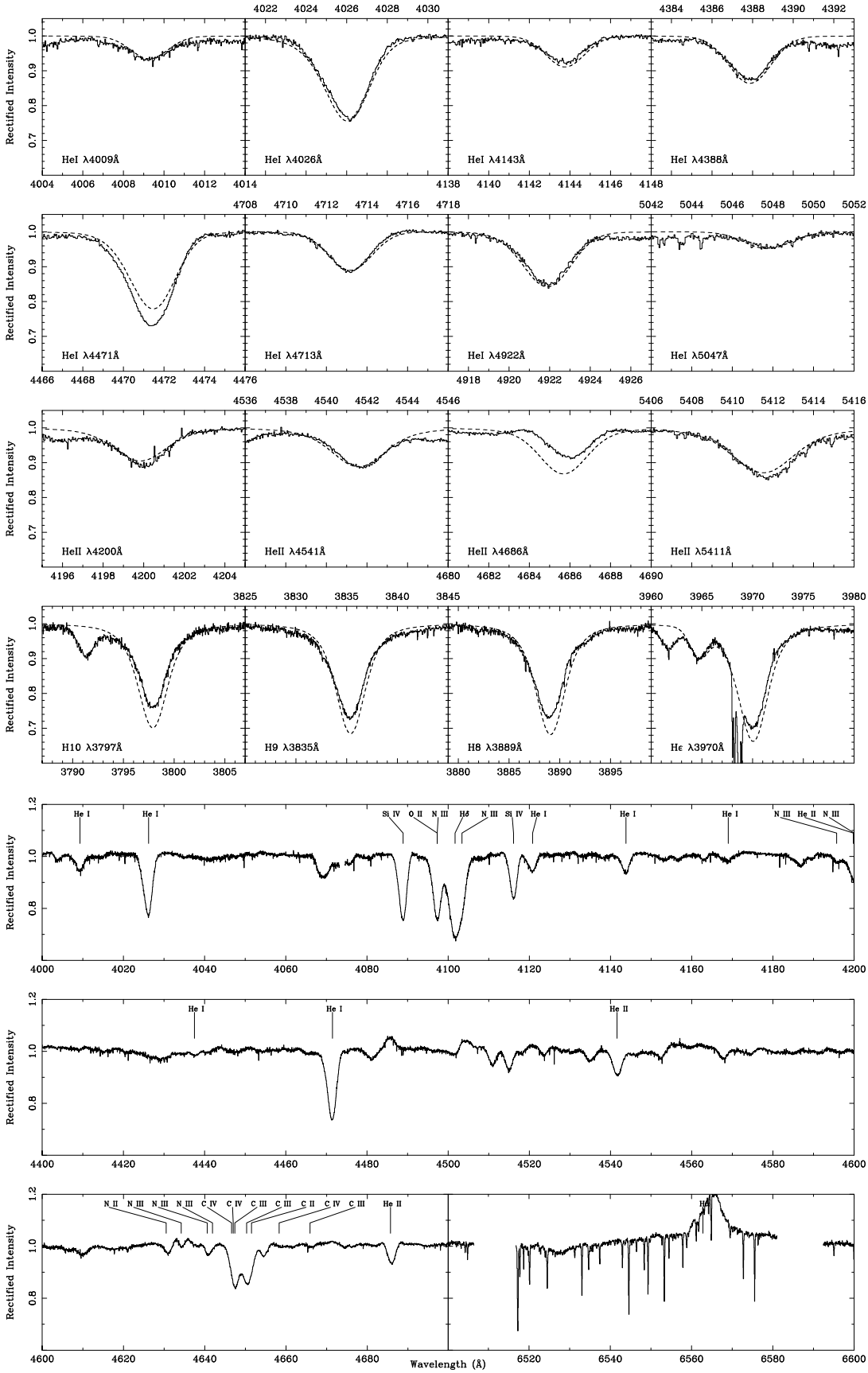
HeI λ4009Å
HeI λ4026Å
HeI λ4143Å
HeI λ4388Å
HeI λ4471Å
HeI λ4713Å
HeI λ4922Å
HeI λ5047Å
HeII λ4200Å
HeII λ4541Å
HeII λ4686Å
HeII λ5411Å
H10 λ3797Å
H9 λ3835Å
H8 λ3889Å
Hε λ3970Å
Rectified Intensity
Wavelength (Å)

C.16 HD 207198

Spectral Type:	O9 Ib-II
$T_{\rm eff}$:	36000 K
$\log_{10} g$:	3.4
y:	0.12
Broadening function:	macroturbulent
Broadening velocity:	67 km s^{-1}

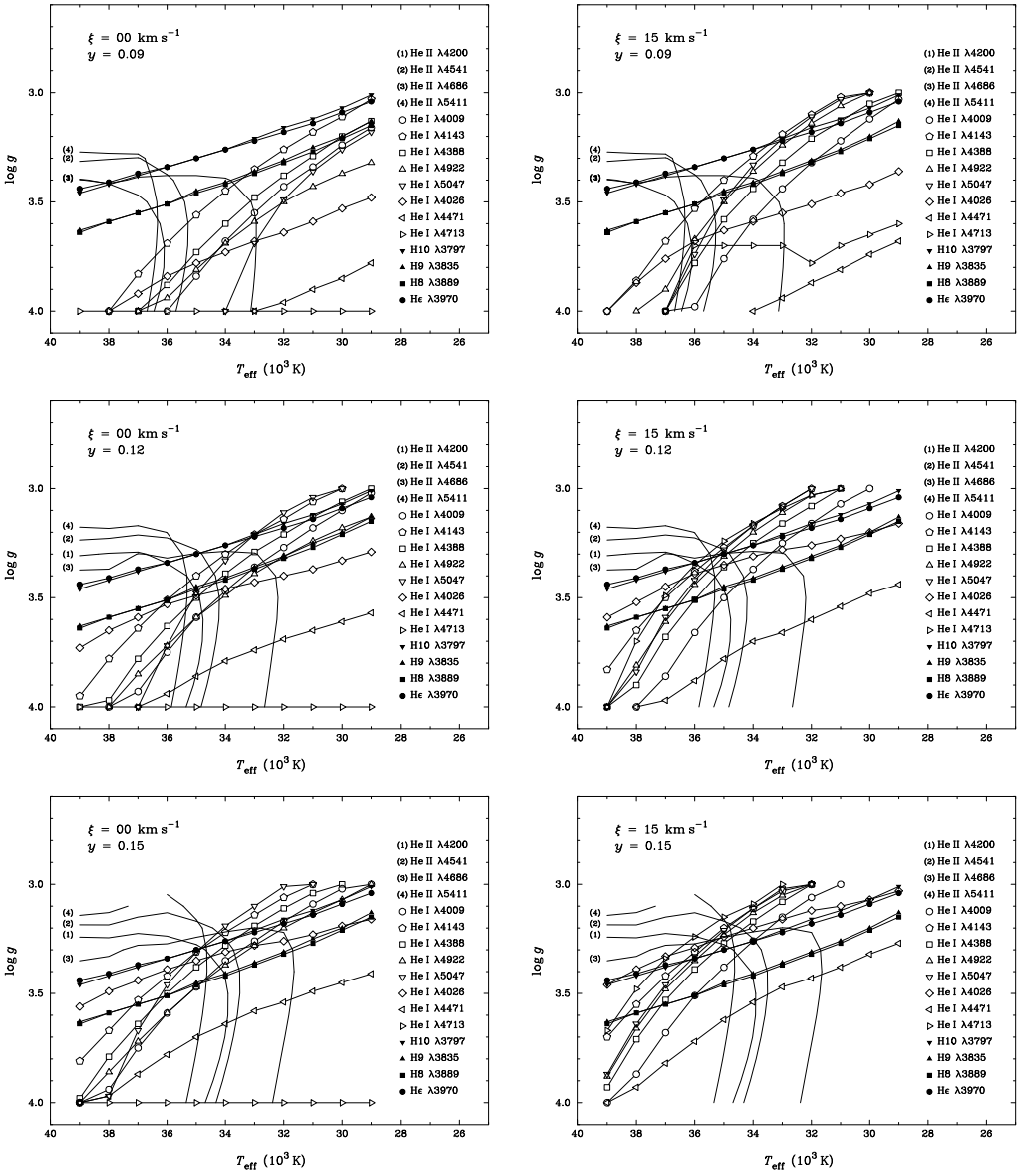

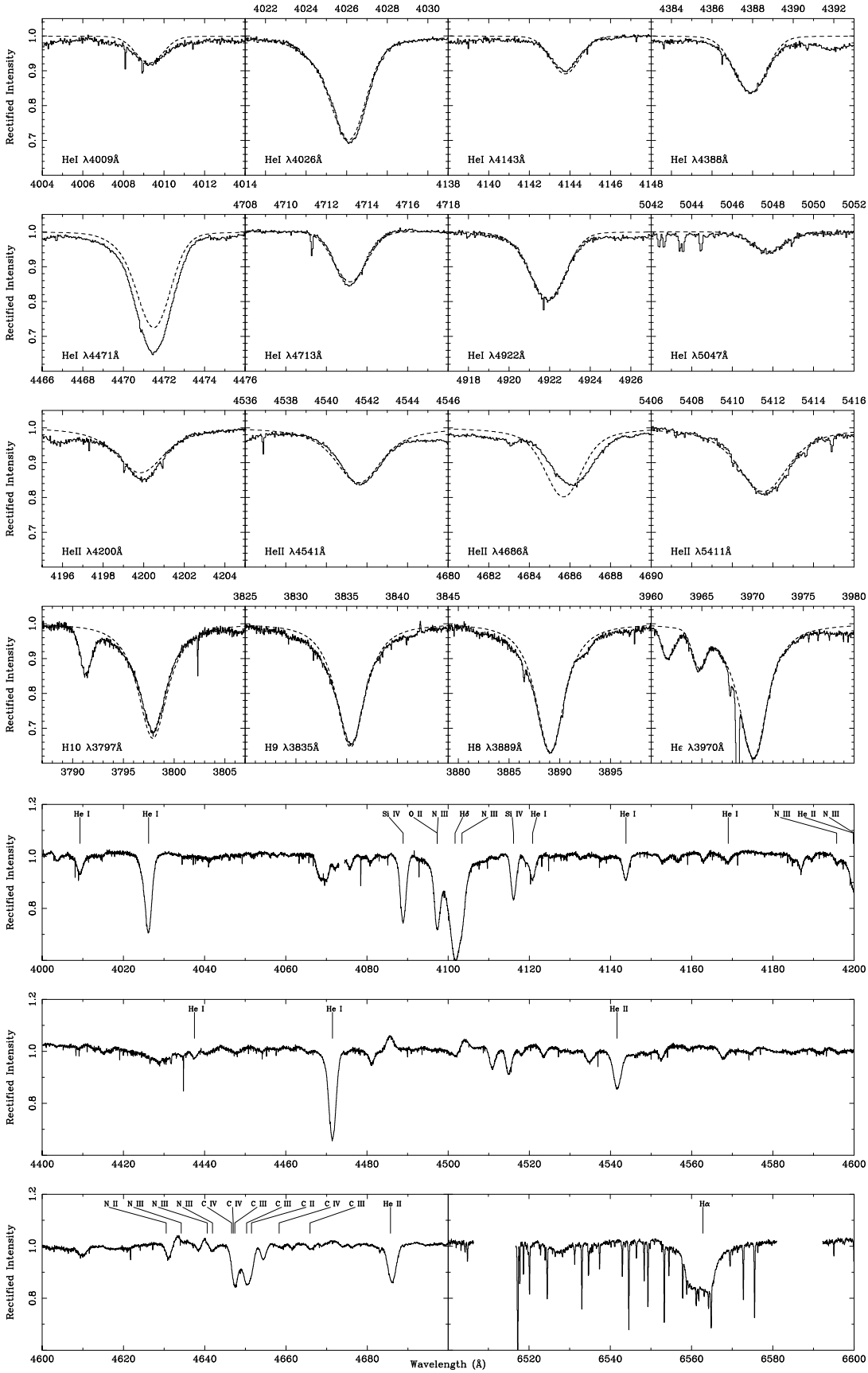
HeI λ4009Å
HeI λ4026Å
HeI λ4143Å
HeI λ4388Å
HeI λ4471Å
HeI λ4713Å
HeI λ4922Å
HeI λ5047Å
HeII λ4200Å
HeII λ4541Å
HeII λ4686Å
HeII λ5411Å
H10 λ3797Å
H9 λ3835Å
H8 λ3889Å
Hε λ3970Å
Rectified Intensity
Wavelength (Å)

C.17 HD 209975

Spectral Type:	O9.5 Ib
$T_{\rm eff}$:	35000 K
$\log_{10} g$:	3.4
y:	0.09
Broadening function:	macroturbulent
Broadening velocity:	69 km s^{-1}

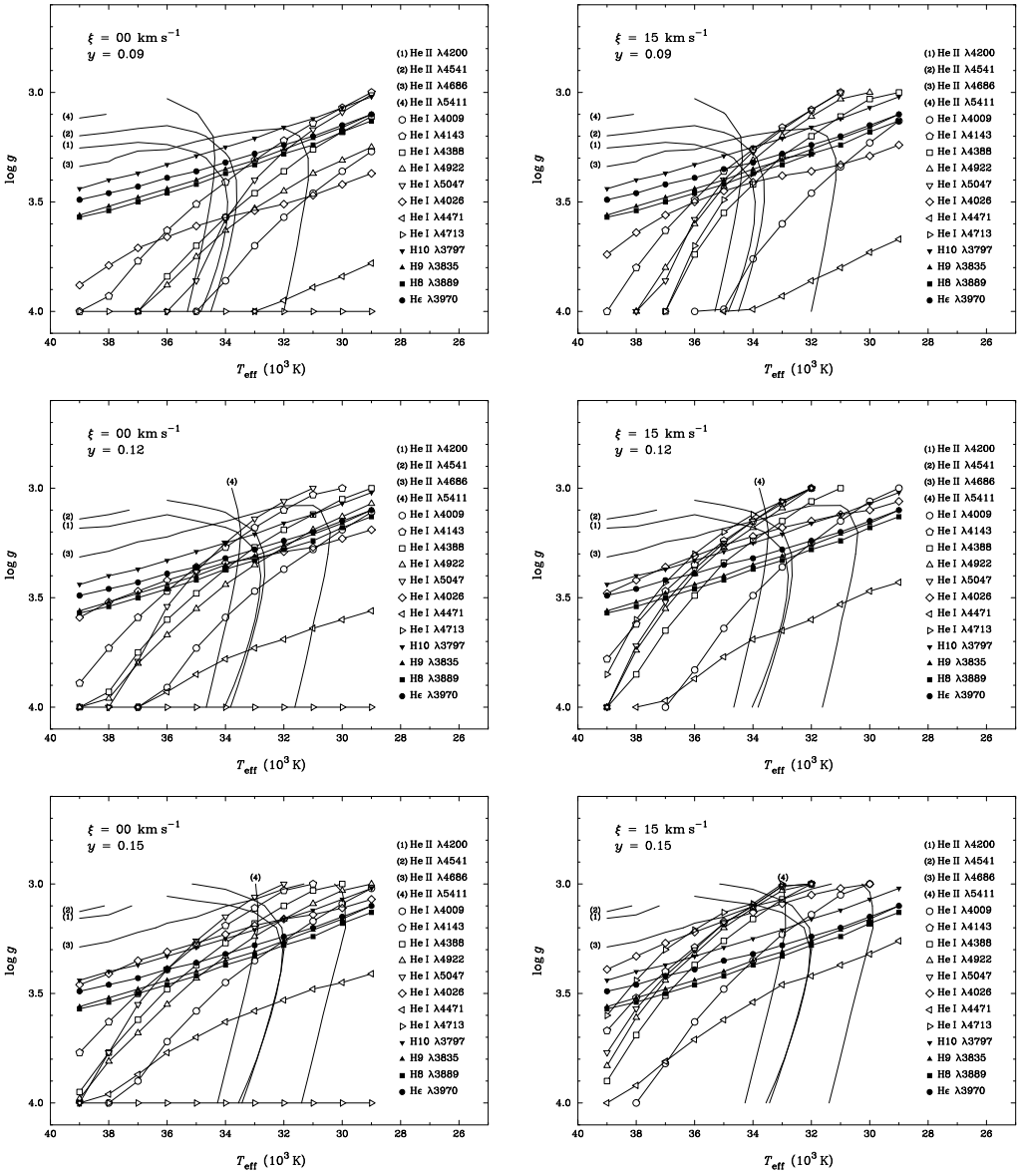

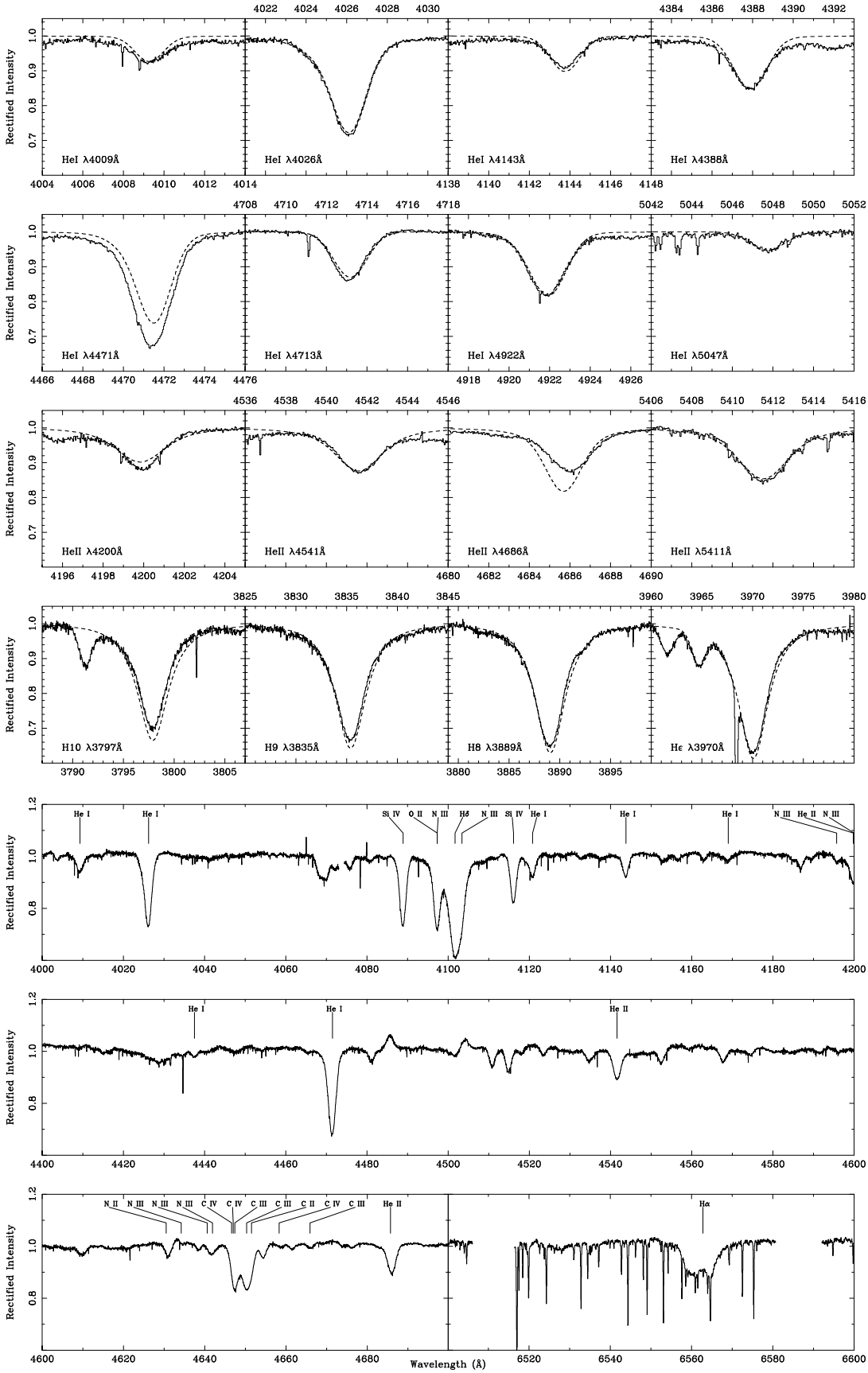
HeI λ4009Å
HeI λ4026Å
HeI λ4143Å
HeI λ4388Å
HeI λ4471Å
HeI λ4713Å
HeI λ4922Å
HeI λ5047Å
HeII λ4200Å
HeII λ4541Å
HeII λ4686Å
HeII λ5411Å
H10 λ3797Å
H9 λ3835Å
H8 λ3889Å
Hε λ3970Å
Rectified Intensity
Wavelength (Å)

C.18 HD 210809

Spectral Type:	O9 Iab
$T_{\rm eff}$:	36000 K
$\log_{10} g$:	3.3
y:	0.13
Broadening function:	macroturbulent
Broadening velocity:	89 km s^{-1}

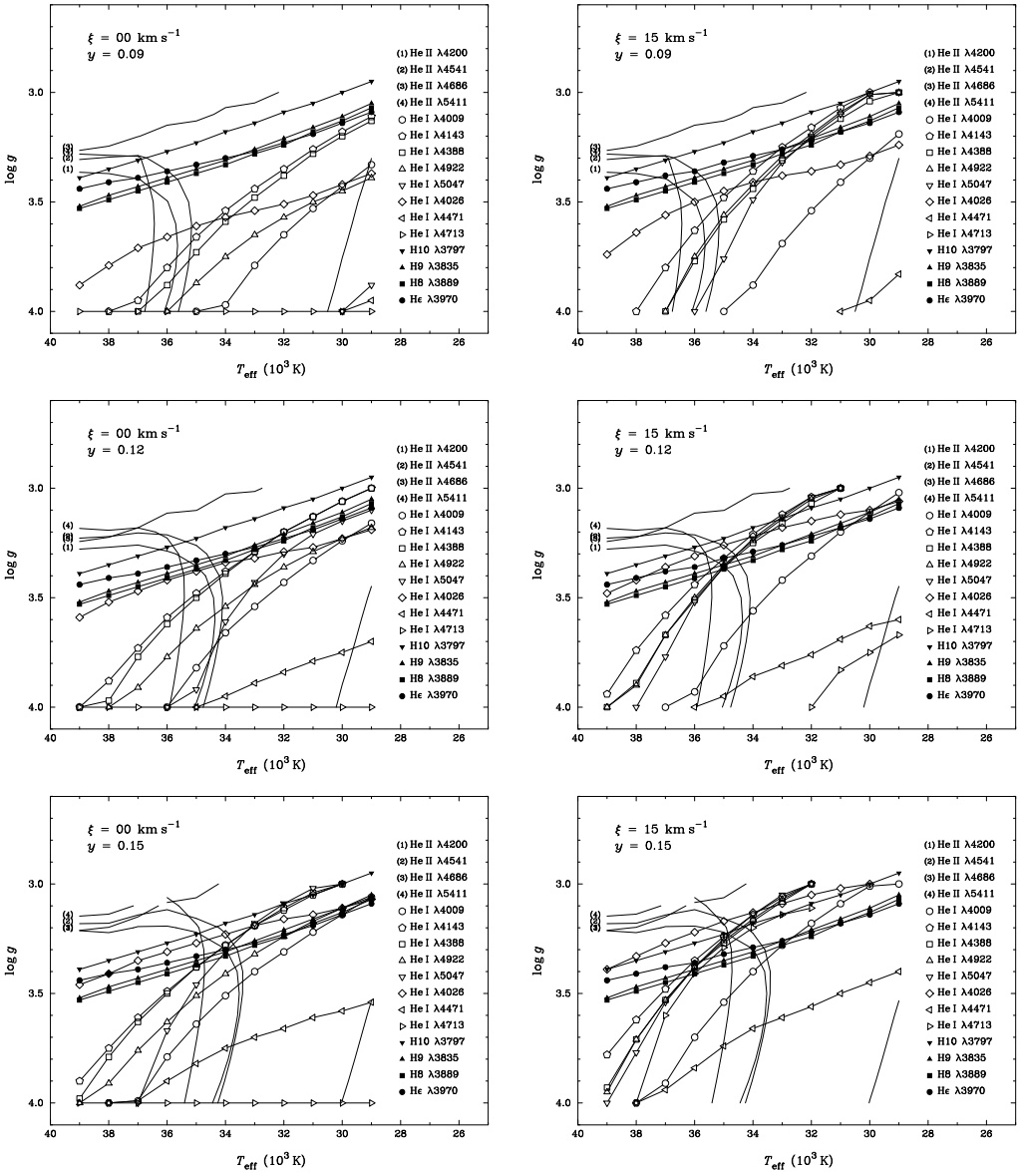

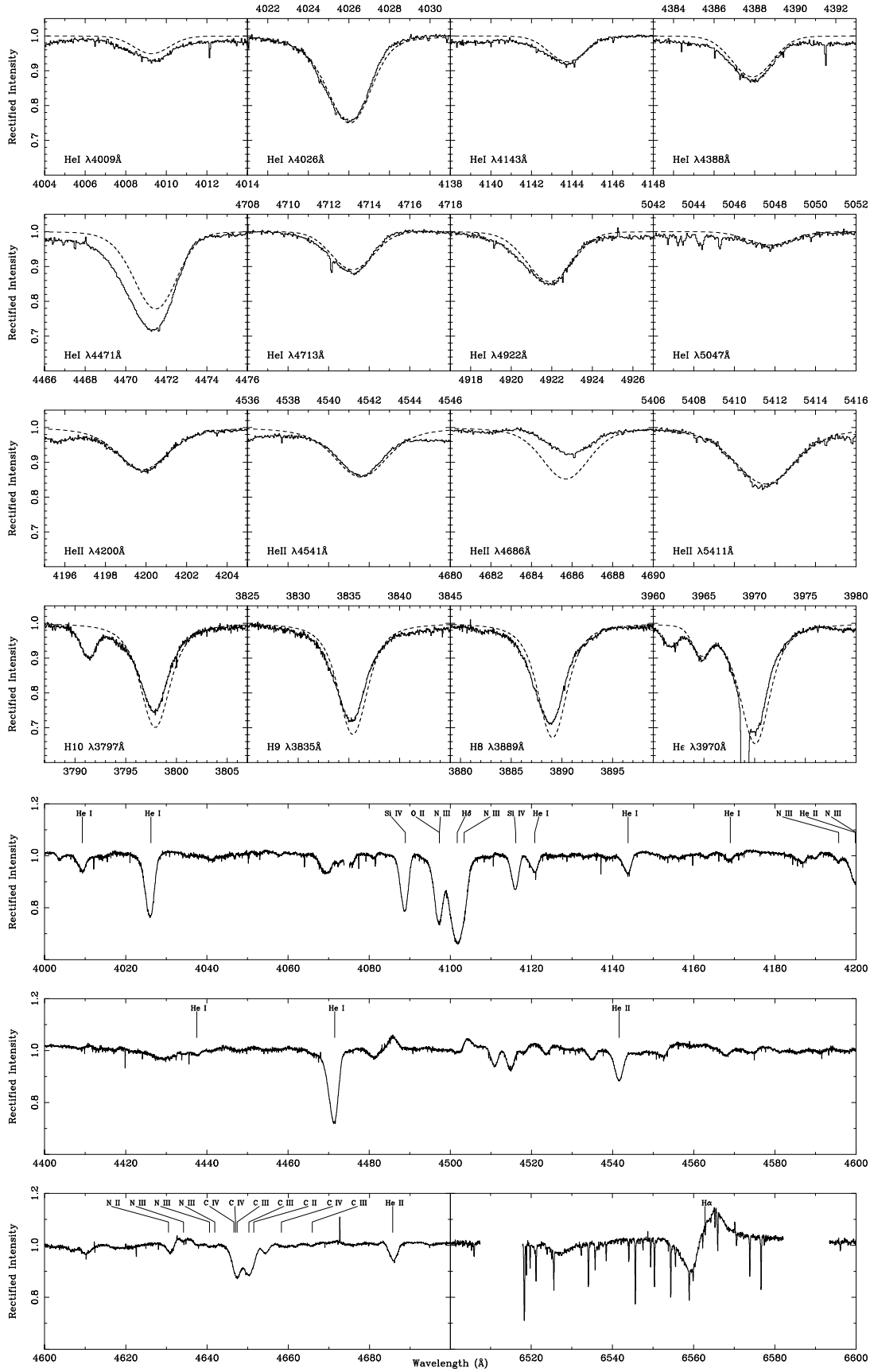
HeI λ4009Å
HeI λ4026Å
HeI λ4143Å
HeI λ4388Å
HeI λ4471Å
HeI λ4713Å
HeI λ4922Å
HeI λ5047Å
HeII λ4200Å
HeII λ4541Å
HeII λ4686Å
HeII λ5411Å
H10 λ3797Å
H9 λ3835Å
H8 λ3889Å
Hε λ3970Å
Rectified Intensity
Wavelength (Å)

C.19 HD 214680

Spectral Type:	O9 V
$T_{\rm eff}$:	38000 K
$\log_{10} g$:	4.2
y:	0.09
Broadening function:	rotational
Broadening velocity:	30 km s^{-1}

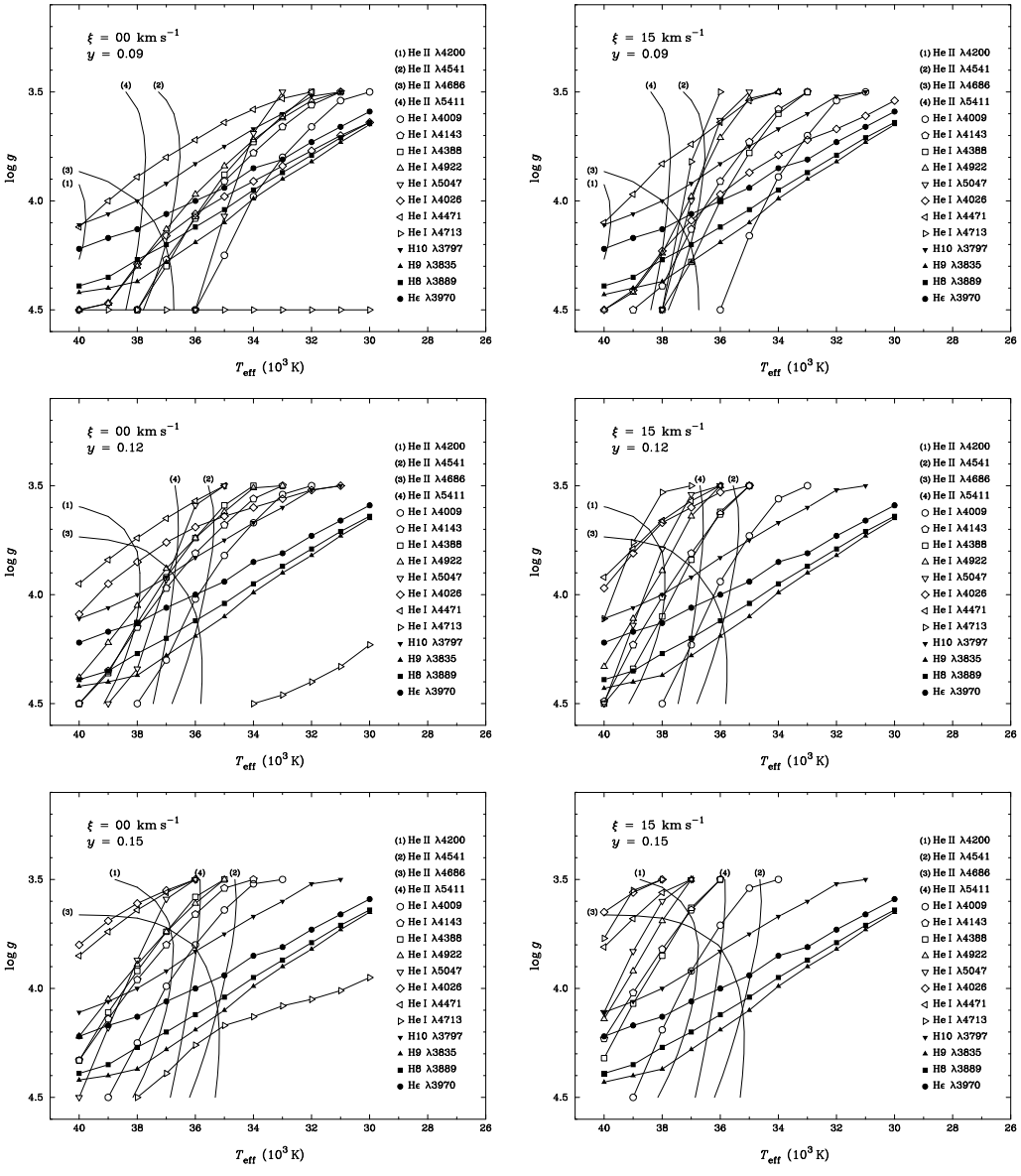

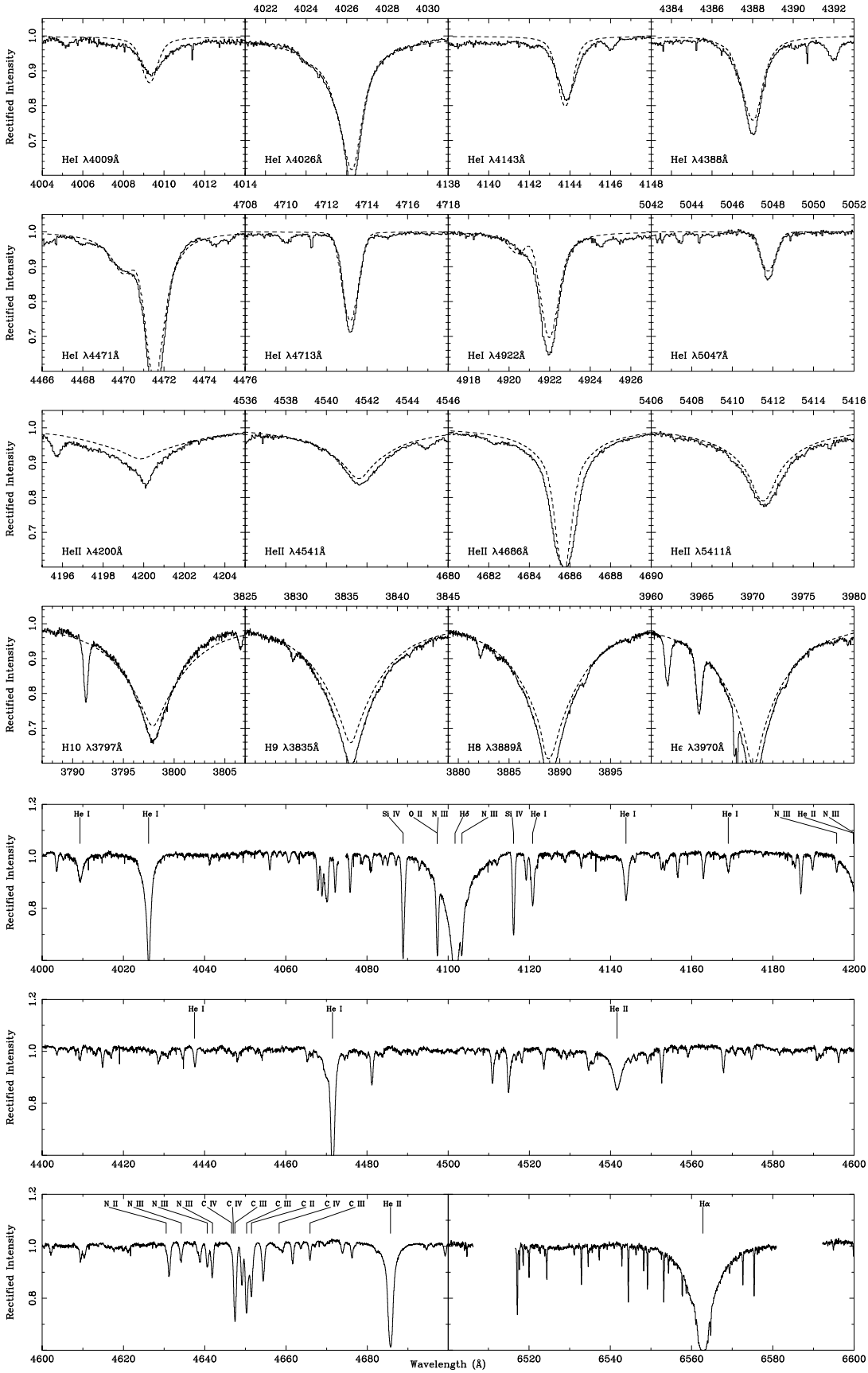
HeI λ4009Å
HeI λ4026Å
HeI λ4143Å
HeI λ4388Å
HeI λ4471Å
HeI λ4713Å
HeI λ4922Å
HeI λ5047Å
HeII λ4200Å
HeII λ4541Å
HeII λ4686Å
HeII λ5411Å
H10 λ3797Å
H9 λ3835Å
H8 λ3889Å
Hε λ3970Å
Rectified Intensity
Wavelength (Å)

C.20 HD 218195

Spectral Type:	O9 III
$T_{\rm eff}$:	37000 K
$\log_{10} g$:	3.6
y:	0.12
Broadening function:	macroturbulent
Broadening velocity:	59 km s^{-1}

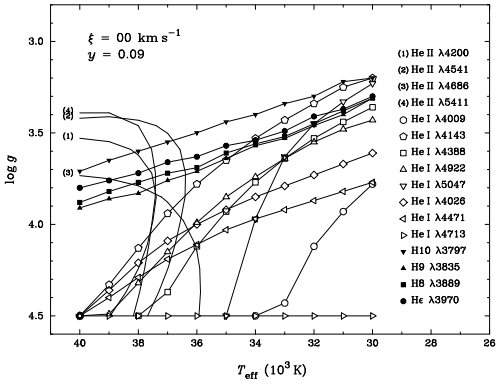

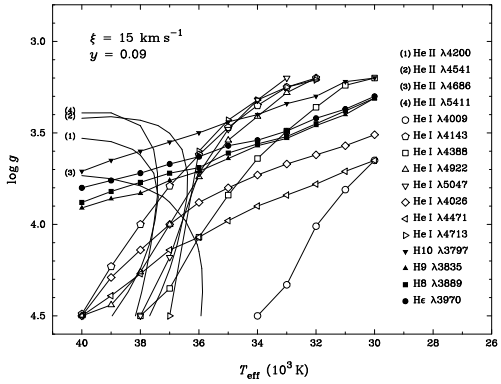

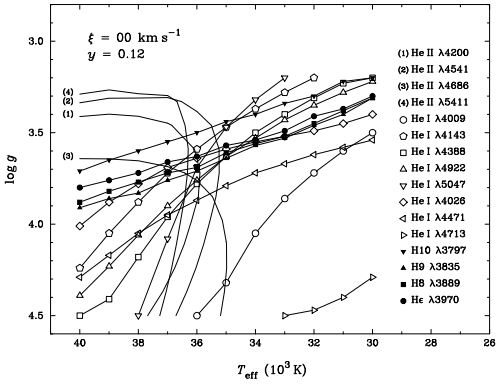

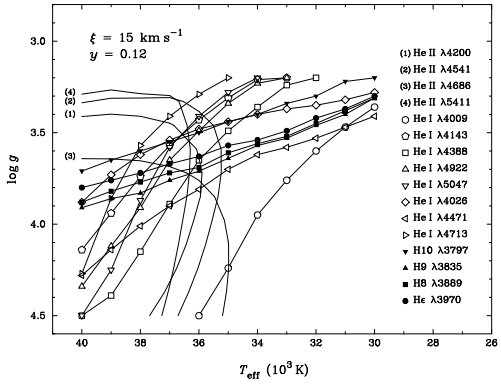

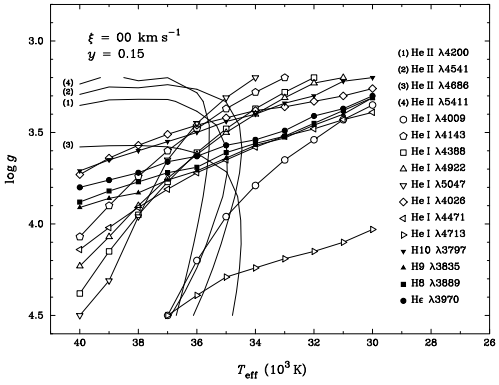

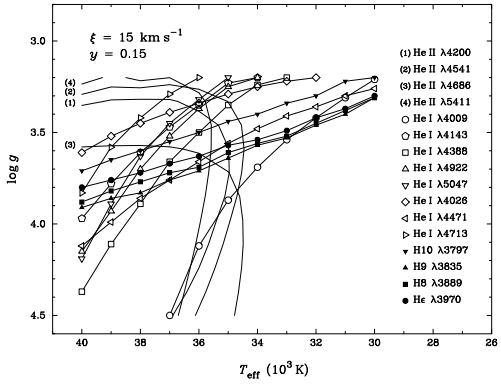

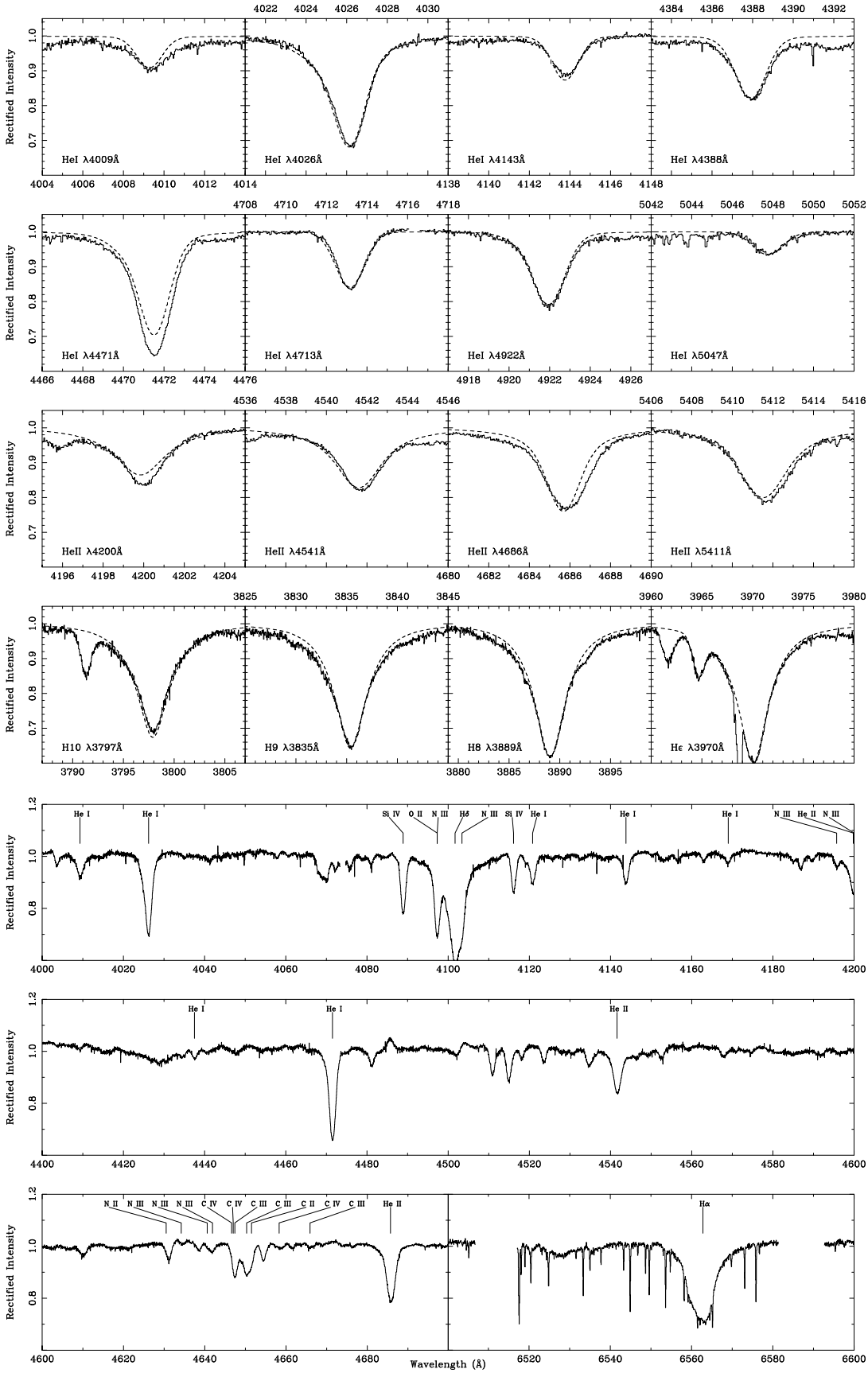
Rectified Intensity
HeI λ4009Å
HeI λ4026Å
HeI λ4143Å
HeI λ4388Å
HeI λ4471Å
HeI λ4713Å
HeI λ4922Å
HeI λ5047Å
HeII λ4200Å
HeII λ4541Å
HeII λ4686Å
HeII λ5411Å
H10 λ3797Å
H9 λ3835Å
H8 λ3889Å
Hε λ3970Å
He I
Si IV
O II
N III
Hδ
Si IV
He II
Hα
Wavelength (Å)

C.21 HD 218915

Spectral Type:	O9.5 Iab
$T_{\rm eff}$:	34000 K
$\log_{10} g$:	3.2
y:	0.10
Broadening function:	macroturbulent
Broadening velocity:	68 km s^{-1}

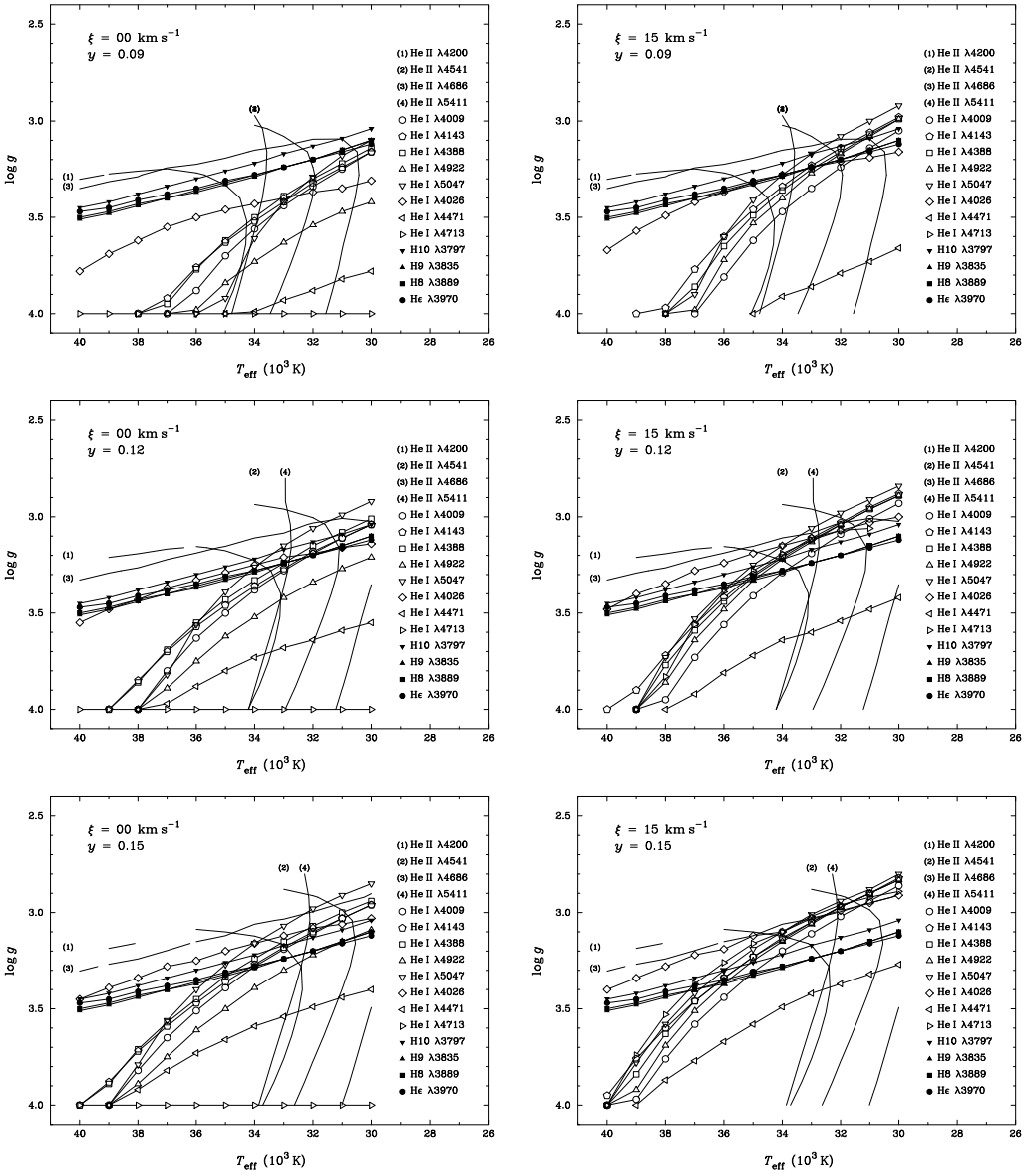

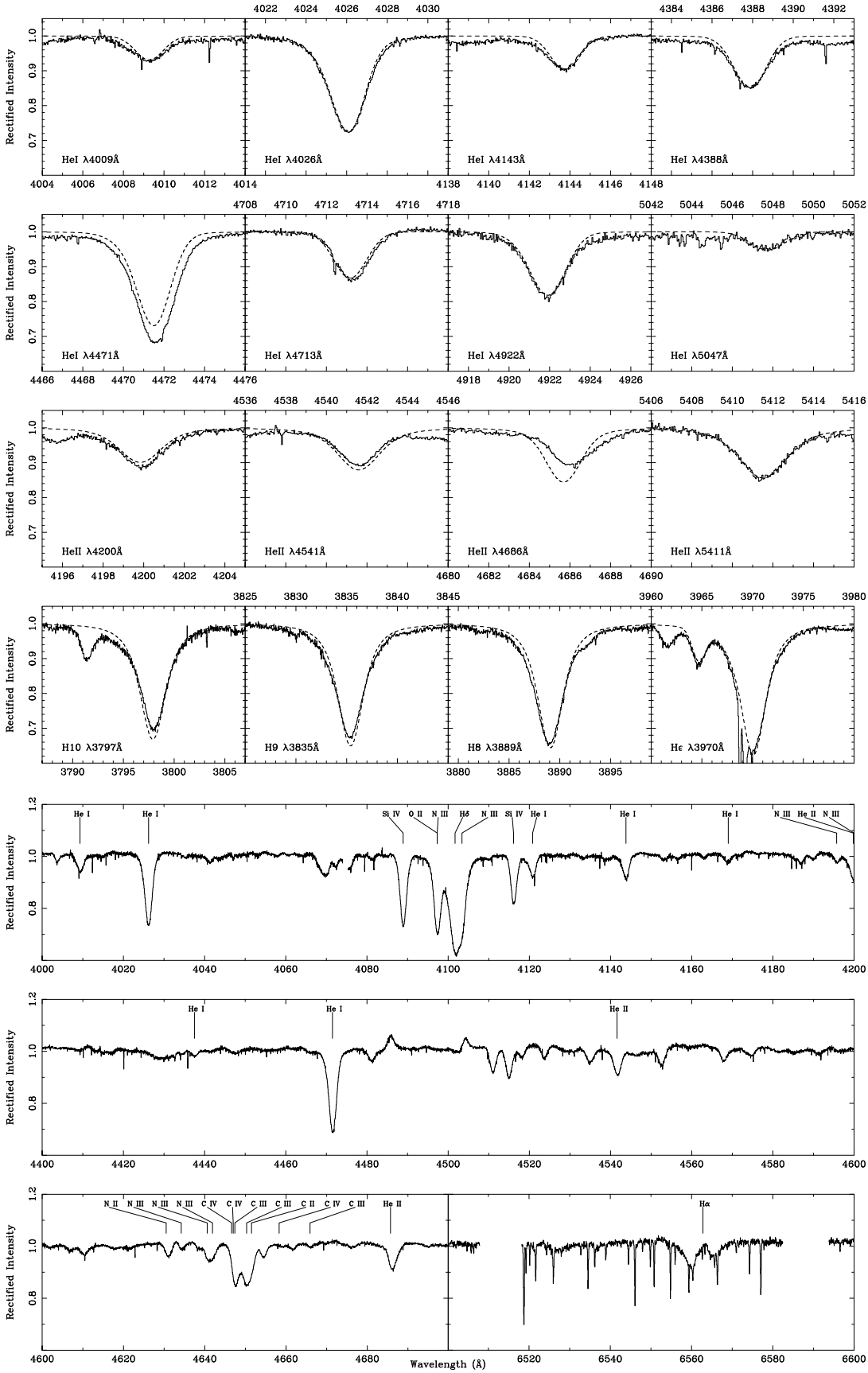
HeI λ4009Å
HeI λ4026Å
HeI λ4143Å
HeI λ4388Å
HeI λ4471Å
HeI λ4713Å
HeI λ4922Å
HeI λ5047Å
HeII λ4200Å
HeII λ4541Å
HeII λ4686Å
HeII λ5411Å
H10 λ3797Å
H9 λ3835Å
H8 λ3889Å
Hε λ3970Å
Rectified Intensity
Wavelength (Å)

C.22 HD 225160

Spectral Type:	O8 Ib(f)
$T_{\rm eff}$:	38000 K
$\log_{10} g$:	3.4
y:	0.15
Broadening function:	macroturbulent
Broadening velocity:	109 km s^{-1}

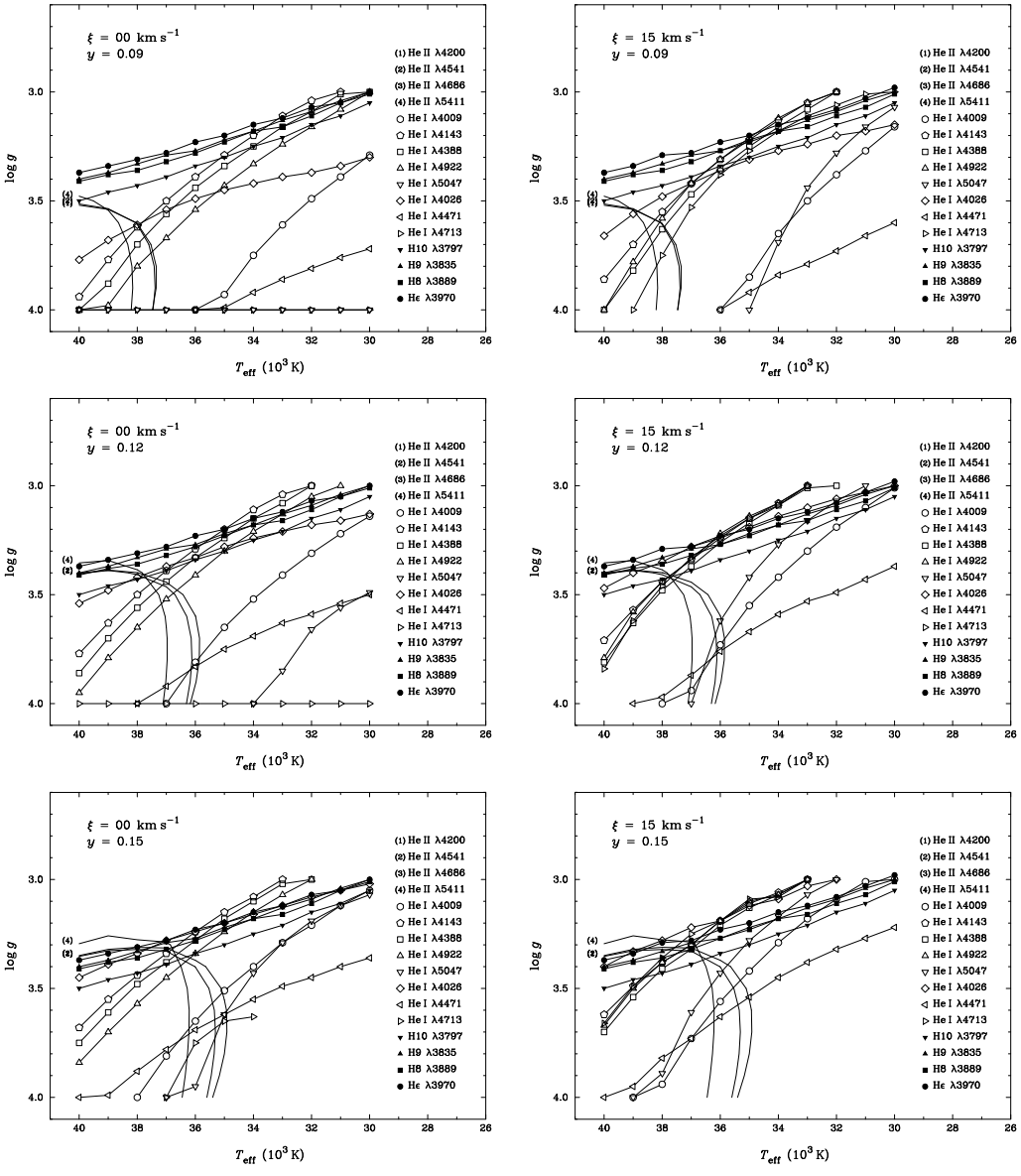

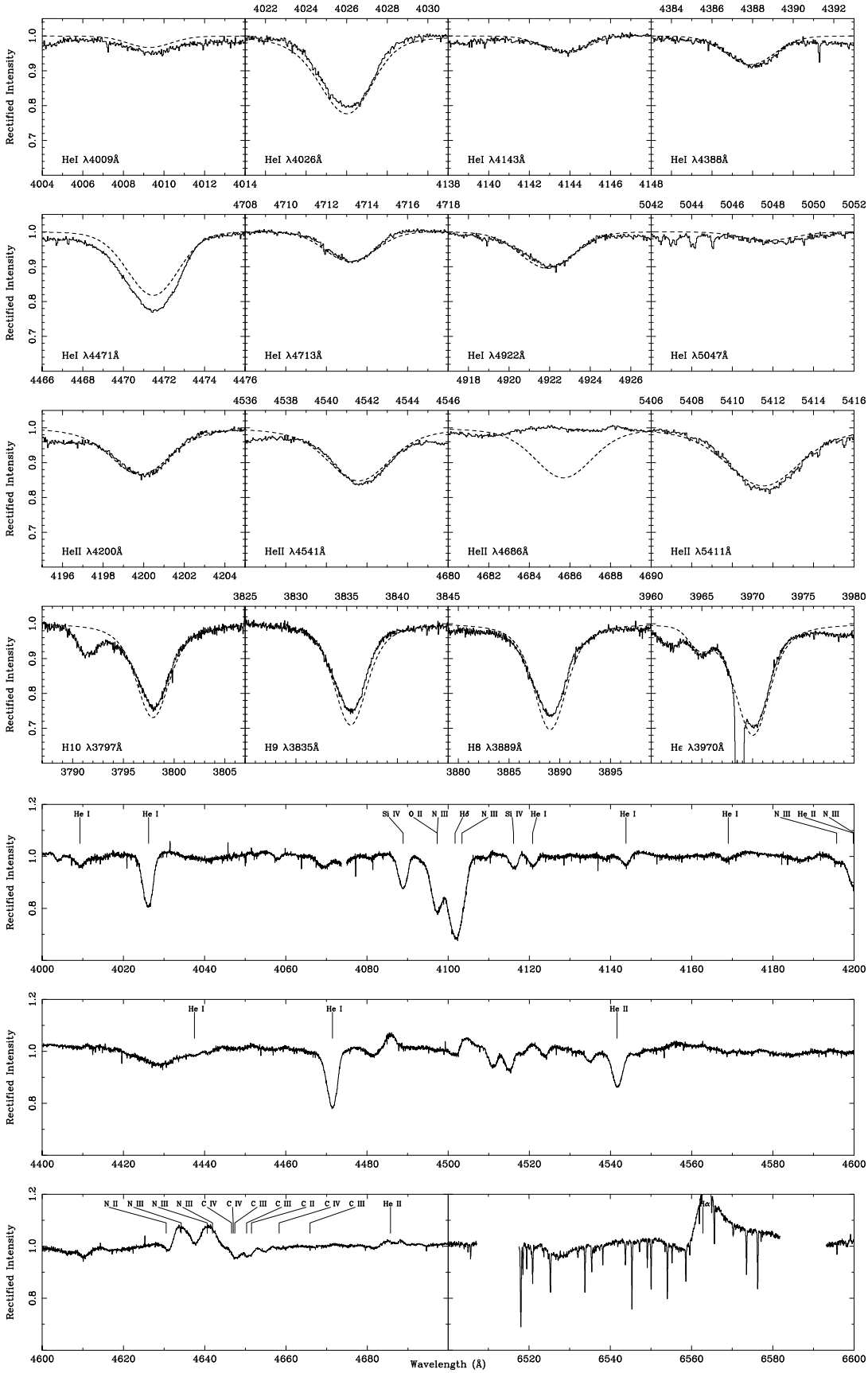
HeI λ4009Å
HeI λ4026Å
HeI λ4143Å
HeI λ4388Å
HeI λ4471Å
HeI λ4713Å
HeI λ4922Å
HeI λ5047Å
HeII λ4200Å
HeII λ4541Å
HeII λ4686Å
HeII λ5411Å
H10 λ3797Å
H9 λ3835Å
H8 λ3889Å
Hε λ3970Å
Rectified Intensity
Wavelength (Å)

C.23 BD +36 4063

Spectral Type:	ON9.7 I
$T_{\rm eff}$:	32000 K
$\log_{10} g$:	3.1
y:	0.11
Broadening function:	macroturbulent
Broadening velocity:	84 km s^{-1}

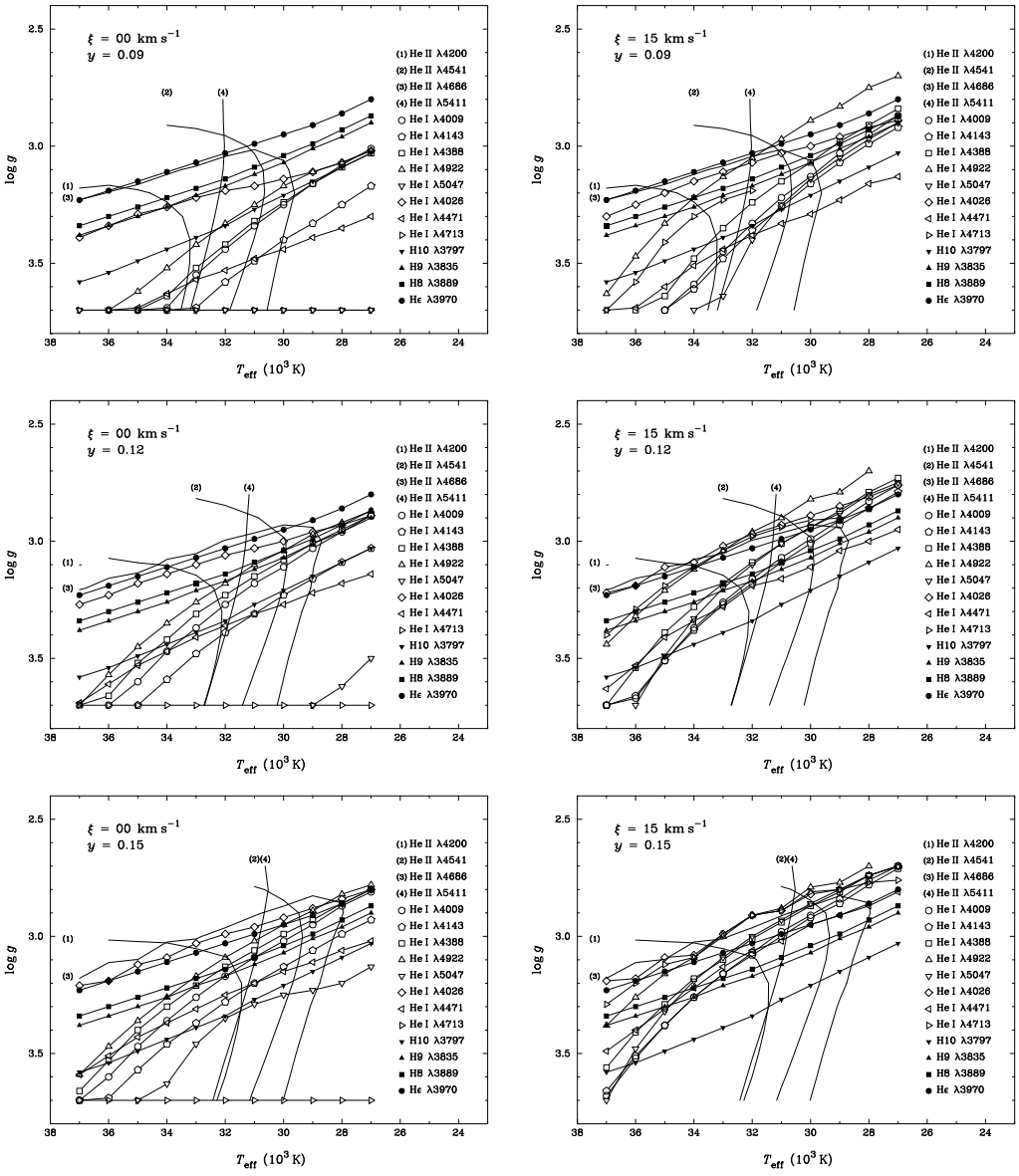

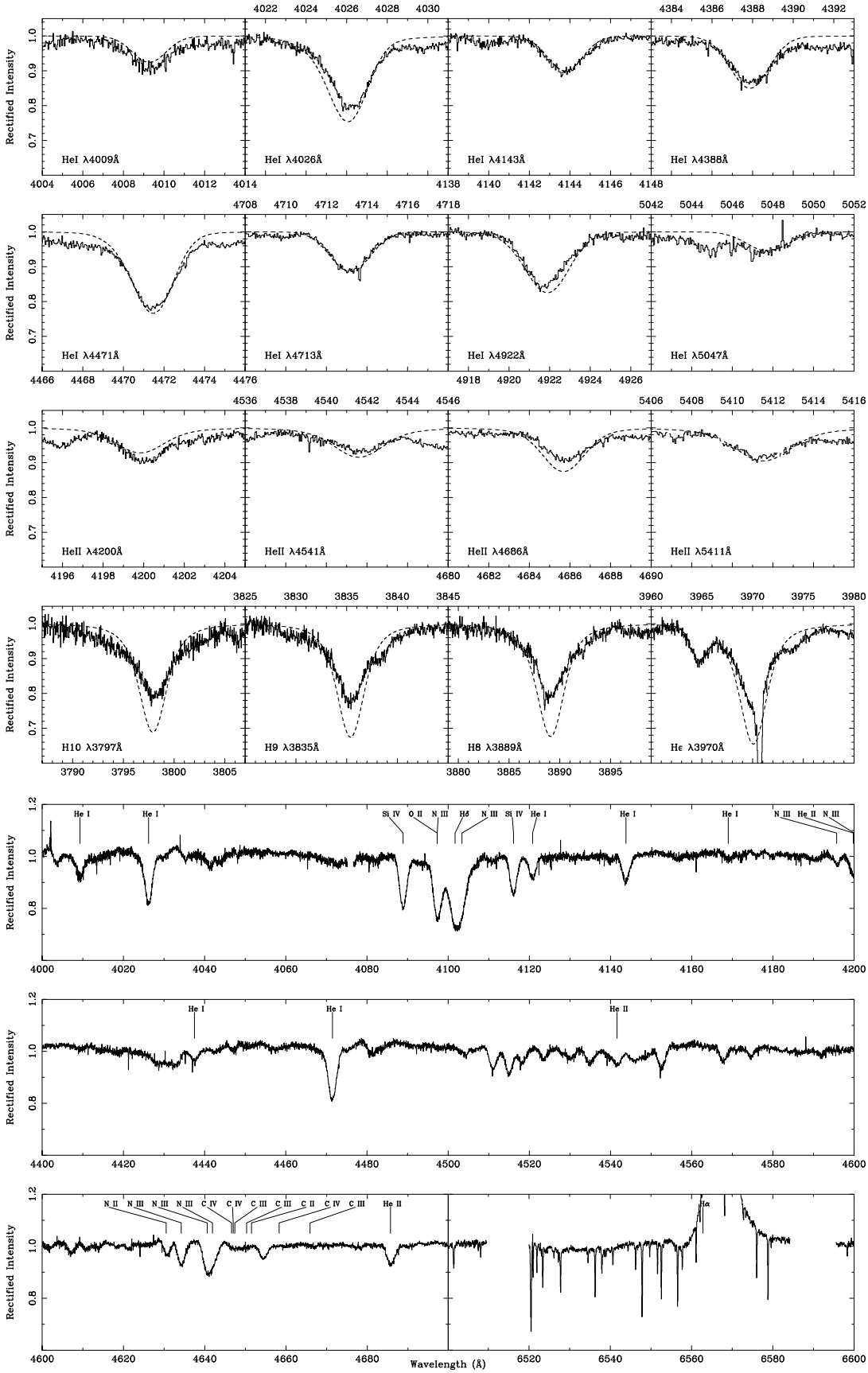
Rectified Intensity
HeI λ4009Å
HeI λ4026Å
HeI λ4143Å
HeI λ4388Å
HeI λ4471Å
HeI λ4713Å
HeI λ4922Å
HeI λ5047Å
HeII λ4200Å
HeII λ4541Å
HeII λ4686Å
HeII λ5411Å
H10 λ3797Å
H9 λ3835Å
H8 λ3889Å
Hε λ3970Å
He I
He II
Si IV
O II
N III
Hδ
Si IV
Hα
N II
C IV
C III
C II
Wavelength (Å)

Appendix D

Line broadening parameters

The results from the cross-correlation analyses discussed in chapter 7 are summarised in the table on the following pages. Column one gives the HD catalogue number, columns two and three give spectral type and reference respectively, column four gives the Bright Star Catalogue (BSC) spectral type. Column five shows stars flagged as spectroscopic binaries (SB) in the BSC. A question mark denotes a possible spectroscopic binary, 1 or 2 are for single or double lined spectroscopic binaries respectively, and an O marks systems where orbital data exist (all according to the BSC). Column six gives the observation catalogue number (SWP – Short Wavelength Prime camera), and columns seven through ten give the corrected $v_e \sin i$ found using each of the four template spectra (see section 7.3). Velocities set in **bold** indicate the 'strongest' cross-correlation function (found from the integrated area under the c.c.f.). Column 11 gives the adopted velocity, which, when there are multiple spectra, is the mean of the corrected velocites from the strongest CCFs. The spectral type references are:

GG – Garrison and Gray (1994)
HS – Hauck and Slettebak (1989)
L68 – Lesh (1968)
W71 – Walborn (1971b)
W76 – Walborn (1976)

An asterix (*) in any column indicates that a more extensive entry for the star is to be found at the end of the table. " ... " indicates observations that failed to give a significant cross-correlation peak, or where the automatic routines could not complete (this would

sometimes occur if the cross-correlation peak was very narrow or extremely wide). The hypertext table on the CD-ROM can, in some cases, reveal why the analysis failed for a given star.

Results of line broadening analysis

			B.S.C.			$v_e \sin i$ (km s^{-1})				
HD	Spectral Type	Ref	Spectral Type	SB	SWP	τSco	ιHer	πCet	αLyr	Ad.
144			B9III		15936	...	100	**89**	100	94
					29402	...	127	**98**	106	
315			B8IIIpSi		51670	...	138	**77**	56	77
358	kB9hB ... *	GG	B8IVpMnHg	O	14954	...	54	**44**	34	37
					40448	...	53	**30**	28	
886	B2 IV	HS	B2IV	O	5260	$\leq$ **20**	...	46	50	$\leq$ 20
					52777	**24**	...	43	41	
					52783	$\leq$ **20**	...	45	47	
1279	B7 II+	GG	B7III		6756	...	25	$\leq$ **20**	$\leq$ 20	$\leq$ 20
1909			B9IVMn	1	23106	...	23	$\leq$ **20**	$\leq$ 20	$\leq$ 20
1976	B5 IV	L68	B5IV	O	6250	107	**115**	118	121	115
2626			B9IIIn		46894	...	263	**231**	245	231
2884	B9 IV	GG	B9V	SB	53043	...	201	135	**129**	129
2905	BC0.7 Ia var	W76	B1Ia	SB	14939	**95**	79	61	...	90
					40359	**89**	82	68	...	
					54038	**87**	83	58	...	
3240	B7 III	L68	B7III		53240	78	68	**53**	51	53
3360	B2 IV	L68	B2IV	?	10057	**30**	...	46	49	27
					53874	26	**24**	50	42	
3369	B5 V	L68	B5V	1O	9141	80	**39**	60	49	39
3379	B2.5 IV	L68	B2.5IV	SB	20584	67	**52**	66	52	52
3901	B2.5 V	L68	B2V	1	52659	143	**151**	133	138	151
4142	B4 V	L68	B5V	SB	14612	167	148	**157**	147	157
4180	B5 III	L68	B5IIIe	1O	20436	117	**160**	178	171	160
4727	B5 V	L68	B5V+F8V	2O	51960	45	**25**	24	$\leq$ 20	25
5394	B0.5 IVe	L68	B0IVe	SB	17093	**308**	321	...	...	276
					53910	**268**	242	220	...	
					56621	**251**	234	...	...	
5737	B7 II+	GG	B7IIIp	O	14984	...	24	**21**	$\leq$ 20	22
					32137	30	24	**22**	$\leq$ 20	
6811			B7Ve		20437	74	67	**69**	56	69
6882			B6V+B9V	2O	16499	...	...	...	...	...
					16512	...	...	...	...	
7374	B8 IV	GG	B8III		18972	...	24	$\leq$ **20**	$\leq$ 20	$\leq$ 20
9996			B9pCrEu	1O	18437	...	...	**22**	$\leq$ 20	22
10390			B9IV-V		18023	...	48	44	**48**	48
10516	B2 Vpe	L68	B2Vep	2O	14690	255	**376**	319	...	323
					18104	280	**270**	276	...	
10982			B9.5V	SB	6814	...	39	29	**30**	30
11241	B1.5 V	L68	B1.5V	O	49469	141	**161**	176	...	161
11415	B3 Vp	L68	B3III		32615	50	**39**	45	30	39
12301	B8 Ib	L68	B8Ib		4265	50	36	**27**	$\leq$ 20	27

continues next page ...

Results of line broadening analysis — *continued*

			B.S.C.			$v_e \sin i$ (km s^{-1})				
HD	Spectral Type	Ref	Spectral Type	SB	SWP	τSco	ιHer	πCet	αLyr	Ad.
12767	kB8hB ... *	GG	B9.5pSi		51130	...	50	**37**	$\leq$ 20	37
13267	B5 Ia	L68	B5Ia		51892	76	**44**	40	34	44
13294	B9 IVn	GG	B9V		40511	...	175	123	**128**	128
13709			B9V		55256	...	300	220	**210**	210
14228	B8 IV	GG	B8V-IV		51597	...	244	**214**	202	214
14818	B2 Ia	L68	B2Ia		9416	83	**63**	45	...	63
14951	B7 IV	L68	B7IV	SB	5605	...	132	**117**	121	117
15130			B9.5Vn		18007	...	237	185	**180**	180
15318			B9III	?	48525	...	48	44	**47**	47
15371	B5 IV	HS	B5IV	?	21046	28	22	$\leq$ **20**	$\leq$ 20	$\leq$ 20
16582	B2 IV	L68	B2IV	SB	4492	$\leq$ **20**	...	55	31	$\leq$ 20
16978	B9 Va	GG	B9V		24455	...	101	82	**83**	83
17036	B8 IV	GG	B9Vn		46700	...	195	**180**	162	180
					46760	...	...	...	...	
17081	B7 V	L68	B7V	SB	16256	$\leq$ 20	25	$\leq$ **20**	$\leq$ 20	$\leq$ 20
					32303	21	...	$\leq$ **20**	$\leq$ 20	
					32304	25	26	$\leq$ **20**	$\leq$ 20	
17543			B6V	O	42210	82	64	**56**	47	56
17573	B8 Vn	GG	B8Vn	SB	40510	...	193	**175**	157	175
17769	B7 V	L68	B7V		18008	122	143	**125**	137	125
18296			B9pSi	SB	3154	...	31	**25**	$\leq$ 20	25
18537	B7 III	L68	B7V	SB	48527	...	83	**78**	77	78
18552			B8Vne	SB	55906	264	**277**	...	...	277
19356	B8 Vs	GG	B8V	O	2643	...	...	...	...	45
					37021	...	48	**45**	40	
19374	B1.5 V	L68	B1.5V	SB	20594	**32**	...	57	95	32
19400			B3V+A0IV		4415	$\leq$ 20	29	$\leq$ **20**	$\leq$ 20	$\leq$ 20
19832			B9pSi		39685	...	220	**167**	152	167
20315	B8 IV	L68	B8V	SB	18024	...	233	**211**	207	211
20319			B9V		7840	...	134	**121**	114	121
20336	B2.5 Vne	L68	B2.5Ven	SB	29401	225	**249**	257	260	249
20809	B4 V	L68	B5V	?	49124	127	**155**	159	181	155
21278	B4 V	L68	B5V	1O	2838	...	...	...	...	...
21291	B9 Ia	GG	B9Ia		10612	49	39	**27**	$\leq$ 20	27
21362	B7 Vn	L68	B6Vn	SB	18027	...	**268**	219	251	268
21428	B5 V	L68	B3V		49532	119	**123**	128	111	123
21551	B8 III-IVn	GG	B8V	SB	26895	...	286	**286**	277	286
21699	kB8hB ... *	GG	B8IIIpMn		4377	33	**41**	39	30	38
					32136	50	**36**	27	$\leq$ 20	
21790	B9 III	GG	B9V s		24553	...	80	71	**64**	64
22192	B5 Ve	L68	B5Ve		4558	...	202	**202**	167	205
					42673	...	**208**	184	167	
22203	B8 IV	GG	B8V+B8V	2O	1946	...	...	...	...	...

continues next page ...

Results of line broadening analysis — *continued*

			B.S.C.			$v_e \sin i$ (km s^{-1})				
HD	Spectral Type	Ref	Spectral Type	SB	SWP	τSco	ιHer	πCet	αLyr	Ad.
22316			B9p		49775	...	21	$\leq$ **20**	$\leq$ 20	$\leq$ 20
					49777	...	23	$\leq$ **20**	$\leq$ 20	
22470			B9.5p		4542	...	60	**52**	42	52
					21943	...	...	...	...	
22780	B7 Vn	L68	B7Vne		29392	...	251	**261**	248	261
22920			B9IIIpSi4200		14506	45	38	**33**	$\leq$ 20	33
22928	B5 III	L68	B5IIIe	SB	47041	164	179	**168**	178	168
22951	B1 IV	L68	B0.5V	SB	6248	**44**	40	99	...	48
					8023	**52**	54	139	...	
23016			B9Vne	SB	40509	...	248	**239**	228	239
23180	B1 III	L68	B1III	2O	50031	86	**73**	236	...	73
23227			B5IV	SB	40256	138	**164**	172	200	164
23288	B7 IV	L68	B7IV		5947	...	...	...	...	...
23302	B6 III	L68	B6III	1O	7920	126	142	**132**	133	140
					27514	123	141	**147**	146	
23324	B8 Vn	GG	B8V	2	7923	...	221	**178**	161	178
23338	B6 IV	L68	B6IV	1	40508	100	113	**93**	85	93
23383			B9Vnn		19342	...	269	**296**	233	296
23408	B8 III	L68	B8III	SB	5985	31	29	**25**	$\leq$ 20	25
23432	B8 Vn	GG	B8V	SB	5974	...	...	...	...	...
23466	B3 V	L68	B3V	2O	20582	95	**91**	105	97	91
23480	B6 IV	L68	B6IVe		5944	...	196	**189**	207	210
					27666	...	215	**231**	204	
23552			B8Vne		10046	...	204	**183**	177	183
23630	B7 III	L68	B7IIIe		8021	...	173	**130**	121	130
23793	B3 V	L68	B3V+F5V		20583	52	**41**	48	30	41
23850	B8 III	GG	B8III	1O	5977	...	184	**155**	154	155
23862			B8Vpe	SB	53233	...	281	**254**	224	246
					54080	...	266	**239**	226	
24072			B9V		40455	...	278	208	**167**	111
					48345	...	48	36	**55**	
24131	B0.5 V	L68	B1V		20845	**82**	73	117	...	82
24388	B7.5 IV	GG	B8V		40456	103	110	**107**	111	107
24398	B1 Ib	W76	B1Ib	SB	6454	64	**55**	72	...	55
24479			B9.5V		20434	...	65	64	**61**	61
24504	B6 V	L68	B6V	SB	18025	157	190	**178**	184	178
24534	O9.5 pe	L68			2082	**225**	194	...	...	231
					10789	**237**	289	...	...	
24626			B6V		4788	39	42	**41**	28	41
24640	B1.5 V	L68	B1.5V	SB	53315	102	**102**	132	...	102
24760	B0.7 III	W71	B0.5V+A2V	2	6711	**149**	118	158	...	140
					56579	**131**	113	146	...	
25204	B3 IV	L68	B3V+A4IV	2O	3297	78	**81**	98	83	81

continues next page ...

Results of line broadening analysis — *continued*

			B.S.C.			$v_e \sin i$ (km s^{-1})				
HD	Spectral Type	Ref	Spectral Type	SB	SWP	τSco	ιHer	πCet	αLyr	Ad.
25267			B6V+B9.5V	O	7540	...	40	**26**	$\leq$ 20	26
25340	B5 V	L68	B5V		18020	86	76	**75**	66	75
25558	B3 V	L68	B3V		20595	70	**48**	53	42	48
25823			B9pSi	1O	30567	...	...	...	...	...
25940	B3 Ve	L68	B3Ve		54081	100	**138**	167	166	138
26326	B4 V	L68	B4V		20586	48	**25**	24	$\leq$ 20	25
26356	B5 V	L68	B5V		29400	212	**220**	219	249	220
26571			B9IIIp:Si:	SB	19628	...	**21**	23	47	21
26670			B5Vn		20435	...	257	**257**	244	257
26676			B8Vn		34223	...	230	**207**	200	207
26912	B3 IV	L68	B3IV	?	22280	67	**59**	61	53	59
27192	B1.5 IV	L68	B1.5IV	SB	49849	**131**	123	137	...	131
27295			B9IV	O	49761	...	23	**22**	$\leq$ 20	22
27376			B9V	2O	53040	33	30	$\leq$ **20**	$\leq$ 20	$\leq$ 20
27638			B9V		30557	...	...	...	...	...
27742			B8IV-V		46672	...	201	**173**	152	173
27778			B3V		21298	112	**114**	101	104	114
28149	B7 V	L68	B7V		45496	142	125	**117**	115	117
28446	B0 IIIn	L68	B0III	SB	22429	**289**	241	...	...	289
28459			B9.5Vn		18022	...	269	342	**277**	277
28497	B1.5 Ve	L68	B1Vne		8594	298	**289**	315	...	289
28843			B9III		7522	110	113	**86**	71	94
					21098	...	114	**101**	86	
28867			B9IVn		49847	...	278	**229**	270	229
28873			B2IV-V		53193	25	...	**35**	30	35
28929			B9pHg		30558	...	...	...	...	...
29248	B2 III	L68	B2III	SB	4359	29	**29**	56	...	29
29335	B7 V	L68	B7V		39767	88	81	**75**	58	75
29763			B3V	2O	2637	109	**90**	100	90	87
					45931	95	**84**	87	79	
29866	B8 IVn	L68	B8IVne		10047	...	259	**239**	237	239
30836	B2 III	L68	B2III+B2IV	O	2358	43	**39**	61	51	39
31237	B2 III	L68	B3III+B0V	O	21998	77	**78**	99	90	78
31327	B2.5 Ib	L68	B2Ib		21280	75	**51**	49	34	51
31331	B5 V	L68	B5V	SB	40502	132	148	**153**	137	153
31726	B1 V	L68	B1V		21681	**21**	...	63	...	21
32249			B3V		48993	52	**49**	74	50	49
32309			B9.5Vn		40454	...	339	324	**279**	279
32343	B2.5 Ve	L68	B2.5Ve		6932	60	**67**	79	72	70
					32558	76	**74**	78	68	
32612	B2.5 IV	L68	B2.5IV		20588	54	**47**	71	63	47
32630	B3 V	W71	B3V		44004	83	**85**	97	89	85
32990	B2 V	L68	B2V	O	14842	64	**54**	83	86	54

continues next page ...

Results of line broadening analysis — *continued*

			B.S.C.			$v_e \sin i$ (km s^{-1})				
HD	Spectral Type	Ref	Spectral Type	SB	SWP	τSco	ιHer	πCet	αLyr	Ad.
					21489	71	**55**	82	77	
32991	B2 Ve	L68	B2Ve		14840	138	**169**	191	268	169
33328	B2 IVn	L68	B2IVne		55944	181	**218**	235	235	218
33904			B9IIIpHgMn		40118	31	24	$\leq$ **20**	$\leq$ 20	$\leq$ 20
34085			B8Ia:	SB	15001	55	42	**31**	28	32
					41077	52	40	**33**	$\leq$ 20	
34310			B9V		40255	...	176	127	**123**	123
34759	B5 V	L68	B3V	O	10389	49	**47**	59	52	54
					38308	62	**61**	73	62	
34797			B8/9III/IV		24995	...	131	**50**	48	50
34798			B3V		21787	56	**45**	55	53	45
34816	B0.5 IV	L68	B0.5IV		56888	**36**	37	70	...	36
34863	B7 IVnn	L68	B7IVnn		40254	...	285	**282**	272	282
34959	B5 Vp	L68	B5Vp		35918	...	245	**211**	167	211
35149			B1V		30052	270	**286**	340	...	286
35337	B2 IV	L68	B2IV		49749	$\leq$ **20**	...	50	78	$\leq$ 20
35407	B4 IVn	L68	B4IVn	SB	22663	...	**226**	283	301	226
35411	B0.5 Vnn	L68	B1V+B2e	2O	13401	**47**	102	153	...	52
					52811	**56**	168	174	...	
35439	B1 Vn	L68	B1Vpe		7716	294	**308**	331	...	289
					50413	282	**270**	342	...	
35468	B2 III	W71	B2III	?	44092	52	**45**	72	83	45
35497	B7 III	HS	B7III		31878	80	53	**45**	31	45
35532	B2 Vn	L68	B2Vn		35853	203	**216**	279	359	216
35588	B2.5 V	L68	B2.5V	O	35893	131	**155**	158	181	155
35600			B9Ib		52723	...	32	**22**	$\leq$ 20	22
35640			B9.5Vn		40253	...	231	203	**196**	196
35715	B1 V	L68	B2IV	2O	3264	**95**	140	166	...	96
					35892	**98**	97	265	...	
36267	B5 V	L68	B5V		35943	97	139	**137**	137	137
36285	B2 IV-V	L68	B2IV-V		50056	$\leq$ **20**	...	50	$\leq$ 20	$\leq$ 20
36351	B1.5 V	L68	B1IV+B1.5V		49065	38	**30**	88	106	30
36371	B5 Iab	L68	B5Iab	O	2945	65	**49**	43	47	49
36408			B7IIIe	SB	29394	77	67	**59**	53	59
36512	B0 V	W71	B0V		40415	**29**	27	52	...	29
36576	B2 IV-Ve	L68	B2IV-Ve		47042	196	**248**	301	...	248
36591	B1 IV	L68	B1IV		4695	$\leq$ **20**	...	102	...	$\leq$ 20
36653	B3 V	L68	B3V		35897	119	**134**	166	181	134
36695			B1V	1O	15639	**145**	149	231	...	145
36779	B2.5 V	L68	B2.5V		32291	130	**132**	191	...	132
36819	B2.5 IV	L68	B2.5IV	SB	46138	77	**74**	94	82	74
36822	B0.5 IV-V	L68	B0III	O	8595	**36**	40	81	...	36
					35898	**37**	40	98	...	

continues next page ...

Results of line broadening analysis — *continued*

			B.S.C.			$v_e \sin i$ (km s^{-1})				
HD	Spectral Type	Ref	Spectral Type	SB	SWP	τSco	ιHer	πCet	αLyr	Ad.
36960	B0.5 V	W76	B0.5V		56185	**41**	34	64	...	41
37017	B1.5 V	L68	B1.5V	1O	15816	99	**128**	140	145	128
37018	B1 V	L68	B1V	SB	20782	**64**	67	132	...	64
37020			B0.5V	O	50204	...	...	...	...	...
37021			B0V	O	53178	**112**	148	185	264	112
37023			B0.5Vp	SB	50205	...	...	...	...	...
37055	B3 IV	L68	B3IV		32216	88	**89**	106	103	89
37098			B9IV-V		46843	51	103	**60**	52	60
37128	B0 Ia	W76	B0Ia	SB	8110	**99**	94	...	...	97
					8130	**95**	92	...	...	
37202	B4 IIIp	L68	B4IIIpe	1O	3138	171	**145**	92	64	168
					54067	255	**191**	144	72	
37232	B2 IV-V	L68	B2IV-V		35945	84	**86**	137	...	86
37303	B1.5 V	L68	B1V		36897	238	**304**	301	...	304
37356	B2 IV-V	L68	B2IV-V		22114	**26**	...	69	82	26
37367	B2 IV-V	L68	B2IV-V	SB	21013	48	**30**	44	36	30
37438	B3 IV	L68	B3IV	O	53869	53	**44**	53	33	44
37479	B2 Vp	L68	B2Vp		2231	98	**105**	131	...	116
					15817	114	**127**	151	...	
37481	B1.5 IV	L68	B1.5IV		32215	75	**66**	118	...	66
37490	B2 IIIe	L68	B3IIIe		15982	136	**148**	164	...	144
					56758	125	**141**	164	...	
37519			B9.5III-IVp:		46851	...	231	**224**	185	224
37744	B1.5 V	L68	B1.5V		8059	36	**31**	90	...	31
37752			B8p		14987	38	36	**27**	≤ 20	27
37756	B2 IV-V	L68	B2IV-V	O	32293	59	**55**	96	93	55
37795			B7IVe		55941	157	**180**	203	216	180
37967	B2.5 Ve	L68	B2.5Ve		21491	133	**171**	163	171	171
38771	B0.5 Ia	W76	B0.5Ia		6736	**88**	84	96	...	82
					8259	**78**	78	83	...	
					30267	**80**	80	95	...	
38899			B9IV		16641	...	28	**25**	≤ 20	25
39698	B2 V	L68	B2V	O	3437	106	**109**	144	...	109
39777	B1.5 V	L68	B1.5V		16881	25	**24**	51	60	24
39844			B6V		4298	≤ 20	24	$\leq$ **20**	≤ 20	≤ 20
40111	B1 Ib	L68	B0.5II	SB	4235	**129**	107	110	...	129
40494			B2.5IV		53044	59	**55**	63	52	55
40626			B9.5IV		50181	...	...	...	...	...
40967			B5III	SB	50278	32	**33**	65	82	33
41040			B8III	2	4709	...	69	**61**	58	62
					4710	...	67	**62**	56	
41117	B2 Ia	W76	B2Ia		6471	80	**60**	42	...	62
					40669	75	**64**	58	...	

continues next page ...

Results of line broadening analysis — *continued*

			B.S.C.			$v_e \sin i$ (km s^{-1})				
HD	Spectral Type	Ref	Spectral Type	SB	SWP	τSco	ιHer	πCet	αLyr	Ad.
41335	B2 Vne+	L68	B2Ven	SB	16526	227	**263**	327	...	248
					55943	240	**233**	227	...	
41534			B2.5V		10021	74	**64**	97	94	64
41753	B3 IV	L68	B3V	1O	9934	44	**44**	57	49	44
42054	B5 V	HS	B4IVe		29370	...	151	**172**	194	172
42087	B2.5 Ib	W71	B2.5Ib		8646	76	**68**	62	...	68
42545	B5 Vn	L68	B5Vn	SB	9896	...	**215**	218	304	215
42560	B3 IV	L68	B3IV	1O	9932	130	**121**	150	321	121
42933	B0.5 IV	HS	B3III+O9V	2O	7663	**178**	175	191	...	178
43112	B1 V	L68	B1V		9935	$\leq$ **20**	...	76	...	$\leq$ 20
43317	B3 IV	L68	B3IV	SB	9949	85	**88**	122	117	88
43384	B3 Iab	L68	B3Ib		4656	56	**42**	52	55	42
43445			B9Vn		40504	...	266	**226**	215	226
43544	B2.5 Vne	L68	B2.5Vn		21911	180	**257**	300	309	257
44112	B2.5 V	L68	B2.5V	SB	49490	85	**94**	151	217	94
44173	B5 III	L68	B5III		6803	...	142	**181**	261	181
44402	B2.5 IV	HS	B2.5V	O	22111	56	**60**	92	61	60
44458	B1 Ve	L68	B1Vpe	SB	54066	224	**230**	230	...	230
44506			B1.5Ve		36893	222	**217**	253	...	217
44700	B3 V	L68	B3V	SB	9948	29	**25**	27	$\leq$ 20	25
44743	B1 II-III	L68	B1II-III	SB	4537	31	**28**	59	...	28
44953			B8IIIHe wk		14979	...	**27**	27	$\leq$ 20	27
45542	B6 III	L68	B6IIIe	SB	27663	...	179	**165**	149	165
45546	B2 V	L68	B2V		22112	59	**56**	94	113	56
45725	B3 Ve	L68	B3Ve	O	30191	...	**283**	288	...	283
45727			B3e		30702	...	244	**267**	...	267
45789	B2.5 IV-V	W71			9884	100	**93**	111	135	93
45813	B4 V	HS	B4V		20783	103	**108**	123	107	108
45911	B2 IV-V	W71			9885	22	**23**	45	$\leq$ 20	23
45995	B2.5 Ve	L68	B2V:nne		9936	200	**200**	229	...	200
46328			B0.5IV	SB	5114	$\leq$ **20**	...	42	...	$\leq$ 20
46485	O7 V:n(e)	W71			9913	**316**	...	...	...	316
46487	B5 Vn	L68	B5Vn		18037	...	223	**249**	256	249
46769	B8 Ib	L68	B8Ib		6341	56	53	**58**	46	58
46885			B9III		30298	36	41	34	**30**	30
47054	B8 IV	HS	B8V		21909	...	202	**198**	203	198
47152			B9npEu		14957	...	178	165	**206**	206
47240	B1 II	L68	B1Ib		4704	**127**	113	108	...	118
					48909	**108**	107	87	...	
47382	B0 III-IV	W71			9882	**65**	64	89	...	65
47431			B8IIIn		11011	...	115	**98**	96	98
47670	B8 III	HS	B8III	SB	33338	...	191	**172**	136	172
47964			B8III		9887	...	48	**44**	31	44

continues next page ...

Results of line broadening analysis — *continued*

			B.S.C.			$v_e \sin i$ (km s^{-1})				
HD	Spectral Type	Ref	Spectral Type	SB	SWP	τSco	ιHer	πCet	αLyr	Ad.
48279	O8 V	W76			11299	**150**	...	...	...	150
48434	B0 III	W76	B0III		6447	**74**	71	86	...	74
48879	B4 IV	L68	B4IV	SB	50256	84	**101**	101	94	101
48917	B2 III	HS	B2IIIe		53908	194	**183**	192	...	183
48977	B2.5 V	L68	B2.5V		9893	24	**25**	44	30	25
49319			B6Vnne		52923	...	297	**225**	213	225
49333			B7IIIn		4613	53	60	**66**	47	66
49567	B3 II-III	L68	B3II-III		9888	56	**62**	78	70	62
49591			B9IV		40505	...	134	107	**117**	117
49606			B7III		14966	≤ 20	24	**23**	≤ 20	23
50013	B2 IV	HS	B1.5IVne		15981	183	**233**	269	...	233
50123			B6Vnpe		56825	...	156	**162**	134	162
50707			B1IV		27758	**45**	40	73	...	45
50820	B3 IVE+F	L68	B3IVe+K2II	SB	21027	64	**54**	73	55	54
51283			B3II-III		19710	152	**162**	173	...	162
51309	B3 II	L68	B3II		13937	54	**42**	40	30	42
52089	B2 II	HS	B2II		54337	47	**40**	62	...	40
52382	B1 Ib	L68	B1Ib		33293	**85**	78	69	...	85
52559	B2 IV-V	L68	B2IV-V		16535	...	...	...	...	...
52918	B1 IV	L68	B1V		52939	261	**257**	296	...	257
53138	B3 Ia	W76	B3Iab	SB	30169	63	**50**	41	30	50
53755	B0.5 IVn	L68	B0.5V+F5III	SB	8851	**294**	207	227	...	288
					27974	**281**	249	271	...	
53929			B9.5III		18961	25	26	$\leq$ **20**	≤ 20	≤ 20
53974	B0.5 III	L68	B0.5IV		10580	**129**	108	107	...	129
54031			B3V	SB	41438	29	...	**27**	≤ 20	27
54309	B2 IV	HS	B2IVe		29373	160	**155**	174	...	155
54893			B2IV-V		53220	32	**27**	41	≤ 20	27
55857			B0.5V		46933	**157**	150	191	...	157
55879	B0 III	L68	B0III		8852	**51**	70	103	...	51
56014			B3IIIe	2	38150	**223**	129	157	...	268
					41294	**312**	213	221	...	
56139			B2IV-Ve	?	15980	83	**88**	99	105	88
56456			B8-9V		34188	...	251	284	**250**	250
58050	B2 Ve	L68	B2Ve		16536	97	**119**	141	...	119
58343	B2.5 IVe	L68	B2.5IVe		16264	51	**43**	55	35	43
58350			B5Ia		7704	62	**47**	44	37	46
					30198	62	**46**	41	30	
58661			B9pHgMn		18985	≤ 20	34	**26**	≤ 20	26
58715	B8 V	HS	B8Ve	SB	31890	...	193	**197**	198	197
58978			B0IV:pe		54238	**304**	252	250	...	304
59635			B5Vp		52272	43	**27**	41	≤ 20	27
60606	B3 V	HS	B3Vne	SB	29375	162	**184**	196	215	184

continues next page ...

Results of line broadening analysis — *continued*

			B.S.C.			$v_e \sin i$ (km s^{-1})				
HD	Spectral Type	Ref	Spectral Type	SB	SWP	τSco	ιHer	πCet	αLyr	Ad.
60855	B2 Ve	L68	B2Ve		53906	190	**219**	241	325	219
61429			B8IV		4611	...	97	**92**	89	92
62226			B5V	2	39770	38	**34**	105	33	34
63462			B0V:pe:		41304	**359**	317	329	...	359
63578			B1.5IV	SB	5532	**79**	112	162	...	79
63922	B0 III	HS	B0III		40146	**45**	44	84	...	45
64503	B2.5 V	HS	B2.5V	SB	21950	112	**121**	155	300	121
64740			B1.5Vp		19153	125	**133**	175	...	133
64760			B0.5Ib		53781	**231**	175	...	...	231
64802			B2V		46848	56	**49**	64	53	49
65575	B3 IV	HS	B3IVp		21952	57	**50**	57	45	50
65818			B1Vp+B3IV:	2O	54424	**266**	311	310	...	266
65904			B4V		46849	127	**142**	155	157	142
66194			B2IVpne		31232	178	**214**	218	...	214
67536			B2.5Vn		53912	211	**220**	259	...	220
67880	B2.5 V	L68	B2.5V		53222	37	...	**47**	40	47
67888			B4V		31233	45	**36**	41	31	36
68217			B2IV-V		24913	98	**113**	134	158	113
68243	B1 IV	HS	B1IV	O	32437	**92**	99	133	...	92
68351			B9pSiCr	O	18969	...	44	**30**	≤ 20	30
68520	B6 IV	HS	B6IV	O	24456	42	23	$\leq$ **20**	≤ 20	≤ 20
68980			B1.5IIIe	2	36214	130	**144**	185	...	144
69081			B1.5IV		10159	160	**153**	174	...	153
69082			B2IV-V	2	7926	29	**24**	41	51	24
70556			B2IV-V	SB	51420	38	**33**	73	64	33
70930			B1V		5531	103	**100**	137	...	100
72067			B2Vn		29376	117	**154**	173	180	154
72232			B5III		14105	...	...	...	...	...
72350			B4IV		44774	111	**141**	171	173	141
73340			B8Si		9032	...	...	...	...	...
74067			B9V		24821	...	...	...	...	...
74195			B3IV	SB	21415	31	**23**	26	≤ 20	23
74196			B7Vn	SB	7908	...	270	**290**	273	290
74273			B1.5V		53919	**127**	135	167	...	127
74280	B4 V	L68	B3V	?	54052	82	**93**	106	89	93
74371			B6Iae		37494	60	**46**	45	42	46
74375	B1.5 III	HS	B1.5III	SB	53228	57	**47**	70	...	47
74455			B1.5Vn		5558	**169**	170	213	...	209
					52931	**249**	241	280	...	
74535			B8Si		48065	42	40	**36**	≤ 20	36
74560			B3IV	SB	53219	39	**27**	27	≤ 20	27
74575	B1.5 III	HS	B1.5III		5145	28	**28**	49	...	28
74753			B0IIIn		5557	**284**	198	224	...	284

continues next page ...

Results of line broadening analysis — *continued*

			B.S.C.			$v_e \sin i$ (km s^{-1})				
HD	Spectral Type	Ref	Spectral Type	SB	SWP	τSco	ιHer	πCet	αLyr	Ad.
75311	B3 V	HS	B3Vne		21953	182	**237**	273	312	237
75387			B2IV-V		7911	**28**	...	45	28	28
75759			B1-2III	2O	54009	**120**	...	...	...	120
76161			B3Vn		14122	...	230	**265**	275	265
76566			B3IV		14121	$\leq$ 20	...	**27**	$\leq$ 20	27
76805			B5V	1O	32421	68	54	**63**	56	63
78764	B2 IV	HS	B2IVe		26389	122	**126**	143	...	126
79158			B8IIIpMn		32947	...	48	**40**	34	40
79186			B5Ia		37499	64	**52**	45	38	52
79447	B3 III	HS	B3III		53231	24	$\leq$ **20**	$\leq$ 20	$\leq$ 20	$\leq$ 20
79469			B9.5V	SB	21401	...	185	**79**	72	79
79694			B5/6IV/V		46931	162	173	**168**	167	168
79931			B9III		4630	...	57	**51**	52	51
81188			B2IV-V	O	2081	35	**41**	97	59	41
					36789	...	...	...	...	
83058			B1.5IV	SB	53221	**64**	71	141	...	64
83754	B5 V	L68	B5V		54740	110	133	**136**	121	136
83953	B5 V	HS	B6Ve		56848	180	**252**	234	268	252
85871			B1IV	SB	15201	229	**226**	238	...	226
86360			B9IV	SB	9038	...	99	87	**95**	95
86440			B5Ib		6323	31	**30**	25	$\leq$ 20	30
86606	B1 Ib	W76	B9Ib		38784	**59**	47	74	...	59
86612			B4Ve		54628	114	**149**	165	158	149
87015	B2.5 IV	L68	B2.5IV		21988	152	**179**	198	288	179
87504			B9III-IV	2	50698	...	53	47	**46**	46
87543			B7IVne		33318	...	231	**221**	204	221
87901	B7 V	HS	B7V	SB	8648	...	264	**264**	247	247
					8649	...	236	**238**	309	
					10379	...	216	**213**	255	
					54284	...	254	**273**	276	
88661	B2 IV	HS	B2IVpne		53905	206	**220**	258	...	220
88825			B4Ve		31231	108	128	**116**	107	116
89080			B8III		32560	...	219	**184**	171	184
89688	B2.5 IV	L68	B2.5IV		10472	212	**190**	179	245	168
					21987	145	**146**	176	238	
89890			B3IIIe		33319	70	**60**	74	61	60
90264			B8V	2	7362	...	65	**48**	46	48
90994	B6 V	L68	B6V		9220	92	93	**81**	67	81
91120			B9Vn	SB	30911	...	243	**223**	209	223
91316	B1 Iab	W76	B1Ib	SB	4553	76	**67**	87	...	72
					8651	**77**	68	82	...	
					11312	76	**69**	80	...	
					53059	**73**	62	81	...	

continues next page ...

Results of line broadening analysis — *continued*

			B.S.C.			$v_e \sin i$ (km s^{-1})				
HD	Spectral Type	Ref	Spectral Type	SB	SWP	τSco	ιHer	πCet	αLyr	Ad.
91465			B4Vne		54082	169	**216**	226	254	216
91619			B7Iae		6324	59	**46**	42	29	46
92664			B9pSi		7905	79	53	**48**	30	48
93030			B0Vp	SB	54100	**100**	100	132	...	100
93563			B8-9IIIe		33317	...	226	**202**	171	202
93845	B2.5 IV	HS	B2.5IV		53883	50	**41**	47	33	41
96919			B9Ia		48010	80	43	**28**	26	28
98664			B9.5V s	SB	24818	...	...	...	...	...
98718			B5Vn		20793	...	**269**	309	269	269
100600	B4 V	L68	B4V	SB	9209	122	**141**	146	144	141
100673			B9Ve		36404	...	200	124	**128**	128
100889			B9.5Vn	SB	46757	...	231	144	**160**	160
101431			B9V		54190	...	179	103	**108**	108
102232			B6III		4628	33	37	**28**	$\leq$ 20	28
103192			B9IIIpSi		54240	...	191	**61**	52	61
104174			B9Vn		54669	...	272	229	**233**	233
104337	B1 V	L68	B1.5V	O	36492	96	**89**	215	...	89
105382	B4 III	HS	B6IIIe		36403	52	**61**	74	55	61
105937			B3V		44211	84	**95**	103	95	95
106231			B4IV		5658	126	**108**	129	156	108
106343			B1.5Ia		6320	85	**67**	57	...	67
106490	B2 IV	HS	B2IV		21954	**127**	137	170	...	127
106625			B8IIIpHgMn	SB	19063	...	32	**26**	$\leq$ 20	26
106911	B5 V	HS	B5Vn		21957	...	208	**234**	238	234
106983	B2.5 V	HS	B2.5V		46634	77	**60**	78	55	60
107348	B8 V	HS	B8Vne	SB	53833	...	214	**193**	200	193
108248	B0.5 IV	HS	B0.5IV	O	33950	**100**	95	131	...	104
					44493	**109**	115	124	...	
108257			B3Vn		19345	...	**257**	290	210	257
108483	B2 V	HS	B2V		20792	141	**162**	189	237	162
109026			B5V		51268	143	148	**151**	137	151
109387	B6 IIIp	L68	B6IIIpe	O	15056	...	175	**167**	187	160
					39973	...	170	**153**	134	
109668	B2 IV-V	HS	B2IV-V		20873	86	**100**	139	130	100
109857			B8Vne		36405	...	351	251	**204**	204
					39434	...	...	...	...	
109867	B0.7 Ib	W76	B1Ia		44494	**83**	74	81	...	83
110073			B8II/III	1	54182	41	...	$\leq$ **20**	$\leq$ 20	$\leq$ 20
110335			B6IVe	SB	44487	...	213	**179**	170	179
110432			B1IIIe	SB	40695	**274**	235	235	...	274
110879			B2.5V		45089	109	**121**	156	207	121
111123	B0.5 III	HS	B0.5III	SB	14931	**48**	43	102	...	48
111226			B8III		20277	...	69	**72**	75	72

continues next page ...

Results of line broadening analysis — *continued*

			B.S.C.			$v_e \sin i$ (km s^{-1})				
HD	Spectral Type	Ref	Spectral Type	SB	SWP	τSco	ιHer	πCet	αLyr	Ad.
111774			B8V		30559	...	...	...	...	...
111904			B9Ia		46883	75	39	**26**	$\leq$ 20	26
111973			B5Ia		46847	78	**58**	45	49	58
112078	B4 V	HS	B4Vne		21965	...	**325**	320	319	325
112091	B5 V	HS	B5Vne		40675	...	182	**174**	174	174
112092	B2 IV-V	HS	B2IV-V		21955	51	**33**	50	47	33
112413					4813	...	...	...	...	...
113120	B2 III	HS	B1.5IIIne		30910	345	**322**	367	...	322
113791			B1.5V	1O	44645	**21**	...	44	30	21
113797			B9V		22295	...	201	125	**127**	127
113904			B0Ia+WC5:	O	39551	**133**	...	...	...	133
116072			B2.5Vn		20362	150	**211**	212	212	211
116084			B2.5Ib		44795	83	**62**	46	34	62
116087			B3V		20791	165	**182**	198	196	182
118991			B8Vn		30072	...	334	283	**271**	271
119159			B0.5III		10807	**131**	112	125	...	131
119361			B8III		30561	...	...	...	...	...
120307	B2 IV	HS	B2IV	1O	36482	62	**54**	91	...	54
120315	B3 V	W71	B3V	?	10894	150	**121**	129	130	118
					55240	111	**114**	125	111	
120324	B2 IV-V	HS	B2IV-Ve	SB	51095	111	**139**	144	160	139
120640			B2Vp		14685	30	...	**40**	30	40
120709			B5IIIp		30546	29	...	$\leq$ **20**	$\leq$ 20	$\leq$ 20
120955			B4IV	O	30545	...	...	...	...	...
120991	B2 III	HS	B2IIIe		27498	66	**55**	89	...	55
121263			B2.5IV	2O	54855	**155**	184	205	...	155
121743	B2 IV	HS	B2IV		21956	70	**60**	91	80	60
121790	B2 IV-V	HS	B2IV-V		45209	108	**112**	131	118	112
121847			B8VpShell	SB	30530	...	...	...	...	...
122879	B0 Ia	W76	B0Ia		40897	**100**	90	...	...	100
122980	B2 V	HS	B2V		42106	$\leq$ **20**	...	34	27	$\leq$ 20
125238	B2.5 IV	HS	B2.5IV		20891	154	**192**	274	360	192
125288			B6Ib		6321	40	36	**26**	$\leq$ 20	26
125745			B8V		30543	...	...	...	...	...
125823			B7IIIp		14088	22	...	**37**	28	37
126341			B2IV		5208	$\leq$ **20**	...	43	51	$\leq$ 20
127381	B2 III	HS	B2III		48225	57	**54**	102	94	54
127971			B7V		50485	168	133	**126**	129	126
127972	B1.5 V	HS	B1.5Vne	SB	41260	230	**260**	264	...	260
128345	B5 V	HS	B5V		20786	118	155	**168**	161	168
129116	B3 V	HS	B3V		45090	112	**130**	146	145	130
132058	B2 III	HS	B2III/IV	SB	17458	85	**84**	123	...	84
132200	B2 IV	HS	B2IV	SB	17459	32	**27**	45	29	27

continues next page ...

Results of line broadening analysis — *continued*

			B.S.C.			$v_e \sin i$ (km s^{-1})				
HD	Spectral Type	Ref	Spectral Type	SB	SWP	τSco	ιHer	πCet	αLyr	Ad.
132742			B9.5V	O	45452	...	74	61	**68**	68
133029			B9pSiSrCr		6102	...	28	$\leq$ **20**	$\leq$ 20	$\leq$ 20
133242			B5V	SB	20364	...	152	**159**	163	159
134481	B9 V	HS	B9.5Vne		36776	...	206	137	**136**	136
134687			B3IV	1O	20219	29	...	**27**	$\leq$ 20	27
135160			B0.5Ve		16726	**164**	194	176	...	164
135348			B3IV		7685	90	**86**	84	79	86
136298	B1.5 IV	HS	B1.5IV		16778	185	**162**	183	...	162
136504			B2IV-V	2O	33285	85	**87**	109	117	87
136664	B4 V	HS	B4V		20789	107	**157**	168	180	157
137387			B3IVe		41240	199	**221**	225	...	221
137432			B4Vp		7689	75	60	**63**	57	63
138485	B2 Vn	L68	B2Vn	SB	20597	166	**201**	254	286	201
138690			B2IV		20890	189	**254**	288	...	254
138749	B6 Vnn	L68	B6Vnne		13588	...	**265**	293	272	284
					17096	...	**305**	306	272	
					50410	...	**283**	298	316	
138769	B3 IV	HS	B3IVp	SB	50593	72	**64**	70	51	64
139365			B2.5V	SB	40902	145	**180**	182	211	180
139892			B7V	2O	20197	...	...	...	...	...
140008			B5V	2O	22093	115	106	**112**	111	112
140436			B9IV+A3V		50595	...	221	107	**110**	110
141318			B2II	SB	39022	51	**41**	54	47	41
141556			B9IV	2O	48509	...	27	$\leq$ **20**	$\leq$ 20	$\leq$ 20
141637			B3V		22092	196	**238**	243	...	238
142184	B3 V	HS	B2.5Vne		34217	...	**275**	301	254	275
142301			B8IIIp		7899	106	75	**77**	57	76
					51414	78	78	**75**	52	
142514			B7III		23434	129	76	**68**	58	68
142669			B2IV-V		55200	79	**88**	108	84	88
142926			B9pe	O	44981	...	264	**249**	221	249
142983	B5 IIIp	L68	B5IIIp	?	8810	...	65	42	**23**	21
					54091	...	45	27	$\leq$ **20**	
142990			B5IV		51412	97	**100**	105	94	100
143018			B1V+B2V	2O	54422	**112**	237	252	...	112
143118			B2.5IV		42117	172	**180**	210	...	180
143275	B0.3 IV	HS	B0.3IV	SB	17395	**137**	160	149	...	137
143699			B6IV		50532	...	...	...	...	81
					51385	94	87	**81**	72	
144206			B9III		40560	...	...	$\leq$ **20**	$\leq$ 20	$\leq$ 20
144217	B0.5 V	L68	B1V	O	6233	**96**	158	246	...	96
144294	B2.5 V	HS	B2.5Vn		20787	215	**265**	315	...	259
					22090	192	**253**	265	304	

continues next page ...

Results of line broadening analysis — *continued*

			B.S.C.			$v_e \sin i$ (km s^{-1})				
HD	Spectral Type	Ref	Spectral Type	SB	SWP	τSco	ιHer	πCet	αLyr	Ad.
144334			B8p		9224	64	59	**50**	41	51
					51411	53	55	**52**	31	
144470	B1 V	W71	B1V		13906	**102**	101	144	...	102
144661			B7IIIp:		13953	52	42	**29**	22	29
144844			B9IVp:	2	51322	73	25	$\leq$ **20**	$\leq$ 20	$\leq$ 20
145389			B9p:Mn:	1O	6886	...	...	...	...	...
145482			B2V		19351	166	**165**	166	224	165
145483			B9V		16306	...	214	174	**172**	172
145502	B2 IVp	L68	B3V	O	29140	114	**119**	140	177	119
145842			B8V		50530	...	112	**97**	95	97
146001			B7IV		51399	...	106	**79**	66	79
147152			B6IV		19346	107	96	**100**	89	100
147165	B1 III	W71	B1III	O	39508	**61**	56	94	...	61
147628			B8IV		50531	...	128	**115**	117	115
147971			B4V	2O	50529	...	...	...	...	...
148112			B9pCr		2726	...	61	**34**	$\leq$ 20	34
					7548	...	...	...	...	
148184	B1.5 Ve	L68	B2IV:pe	1O	15059	**108**	121	140	...	110
					54090	**113**	109	144	...	
148199					4561	...	27	$\leq$ **20**	$\leq$ 20	$\leq$ 20
148379			B1.5Iape		4349	77	**60**	45	...	60
148605	B2 V	HS	B2V		39506	149	**160**	172	212	160
148688	B1 Ia	W76	B1Iae		1871	106	**78**	46	...	78
148703	B2 III	HS	B2III-IV	SB	39707	56	**53**	98	151	53
149038	O9.7 Iab	W76	B0Ia		36166	**100**	79	...	...	100
149121			B9.5III		19757	...	21	$\leq$ **20**	$\leq$ 20	$\leq$ 20
149438	B0.2 V	W71	B0V		9809	$\leq$ **20**	26	126	...	$\leq$ 20
					39686	$\leq$ **20**	23	132	...	
					52043	$\leq$ **20**	...	...	...	
149485			B7Vn		22216	...	264	**278**	286	278
149630			B9V		29408	...	315	216	**215**	215
149757	O9.5 Vnn	L68			15137	**405**	...	...	...	405
149822			B9pSiCrSr:		18973	...	86	**41**	33	41
150168			B1Iab-Ib	SB	47256	**126**	107	102	...	126
150745			B2IV-V		22218	106	**108**	125	138	108
150898			B0.5Ia		50552	**108**	75	80	...	108
151890	B1.5 IV	HS	B1.5V+B6.5V	2O	39367	217	**223**	276	...	223
152234	B0.5 Ia	W76	B0.5Ia	SB	16206	**100**	76	69	...	100
152235	B0.7 Ia	W76	B1Ia		33294	**86**	74	63	...	86
152236	B1.5 Ia+	W76	B1Iape		54152	123	**86**	66	...	86
152478			B3Vnep		36197	259	**321**	326	305	321
152614			B8V	2	6987	...	100	**93**	92	93
153261			B2IVne		31221	215	**241**	255	...	241

continues next page ...

Results of line broadening analysis — *continued*

			B.S.C.			$v_e \sin i$ (km s^{-1})				
HD	Spectral Type	Ref	Spectral Type	SB	SWP	τSco	ιHer	πCet	αLyr	Ad.
153613			B8V		51847	...	130	**129**	129	129
154090	B0.7 Ia	W76	B1Ia		14828	**88**	77	59	...	88
155763	B6 III	L68	B6III		4577	33	37	**34**	27	34
156247			B5Vnn+B5V	2O	14864	...	**77**	453	104	77
156633	B1.5 Vp	L68	B1.5Vp+B5III	2O	20596	110	**128**	175	434	128
157038			B4Ia		30759	92	**60**	44	97	60
157042			B2IIIne		29404	237	**273**	329	...	273
157056			B2IV	SB	4430	29	**24**	47	52	24
157246	B1 Ib	HS	B1Ib		54241	**260**	198	...	...	260
157741			B9V		17999	...	268	270	**286**	286
158408	B2 IV	HS	B2IV	SB	31685	54	**54**	104	94	54
158427	B3 V	HS	B2Vne	SB	50432	192	**240**	235	233	240
158643			B9.5Ve		54144	...	284	151	**167**	167
158926			B2IV+B	2	20627	**125**	136	166	...	125
159975			B8II-IIIp:Mn		2724	...	100	**86**	84	86
160578	B1.5 III	HS	B1.5III	SB	4348	101	**105**	151	...	105
160762	B3 IV	L68	B3IV	1O	5720	$\leq$ 20	$\leq$ **20**	23	$\leq$ 20	$\leq$ 20
					29958	36	...	**25**	$\leq$ 20	
162374			B6V		14091	55	**44**	49	31	44
162732			BepShell	O	44980	...	63	44	**29**	29
163955			B9V		48332	...	216	120	**121**	121
164284	B2 Ve	L68	B2Ve	SB	15482	208	**238**	258	...	256
					55946	310	**274**	...	...	
164353	B5 Ib	L68	B5Ib		4267	56	**40**	34	28	40
164402	B0 Ib	W76	B0Ib		54242	**91**	89	80	...	91
164637			B0.5III	SB	42280	**62**	52	73	...	62
164852	B3 IV	L68	B3IV	2O	29534	122	**156**	149	148	156
165024			B2Ib		6020	97	**87**	113	...	87
165174	B0 IIIn	L68	B0IIIn	?	5228	**320**	...	...	...	320
165516			B0.5Ib		48276	**72**	64	85	...	72
165793			B1II		50429	**61**	51	63	...	61
166014			B9.5V	SB	20852	...	282	129	**128**	128
166182	B2 IV	L68	B2IV		41861	51	**37**	57	40	37
166469			B9IVpSrEuCr		48396	...	33	$\leq$ **20**	$\leq$ 20	$\leq$ 20
166596			B2.5III		18143	173	**167**	181	...	167
166937			B8Iap	O	7080	153	49	**43**	40	40
					26610	59	45	**36**	31	
167128	B3 III	HS	B3IIIep	SB	31220	74	**70**	82	74	70
167264			B0Ia	SB	24190	**91**	95	...	...	91
167756			B0.5Ia		30452	**86**	74	78	...	86
168905			B2.5Vn		57019	200	**227**	212	246	227
169022			B9.5III		44754	...	207	147	**148**	148
169033	B8 V	HS	B8IV-Ve		19929	...	174	**144**	152	144

continues next page ...

Results of line broadening analysis — *continued*

			B.S.C.			$v_e \sin i$ (km s^{-1})				
HD	Spectral Type	Ref	Spectral Type	SB	SWP	τSco	ιHer	πCet	αLyr	Ad.
169467	B3 IV	HS	B3IV		39861	31	**25**	33	$\leq$ 20	25
170235			B2IVpe		36202	143	**155**	159	212	155
170740	B2 IV-V	L68	B2V		18314	40	**38**	72	60	38
171406	B4 V	L68	B4Ve		54738	175	**232**	211	226	232
171961			B8III		45848	83	57	**45**	37	45
172044			B8II-IIIpHg	O	3013	...	33	**25**	$\leq$ 20	25
172167					42521	...	23	$\leq$ 20	$\leq$ **20**	$\leq$ 20
					45285	...	25	$\leq$ 20	**23**	
172910			B2.5V		54739	37	...	**27**	$\leq$ 20	27
173300			B8III	SB	34012	59	35	**26**	$\leq$ 20	26
173948			B2II-IIIe		33589	140	**134**	145	...	134
174237	B2.5 V	L68	B2.5Ve	O	14703	126	**128**	148	146	139
					51040	144	**150**	159	174	
174632			B8V		44787	...	73	**65**	70	65
174638			B8IIpe	O	35836	...	**68**	...	116	68
175156	B5 II	L68	B5II		4479	33	**22**	$\leq$ 20	$\leq$ 20	22
					23985	$\leq$ 20	**22**	$\leq$ 20	$\leq$ 20	
175362			B8IVSi		44757	44	...	$\leq$ **20**	$\leq$ 20	$\leq$ 20
175640			B9III		13510	...	21	$\leq$ **20**	$\leq$ 20	$\leq$ 20
176162	B5 IV	L68	B5IV	SB	21008	31	**24**	30	$\leq$ 20	24
176437	B9 III	HS	B9III		24358	...	63	58	**58**	58
177003	B2.5 IV	L68	B2.5IV	SB	54674	40	$\leq$ **20**	24	$\leq$ 20	$\leq$ 20
177756			B9Vn		18018	...	206	**154**	150	154
177863			B8III		48407	83	70	**58**	57	58
178125			B8III	O	14866	88	54	**51**	49	51
178175	B2 Ve	L68	B2Ve	SB	15058	90	**128**	144	177	123
					19928	106	**118**	122	137	
178475	B6 IV	L68	B6IV		20851	...	202	**219**	202	219
179406	B3 V	L68	B3V		13865	127	**148**	138	135	166
					36940	141	**184**	171	154	
179761			B8II-III		20176	72	26	$\leq$ **20**	$\leq$ 20	$\leq$ 20
180163	B2.5 IV	L68	B2.5IV	1O	50600	48	**27**	26	$\leq$ 20	27
180554	B4 IV	L68	B4IV	1O	55228	103	**82**	83	69	82
180968	B1 IV	L68	B0.5IV		15214	255	**238**	234	...	234
					45641	**229**	226	...	...	
181182			B8III+K:	O	51044	...	135	**112**	99	112
181558			B5V		47819	56	24	$\leq$ **20**	$\leq$ 20	$\leq$ 20
181615			B2Vpe+ ... *	O	26881	273	182	**56**	49	56
181858	B3 V	W71	B3IVp		6037	24	**24**	27	$\leq$ 20	24
181869	B9 III	HS	B8V	SB	44759	...	67	**57**	57	57
182180			B2Vn		39596	...	**261**	263	258	261
182308			B9IVpHgMn		13512	...	24	$\leq$ **20**	$\leq$ 20	$\leq$ 20
183056			B9pSi	O	14982	...	121	**77**	57	77

continues next page ...

Results of line broadening analysis — *continued*

			B.S.C.			$v_e \sin i$ (km s^{-1})				
HD	Spectral Type	Ref	Spectral Type	SB	SWP	τSco	ιHer	πCet	αLyr	Ad.
183362	B3 Ve	L68	B3Ve		31218	242	**233**	250	259	233
184171	B3 IV	L68	B3IV		48876	40	**26**	25	$\leq$ 20	26
184279	B1 IV	W71			6034	150	**68**	63	49	68
184606			B8IIIn		4559	...	188	**202**	244	202
185037	B8 V	HS	B8Vne		26897	...	239	**245**	300	245
185330			B5II-III		18992	42	$\leq$ 20	$\leq$ **20**	$\leq$ 20	$\leq$ 20
185859	B0.5 Ia	L68	B0.5Iae		14207	**76**	63	79	...	76
185915	B6 IV	L68	B6IV	SB	14208	90	65	**64**	57	64
186122			B9IIIpHgMn		9528	...	$\leq$ 20	$\leq$ **20**	$\leq$ 20	$\leq$ 20
186500			B8V		50991	149	117	**96**	99	96
186882	B9.5 III	HS	B9.5IV+F1V	SB	9597	...	216	134	**143**	142
					14844	...	198	127	**140**	
186994	B0.2 IV	W71			5654	**149**	121	131	...	149
187235			B8Vn		26896	...	287	**304**	301	304
187567	B2.5 IVe	L68	B2.5IVe		36401	144	**174**	210	...	174
187811	B2.5 V	L68	B2.5Ve	?	21488	167	**221**	231	262	221
187879	B1 III	L68	B1III+B3V	O	6605	97	**87**	102	...	92
					38552	107	**98**	123	...	
188439	B0.5 IIIn	L68	B0.5IIIn	SB	10852	307	**229**	...	...	229
188665	B5 V	L68	B5V		8919	118	103	**105**	110	105
188892	B5 IV	L68	B5IV		20974	59	**38**	36	30	38
189103			B3IV	O	52095	36	**24**	30	$\leq$ 20	24
189395			B9Vn		4966	...	164	**151**	150	151
189687	B3 IV	L68	B3IVe	SB	19936	164	**206**	190	185	206
190229			B9pHgMn	1	4962	...	23	$\leq$ **20**	$\leq$ 20	$\leq$ 20
190603	B1.5 Ia	W71	B1.5Ia		14942	82	**70**	82	...	70
190993	B3 V	L68	B3V	SB	9960	105	**114**	125	116	114
191456	B0.5 II-III	W71			6136	**56**	53	75	...	56
191610	B2.5 V	L68	B2.5Ve	?	8600	251	**260**	260	304	245
					37154	185	**230**	242	260	
191877	B1 Ib	L68	B1Ibe		14825	159	**124**	134	...	124
192044			B7Ve		28251	...	...	...	...	...
192907			B9III		5719	...	24	$\leq$ 20	$\leq$ **20**	$\leq$ 20
193237	B2 pe	L68	B2pe		43339	101	**70**	...	...	70
193432			B9.5V		32300	...	...	...	...	...
193911			B8IIIne		29406	118	155	**148**	154	148
194092	B0.5 V	W71			16213	$\leq$ **20**	23	143	...	$\leq$ 20
194335	B2 Vne	L68	B2Ven	SB	52946	245	**315**	334	...	315
194636			B8II-III		47832	88	38	**26**	$\leq$ 20	26
195810	B6 III	L68	B6III		52067	98	47	**44**	34	44
196426			B8IIIp		19759	48	23	$\leq$ **20**	$\leq$ 20	$\leq$ 20
196519			B9III		48309	...	198	155	**140**	140
196740	B5 IV	L68	B5IV		18017	...	226	**271**	261	271

continues next page ...

Results of line broadening analysis — *continued*

			B.S.C.			$v_e \sin i$ (km s^{-1})				
HD	Spectral Type	Ref	Spectral Type	SB	SWP	τSco	ιHer	πCet	αLyr	Ad.
196867	B9 IV	HS	B9IV	SB	24451	...	155	112	**111**	111
197018			B6IIIpMn		14051	59	42	**40**	30	40
197511	B2 V	L68	B2V		10844	33	**37**	54	36	37
197702	B1 III(n)	W71			11290	277	**264**	359	...	264
197770	B2 III	L68	B2III	SB	49267	74	**67**	89	...	67
198174			B7IIIp		51082	...	47	**41**	31	41
198183	B6 IV	L68	B5Ve	?	14209	119	108	**104**	108	102
					25780	113	102	**101**	97	
198478	B2.5 Ia	W71	B3Ia		13907	77	**55**	46	46	53
					38688	70	**51**	39	46	
198625	B4 V	L68	B4Ve		36195	150	**207**	232	218	207
198667			B9III		14045	...	32	$\leq$ **20**	$\leq$ 20	$\leq$ 20
198820	B3 III	L68	B3III		8331	39	**27**	26	23	32
					19872	57	**38**	41	30	
199081	B5 V	L68	B5V	2O	10841	...	128	**146**	176	146
199140	B2 III	L68	B2IIIe		5600	**52**	43	88	...	40
					52885	33	**29**	48	...	
199218			B8Vnne		30071	...	281	**275**	237	275
199478			B8Ia		15552	60	**46**	43	31	46
199661	B2.5 IV	L68	B2.5IV		10845	115	**110**	126	372	110
199955			B5Vn		10862	...	134	**99**	104	99
200120	B1.5 Vnne	L68	B1ne	SB	17094	**341**	353	...	...	335
					52944	**329**	356	382	...	
200310	B1 Vn	L68	B1Ve	SB	10853	288	**267**	293	...	267
201345	ON9 V	W76			15004	**100**	95	119	...	100
201908			B8Vn	SB	45273	...	88	82	**93**	93
202214	B0 V	L68	B0II		21011	**38**	30	55	...	38
202654	B4 IV	L68	B4IV	SB	22646	114	**123**	127	105	123
202753			B5V		52920	36	36	**34**	$\leq$ 20	34
202850			B9Iab	SB	13460	...	...	...	...	...
202904	B2 Ve	L68	B2Vne	?	8601	138	**165**	177	196	165
203245	B6 V	L68	B6V	SB	22755	109	67	**66**	59	66
203467	B3 IVe	L68	B3IVe	SB	42020	127	**142**	152	148	142
203532			B3IV		16399	65	**59**	63	49	59
203664	B0.5 III(n)	W71			7355	**206**	172	206	...	206
204172	B0 Ib	W76	B0Ib		6481	**95**	78	86	...	95
					48946	**95**	88	83	...	
204770	B7 V	L68	B7V		8922	...	207	**172**	167	172
205021	B1 III	L68	B1IV	O	4609	**31**	34	96	...	35
					6235	**38**	33	59	...	
					52941	**36**	29	88	...	
205139	B1 Ib	L68	B1II		46540	**65**	51	74	...	65
205637	B2.5 Vp	L68	B2.5Vpe	?	34400	176	**165**	139	122	165

continues next page ...

Results of line broadening analysis — *continued*

			B.S.C.			$v_e \sin i$ (km s^{-1})				
HD	Spectral Type	Ref	Spectral Type	SB	SWP	τSco	ιHer	πCet	αLyr	Ad.
206165	B2 Ib	W71	B2Ib		6336	78	**63**	52	...	63
206540			B5IV		14023	57	25	$\leq$ **20**	$\leq$ 20	$\leq$ 20
206672	B3 IV	L68	B3IV	O	24332	77	**75**	92	74	75
207330	B2.5 III	L68	B3III	O	9210	67	**45**	50	38	45
207857			B9pHgMn		34436	...	...	...	...	...
207971	B8 III	HS	B8III		44768	...	51	**41**	33	41
208057	B3 V	L68	B3Ve	SB	5909	101	**89**	98	101	87
					33664	90	**85**	94	83	
208501			B8Ib		4217	...	**38**	33	40	38
208682	B2.5 Ve	L68	B2.5Ve		52942	224	**250**	270	...	250
209008	B3 III	L68	B3III		20593	37	**23**	26	$\leq$ 20	23
209014			B8V		31219	...	264	**264**	228	264
209409	B7 IVe	L68	B7IVe		5912	...	184	**185**	206	185
					39200	...	223	**185**	155	
209419	B5 III	L68	B5III		8921	40	27	**26**	$\leq$ 20	26
209459			B9.5V		21398	...	21	$\leq$ 20	$\leq$ **20**	$\leq$ 20
209522			B4IVne		52358	274	**255**	286	368	255
209952	B7 IV	HS	B7IV		48408	...	202	**192**	206	192
210129			B7Vne		44770	132	130	**106**	118	106
210191	B2.5 IV	L68	B2.5IV		23304	37	**24**	23	$\leq$ 20	24
210424			B7III		9041	35	22	$\leq$ **20**	$\leq$ 20	$\leq$ 20
211924	B5 IV	L68	B5IV		15217	53	44	**44**	30	44
212120	B6 V	L68	B6V	2O	26322	96	67	**63**	59	63
212454			B8III-IV		14974	57	41	**31**	30	31
212571	B1 Ve	L68	B1Ve		7009	**268**	276	283	...	272
					54752	**275**	291	...	...	
212581	B9.5 V	HS	B9.5V		26185	...	234	199	**194**	194
212710			B9.5Vn	2	48238	...	...	...	...	...
212978	B1.5 V	L68	B2V		6237	113	**102**	121	140	102
213420	B2 IV	L68	B2IV	O	20267	79	**60**	85	82	60
214168	B1.5 V	L68	B2Ve	SB	49149	288	**295**	274	...	295
214240	B3 IV	L68	B3V	2O	44796	80	**56**	54	48	56
214923	B8 V	HS	B8V		42071	...	185	129	**134**	134
214993	B1.5 III	W71	B2III	SB	5407	74	**60**	106	...	60
215573			B6IV		29817	39	22	$\leq$ **20**	$\leq$ 20	$\leq$ 20
216200	B4 III	L68	B3IV:	2	9205	134	**161**	177	194	161
216494			B9III	2O	55266	...	85	**64**	60	64
216916	B2 IV	L68	B2IV	1O	5361	**24**	...	46	...	24
217101	B2 IV-V	L68	B2IV-V		18309	99	**109**	127	156	109
217543	B3 Vp	L68	B3Vpe	SB	33666	183	**270**	245	194	270
217675			B6IIIpe+A2p	2O	52943	113	**181**	164	162	181
217833			B9IIIHe wk		14972	39	30	**25**	$\leq$ 20	25
217891	B6 Ve	L68	B6Ve		15512	61	81	**82**	72	82

continues next page ...

Results of line broadening analysis — *continued*

			B.S.C.			$v_e \sin i$ (km s^{-1})				
HD	Spectral Type	Ref	Spectral Type	SB	SWP	τSco	ιHer	πCet	αLyr	Ad.
218045	B9.5 III	HS	B9V	SB	41819	...	263	100	**107**	107
218376	B0.5 III	W71	B0.5IV		5363	**55**	46	85	...	55
219188	B0.5 ... *	W71			7711	**278**	230	...	...	278
219688	B5 Vn	L68	B5V		10385	...	**200**	217	290	200
219749			B9pSi	1O	6095	...	74	**73**	61	73
220599			B9III		48983	...	...	...	...	...
220885			B9III	SB	14970	...	66	**53**	47	53
221253	B3 IV	L68	B3IV	1O	51974	129	**133**	127	133	133
221507			B9.5IVpHgMnEu		18991	...	35	$\leq$ **20**	$\leq$ 20	$\leq$ 20
222173			B8V	SB	10376	...	60	**51**	51	51
222439			B9IVn		52658	...	196	144	**143**	143
222661	B9.5 V	HS	B9.5V	SB	24450	...	243	131	**129**	129
223640			B9pSiSrCr		5723	...	40	**26**	$\leq$ 20	26
223987	B1 II-III	W71			13763	105	**74**	67	...	74
224112			B8V		5718	...	37	**52**	30	52
224113			B6V	1O	5738	89	67	**63**	57	63
224151	B0.5 II-III	L68	B0.5II+B0.5II	O	26321	**102**	77	82	...	102
224572	B1 V	L68	B1V	2	20971	**142**	141	164	...	142
224686	B9 IV	HS	B9IV		22848	...	257	240	**207**	207
225094	B3 Iab	L68	B3Ia		9415	113	**74**	62	63	65
					18688	78	**56**	52	51	
225253			B8IV-V		4413	$\leq$ 20	25	$\leq$ **20**	$\leq$ 20	$\leq$ 20
269128					7138	130	**122**	140	92	122

REFERENCES: *GG – Garrison and Gray (1994); HS – Hauck and Slettebak (1989); L68 – Lesh (1968); W71 – Walborn (1971b); – W76 – Walborn (1976)*

HD 358. GG spectral type is kB9hB8HeB9 III.

HD 12767. GG spectral type is kB8hB8heB9 III.

HD 21699. GG spectral type is kB8hB7HeB9.5 III.

HD 181615. BSC spectral type is B2Vpe+A2IaShell.

HD 219188. W71 spectral type is B0.5 II-III(n).

Appendix E

Description of CD-ROM

The attached CD-ROM is written in ISO-9660 Level 1 format. Filenames are restricted to 8+3 uppercase characters for maximum portability.

The filesystem is as follows:

`/` The root directory contains several 'index' files. The files 00README.TXT and 00README.HTM contain descriptions of the CD contents. A hypertext version of the table in appendix D can be found in XCORR.HTM (or by following the links in 00README.HTM).

- `IMG/` Contains images for 00README.HTM.
- `THESIS/` Postscript version of this thesis.
  - `DOUBLE/` Typeset for double sided printing.
  - `SINGLE/` Typeset for single sided printing.

  Each chapter is stored in a separate .PS file. Each filename starts with a two digit number denoting the order the files should be printed in.
- `WHT_0895/` WHT/UES observations from August 1995 (see chapter 2). Observations are available as .SDF files and in printable postscript (.PS) format similar to appendix A.
- `XCORR/` This directory contains files used for the hypertext version of appendix D.
  - `EPS/` Contains encapsulated postscript plots of the cross-correlation functions. The plots are stored in subdirectories named after the cross-correlation template. Files are named with the

SWP number and this number is appended a C for 'raw' cross-correlation function, and F for normalised function with fit. The files are compressed using GZIP (Lempel-Ziv) compression.

`HTML/` Contains a hypertext summary of the results for each star. The files are named by the six digit HD number.

`JPG/` Contains low-resolution versions of the postscript files above for the HTML summaries.

`PSFILES/` Postscript versions of the hypertext summaries. Named by the HD catalogue number. The files are compressed using GZIP compression. Each file contains plots of the cross-correlation functions and a summary of the measurements and results for each star.

Bibliography

Abbott, D. C., 1982, *Astrophys. J.* **263**, 723

Adams, W. S. and Kohlschütter, A., 1914, *Astrophys. J.* **40**, 385

Aparicio, A., Herrero, A., and Sánchez, F. (eds.), 1998, *Stellar Astrophysic for the Local Group*, Cambridge University Press

Auer, L. H. and Heasley, J. N., 1974, *Astrophys. J.* **205**, 165

Baade, D. and Balona, L. A., 1994, in L. A. Balona, H. F. Henrichs, and J. M. Le Contel (eds.), *Pulsation, rotation and mass loss in early-type stars*, Vol. 162 of *IAU Symposia*, p. 311

Barker, P. K., 1984, *Astron. J.* **89**, 899

Bernacca, P. L. and Perinotto, M., 1970, *Contributions dell'Osservatorio Astrofisica dell'Universita di Padova in Asiago* **239**, 1

Bisiacchi, G. F., Lopez, J. A., and Firmani, C., 1982, *Astron. Astrophys.* **107**, 252

Bjorkman, J. E. and Cassinelli, J. P., 1993, *Astrophys. J.* **409**, 429

Bohannan, B., Abbott, D. C., Voels, S. A., and Hummer, D. G., 1986, *Astrophys. J.* **308**, 728

Bolton, C. T. and Rogers, G. L., 1978, *Astrophys. J.* **222**, 234

Butler, K., 1984, *Ph.D. thesis*, University of London

Butler, K. and Giddings, J. R., 1985, *CCP7 Newsletter on Analysis of Astronomical Spectra No. 9*, Daresbury Laboratory, UK

Cannon, A. J. and Pickering, E. C., 1918, *Ann. Astron. Obs. Harvard Coll.* 91-99

Castor, J. I., 1993, in J. P. Cassinelli and E. B. Churchwell (eds.), *Massive stars: Their lives in the interstellar medium*, Vol. 35 of *ASP Conference Series*, p. 297

Chiosi, C., 1998, in A. Aparicio, A. Herrero, and F. Sánchez (eds.), *Stellar Astrophysic for the Local Group*, p. 1, Cambridge University Press

Clayton, M., 1996, *Starlink Guide 9*

Code, A. D., Davis, J., C., B. R., and Hanbury Brown, R., 1976, *Astrophys. J.* **203**, 417

Collins, George W., I. and Truax, R. J., 1995, ApJ **439**, 860

Conti, P. S. and Alschuler, W. R., 1971, *Astron. J.* **170**, 325

Conti, P. S. and Ebbets, D., 1977, *Astrophys. J.* **213**, 438

Conti, P. S. and Frost, S. A., 1977, *Astrophys. J.* **212**, 728

Conti, P. S., Garmany, C. D., C., d., and Vanbeveren, D., 1983, *Astrophys. J.* **274**, 302

Conti, P. S. and Leep, E. M., 1974, *Astrophys. J.* **193**, 113

Conti, P. S., Leep, E. M., and Lorre, J. J., 1977, *Astrophys. J.* **214**, 759

Conti, P. S. and Underhill, A. B. (eds.), 1988, *O-type stars and Wolf-Rayet stars*, NASA SP

Day, R. W. and Warner, B., 1975, *Mon. Not. R. Astron. Soc.* **173**, 419

Doazan, V., 1987, in A. Slettebak and T. P. Snow (eds.), *Physics of Be stars*, Vol. 92 of *IAU Symposia*, p. 384

Franceschini, A., Silva, L., Fasano, G., Granato, L., Bressan, A., Arnouts, S., and Danese, L., 1998, *Astrophys. J.* **506**, 600

Fullerton, A. W., Gies, D. R., and Bolton, C. T., 1996, *Astrophys. J., Suppl. Ser.* **103**, 475

Garmany, C. D., 1994, *Publ. Astron. Soc. Pac.* **106**, 25

Garmany, C. D., Conti, P. S., and Chiosi, C., 1982, *Astrophys. J.* **263**, 777

Garmany, C. D., Conti, P. S., and Massey, P., 1980, *Astrophys. J.* **242**, 106

Garrison, R. F. and Gray, R. O., 1994, *Astron. J.* **107**, 1556

Giddings, J., Rees, P., Mills, D., and Clayton, M., 1996, *Starlink User Note 37*

Giddings, J. R., 1981, *Ph.D. thesis*, University of London

Gies, D. R., 1987, *Astrophys. J., Suppl. Ser.* **64**, 545

Gies, D. R. and Bolton, C. T., 1986, *Astrophys. J., Suppl. Ser.* **61**, 419

Gies, D. R. and Lambert, D. L., 1992, ApJ **387**, 673

Gray, D. F., 1992, *The observation and analysis of stellar photospheres*, Cambridge University Press

Grigsby, J. A., Morrison, N. D., and Anderson, L. S., 1992, *Astrophys. J., Suppl. Ser.* **78**, 205

Groenewegen, M. A. T., Lamers, H. J. G. L. M., and Pauldrach, A. W. A., 1989, *Astron. Astrophys.* **221**, 78

Hanson, M. M., 1998, in I. D. Howarth (ed.), *Boulder-Munich II: Properties of Hot,*

Luminous Stars, Vol. 131 of *ASP Conference Proceedings*, p. 1

Harmanec, P., 1987, in A. Slettebak and T. P. Snow (eds.), *Physics of Be stars*, Vol. 92 of *IAU Symposia*, p. 339

Hauck, B. and Slettebak, A., 1989, *Astron. Astrophys.* **214**, 153

Heber, U. and Jeffery, C. S. (eds.), 1992, *The Atmospheres of Early-Type Stars*, Vol. 401 of *Lecture Notes in Physics*

Herrero, A., 1987a, *Astron. Astrophys.* **171**, 189

Herrero, A., 1987b, *Astron. Astrophys.* **186**, 231

Herrero, A., Kudritzki, R. P., Vilchez, J. M., Kunze, D., Butler, K., and Haser, S., 1992, *Astron. Astrophys.* **261**, 209

Hjellming, R. M., 1968, *Astrophys. J.* **154**, 533

Hoffleit, D. and Warren Jr., W. H., 1991, *Bright Star Catalogue*, Electronic 5th Revised Edition

Howarth, I. D., 1997, *Observatory* **117**, 335

Howarth, I. D., Murray, J., Mills, D., and Berry, D. S., 1997a, *Starlink User Note 50*

Howarth, I. D. and Prinja, R. K., 1989, *Astrophys. J., Suppl. Ser.* **69**, 527

Howarth, I. D., Siebert, K. W., Hussain, G. A. J., and Prinja, R. K., 1997b, *Mon. Not. R. Astron. Soc.* **284**, 265

Hubeny, I., 1988, *Comput. Phys. Commun.* **52**, 103

Hubeny, I., 1998, in I. D. Howarth (ed.), *Boulder-Munich II: Properties of Hot, Luminous Stars*, Vol. 131 of *ASP Conference Proceedings*, p. 108

Hubeny, I. and Lanz, T., 1995, *Astrophys. J.* **439**, 875

Hummer, D. G., Abbot, D. C., Voels, S. A., and Bohannan, B., 1988, *Astrophys. J.* **328**, 704

Hummer, D. G. and Hubeny, I., 1991, in L. Crivellari, I. Hubeny, and D. G. Hummer (eds.), *Proceedings of the NATO Advanced Research Workshop on Stellar Atmospheres: Beyond Classical Models*, Vol. C 341 of *NATO ASI series*, p. 119

Humphreys, R. M., 1978, *Astrophys. J., Suppl. Ser.* **38**, 309

Jaschek, C. and Jaschek, M., 1987, *The classification of stars*, Cambridge University Press

Jaschek, M. and Jaschek, C., 1967, *Astrophys. J.* **150**, 355

Jaschek, M. and Jaschek, C., 1974, *Astron. Astrophys.* **36**, 401

Jenkner, H., Lasker, B. M., Sturch, C. R., McLean, B. J., Shara, M. M., and Russel, J. L., 1990, *Astron. J.* **99**, 2082

Kapteyn, J. C., 1914, *Astrophys. J.* **40**, 43

Kippenhahn, R. and Weigert, A., 1990, *Stellar Structure and Evolution*, Springer-Verlag

Kudritzki, R. P., 1988, *The Atmospheres of Hot Stars: Modern Theory and Observation*, Lecture notes for 18th Advanced Course by Swiss Society of Astronomy and Astrophysics

Kudritzki, R. P., 1992, A&A **266**, 395

Kudritzki, R. P. and Hummer, D. G., 1990, *Annu. Rev. Astron. Astrophys.* **28**, 303

Kudritzki, R. P., Simon, K. P., and Hamann, W.-R., 1983, *Astron. Astrophys.* **118**, 245

Lamers, H. J. G. L. M. and Fitzpatrick, E. L., 1988, ApJ **324**, 279

Lamers, H. J. G. L. M. and Leitherer, C., 1993, ApJ **412**, 771

Langer, N. and Heger, A., 1998, in I. D. Howarth (ed.), *Boulder-Munich II: Properties of Hot, Luminous Stars*, Vol. 131 of *ASP Conference Proceedings*, p. 76

Lanz, T., De Koter, A., Hubeny, I., and Heap, S. R., 1996, ApJ **465**, 359+

Lasker, B. M., Sturch, C. R., McLean, B. J., Russell, J. L., Jenkner, H., and Shara, M. M., 1990, *Astron. J.* **99**, 2019

Leitherer, C., Fritze-von Alvensleben, U., and Huchra, J. (eds.), 1996, *From stars to galaxies: The impact of stellar physics on galaxy evolution*, Vol. 98 of *ASP Conference Series*

Leonard, P. J. T. and Duncan, M. J., 1990, *Astron. J.* **99(2)**, 608

Lesh, J. R., 1968, *Astrophys. J., Suppl. Ser.* **17**, 371

Levato, H., Morrell, N., Garcia, B., and Malaroda, S., 1988, *Astrophys. J., Suppl. Ser.* **68**, 319

Maeder, A., 1998, in I. D. Howarth (ed.), *Boulder-Munich II: Properties of Hot, Luminous Stars*, Vol. 131 of *ASP Conference Proceedings*, p. 85

Maeder, A. and Meynet, G., 1987, *Astron. Astrophys.* **182**, 243

Maeder, A. and Meynet, G., 1989, A&A **210**, 155

Mason, B. D., Gies, D. R., Hartkopf, W. I., Bagnuolo., William G., J., Ten Brummelaar, T., and McAlister, H. A., 1998, *Astron. J.* **115**, 821

Mathys, G., 1988, *Astron. Astrophys. Suppl. Ser.* **76**, 427

Mathys, G., 1989, *Astron. Astrophys. Suppl. Ser.* **81**, 237

McErlean, N. D., Lennon, D. J., and Dufton, P. L., 1998, *Astron. Astrophys.* **329**, 613

Meynet, G., 1998, in I. D. Howarth (ed.), *Boulder-Munich II: Properties of Hot, Luminous Stars*, Vol. 131 of *ASP Conference Proceedings*, p. 96

Mills, D., Webb, J., and Clayton, M., 1997, *Starlink User Note 152*

Moffat, A. F. J., Marchenko, S. V., Seggewiss, W., Van Der Hucht, K. A., Schrijver, H., Stenholm, B., Lundstrom, I., Gunawan, D. Y. A. S., Sutantyo, W., Van Den Heuvel, E. P. J., De Cuyper, J. P., and Gomez, A. E., 1998, *Astron. Astrophys.* **331**, 949

Monteverde, M. I. and Herrero, A., 1998, in I. D. Howarth (ed.), *Boulder-Munich II: Properties of Hot, Luminous Stars*, Vol. 131 of *ASP Conference Proceedings*, p. 192

Monteverde, M. I., Herrero, A., Lennon, D. J., and Kudritzki, R. P., 1997, *Astrophys. J.* **474**, 107

Morton, D. C., 1969, *Astrophys. J.* **158**, 629

Murdoch, K. A., Drew, J. E., and Anderson, L. S., 1994, A&A **284**, L27

Palla, F. and Stahler, S. W., 1993, *Astrophys. J.* p. 414

Penny, L., 1996, *Astrophys. J.* **463**, 737

Plavec, M., 1976, in A. Slettebak (ed.), *Be and shell stars*, Vol. 70 of *IAU Symposia*, p. 439

Poveda, A., Ruiz, J., and Allen, C., 1967, *Bol. Obs. Tonantzintla y Tacubaya* **4**, 86

Press, W. H., Teukolsky, S. A., Vetterling, W. T., and Flannery, B. P., 1992, *Numerical Recipes in FORTRAN*, Cambridge University Press, 2nd edition

Puls, J., Kudritzki, R. P., Herrero, A., Pauldrach, A. W. A., Haser, S. M., Lennon, D. J. Gabler, R., Voels, S. A., Vilchez, J. M., Wachter, S., and Feldmeier, A., 1996, *Astron. Astrophys.* **305**, 171

Reid, A. H. N., 1994, *Ph.D. thesis*, University of London

Ringuelet, A. E., Fontenla, J. M., and Rovira, M., 1981, *Astron. Astrophys.* **100**, 79

Russell, J. L., Lasker, B. M., McLean, B. J., Sturch, C. R., and Jenkner, H., 1990, *Astron. J.* **99**, 2059

Schaller, G., Schaerer, D., Meynet, G., and Maeder, A., 1992, *Astron. Astrophys. Suppl. Ser.* **96**, 269

Schild, H., 1985, A&A **146**, 113

Schild, H. and Berthet, S., 1986, A&A **162**, 369

Scholtz, M., 1972, *Astron. Astrophys. Suppl. Ser.* **7**, 469

Schönberner, D., Herrero, A., Becker, S., Eber, F., Butler, K., Kudritzki, R. P., and Simon, K. P., 1988, *Astron. Astrophys.* **197**, 209

Shortridge, K., Meyerdierks, H., Currie, M., Clayton, M., and Lockley, J., 1997, *Starlink User Note 86*

Slettebak, A., 1956, *Astrophys. J.* **124**, 173

Slettebak, A., 1982, *Astrophys. J., Suppl. Ser.* **50**, 55

Slettebak, A., 1988, *Publ. Astron. Soc. Pac.* **100**, 770

Slettebak, A., Collins, G. W., Boyce, P. B., White, N. M., and Parkinson, T. D., 1975, *Astrophys. J., Suppl. Ser.* **29**, 137

Smith, K. C. and Howarth, I. D., 1994, *Astron. Astrophys.* **290**, 868

Smith, K. C. and Howarth, I. D., 1998, *Mon. Not. R. Astron. Soc.* **299**, 1146

Smith, M. A., Murakami, T., Ezuka, H., Anandarao, B. G., Chakraborty, A., Corcoran, M. F., and Hirata, R., 1997, *Astrophys. J.* **481**, 479

Stone, R. C., 1991, *Astron. J.* **102(1)**, 333

Striganov, A. R. and Sventitskii, N. S., 1968, *Tables of Spectral Lines of Neutral and Ionized Atoms*, IFI/Plenum Data Corporation, New York, N.Y. 10011

Thaller, M. L., 1997, ApJ **487**, 380+

Tweedy, R. W. and Clayton, M., 1996, *Starlink Guide 7*

Uesugi, A. and Fukuda, I., 1982, *Revised Catalogue of Stellar Rotational Velocities*, Department of Physics & Astronomy, Kyoto University

Underhill, A. B., 1953, *Astron. J.* **58**, 210

Underhill, A. B., 1982, *Astrophys. J.* **263**, 741

Underhill, A. B., 1987, in *Physics of Be stars*, Vol. 92 of *IAU Symposia*

Underhill, A. B., Divan, L., Prévot-Burnichon, M. L., and Doazan, V., 1979, *Mon. Not. R. Astron. Soc.* **189**, 601

Vacca, W. D., Garmany, C. D., and Shull, J. M., 1996, ApJ **460**, 914+

Voels, S. A., Bohannan, B., Abbott, D. C., and Hummer, D. G., 1989, *Astrophys. J.* **340**, 1073

von Zeipel, H., 1924, *Mon. Not. R. Astron. Soc.* p. 665

Walborn, N. R., 1970, *Astrophys. J.* **161**, L149

Walborn, N. R., 1971a, *Astrophys. J.* **164**, L67

Walborn, N. R., 1971b, *Astrophys. J., Suppl. Ser.* **23**, 257

Walborn, N. R., 1973, *Astron. J.* **78**, 1067

Walborn, N. R., 1976, *Astrophys. J.* **205**, 419

Walborn, N. R., 1988, in K. Nomoto (ed.), *Atmospheric Diagnostics of Stellar Evolution: Chemical peculiarity, mass loss, and explosion*, Vol. 108 of *IAU Symposia*

Walborn, N. R. and Bohlin, R. C., 1996, *Publ. Astron. Soc. Pac.* **108**, 477

Walborn, N. R. and Nichols-Bohlin, J., 1987, *Publ. Astron. Soc. Pac.* **99**, 40

Walborn, N. R. and Panek, R. J., 1984a, *Astrophys. J., Lett.* **280**, L27

Walborn, N. R. and Panek, R. J., 1984b, *Astrophys. J.* **286**, 718

Walborn, N. R. and Panek, R. J., 1985, *Astrophys. J.* **291**, 806

Williams, R. E., Blacker, B., Dickinson, M., Dixon, W. V. D., Ferguson, H. C., Fruchter, A. S., Giavalisco, M., Gilliland, R. L., Heyer, I., Katsanis, R., Levay, Z., Lucas, R. A., McElroy, D. B., Petro, L., Postman, M., Adorf, H.-M., and Hook, R., 1996, *Astron. J.* **112**, 1335